Looking for hot Jupiters around young stars

Louise Fey Yu

Université Fédérale

Toulouse Midi-Pyrénées

THÈSE

En vue de l'obtention du

DOCTORAT DE L'UNIVERSITÉ DE TOULOUSE

Délivré par : *l'Université Toulouse 3 Paul Sabatier (UT3 Paul Sabatier)*

Présentée et soutenue le *06/12/2019* **par :**

Louise Yu

Recherche de Jupiters chauds autour d'étoiles jeunes

JURY

RIEUTORD	Michel	Président du Jury
DELEUIL	Magali	Rapportrice
DOUGADOS	Catherine	Rapportrice
BARUTEAU	Clément	Examinateur
BOUVIER	Jérôme	Examinateur
COLLIER CAMERON	Andrew	Examinateur
MOUTOU	Claire	Co-Encadrante

École doctorale et spécialité :
SDU2E : Astrophysique, Sciences de l'Espace, Planétologie

Unité de Recherche :
Institut de Recherche en Astrophysique en Planétologie (IRAP, UMR 5277)

Directeur de Thèse :
Jean-François DONATI

Rapporteurs :
Magali DELEUIL et *Catherine DOUGADOS*

Abstract

The past 25 years have seen the detection of about 400 hot Jupiters (hJs), giant exoplanets similar to Jupiter but orbiting their star a hundred times closer than Jupiter does the Sun. These puzzling planets are believed to have formed far from their star before migrating inwards, however the physical processes that drive this orbital transfer are still poorly constrained by observations. This question, essential to our understanding of planetary system formation, has profound implications for the architecture of these systems, and in particular for the probability of forming planets like the Earth in the habitable zone of stars.

In order to better constrain the early orbital evolution of planetary systems, we analyze data collected within the frame of the MaTYSSE programme to search for hJs around weak-line T Tauri stars (wTTSs), i.e. very young Sun-like stars that stopped accreting. The main goal of MaTYSSE is to characterize the high magnetic activity of wTTSs. This activity makes hJ detection difficult, indeed, we look for hJs with the velocimetry technique, but the strong presence of magnetic dark spots and bright plages on the surface of wTTSs adds a jitter in the radial velocities (RVs), of much greater amplitude than that expected of a hJ signature.

In this thesis, we model the magnetic activity of wTTSs TAP 26 and V410 Tau and filter the activity jitter out of their RVs. We also present the MaTYSSE results for star V830 Tau, for comparison. Using Zeeman-Doppler Imaging on spectropolarimetric data sets to reconstruct surface brightness distributions and magnetic topologies, we derive spot-and-plage coverages of 10 – 18 % and field strengths of 300 – 600 G. All three stars exhibit intrinsic variability not explained by differential rotation.

The activity jitter is modelled with two independent methods: deriving it from our ZDI maps, or applying Gaussian Process Regression to the raw RVs. Both methods concur on the detection of a hJ around V830 Tau and another around TAP 26. The $\sim$2 Myr V830 Tau b has a $M \sin i$ of $0.57 \pm 0.10\,\mathrm{M_{Jup}}$ and orbits at 0.057 ± 0.001 au from its star (orbital period $\sim$4.93 d). Due to the observing window, the orbital period of TAP 26 b cannot be uniquely determined; the case with highest likelihood is a hJ with $M \sin i = 1.66 \pm 0.31\,\mathrm{M_{Jup}}$ on an orbit of semi-major axis 0.0968 ± 0.0032 au (orbital period 10.79 ± 0.14 d). These detections suggest that type II disc migration is efficient at generating newborn hJs, and that hJs may be more frequent around young stars than around mature stars, or the MaTYSSE sample is biased towards hJ-hosting stars.

Our V410 Tau RVs exclude the presence of a Jupiter-mass companion below $\sim$0.1 au, which is suggestive that hJ formation may be inhibited by the early depletion of the circumstellar disc, which for V410 Tau may have been caused by the M dwarf stellar companion orbiting a few tens of au away.

Resumé

Les 25 dernières années ont vu la détection d'environ 400 Jupiters chauds (hJs), exoplanètes géantes semblables à Jupiter mais sur des orbites cent fois plus resserrées. Ces planètes étonnantes se seraient formées loin de leur étoile avant de migrer vers elle, cependant les processus physiques à l'origine de ce transfert orbital sont encore peu contraints par les observations. Cette question, essentielle à notre compréhension de la formation des systèmes planétaires, a de profondes répercussions sur l'architecture de ces systèmes, et en particulier sur la probabilité de former des planètes telles que la Terre dans la zone habitable des étoiles.

Afin de mieux contraindre l'évolution orbitale précoce des systèmes planétaires, nous analysons des données recueillies dans le cadre du programme MaTYSSE pour rechercher des hJs autour d'étoiles T Tauri à raies faibles (wTTSs), c'est-à-dire de très jeunes étoiles de type solaire qui n'accrètent plus. L'objectif principal de MaTYSSE est de caractériser l'importante activité magnétique des wTTSs. Cette activité rend la détection de hJs difficile, en effet, nous recherchons des hJs par la technique de vélocimétrie, mais la forte présence de taches sombres et de plages brillantes magnétiques à la surface des wTTSs ajoute une perturbation dans les vitesses radiales (RVs), d'amplitude bien supérieure à celle attendue d'une signature de hJ.

Dans cette thèse, nous modélisons l'activité magnétique des wTTSs TAP 26 et V410 Tau et filtrons la perturbation des RVs due à l'activité. Nous présentons également les résultats MaTYSSE sur l'étoile V830 Tau pour comparaison. En utilisant l'imagerie Zeeman-Doppler sur des jeux de données spectropolarimétriques pour reconstruire les distributions surfaciques de brillance et les topologies magnétiques, nous obtenons des couvertures en taches et plages de $10 - 18\,\%$ et des champs de $300 - 600\,\mathrm{G}$. Les trois étoiles présentent une variabilité intrinsèque non expliquée par la rotation différentielle.

La perturbation RV due à l'activité est modélisée à l'aide de deux méthodes indépendantes : nous la dérivons à partir de nos cartes ZDI, ou nous appliquons la régression par processus gaussiens aux RVs brutes. Les deux méthodes s'accordent sur la détection d'un hJ autour de V830 Tau et d'un autre autour de TAP 26. V830 Tau b, âgé de $\sim 2\,\mathrm{Myr}$, a un $M \sin i$ de $0.57 \pm 0.10\,\mathrm{M_{Jup}}$ et orbite à $0.057 \pm 0.001\,\mathrm{au}$ de son étoile (période orbitale $\sim 4.93\,\mathrm{d}$). La période orbitale de TAP 26 b ne peut être déterminée de façon unique à cause de la fenêtre d'observation ; le cas le plus probable est un hJ avec $M \sin i = 1.66 \pm 0.31\,\mathrm{M_{Jup}}$ sur une orbite de demi-grand axe $0.0968 \pm 0.0032\,\mathrm{au}$ (période orbitale $10.79 \pm 0.14\,\mathrm{d}$). Ces détections suggèrent que la migration de type II dans le disque est efficace pour générer des hJs nouveau-nés, et que les hJs sont peut-être plus fréquents autour des étoiles jeunes qu'autour des étoiles matures, ou que l'échantillon MaTYSSE est biaisé vers les étoiles hôtes de hJs.

Nos RVs de V410 Tau excluent la présence d'un compagnon de masse Jovienne en-deçà de $\sim 0.1\,\mathrm{au}$, ce qui suggère que la formation de hJs est peut-être inhibée par l'épuisement précoce du disque circumstellaire, qui pour V410 Tau aurait été causé par le compagnon stellaire, une naine M orbitant à quelques dizaines de au de l'étoile.

Contents

Remerciements

Tout d'abord, un énorme merci à Magali et Catherine pour avoir bien voulu lire et évaluer mon manuscrit en un intervalle de temps restreint. Merci bien sûr à Jean-François, sans qui cette thèse n'aurait pas eu lieu, pour ton accompagnement durant presque quatre ans, pour ta patience, le temps que tu as toujours pu me consacrer, et pour tout ce que tu m'as appris. Merci beaucoup à Claire et Clément pour des discussions toujours enrichissantes et pour votre bonne humeur constante. Enfin, merci à Michel, Andrew et Jérôme d'avoir bien voulu être examinateurs de ma soutenance et pour des discussions intéressantes pendant ma thèse.

Ces trois ans et demi ont été l'occasion de former de belles amitiés, qui ont agrémenté ce passage de vie particulier de précieux moments de bonheur. Un merci plein de tendresse donc aux Bras Cassés : Adrien, Mathilde, Edo, Pauline, Geoffroy, pour les jeux, les soirées, les rires. Et un grand merci à Babak, pour tous les fous rires, la musique, ton soutien, ton aide, ta bonne humeur et ta joie de partager inépuisables.

Je remercie l'équipe du PS2E pour leur accueil, pour les discussions, les Journal Clubs, les workshops : les sus-mentionnés Clément et Michel, mais aussi Pascal, Arturo, Laurène (merci pour l'école SunStars à Banyuls !), Sébastien. Merci également à tous ceux, au sein de l'IRAP, qui m'ont aidée à diverses occasions : Geneviève, Émilie, Carole, Patricia, Isabelle, Loïc.

A special thank you to those who welcomed me in St Andrews in October 2017 : Andrew and Moira, and the students Josh, Chris, Dom, Laith, Kirsten, Meng and Fran for the Friday meals and game nights. Finally, thanks to Paloma for your company and to Maries for hosting me.

Merci également à toute l'équipe d'UniverSCiel, pour d'inoubliables moments lors des festivals astrojeunes et autres sorties : Marina, Gab, Wilou, Turpin, Jason, Ppeille, Tata, Lulu, Neuha, Heussaff, Edo, Didi, Jeff, Babak, Ines, Damien, Sacha, Gabi, Simon, Mika, PM, Momo, Hadrien, Mehdi, Abe.

Je remercie tous les doctorants et post-doctorants qui sont passés à l'IRAP avant, en même temps et après moi, pour les conseils, les discussions, les parties de tarot et, pour certains, leur amitié : CHill, Colin F, Andres, Logithan, Elodie, Giovanni, Cyril, Damien, Ppeille, Wrappin, Fitouss, Kevin, Nicolas, Jessie, David, Najda, Annick, Armelle, Étienne, Damien, Gaylor, Paul, Abe, Anthony, Bonnie, Tianqi, Benjamin, Nu, Grégoire, Paul, Benjamin, Florian, Ludivine, Mélina, Léo, Mégane.

Merci aux amis d'horizons divers, pour certains loin de Toulouse, mais toujours là dans ma vie : Antoine, Audrey, Florian, Marine, Raphaël, Élise, Ao, Julien, Luana, Marion, Ambroise, Momo, Fred, Lina, HS, Jenn, Lilly, Claire et Lætitia.

Et enfin, le plus grand des mercis à ma famille, Maman, Papa, Raph, qui ont toujours été là pour moi, merci pour votre soutien et votre amour inconditionnels, j'ai beaucoup de chance de vous avoir.

Foreword

The search for exoplanets has yielded around 4000 confirmed detections in the past 30 years, in around 3000 planetary systems. Those extrasolar systems are of very diverse configurations, with many tightly-packed systems of terrestrial planets all on orbits smaller than the orbit of Mercury, some systems with one or several gas giants as massive as Jupiter or Saturn, a few systems orbiting two stars (Winn & Fabrycky, 2015)... A few candidate Solar system analogs, with a gas giant on a low-eccentricity orbit of several astronomical units around a Sun-like star, were detected as well (Barbato et al., 2018). Simultaneously to observational efforts of establishing exoplanetary population statistics, theories on the formation and evolution of planetary systems were developed to explain the current diversity of orbital configurations, and eventually assess how much of an exception the Solar system is (e.g. Mordasini, 2018).

In particular, the origins of hot Jupiters (hJs), i.e. giant planets on close-in orbits, estimated to occur around $\sim$1 % of Sun-like stars (Wright et al., 2012), are mysterious. In-situ formation in the protoplanetary disc, the primordial dust and gas planet-forming matrix around the forming star, has long been considered implausible, because the high keplerian velocities and the limited quantity of material close to the star make it difficult to build up sufficiently massive cores. Some recent studies have argued in favor of it (e.g. Batygin et al., 2016), but its feasibility is still debated (Dawson & Johnson, 2018). Two theories suggesting that giant planets form far from the star and then migrate inwards have been proposed. Such massive planets have a large gravitational influence impacting their whole planetary systems, constraining their migration would therefore be an essential first step to model the evolution of planetary systems. Shortly after the first confirmed detection of a planet around a Sun-like star (Mayor & Queloz, 1995), a circular hJ in fact, Lin et al. (1996) showed that a scenario where the giant planet migrated within its protoplanetary disc through interactions with the surrounding dust and gas, on a time scale shorter than the lifetime of the disc ($\sim$1 Myr), could explain the observations. As more giant planets got detected, their distributions of orbital eccentricities and of obliquities, depending on the distance separating them to their host star, led to another scenario where gravitational interactions between planets and with their star caused instabilities, sending them on eccentric and inclined orbits. Those which were sent on orbits crossing the influence area of stellar tidal forces would then lose orbital energy and see their orbit become circular again, over time scales of 10^2 – 10^3 Myr (Dawson & Johnson, 2018). The study of hJs aged a few Myr, around stars whose protoplanetary discs have dissipated, can therefore be a key element to investigate which migration processes dominate.

However, Sun-like stars of a few Myr that have lost their discs, called weak-line T Tauri stars (wTTSs), have an important magnetic activity that causes large-amplitude modulations of their measured luminosity and radial velocity (RV; Grankin et al., 2008; Crockett et al., 2012). As a result, potential hints of a planetary presence, either a dip in the light curve betraying a transiting planet, or a wobble in the RV curve indicating the star's reflex motion from the planet's gravitational pull, are drowned in variations an order of magnitude larger than the expected planetary signature amplitudes. Astronomers have studied the variability and activity of wTTSs since the mid-20th century, but the research for hJs around them had to wait for the advent of spectropolarimetry,

combined with magnetic imaging techniques, and its application to wTTS targets. This thesis is part of one of the pioneering programmes in the search for young hJs: MaTYSSE (Donati et al., 2014).

More precisely, MaTYSSE, which stands for Magnetic Topologies of Young Stars and the Survival of close-in massive Exoplanets, aims at characterizing the magnetic activity of wTTSs, comparing it to the magnetic activity of Sun-like stars at earlier and later evolution stages, and searching for hJs around them. It is based upon the spectropolarimetric monitoring of 35 wTTSs, with observations collected between 2013 and 2016 with the twin echelle spectropolarimeters ESPaDOnS (Donati, 2003), installed at the Canada-France-Hawaii Telescope (CFHT), Hawaii since 2004, and NARVAL, installed at the Télescope Bernard Lyot (TBL), France since 2006. From the spectra provided by these instruments, both unpolarized and circularly polarized, we use the Zeeman-Doppler Imaging (ZDI) technique, first developed in the 90s (Semel, 1989) and having undergone successive updates until 2014 (Donati et al., 2014), to reconstruct the surface distribution of brightness and of magnetic field for our wTTSs. Because RVs are measured from the spectral lines in the unpolarized spectra, the activity RV jitter originates from distorsions of the spectral lines mainly due to surface brightness inhomogeneities; therefore our ZDI brightness maps are used to model the activity RV jitter and filter it out, in order to investigate the potential presence of hJ signatures in the filtered RV curves. ZDI has proven an efficient filtering technique for wTTSs prior to this thesis, with the first two MaTYSSE papers on stars LkCa 4 (Donati et al., 2014), V819 Tau and V830 Tau (Donati et al., 2015).

This thesis presents the investigation of the activity and RVs of two more MaTYSSE stars, $\sim$17 Myr, $\sim$1 $M_\odot$ TAP 26 and $\sim$0.8 Myr, $\sim$1.4 $M_\odot$ V410 Tau, as well as V830 Tau, on which more recent data sets were collected. On top of using ZDI, another numerical technique is applied, called Gaussian Process Regression (GPR) and first proposed to the application of exoplanet hunting by velocimetry in Haywood et al. (2014). Applied directly to the raw RVs, GPR is a technique independent from ZDI, that does not rely on a physical model but assumes a given statistical behaviour of the RV curve, with the RV activity jitter being described as a correlated noise. The modelling process thus consists in finding the main parameters characterizing this statistical behaviour, providing at the same time information on the stellar activity.

The first chapter outlines the context of the whole study and presents the broad lines of what constitutes the current theories of star and planet formation and early evolution; in a second chapter, we detail the problem of modelling wTTS activity and describe the various complementary modelling techniques used for this work; chapter three then presents the results of applying our activity modelling techniques to TAP 26, V410 Tau and V830 Tau, and chapter four presents the investigation of the RV curves of these stars. Finally, we draw some conclusions that this thesis brought to the field of star and planet formation, and give some future perspectives.

Avant-propos

La recherche d'exoplanètes a donné lieu à environ 4000 détections confirmées au cours des 30 dernières années, dans environ 3000 systèmes planétaires. Ces systèmes extrasolaires sont de configurations très diverses, avec de nombreux systèmes de planètes telluriques très resserrés, sur des orbites plus petites que celle de Mercure, certains systèmes avec une ou plusieurs géantes gazeuses aussi massives que Jupiter ou Saturne, quelques systèmes en orbite autour de deux étoiles (Winn & Fabrycky, 2015)... Quelques systèmes potentiellement analogues du système solaire, avec une géante gazeuse sur une orbite à faible excentricité de plusieurs unités astronomiques autour d'une étoile semblable au Soleil, ont également été détectés (Barbato et al., 2018). Parallèlement aux efforts d'observation visant à établir des statistiques sur les populations exoplanétaires, des théories sur la formation et l'évolution des systèmes planétaires ont été élaborées pour expliquer la diversité actuelle des configurations orbitales, et finalement évaluer dans quelle mesure le système solaire fait exception (voir par exemple Mordasini, 2018).

En particulier, les origines des Jupiters chauds (hJ), planètes géantes placées sur des orbites resserrées, dont la fréquence autour des étoiles semblables au Soleil est estimée à $\sim$1 % (Wright et al., 2012), sont mystérieuses. La formation in-situ dans le disque protoplanétaire, la matrice de poussière et de gaz autour de l'étoile et des planètes en formation, a longtemps été considérée comme improbable, car les vitesses képlériennes élevées et la quantité limitée de matière à proximité de l'étoile rendent difficile la constitution de noyaux suffisamment massifs. Certaines études récentes ont plaidé en sa faveur (par exemple Batygin et al., 2016), mais sa faisabilité est encore débattue (Dawson & Johnson, 2018). Deux théories suggérant que les planètes géantes se forment loin de l'étoile et migrent ensuite vers l'intérieur ont été proposées. De telles planètes massives ont une grande influence gravitationnelle qui a un impact sur l'ensemble de leur système planétaire, comprendre leur migration serait donc une première étape essentielle pour modéliser l'évolution des systèmes planétaires. Peu après la première détection confirmée d'une planète autour d'une étoile semblable au Soleil (Mayor & Queloz, 1995), qui était d'ailleurs un hJ sur orbite circulaire, Lin et al. (1996) a montré qu'un scénario où la planète géante migrait à l'intérieur de son disque protoplanétaire par des interactions avec la poussière et le gaz environnant, sur une échelle de temps plus courte que la durée de vie du disque ($\sim$1 Myr), pourrait expliquer les observations. Au fur et à mesure que des planètes géantes furent détectées, la distribution de leurs excentricités et de leurs obliquités orbitales, en fonction de la distance qui les sépare de leur étoile hôte, a conduit à un autre scénario où les interactions gravitationnelles entre les planètes et avec leur étoile provoquent des instabilités, les envoyant sur des orbites excentriques et inclinées. Celles qui étaient envoyées sur des orbites traversant la zone d'influence des forces de marée stellaires perdraient alors de l'énergie orbitale et verraient leur orbite redevenir circulaire, sur des échelles de temps de 10^2 – 10^3 Myr (Dawson & Johnson, 2018). L'étude des hJs âgés de quelques Myr, autour d'étoiles dont les disques protoplanétaires se sont dissipés, peut donc être un élément clé pour étudier les processus de migration.

Cependant, les étoiles de quelques Myr, semblables au Soleil, qui ont perdu leurs disques, appelées étoiles T Tauri à raies faibles (wTTS), ont une activité magnétique importante qui provoque

des modulations de grande amplitude dans leurs courbes de luminosité et de vitesse radiale (RV ; Grankin et al., 2008; Crockett et al., 2012). Par conséquent, les indices potentiels d'une présence planétaire, soit une baisse de la courbe de lumière trahissant une planète en transit, soit une oscillation de la courbe RV indiquant le mouvement réflexe de l'étoile causé par l'attraction gravitationnelle de la planète, sont noyés dans des variations d'un ordre de grandeur supérieur aux amplitudes attendues des signatures planétaires. Les astronomes ont étudié la variabilité et l'activité des wTTSs depuis le milieu du 20e siècle, mais la recherche des hJs autour d'elles a dû attendre l'avènement de la spectropolarimétrie, combinée aux techniques d'imagerie magnétique, et leur application aux wTTSs. Cette thèse fait partie d'un des programmes pionniers dans la recherche de jeunes hJs : MaTYSSE (Donati et al., 2014).

Plus précisément, MaTYSSE, qui signifie Magnetic Topologies of Young Stars and the Survival of close-in massive Exoplanets, vise à caractériser l'activité magnétique des wTTSs, à la comparer à celle des étoiles semblables au Soleil à des stades d'évolution antérieurs et postérieurs, et à rechercher des hJs autour de ces wTTSs. Le programme se base sur le suivi spectropolarimétrique de 35 wTTSs, avec des observations collectées entre 2013 et 2016 avec le spectropolarimètre à échelle ESPaDOnS (Donati, 2003), installé au Télescope Canada-France-Hawaï (CFHT), Hawaï depuis 2004, ainsi que son jumeau NARVAL, installé au Télescope Bernard Lyot (TBL), France depuis 2006. À partir des spectres, non polarisés et polarisés circulairement, fournis par ces instruments, nous utilisons la technique d'imagerie Zeeman-Doppler (ZDI), développée pour la première fois dans les années 90 (Semel, 1989) et ayant subi des mises à jour successives jusqu'en 2014 (Donati et al., 2014), pour reconstruire la distribution surfacique de brillance et de champ magnétique de nos wTTSs. Les RVs étant mesurées à partir des raies spectrales des spectres non polarisés, la perturbation d'activité des RVs provient des distorsions des raies spectrales essentiellement dues aux inhomogénéités de brillance surfacique ; par conséquent, nos cartes de brillance ZDI sont utilisées pour modéliser la perturbation d'activité des RVs et la soustraire de notre signal, afin d'explorer la présence potentielle de signatures de hJs dans les courbes de RVs filtrées. ZDI a prouvé son efficacité en tant que technique de filtrage pour les wTTSs avant cette thèse, avec les deux premiers articles MaTYSSE sur les étoiles LkCa 4 (Donati et al., 2014), V819 Tau et V830 Tau (Donati et al., 2015).

Cette thèse présente l'étude de l'activité et des RVs de deux autres étoiles MaTYSSE : TAP 26, âgée de $\sim$17 Myr et de masse $\sim$1 $M_\odot$, et V410 Tau, âgée de $\sim$0.8 Myr et de masse $\sim$1.4 $M_\odot$. Des résultats sur des jeux de données plus récents de la wTTS V830 Tau sont également présentés. En plus de l'utilisation de ZDI, une autre technique numérique est utilisée, appelée Régression par Processus Gaussiens (GPR) et appliquée pour la première fois à la recherche d'exoplanètes par vélocimétrie dans Haywood et al. (2014). Appliquée directement aux RVs brutes, GPR est une technique indépendante de ZDI, qui ne repose pas sur un modèle physique mais qui suppose un comportement statistique donné de la courbe des RVs, la perturbation d'activité des RVs étant décrite comme un bruit corrélé. Le processus de modélisation consiste donc à trouver les principaux paramètres caractérisant ce comportement statistique, en fournissant en même temps des informations sur l'activité stellaire.

Le premier chapitre décrit le contexte d'ensemble de l'étude et brosse un portrait grossier des théories actuelles sur la formation et de l'évolution précoce des étoiles et des planètes ; dans un deuxième chapitre, nous détaillons le problème de la modélisation de l'activité des wTTSs et décrivons les différentes techniques de modélisation complémentaires utilisées pour ce travail ; le chapitre trois présente ensuite les résultats de l'application de nos techniques de modélisation de l'activité à TAP 26, V410 Tau et V830 Tau, et le chapitre quatre présente l'étude des courbes RV de ces étoiles. Enfin, nous tirons quelques conclusions que cette thèse a apportées au domaine de la formation des étoiles et des planètes, et donnons quelques perspectives d'avenir.

1 Introduction: the formation of stars and their planets

Contents

1.1 A few notions on the diversity of stars and exoplanets

1.1.1 Stages of stellar evolution

Stars form in clouds of dust and gas, accreting plasma until they reach a stable mass. This mass, which varies between ∼0.1 – 100 solar masses ($M_\odot$), is the predominant factor that determines a star's evolution. In particular, one can follow the path of a star along its life on a temperature-luminosity plot, or Hertzsprung-Russell (HR) diagram (see figure 1.1). The main sequence (MS) is a region of the HR diagram where stars spend most of their life: it corresponds to the stage during which they burn hydrogen through nuclear fusion in their cores. In general, the more massive a star is, the hotter and brighter it is on the MS, and the faster it evolves through the various evolutionary stages described in the following paragraphs.

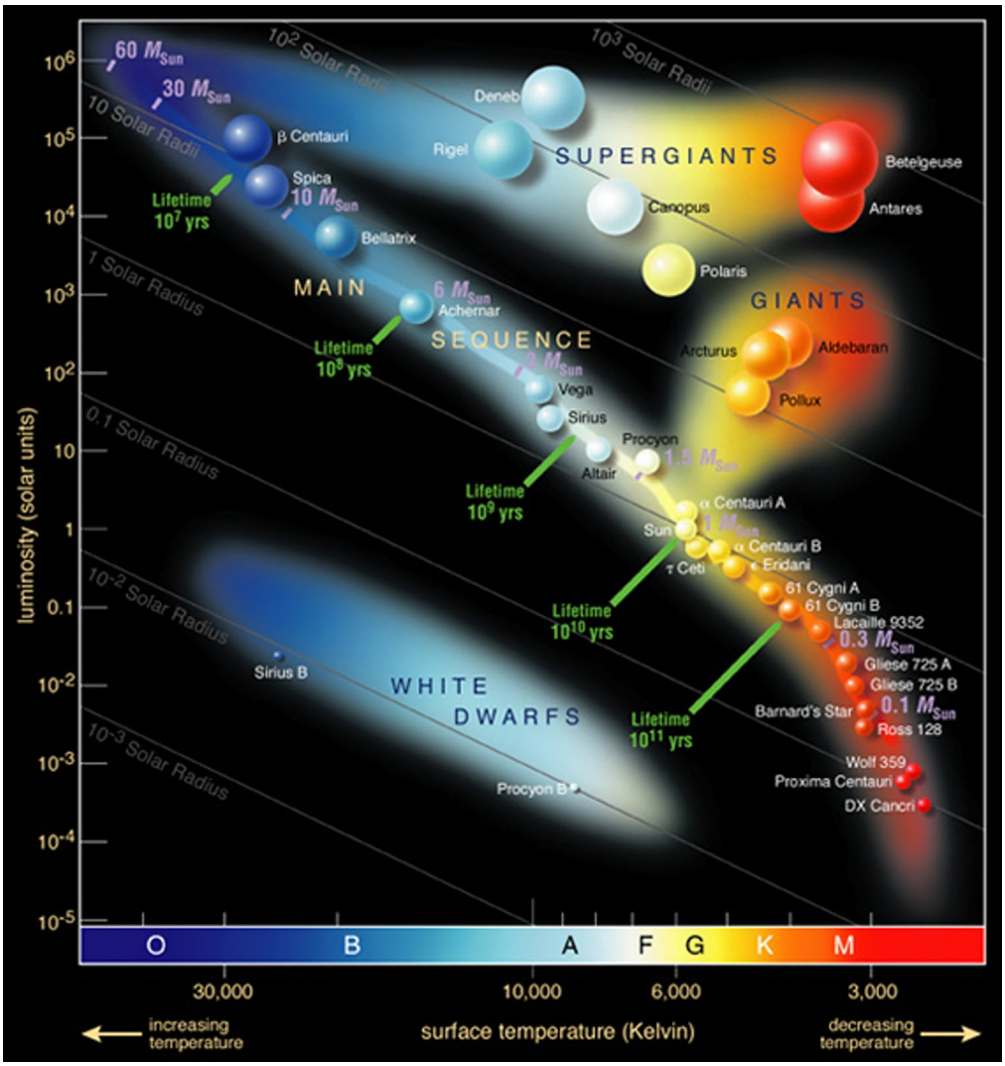

Figure 1.1 – Some famous stars on the Hertzsprung-Russell diagram. Masses and lifetimes are noted along the main sequence. Source: `https://www.eso.org/public/images/eso0728c/` through `https://commons.wikimedia.org/wiki/File:Hertzsprung-Russel_StarData.png`.

- The most massive stars ($M_\star \gtrsim 8\,M_\odot$) reach the MS at ages 0.02 – 0.2 Myr. They initiate hydrogen nuclear fusion in their cores before they have finished accreting their mass, then stay on the MS until ages 3 – 100 Myr (Maeder, 2009, chapter 18). When they have exhausted the

hydrogen reserves in their cores, they leave the MS and enter an inflated state as supergiants for 0.5 – 5 Myr, during which they fuse progressively heavier elements in their cores, until developping an iron core, at which point they explode into supernovae and their cores collapse into neutron stars or black holes (Maeder, 2009).

- Stars of masses $\sim$0.5 – 8 $M_\odot$ reach the MS at ages 0.2 – 100 Myr and stay on the MS until ages 0.1 – 10 Gyr. When they exhaust their core hydrogen fuel, they inflate into red giants, fusing helium at their core for 0.5 – 10^3 Myr. After running out of nuclear fuel (they are not massive enough to initiate full-scale carbon fusion), these stars contract, expelling their outer layers into planetary nebulae through superwinds. Their cores then cool down to become white dwarfs.
- Low-mass stars ($M_\star \lesssim 0.5\,M_\odot$) have a lifetime longer than the age of the Universe, and what happens to them after leaving the MS is yet unobserved.

At the beginning of their life, stars of masses $\lesssim 8\,M_\odot$ go through a protostar phase, during which they accrete most of their mass, and a pre-main sequence (PMS) phase, during which they contract towards the MS. For stars of masses $\sim$0.5 – 2 $M_\odot$, the PMS track on the HR diagram is composed of a phase of luminosity decrease at roughly constant temperature (Hayashi track) and a phase of temperature increase at roughly constant luminosity (Henyey track). These stars follow the Hayashi track for 2 – 20 Myr, during which their interiors are fully convective, and they bifurcate on the Henyey track when a radiative core starts developing. Stars of lower masses stay fully convective, so they follow the Hayashi track up to the MS, and stars of higher masses spend their PMS phase following the Henyey track (e.g. Bodenheimer, 2011, chapter 8).

Protostars and some PMS stars are embedded in circumstellar dust and gas, from which they grow; a protostar/PMS star and its circumstellar environment is referred to as a young stellar object (YSO). YSOs are extensively studied to constrain the theories of stellar formation, for example to explain observed distributions of masses (see studies about the Initial Mass Function, e.g. Offner et al., 2014) and of multiplicity (e.g. solar-type MS stars have on average ~ 0.6 stellar companion gravitationally bound to them, Duchêne & Kraus, 2013) among MS stars. Moreover, planets can form from the circumstellar matter around PMS stars; therefore, investigating YSOs is also important to understand the initial conditions of the evolution of planetary systems.

1.1.2 The diversity of exoplanetary systems

The search for exoplanets, i.e. planets orbiting around stars other than the Sun, has yielded about 4000 confirmed detections as of 2019 October. Traditionally, a substellar object orbiting a star was classified as a planet if its mass was below 13 Jovian masses ($M_{\rm Jup}$), and as a brown dwarf otherwise, that criterion roughly corresponding to the start of the thermonuclear fusion of deuterium in the core (Boss et al., 2007). However the distinction between giant planets and brown dwarfs is still debated as of today (e.g. Schneider, 2018).

Various observation/detection techniques exist, complementing each other (see e.g. Perryman, 2018, for a comprehensive review). Velocimetry (see section 2.4.1) yields orbital periods, lower boundaries on planet masses and orbital eccentricities. Photometry enables to detect transiting planets (planets passing between their host star and the observer), giving access to their radii and orbital periods, potentially to their eccentricities and planetary albedos, as well as an estimate of their masses in multiplanetary systems (from transit time variations, see e.g. Holman et al., 2010). Spectroscopy of transiting planets' host stars unveils their sky-projected obliquities, i.e. the inclinations between planets' orbital axes and their hosts' rotation axes (Rossiter-McLaughlin effect, see e.g. Fabrycky & Winn, 2009), as well as, potentially, some atmospheric characteristics (Madhusudhan, 2019). Other observation/detection techniques include direct imaging and gravitational lensing, which enable the detection of planets located far from their host stars.

Figure 1.2 shows a mass/period diagram of confirmed exoplanets. Three populations stand out: the super-Earths (planets of masses $\sim$1 – 10 Earth masses), the hot giants (massive planets on close-in orbits) and the warm giants (massive planets on intermediate orbits). Many observed systems have architectures that are strikingly different from that of the Solar system (Winn & Fabrycky, 2015): for example, accounting for observational biases, it is estimated that $\sim$30 – 50 % of Sun-like stars have a super-Earth on an orbit closer-in than Mercury's, while $\sim$10 % host a giant planet, usually on either a close-in orbit or a larger one but significantly eccentric (Raymond et al., 2018). The occurrence rate of hot Jupiters, the most massive of hot giants, was estimated at $\sim$1 % around Sun-like stars (Wright et al., 2012).

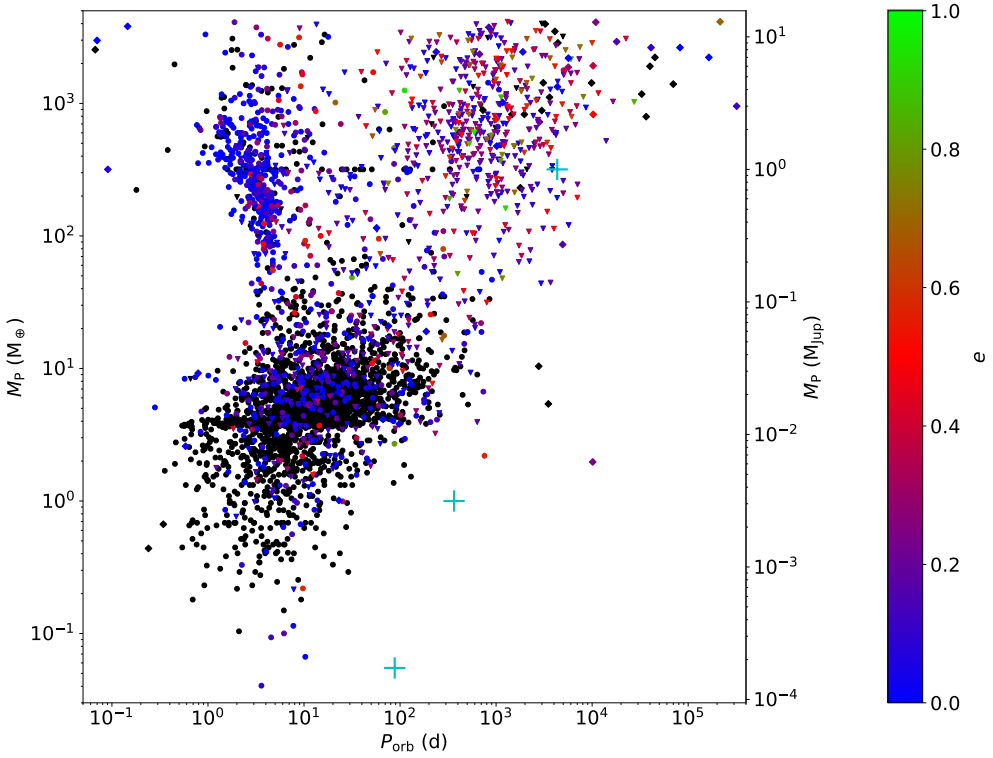

Figure 1.2 – Exoplanets mass-period plot, with the color scale representing the orbit eccentricity, when known. Cyan crosses represent, from left to right, Mercury, the Earth and Jupiter. The data was downloaded from `http://exoplanet.eu` (Schneider et al., 2011) on 2019 October 28, totalling 3725 exoplanets. The masses of 851 among them were known (diamond symbols), those of 768 others were assimilated to their known lower boundaries (triangular symbols), and those of the 2106 remaining planets were derived from their radii (circular dots), following the method described in Han et al. (2014).

Because planets form together with their star, investigating the processes at play early in the life of stars and of their stellar/planetary systems is a primordial first step to understand the evolution of planetary systems, to explain their observed statistics (e.g. Mordasini, 2018), to assess how much of an exception the Solar system is and to estimate the likelihood of finding Solar-System analogs in the galaxy (e.g. Agnew et al., 2018; Barbato et al., 2018). In the next section, we present the broad lines of the current paradigm of stellar formation.

1.2 The formation of stars

YSOs are often seen in groups, whether in gravitationally bound clusters or in associations, within which age and proper motion are roughly homogeneous. These groups bathe in giant clouds of

gas and dust and are called star-forming regions (SFRs). Famous examples of SFRs are: the Taurus-Auriga molecular cloud, located ∼140 pc away from Earth (Galli et al., 2018), the Orion cloud (∼390 pc, Kounkel et al., 2017), the Scorpius-Centaurus association (∼140 pc, de Zeeuw et al., 1999), the ρ Ophiuchi nebula (∼140 pc, Ortiz-León et al., 2017)... It is noted that many SFRs are located in a particular region of the galaxy, the Gould Belt: an elliptic ring of semi-major and semi-minor axes ∼350 pc and ∼230 pc respectively, whose center lies ∼100 pc away from the Sun in the direction opposite to the galactic center (e.g. Perrot & Grenier, 2003), but the physical origin of the Gould Belt is debated (see e.g. Bobylev, 2014; Bouy & Alves, 2015).

The current understanding is that stars are born from the gravitational collapse of dense cores within these clouds, first appearing at the center of the collapsing core and then growing by matter accretion. Best seen in infrared wavelengths, YSOs are categorized into four classes (0, I, II and III) depending on their spectral energy distribution (SED), each class corresponding to an evolutionary stage as illustrated in figure 1.3 (Adams et al., 1987; André, 2015).

1.2.1 From molecular clouds to protostars

Dark regions have been observed in the sky, with low densities of apparent stars. We now know that they are clouds of gas and dust that dim the light coming from background stars. These clouds are composed in large majority of molecular Hydrogen (H_2), with small amounts of interstellar dust and traces of other molecular gases: CO, NH_3, HCN, etc (see e.g. Wilson et al., 1970). Lada (1992) among others showed that molecular clouds are major sites of stellar formation. André et al. (2014) observed that molecular clouds have a filamentary structure, with filaments always roughly 0.1 pc thick and preferentially in the direction of the cloud elongation. At the crossing of filaments, or at various places along these filaments, we can observe denser clumps, called pre-stellar cores, which are defined as the immediate vicinity of local minima of the gravitational potential within the cloud.

Magnetism and turbulence are thought to be the main factors that drive star formation (Bodenheimer, 2011; Crutcher, 2012). In magnetically-controlled star formation scenarios, magnetic fields maintain the core against gravitational collapse but see their influence decrease as the core contracts and acquires mass (ambipolar diffusion), until the core reaches a critical mass and collapses. In turbulence-controlled star formation scenarios, supersonic turbulence within the cloud leads to complicated shock patterns that randomly generate highly-compressed regions that can collapse. Both magnetic fields and turbulence generally coexist at comparable levels in molecular clouds, so formation models including them together are favored (see Crutcher, 2012, for a review). Moreover, star formation can be triggered by factors external to the cloud, like supernovae shocks or cloud-cloud collisions, which create high-density regions that can collapse. YSOs clusters or associations are assumedly a result of either simultaneous collapse, where an external factor (such as galactic density waves) increases the density in the cloud on a global scale, or contagious star formation, where core collapses generate shockwaves that locally increase the density, resulting in more neighboring collapses (Maeder, 2009, Part V); turbulence can also lead to the simultaneous formation of several cores within a molecular cloud (Bodenheimer, 2011, Chapter 2).

Simulations of simplified cases (plasma ball with solid rotation and uniform magnetic field, e.g. Machida & Matsumoto, 2011; Machida & Basu, 2019) show that the birth of a protostar happens after two successive collapses (Masunaga & Inutsuka, 2000):

First collapse - When the density at the center of the pre-stellar core reaches $\sim 10^{10}\,\mathrm{cm}^{-3}$, the pressure at the center becomes high enough to create a shock, which defines the contour of what is called the first core. The first core accretes mass from the rest of the pre-stellar core, supported by thermal pressure and rotation against self-gravity (e.g. Wurster et al., 2018). The higher the

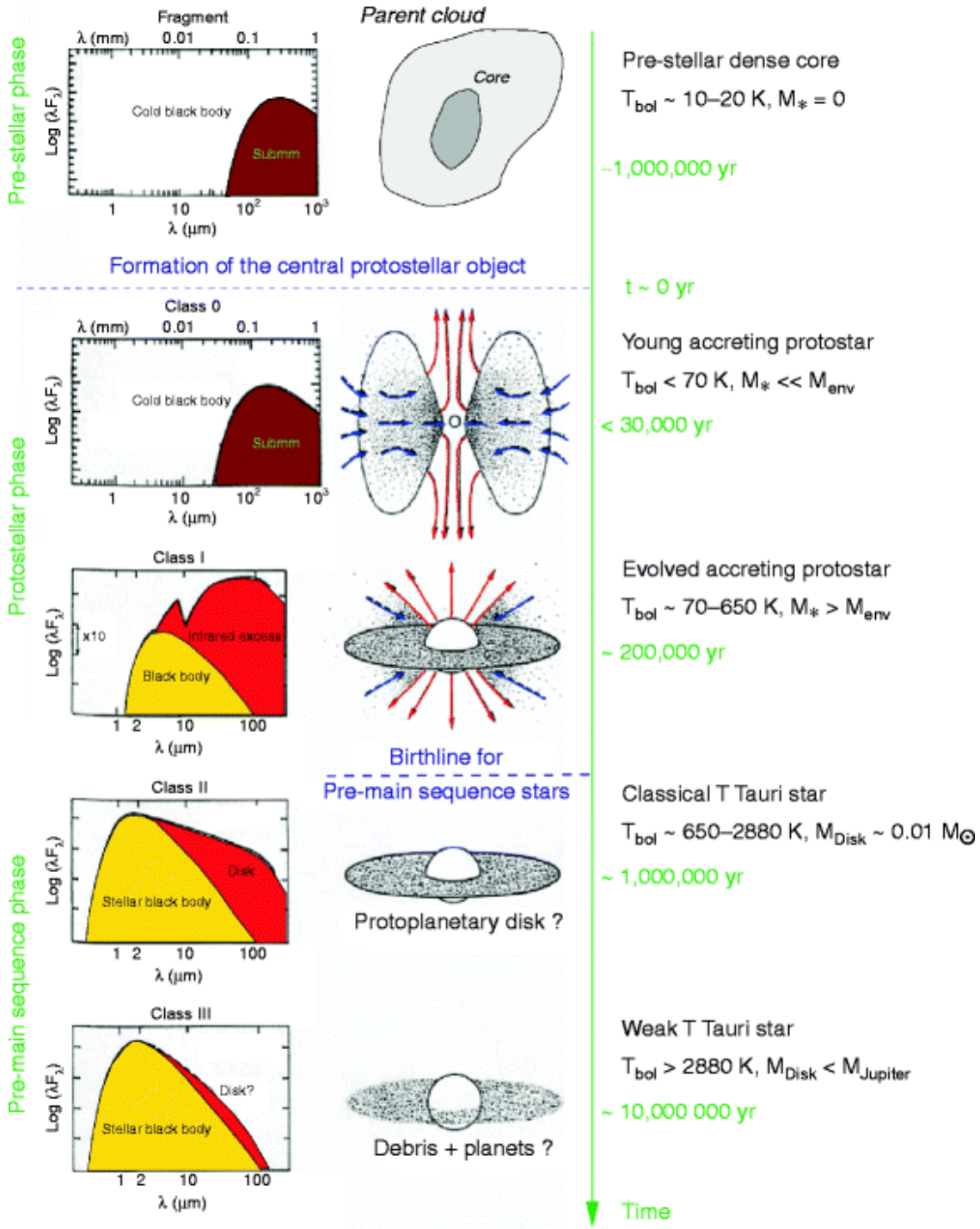

Figure 1.3 – Empirical sequence for the formation and circumstellar evolution of a single star from a prestellar cloud core to a class-III YSO, based on the shape of the SED (*left*), the bolometric temperature, and the mass of circumstellar (envelope + disc) material (*right*). The lifetime of a cTTS can in fact be as long as 10 Myr, making class-II and class-III phases hardly distinguishable in terms of age sample-wise. Source: André (2002).

initial angular momentum, the longer the first core lives before the second collapse, as centrifugal forces play against self-gravity to slow down the increase of density at its center. If given enough time, the first core takes a flattened shape before the second collapse, and the initial magnetic field

inside the first core gets dissipated by Ohmic and ambipolar diffusion, leading to a suppression of the magnetic braking (the magnetic field is no longer well-coupled to the neutral gas). Under some conditions, e.g. on the angle between the magnetic field and the angular momentum axis, the disc can become a Keplerian disc early on (see Hennebelle & Ciardi, 2009; Maury et al., 2019, for precise studies). During the accretion of the outer envelope by the first core, low-velocity outflows are driven from the outer boundary of the first core by magnetic forces, because magnetic field lines are twisted horizontally by the rotation (toroidal magnetic field). A very high angular momentum can lead to a fragmentation of the first core (Goodwin et al., 2007; Boss, 2009), which is one of the potential processes for generating multiple star systems (others being disc fragmentation post-protostar formation or gravitational capture; this question still constitutes an active field of research; see e.g. Goodwin et al., 2007; Maury et al., 2010).

Second collapse - When the temperature at the center of the first core reaches $\gtrsim 2000\,\mathrm{K}$, the dissociation of H_2 at the center changes the thermodynamics and triggers the second collapse. This second collapse can be as fast as a few years, until the density at the center reaches $\sim 10^{18} - 10^{20}\,\mathrm{cm}^{-3}$, at which point we consider that the protostar is born. The rest of the first core surrounds the newborn class-0 protostar. If the angular momentum of the first core is very low, the first core remnant quickly falls onto the protostar. Otherwise, a Keplerian circumstellar disc appears (Machida & Matsumoto, 2011). Far from the star, in the outer envelope, the magnetic field is well coupled with the neutral gas, then in the area $10^{11}\,\mathrm{cm}^{-3} \lesssim n \lesssim 10^{15}\,\mathrm{cm}^{-3}$, the dust absorbs the ions and the magnetic field is efficiently dissipated by Ohmic dissipation and ambipolar diffusion, letting the disc adopt a quasi-Keplerian rotation profile, then close to the star again, the degree of ionization increases and the magnetic field becomes coupled with the neutral gas again (Machida & Basu, 2019).

Main accretion phase - The main accretion phase starts, where the disc accretes mass from the primordial envelope which has not collapsed into the first core, while the protostar accretes mass from the surrounding disc. On top of the low-velocity outflows driven by the disc, high-velocity collimated jets appear near the protostar, fueled by disc material approaching the star at Keplerian velocities and being redirected outwards by toroidal magnetic fields. The accretion and jets are episodic, triggered by gravitational instabilities where clumps of material fall from the disc to the protostar, where a portion is evacuated as jets. The disc and the outer envelope are coupled by magnetic forces and exchange angular momentum, leading to a braking of the disc that prevents it from growing in size. The class-0 stage is characterized by a high mass ratio between the circumstellar environment and the protostar ($M_{\mathrm{env}} \gg M_\star$) and lasts for a few $10^4\,\mathrm{yr}$ (e.g. Andre et al., 2000; Masunaga & Inutsuka, 2000). During that phase, the protostar grows at an accretion rate of $10^{-6} - 10^{-5}\,\mathrm{M}_\odot/\mathrm{yr}$ (André, 2015). From an observational point of view, its SED is almost the same as that of a prestellar core, but the presence of the protostar is betrayed by signatures of powerful highly-collimated jets (Bontemps et al., 1996; Bachiller, 1996). Eventually, the outer envelope depletes, allowing the disc to grow. A YSO enters class-I when the protostar becomes more massive than its circumstellar environment. Jets and outflows then broaden and weaken, and the accretion rate decreases to $10^{-7} - 10^{-6}\,\mathrm{M}_\odot/\mathrm{yr}$ (André, 2015). The envelope is still present but the protostar signature appears in the SED at infrared wavelengths. The class I stage lasts for a few $10^5\,\mathrm{yr}$ (Evans et al., 2009).

1.2.2 Classical T Tauri stars

Eventually, the protostar has accumulated the majority of its mass and becomes a PMS star. It is at first a class-II source; a distinction is made between class-II YSOs of less than $2\,\mathrm{M}_\odot$, called

classical T Tauri stars (cTTSs), and those of more than $2\,M_\odot$, called Herbig Ae/Be stars (we do not discuss the latters). Having emerged from their now depleted envelope, cTTSs become visible at near-infrared and optical wavelengths, surrounded by an optically thick disc that causes an infrared excess in the SED (see figure 1.3). Material is channeled onto the star at a rate of 10^{-9} – $10^{-7}\,M_\odot$/yr (André, 2015).

CTTSs were observed to have strong magnetic fields (several kG), amplified from the remnants of the primordial field by the dynamo of the star (Johns-Krull et al., 1999; Johns-Krull, 2007). These fields open a cavity around the star in the region where magnetic forces dominate over rotation, called the magnetospheric gap. At the edge of this gap, a magnetic coupling exists between the surface of the protostar and the disc (Collier Cameron & Li, 1994; Bessolaz et al., 2008), and accretion happens by funneling disc material along the magnetic field lines. This magnetic coupling induces a rotational braking of the star (Bouvier, 2007; Bouvier et al., 2014), especially in the propeller regime early on, when high-velocity jets are driven from the protostar (e.g. Romanova et al., 2004; Zanni & Ferreira, 2013).

Even though cTTSs are still contracting under their own gravity and gain angular momentum from the accretion, their rotation rates are observed to be much lower than expected (Rebull et al., 2004). Bouvier et al. (2014) provides a review of the sources of angular momentum gain/loss for cTTSs (star-disc interactions, stellar winds...), revising the widely used paradigm of disc-locking proposed by Ghosh & Lamb (1979), where the star would co-rotate with the inner edge of its disc because of magnetic locking between the stellar surface and the disc plasma. Though models have to be refined, it is still apparent that both the disc and the magnetic field play a major role in braking the star rotation. As the star evolves, its structure becomes more complex and so does its magnetic field, meaning the dipole weakens and the field strength quickly decreases with distance to the star. Thus the disc-braking is less and less efficient, eventually leading to a liberation of the star, which starts to spin up.

During this phase, dust grains can agglomerate within the disc, which can eventually lead to the formation of planetesimals and planets (see section 1.3.2).

1.2.3 Weak-line T Tauri stars

As the inner disc depletes due to its material being either accreted or ejected, accretion gets progressively weaker, then intermittent (cTTSs then become transitional T Tauri stars), before the inner disc is finally exhausted, and the star becomes a weak-line T Tauri star (wTTS, class-III YSO, see e.g. White et al., 2007). The age at which this transition occurs varies widely from star to star, being generally between 1 – 10 Myr (e.g. Richert et al., 2018), which implies that the population of $\lesssim 10$ Myr T Tauri stars is composed of both cTTSs and wTTSs, undistinguishable by age alone.

The liberation from disc-locking can be triggered either by the dipole weakening as mentioned above, or by the dissipation of the disc. Free from disc-braking and still contracting, wTTSs spin up until age $\sim$10 – 100 Myr (depending on the mass). On the Hayashi track, the star shrinks at roughly constant temperature (4000 – 4500 K), then, around 1 – 3 Myr, it starts developing a radiative core and bifurcates on the Henyey track: the star keeps contracting, but at roughly constant luminosity and with a temperature rising with time, until reaching 4500 – 6500 K. For a $0.8\,M_\odot$ star, the contraction phase lasts for $\sim$25 Myr and for a $1.35\,M_\odot$ star, it lasts for $\sim$10 Myr; stars shrink by a radius factor of $\sim$20 – 60 (Amard et al., 2019).

After the contraction slows down, WTTSs spin down because of stellar winds until they reach the main sequence (see e.g. figure 1.4 for $1\,M_\odot$ stars; for a more complete study, see Gallet & Bouvier, 2015). The rotation periods of wTTSs reach down to $\sim$0.5 – 5 d when they spin the fastest (figure 1.4); their fast rotation induce a strong magnetic activity (see section 2.1.2).

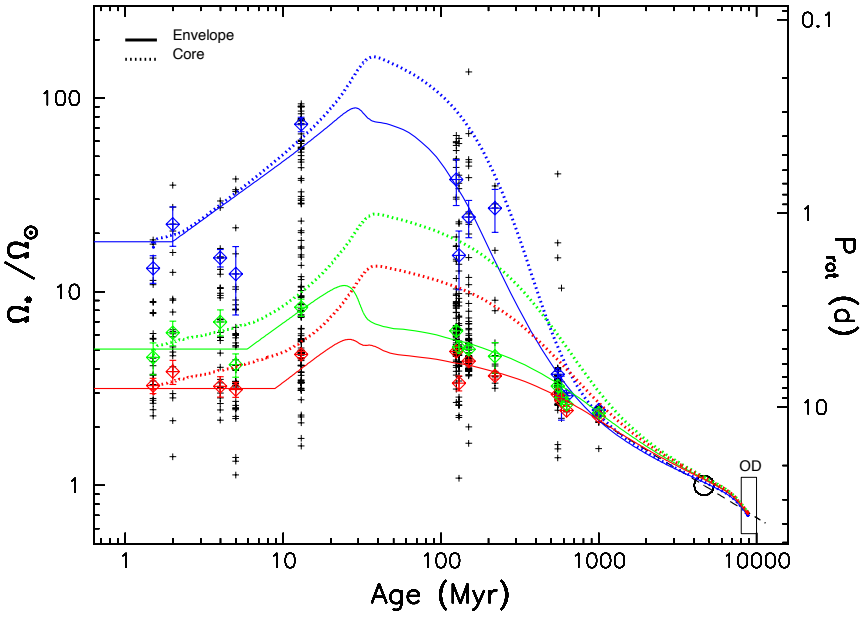

(a) 1 $M_\odot$

Figure 1.4 – Figure extracted from Gallet & Bouvier (2015, figure 5). Angular velocity of the convective envelope (solid lines) and of the radiative core (dashed lines) shown as a function of time between 1 Myr and 10 Gyr for slow (red), median (green), and fast (blue) rotator models in a mass bin centered on 1 $M_\odot$. The left vertical axis is labelled with angular velocity normalised to the Sun's, while the right vertical axis is labelled with rotational periods (days). The black crosses represent the observed angular velocities of stars in a selection of star-forming clusters of various ages. The red, green and blue tilted squares and associated error bars represent the 25th, 50th and 90th percentiles of the observed rotational distributions at each sampled age. The black rectangle labelled OD (lower right corner) shows the angular velocity dispersion of old disc field stars. The open circle is the angular velocity of the present Sun shown for reference, and the dashed black line illustrates Skumanich's relationship (Skumanich, 1972), $\Omega \propto t^{-1/2}$.

1.3 Protoplanetary discs

We now focus on planetary formation within discs, called protoplanetary discs in this context. The content of this section is largely inspired from the review Armitage (2018).

1.3.1 Structure

We consider the disc around a cTTS (see figure 1.5). Discs around cTTSs have been observed to extend up to ∼100 astronomical units (au; e.g. TW Hya, Nomura et al., 2016). Their masses are estimated to be $\sim 10^{-3}$ – 10^{-2} times the mass of the star ($M_\star$; see Andrews et al., 2013; Williams & Best, 2014). The surface density (volumic density integrated over the thickness of the disc) is expected to follow a law $\Sigma \propto r^{-1}$. Moreover, axisymmetric rings and non-axisymmetric structures in discs have been observed (e.g. ALMA Partnership et al., 2015; Dong et al., 2018), the origins of which are uncertain but are hypothesized to be tied to planetary formation (Baruteau et al., 2019).

The disc is heated through various sources. Irradiation from the star leads to a global temperature profile $T \propto r^{-1/2}$ (Kenyon & Hartmann, 1987). Close to the star, accretion heating increases the temperature in the mid-plane, leading to a vertical gradient of temperature (Armitage, 2018). Further away from the star, the thickness of the disc divides it into several regions: an isothermal inner region centered around the mid-plane, where $T_{\rm dust} = T_{\rm gas}$, then a warm layer of dust directly heated by stellar radiation, and a hot gas atmosphere. The temperature profile defines various "ice

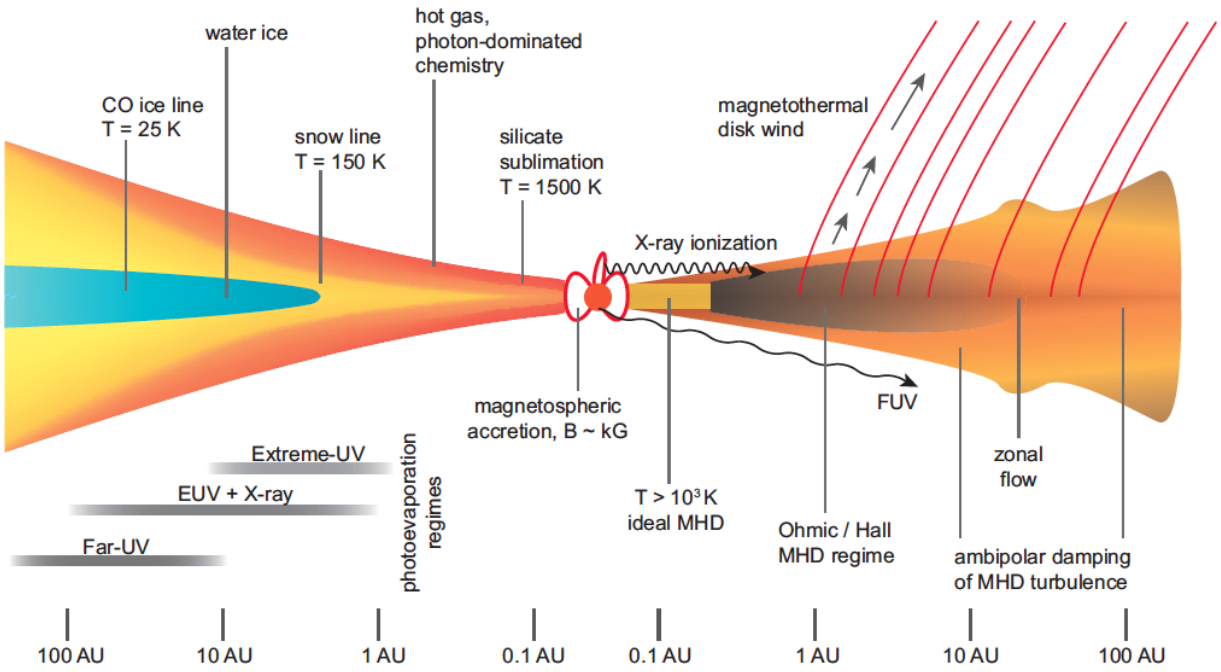

Figure 1.5 – Cartoon of a protoplanetary disc viewed from the side (source: Armitage, 2018). The left part shows the thermal structure of the disc while the right part shows the magnetohydrodynamic regimes in various regions of the disc.

lines", which are the limits between areas where given chemicals are under solid or gaseous form. For example, the water snow line is located where $T \simeq 150\,\mathrm{K}$. Since the accretion heating wanes with time and the radius and temperature of the protostar evolve, the locations of the ice lines also evolve with time.

An important factor in the structure of the disc is the magnetic field. Close to the star ($T > 3000\,\mathrm{K}$), the disc is thermally ionized and the magnetic field is thus efficiently coupled with the gas. Further away, sources of non-thermal ionization (X-rays, UV photons or cosmic rays) are weak enough to let non-ideal MHD effects take place: the Ohmic diffusion and Hall effect decrease the influence of the magnetic field on the charged and neutral species, and beyond $\sim 30\,\mathrm{au}$, the low density opens the way to ambipolar diffusion, where neutral species drift independently of the magnetic field, because the rate of collision with magnetically-tied electrons and ions is low. Magnetic fields also generate winds that participate to depleting the disc.

The phenomenon of photoevaporation, where gas heated by X-rays or UV photons escapes the disc, taking away matter and angular momentum, is most efficient at $2 - 3\,\mathrm{au}$ and can create a dip of density withing the disc, potentially even a gap, and eventually blow the disc away on long time scales.

1.3.2 From dust particles to planets

Not all mechanisms of planet formation within protoplanetary discs are understood as of today, especially as direct observation of disc-embedded planet formation is difficult. The paradigm of planetary formation is that of a bottom-up growth: dust grains (length scale: micrometer) aggregate into pebbles (cm), which themselves aggregate into planetesimals (km), some of which eventually grow into planets (Baruteau et al., 2016).

At first, when the dust grains are very small, aerodynamic forces dominate over gravitational forces, and dust grains grow from µm sized to mm sized thanks to 2-body collisions. Interactions

between the dust grains and their surrounding gas plays a role in the collision velocities and subsequent trajectory of the dust grains. These collisions, at first, can happen anywhere in the disc but as the solid grows, it is submitted to gas drag and tends to join the mid-plane and to drift radially towards the star. Bouncing and fragmentation are barriers to the growth of solids, and the critical relative velocities at which they happen depend on the solid composition (for example water ice is more resistant to fragmentation than silicates, Armitage, 2018). Eventually, these processes reach an equilibrium and the dust solids, now pebbles, can generally reach sizes of mm-cm, with pebble traps at the snow line and at the inner edge of the disc.

How pebbles grow into planetesimals is not well-constrained by observations, especially as meter-sized solids typically fall into the star in $\sim$100 yr from an original distance of 1 au, implying that planetesimal formation has to happen faster than solid infall into the star. Ideas proposed by the theory include porous growth, where pebbles stick to each other with little compression, giving birth to porous aggregates with increased cross sections, or streaming instability (Youdin & Goodman, 2005) where the disc gets fragmented and clumps of dust get trapped together, ending up aggregating.

As the planetesimals grow, gravitational forces become dominant and *runaway growth* starts. The heavier a planetesimal becomes, the faster its cross section grows thanks to its gravitational potential, and the more chances it has to collide with its neighbors. This phase leads to a size distribution of solids where a small number of very large planetesimals stand out. Pebble accretion can occur during this phase, where planetesimals absorb radially-drifting pebbles that arrive on their orbit.

Eventually, the biggest planetesimals, or oligarchs (10^3 km), grow so massive that their interaction with their neighbours scatters them, thus slowing down their growth. During this *oligarchic growth* phase, the oligarchs dominate the gravitational choreography: each of them settles into its own area of gravitational domination, and eventually "eats" the smaller planetesimals in this feeding zone, to grow into a planet embryo. Oligarchs can interact with each other, impacting their respective orbits and the general architecture of the system.

Finally, giant planets are formed from solid cores that have reached at least 10 – 15 Earth masses ($M_\oplus$), massive enough to trigger runaway accretion of a gaseous atmosphere from the surrounding gas (Pollack et al., 1996). The time scale for forming such massive cores can be shorter than the lifetime of the disc, thanks to the enhancement of surface density beyond the snow line (e.g. Kennedy & Kenyon, 2008), and type I migration trapping solids near the snow line (see section 1.4.1).

1.4 The mystery of hot Jupiters

In 1995, the first confirmed detection of an exoplanet around a Sun-like star is published: 51 Peg b is a > 0.5 M_{Jup} planet orbiting at 0.05 au from its host (Mayor & Queloz, 1995). With only the Solar System to compare at that time, finding a giant planet this close to the star was surprising. Furthermore, such close-in orbits are not expected to provide favorable conditions for giant planet formation, since the high Keplerian velocities favor fragmentation during large planetesimal encounters, and the accretion of a massive gaseous envelope is difficult in the limited area around the orbit.

1.4.1 Two theories of giant planet migration

Disc migration - To explain the orbit of 51 Peg b, Lin et al. (1996) showed that giant planets can migrate within their protoplanetary disc from original distances of a few au to the inner edge of the disc, within the lifetime of the disc. In general, interactions between a forming planet and the

surrounding material in the protoplanetary disc impact the orbit of the planet, causing an orbital migration. The nature of the migration, caused by a wake torque and a corotation torque (Baruteau et al., 2016), depends on the mass of the planet and on properties of the disc. Planets below $\sim 10\,M_\oplus$ undergo type I migration, which generally drives them inwards (towards the star), except around the silicate evaporation line and the water ice line. Outward migration around those lines and inward migration elsewhere create "planet traps" behind the silicate evaporation and water ice lines. Massive planets that open deep gaps in the disc around their orbits (masses typically $\gtrsim M_{Jup}$) undergo type II migration, which also drives them inwards on time scales $\gtrsim 10^4 - 10^5$ yr. Planets massive enough to open partial gaps in low- to moderate-density discs follow a migration regime intermediate between type I and type II, but in massive discs, they undergo type III migration which drives them outwards (Baruteau et al., 2016). Type II migration would enable to form hJs, generally keeping their orbit quasi-circular and coplanar. The planet still grows by accreting gas as it migrates, and the migration is slowed down when the planet mass becomes larger than the mass outside the planet gap. The migration stops when the planet reaches the inner edge of the disc.

Eccentricity excitation and tidal circularization - Since 1995, $\sim$400 hot Jupiters have been detected (estimated masses between $0.5 - 13\,M_{Jup}$ and orbital periods lower than 10 day, see figure 1.2 and its caption). Figure 1.6 shows the distribution of orbital eccentricities and sky-projected obliquities of giant planets. The eccentricities of hJs are generally low, whereas they are more dispersed for warm Jupiters. Few obliquities were measured for warm Jupiters, but we observe a large dispersion for hJs. A large eccentricity and/or a large obliquity are interpreted to result from gravitational interactions between oligarchs and/or fully-formed planets, which induce orbital instabilities (e.g. planet-planet scattering, Kozai-Lidov cycles, Dawson & Johnson 2018), changing their orbital angular momentums, eccentricities, semi-major axes and even potentially the planes of their orbits. For a cold giant planet to become a hJ, it would need to be placed on a highly eccentric orbit, with a periastron in the close-in region and an apoastron in the region where the planet originally was. The low eccentricities of hJs are believed to be the result of tidal circularization by the star: tidal forces work on the planet every time it goes through its periastron (close enough to be within reach of the stellar tidal influence), and the orbit circularizes within a few 10^2 Myr. In the latter case, the obliquity does not get dampened as fast as the eccentricity (Dawson & Johnson, 2018).

1.4.2 In-situ formation?

Recent studies have argued in favor of in-situ formation of hot Jupiters, motivated by the difference of mass distribution between hot and cold Jupiters, and the detection of many $10 - 15\,M_\oplus$ exoplanets on very close-in orbits (Batygin et al., 2016). Batygin et al. (2016) ran simulations showing runaway accretion of a gaseous atmosphere onto $15\,M_\oplus$ cores at 0.05 au, however, simulations by Coleman et al. (2017) taking different hypotheses showed no runaway atmosphere accretion on orbits below 0.1 au. The in-situ formation theory is still quite new and its feasibility not yet well established.

1.4.3 Further orbital migration

In the close vicinity of the host star, tidal and magnetic interactions between the star and the planet are strong enough to impact the orbit of the planet; in particular, these interactions transfer angular momentum between the star and the planet, by tending to synchronize the rotation of the star with the revolution of the planet. Thus, once a Jupiter-size planet reaches this region, depending on the geometry of the system, the hot Jupiter can either migrate slightly outwards or fall into the star (Bolmont & Mathis, 2016).

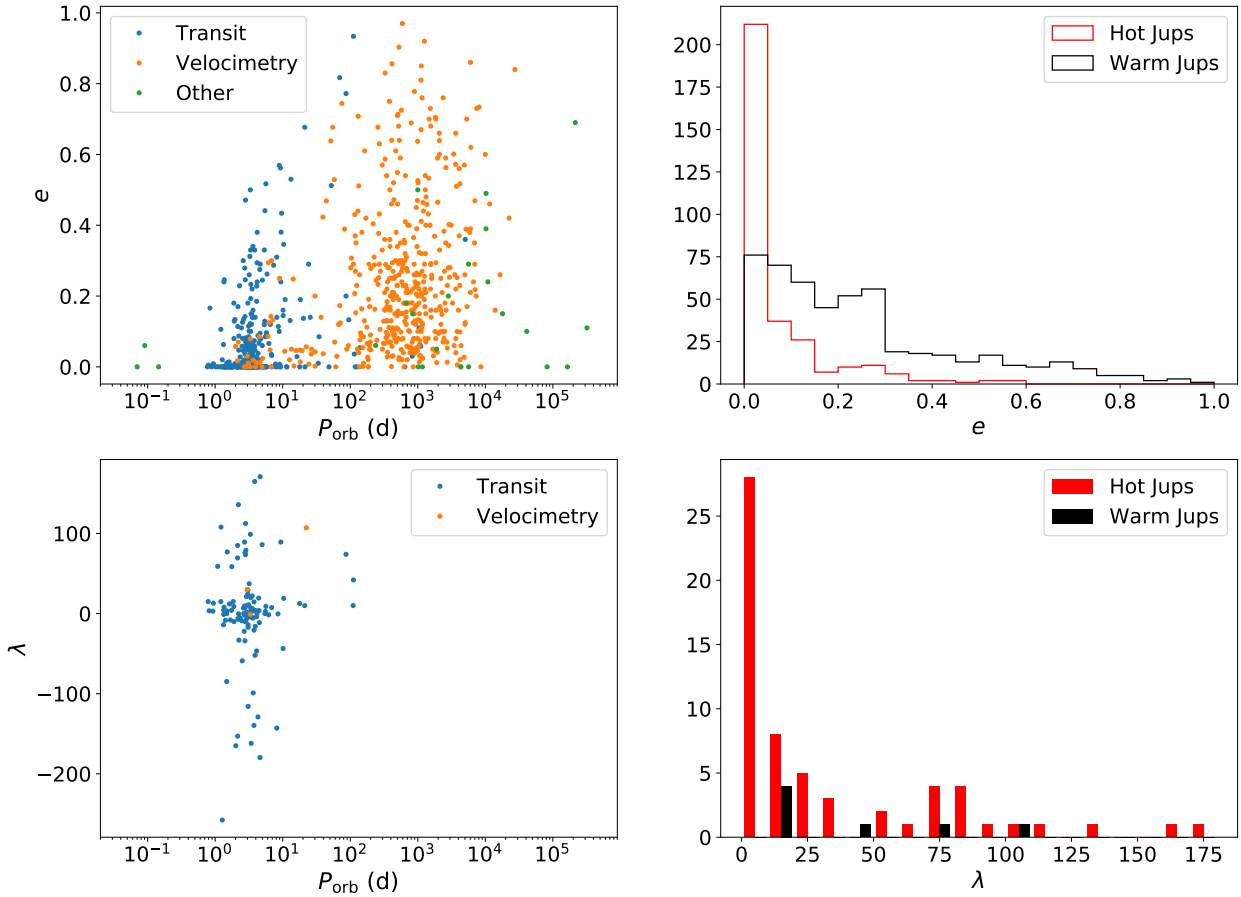

Figure 1.6 – Eccentricities (noted e) and obliquities (noted λ) of giant planets against their orbital periods (*left*) and as distributions (*right*). Data downloaded from `http://exoplanet.eu` on 2019 Oct 28 and from TEPCat (Southworth, 2011).

1.5 Summary

Stars are born at the center of collapsing dense cores within molecular clouds. After a rapid accretion phase during which the protostar is deeply embedded in its envelope, the protostar becomes a pre-main sequence star, emerging from its cocoon. T Tauri stars, PMS stars under $2\,M_\odot$, are still surrounded by an accretion disc at first (classical TTSs), in which planets can form. After the disc dissipates, they become weak-line TTSs surrounded by their planetary systems.

The estimated occurrence of hot Jupiters around $\sim$1 % of mature stars, combined with current planet formation theories, indicate that giant planets likely migrate after/while forming. Giant planets have an enormous gravitational influence on the rest of their planetary systems, it is therefore essential to understand their migration well, so as to accurately predict the architecture and orbital evolution of planetary systems. To distinguish which scenario dominates between type II migration within the protoplanetary disc and eccentricity excitation followed by tidal circularization, they have been confronted to observations of mature hJs, in particular to their statistics, orbital characteristics and potential presence of moons (see Dawson & Johnson, 2018, for a review). But detecting and characterizing actually young hJs, for example when tidal circularization has not had the time to happen yet, is necessary to make the distinction with better certainty; this is why this thesis focuses on the search for hJs around wTTSs, as detailed in the next chapter.

2 | Observing wTTSs

Contents

2.1 Interests

To investigate the mechanisms of formation of hot Jupiters, we propose to search them around stars as young as possible, i.e. around cTTSs and/or wTTSs (1 – 15 Myr), and to characterize their orbital parameters. Because of the large dispersion of disc dissipation ages, wTTSs occupy roughly the same age domain as cTTSs, and because they no longer accrete, wTTSs make ideal targets to search for young hJs, without needing to model the accretion that adds variability in light curves and RV curves .

2.1.1 Hot Jupiters

The very young age of wTTSs makes them ideal targets to differenciate between the two main hypotheses for hJ formation. At their age, a planet that migrated through planet-disc type II migration should have a quasi-circular orbit (Baruteau et al., 2014), while one that got scattered through planet-planet interactions has not yet had the time to circularize to align and circularize its orbit via star-planet tidal interactions, so its orbit should be highly eccentric and perhaps tilted with respect to the stellar equator (see section 1.4). Moreover, comparing the statistics of young hJs to those of mature hJs would enable to better constrain their evolution as a function of their intrinsic and orbital parameters.

In this thesis, we use the velocimetry detection technique to look for hJs around wTTSs, which gives us access to their orbital periods, eccentricities and minimal masses (see section 2.4.1). This technique uses measurements of the radial velocity (RV) of the targetted stars, i.e. their velocity projected onto the line of sight (direction linking the observer and the targetted star).

However, the RVs of wTTSs present a strong variability which makes the detection of hJs around them difficult: the RV modulation of wTTSs typically reach semi-amplitudes of a few $\mathrm{km\,s^{-1}}$, drowning potential RV signals from hot Jupiters whose expected semi-amplitudes are of the order of $0.1\,\mathrm{km\,s^{-1}}$ (Mahmud et al., 2011; Crockett et al., 2012). This RV modulation can be explained by the stellar magnetic activity, which for example manifests itself with dark and bright features covering large fractions of the stellar surface (several tens of percent of the surface, see e.g. Grankin et al., 2008; Gully-Santiago et al., 2017). It is thus necessary to understand and model the stellar activity well enough to be able to filter it out of the data without removing potential planet signatures. Modelling the magnetic field of wTTSs can also inform about potential star-planet magnetic interactions.

2.1.2 Stellar activity

WTTSs have been shown to trigger strong magnetic fields, from a few 100 G to several kG (Skelly et al., 2010; Donati et al., 2014, 2015). The processes driving exchanges between the cinetic energy of the plasma and the magnetic energy, involving the stellar rotation and the convection, are described by the dynamo theory (see e.g. Charbonneau, 2013, for a comprehensive explanation). More precisely, we can describe the magnetic field as the sum of its poloidal and its toroidal components (Chandrasekhar, 1961). The dynamo theory describes how the field is amplified and in particular how both poloidal and toroidal fields are regenerated from each other. For instance, from the field lines of an aligned dipole (poloidal), azimuthal field lines (toroidal) can appear if some latitudinal differential rotation twists the dipole lines (Ω effect). Conversely, poloidal field can be generated from toroidal field thanks to cyclonic convection, which also twists the field lines (α effect, see Parker, 1955). This process is called an α-Ω dynamo, but other types of dynamo are equally possible (Brun & Browning, 2017).

The Rossby number Ro, which is the ratio between the stellar rotation period and the convective turnover time scale, quantifies the capacity of the stellar rotation to generate cyclonic convection,

i.e. orientate the convective cells in a privileged direction. The shorter the rotation, the lower the Rossby number, the more active the star is. For Ro < 0.1 however, the dynamo is saturated, which means that the magnetic field is strong enough to retroact on the velocity field and prevent any further amplification of the field. The convective turnover time scale is of the order of a few hundred days for fully-convective wTTSs, and their rotation periods are well under ten days, which means that most of them have saturated dynamos. They are thus extremely active (Preibisch et al., 2005).

The stellar magnetic activity manifests itself all the way from the stellar interior to the the outer stellar amosphere, through phenomena of various time and space scales. In particular, the magnetic fields of stars with an external convective layer - a fortiori of wTTSs - generate a heated extended stellar atmosphere, composed, just above the photosphere, of a chromosphere and a corona (see e.g. Narain & Ulmschneider, 1996). The following is a list of the main activity-related phenomena relevant to this thesis.

Flares - Flares are impulsive releases of magnetic energy during explosive field line reconnections. They can be accompanied by coronal mass ejections, if clumps of plasma were attached to the field lines that reconnected. They manifest through sudden increases of the luminosity over time scales of a few minutes, followed by a decay and return to the regular luminosity over a few hours (see e.g. Benz, 2017). Flares on the Sun typically release energies of 10^{27} – 10^{32} erg, while on wTTSs, large flares can release energies of the order of 10^{35} erg. Flares happen relatively often on wTTSs: for example Stelzer et al. (2007) measured a frequency of 1 large flare per star every $\sim$9 d in the Taurus molecular region.

Spots and plages - Magnetic fields generate dark and bright features at the surface of low-mass stars. The dark features, called spots, are regions where the magnetic field emerges from (or plunges into) deeper convective layers, and is strong enough to suppress the convective motion, so that the plasma in the spot is darker and cooler than the surrounding photosphere. The bright features, either faculae on the photosphere or plages on the chromosphere, are regions of brighter and hotter plasma. As the star rotates, the distribution of brightness over the visible disc changes, from the point of view of an Earthly observer, causing modulations in the light curve and in the spectral line profiles of the star. Long-term photometric monitorings of wTTSs have shown that they generally exhibit light curves with quasi-periodic high-amplitude modulations (up to 0.6 mag), indicating that dark and/or bright areas cover an important fraction of the surface of wTTSs and have long lifetimes compared to the stellar rotation periods (Grankin et al., 2008). Spot maps reconstructed through Doppler Imaging (DI, see section 2.2) tend to show large dark spots on the surfaces of wTTSs (see e.g. Strassmeier 2009 for a list up to 2009). These high-contrast brightness inhomogeneities cause spectral line distortions, and thus RV changes of the order of a few km s^{-1} over time scales of the order of 1 d (Huerta et al., 2008; Mahmud et al., 2011).

Moreover, latitudinal differential rotation can shear the surface and spots have a limited lifetime, eventually leading to a loss of periodic coherence in the rotational modulations. Differential rotation has been investigated on a few wTTSs, from both light curves and DI techniques: in some cases it did not fit data significantly better than solid-body rotation (Skelly et al., 2010; Donati et al., 2014), whereas in others it was found to present an equator rotating faster than the poles, like on the Sun, but with a somewhat weaker shear (Donati et al., 2015).

Secular evolution and magnetic cycles - Finally, even though wTTSs light curves generally exhibit strong periodicity, astronomers have observed changes in the shape, amplitude and sometimes period of their light curves over the years (Sokoloff et al., 2008; Hambálek et al., 2019). They are attributed to changes in the distribution of brightness features on the surface; in particular,

amplitude changes are associated to longitudinal redistributions of spots while period changes, combined with the presence of latitudinal differential rotation, are associated with latitudinal redistributions of spots. There has been no confirmed detection of a Sun-like magnetic cycle (with total spot coverage variation, mean spot latitude variation and reversal of the magnetic dipole) on a wTTS yet, but an analysis of the light curve of the wTTS V410 Tau over $\sim$50 yr revealed complex variations where several time scales appear (4 – 5 yr spot configuration lifetime, brightness minima every 11 – 13 yr, see Sokoloff et al., 2008).

Other phenomena not related to the magnetic activity, namely acoustic oscillations and granulation, can cause modulations of the brightness and RV. The characteristic time scale of oscillations is a few minutes (Gilliland et al., 2010) so their impact is averaged out for sufficiently long observations. Granulation, i.e. partial coverage of the photosphere by the top of convective cells, adds a negative contribution to the RVs, called the convective blueshift (negative RV balance over the visible disc of hot bright rising plasma and cold dark sinking plasma), estimated at $-100 \pm 50\,\mathrm{m\,s^{-1}}$ for stars of 4500 – 5000 K (Meunier et al., 2017). Because the magnetic field suppresses convection, changes in the magnetic topology lead to granulation-related RV modulations over a few years.

2.2 The MaTYSSE observation programme

2.2.1 Scientific goals

To characterize the magnetic activity of wTTSs and look for their hot Jupiters, the MaTYSSE (Magnetic Topologies of Young Stars and the Survival of massive close-in Exoplanets) observation programme (Donati et al., 2014) carried out the observation between 2013a and 2016b of 35 wTTSs in some of the most well-known SFRs: the Taurus-Auriga SFR, the closest to Earth at a distance of $\sim$140 pc, ρ Ophiuchius, Lupus, the TWA stellar association, etc... More specifically, its aims are:

- to better understand the evolution of magnetic fields in forming stars, by mapping the brightness distribution and magnetic topologies of wTTSs and comparing them to those reconstructed for cTTSs within the sister programme MaPP (Magnetic Protostars and Planets, see Donati et al. 2010b to Donati et al. 2013),
- to bring observational constraints to the formation and/or migration processes of hot Jupiters, by searching for potential close-in giant planets around wTTSs and, if found, by characterizing their orbits.

2.2.2 Instruments and data

The collected data are mainly high-resolution spectra from the intrument ESPaDOnS (Echelle SpectroPolarimetric Device for the Observation of Stars, Donati, 2003) at CFHT (Canada-France-Hawaii Telescope), Mauna Kea, Hawaii, and from its twin NARVAL at TBL (Télescope Bernard Lyot), Pic du Midi, France, complemented with contemporaneous photometric observations from the CrAO (Crimean Astrophysical Observatory).

The raw frames from ESPaDOnS and NARVAL (see figure 2.1) are processed with the nominal reduction package Libre ESpRIT as described in e.g. Donati et al. (2010b), to output them under the form of continuum-normalized 1D spectra. All spectra are automatically corrected for Doppler shifts resulting from instrumental effects (e.g. mechanical flexures, temperature or pressure variations) by using telluric lines as a reference (absorption lines in the spectra that come from the Earth's atmosphere). Though not perfect, this procedure provides spectra with a relative RV precision of better than $30\,\mathrm{m\,s^{-1}}$ (e.g. Moutou et al., 2007; Donati et al., 2008b). The collected stellar spectra span the entire optical domain (370 – 1000 nm) at a resolving power of 65k (i.e. a resolved velocity element of 4.6 $\mathrm{km\,s^{-1}}$).

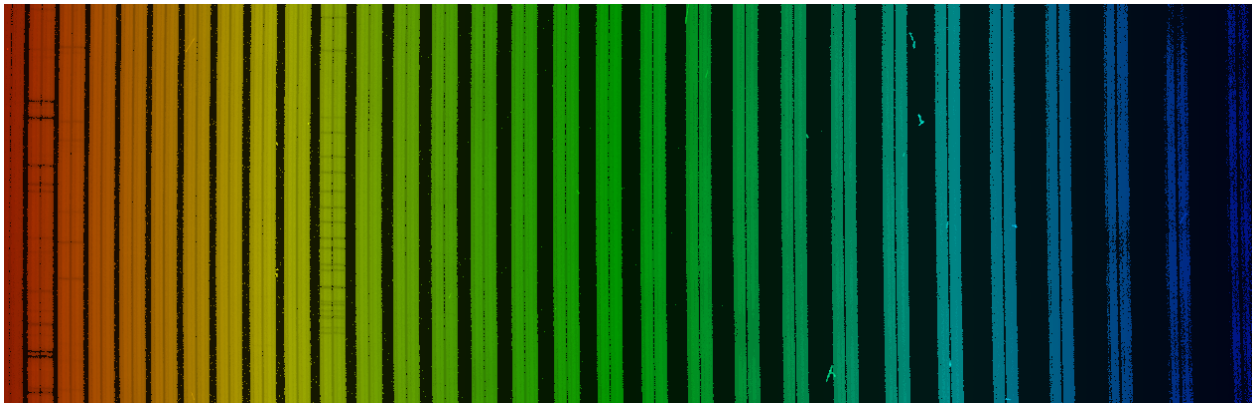

Figure 2.1 – Portion of an ESPaDOnS data frame (TAP 26 in the night of 2015 Nov 18 to 19). The colors were artificially added to show wavelength evolution along the frame. The grating orders separated through prism cross dispersion are roughly vertical, each divided into two polarization channels. Some spectral lines are visible.

ESPaDOnS and NARVAL can provide unpolarized, linearly polarized and circularly polarized spectra. The next section describes the techniques we use to retrieve brightness and magnetic topologies from these data: spectropolarimetry, velocimetry and time-frequency analysis.

2.3 Spectropolarimetry of wTTSs

2.3.1 Spectroscopy and Doppler Imaging

First we consider unpolarized spectra, i.e. intensity spectra, and in particular their spectral lines. Let us consider an element of surface on the visible disc of an observed star. The spectra we receive from it are Doppler-shifted according to its local RV (impacted by stellar rotation, convection, pulsations...) and the shape of the spectral lines depends on local physical parameters (e.g. chemical composition, temperature, turbulence, magnetic field) and geometric parameters (projected area, limb darkening). This shape is called the intrinsic profile and is not well-constrained for most stars, since very few stars are spatially resolved.

Stellar rotation induces a RV dispersion between -$v \sin i$ and $v \sin i$ over the visible disc, where v is the rotation velocity at the equator of the star, and i is the inclination of its rotation axis to the line of sight (see e.g. figure 2.5 for solid-body rotation). WTTSs generally have a $v \sin i$ of several $10\,\mathrm{km\,s^{-1}}$ (e.g. Bouvier et al., 1997; Strassmeier, 2009), unless i is very low. For these stars, rotation dominates over other effects as far as surface RV is concerned, so the RV distribution over the visible disc is well-approximated by the rotation-induced RV distribution. The spectral lines in the collected spectrum, integrated over the visible disc, are thus subjected to a Doppler broadening $v \sin i$, as the spectral contributions of the elemental surface regions undergo various Doppler shifts, and a strong correlation between surface rotational RV and position within the spectral lines appears. For instance, the presence of a spot/plage on the photosphere respectively lessens/enhances the contribution of the corresponding area to the integrated spectrum, causing distorsions in the integrated line profiles at positions corresponding to the rotational RV of the spot/plage. Therefore, a distorsion in the spectral lines indicates the presence of brightness features in the area whose rotational RV corresponds to the position of the distorsion. The effect of spots on the spectral lines of fast rotators is illustrated in figure 2.2).

Doppler imaging (DI) of starspots, a technique first described by Vogt & Penrod (1983b) and further elaborated by Vogt et al. (1987), takes advantage of this correlation on high-$v \sin i$ stars to

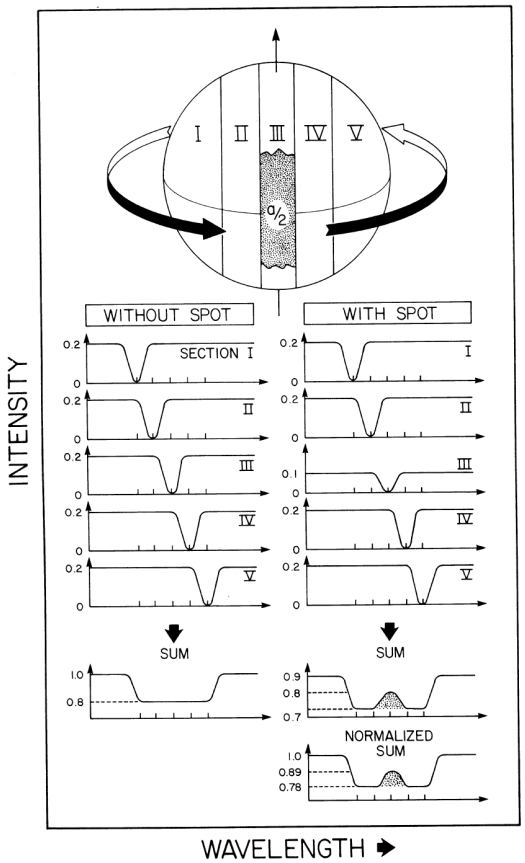

Figure 2.2 – Effet of a dark spot on a spectral absorption line of a fast rotator: the visible disc of the star is partitioned into areas of different local surfacic RVs, and the contribution of each individual area is shown. Note how, after rescaling the profile, the spot-related distorsion appears as a bump in the line profile in the wavelength band corresponding to the RVs affected by the spot, but also an enhancement of the line profile on both sides of that wavelength band. Illustration taken from Vogt & Penrod (1983a).

derive the spot distribution at their surfaces. Akin to medical tomography techniques, DI derives the two-dimensional brightness distribution on the photosphere from a series of one-dimensional spectra, observed at various phases of the stellar rotation (figure 2.3 illustrates the different effects of low-latitude and high-latitude spots on time-series of spectra). However, the number of solutions that can fit the data down to noise level is usually inifinite. The degeneracy of the inversion problem is lifted by choosing the solution with maximum entropy (minimal amount of information; unicity demonstrated in Skilling & Bryan, 1984), thus ensuring that the retrieved model, bearing an amount of information as low as possible while still fitting the data, is reliable.

DI can be applied to many spectral absorption lines that originate from photospheric chemical elements. As a matter of fact, building "average" line profiles to increase the signal-to-noise ratio (S/N), by applying least-squares deconvolution (LSD, see appendix A.2) to thousands of spectral absorption lines across the spectra, has proven an efficient way to extract the information repeated in all those lines under a compact form (Donati et al., 1997).

2.3.2 Polarimetry and Zeeman-Doppler Imaging

Light, as an electromagnetic wave, can be polarized. Polarization characterizes the way a vectorial wave vibrates as it propagates. In isotropic media, it describes the vibration of the electric field

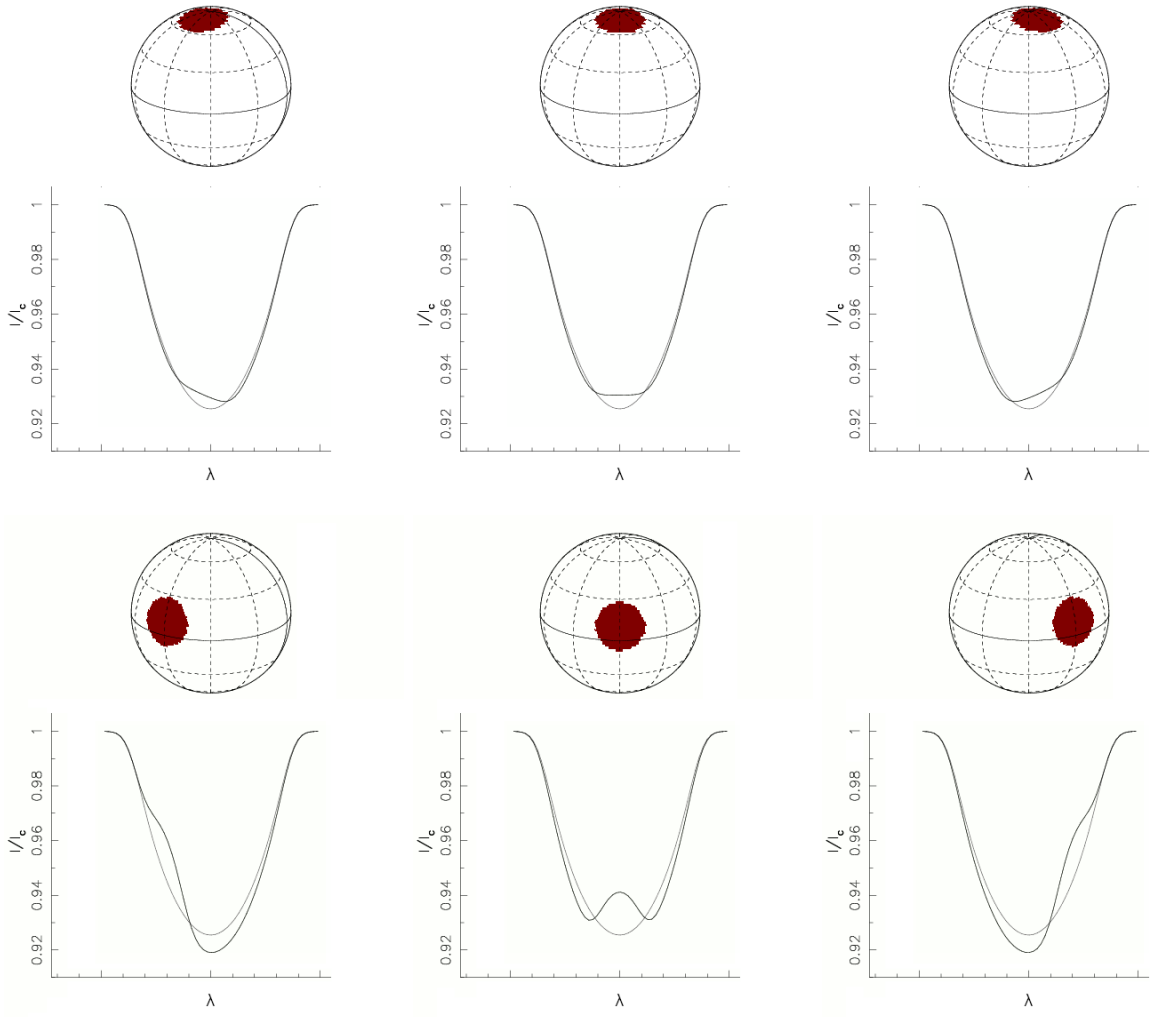

Figure 2.3 – Effect of a dark spot on intensity line profiles as the star rotates, depending on its latitude. *Top row*: high-latitude spot and corresponding spectral absorption line at different rotation phases. *Bottom row*: low-latitude spot and corresponding spectral absorption line at different rotation phases. The spotless line profile is displayed in gray for each case. Credit: Dr. Jean-François Donati. Extracted from: `http://www.ast.obs-mip.fr/article.php3?id_article=457`.

component of light in the plane perpendicular to the propagation direction: polarisation can be linear if it vibrates only in one other direction than the propagation direction, circular if the vector describes circles in the plane perpendicular to the propagation, or a combination of both (elliptic). The polarization of light can be described with the Stokes parameters I, Q, U and V, with I corresponding to the intensity, Q and U characterizing linear polarization and V circular polarization (see Appendix A.1).

The presence of a magnetic field introduces polarization in a beam of light by virtue of the Zeeman effect. For a detailed explanation and rigorous demonstrations about the Zeeman effect, the reader is invited to refer to Landi degl'Innocenti & Landolfi (2004). In short, magnetic fields such as those encountered in wTTSs split the excitation energy levels $(E_J)_{J=0,1,2...}$ of an element into:

$$(E_{J,M})_M = E_J + \mu_0 g B M,$$

where $M = -J, -J+1, ..., J-1, J$, and μ_0 and g are respectively the Bohr magneton and a property

of energy level E_J called the Landé factor.

Transitions between levels E_J and $E_{J'}$ can then occur between $E_{J,M}$ and $E_{J',M'}$ for any M, M' such that $|M - M'| \leq 1$. Among these transitions, those where $M' = M - 1, M, M + 1$ are called π, σ_b, σ_r transitions respectively. This therefore creates a splitting of the spectral lines: when summing over the transitions for all values of M, the π group adds up to a spectral line centered around the line wavelength without magnetic field λ_0, but the $\sigma_{b,r}$ groups have shorter/longer mean wavelengths respectively, the distance to λ_0 being proportional to B.

Because these three types of transitions have different vibration modes, this results in a net balance of polarization in the Q, U and V spectra (see appendix A.1 for more details).

In the case of wTTSs, the Doppler broadening of Stokes I spectral lines is already so large that the Zeeman effect is barely noticeable in Stokes I. But the Stokes V profiles, null in the absence of magnetic fields, present clear signatures in their presence, as illustrated on figure 2.4.

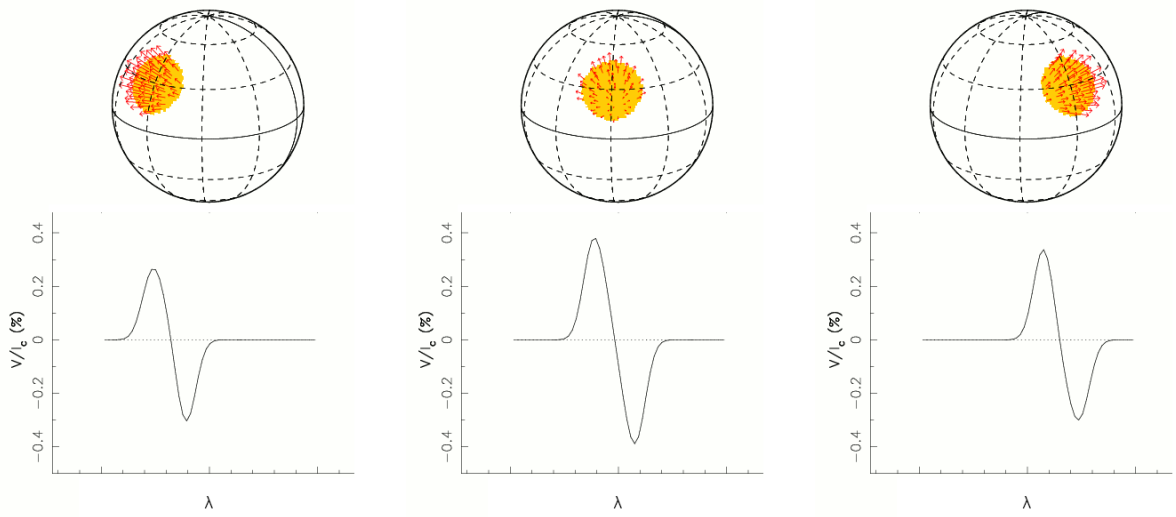

Figure 2.4 – Effect of a radial field spot on Stokes V line profiles as the star rotates. Credit: Dr. Jean-François Donati. Extracted from: `http://www.ast.obs-mip.fr/article.php3?id_article=457`

Zeeman-Doppler Imaging (ZDI) of active stars, described in a series of papers from Semel (1989) to Donati & Brown (1997) and with major updates detailed in Donati et al. (2006, 2014), is a tomography technique inspired from DI which inverts simultaneous series of Stokes I and Stokes V profiles into surface maps of brightness and magnetic field. The next three paragraphs give a short summary of how ZDI works; further explanation is provided in appendix A.3.

ZDI is an inversion problem which looks for the maps that will give the best fit to the spectral data. For the direct problem, ZDI builds a spherical mesh where each cell has a given brightness value and magnetic field vector (radial, meridional and azimuthal components), and the local line profiles of each cell, in Stokes I and Stokes V, are derived using Unno-Rachkovsky's analytical solution to the polarised radiative transfer equations in a Milne-Eddington model atmosphere (Landi degl'Innocenti & Landolfi, 2004). Then, at each observation date, the local profiles are Doppler-shifted and weighted according to the geometry of the system (inclination, current rotation phase, rotation velocity, see figure 2.5), before being added up into the integrated line profile.

Like for DI, the inversion problem is ill-posed and the degeneracy is lifted by looking for the maximum entropy solution. The inversion algorithm, inspired from Skilling & Bryan (1984), is thus an iterative conjugate gradient algorithm, where the model line profiles are to approach the data until noise level is reached (χ^2_r decreases towards 1) and the entropy of the surface maps is to

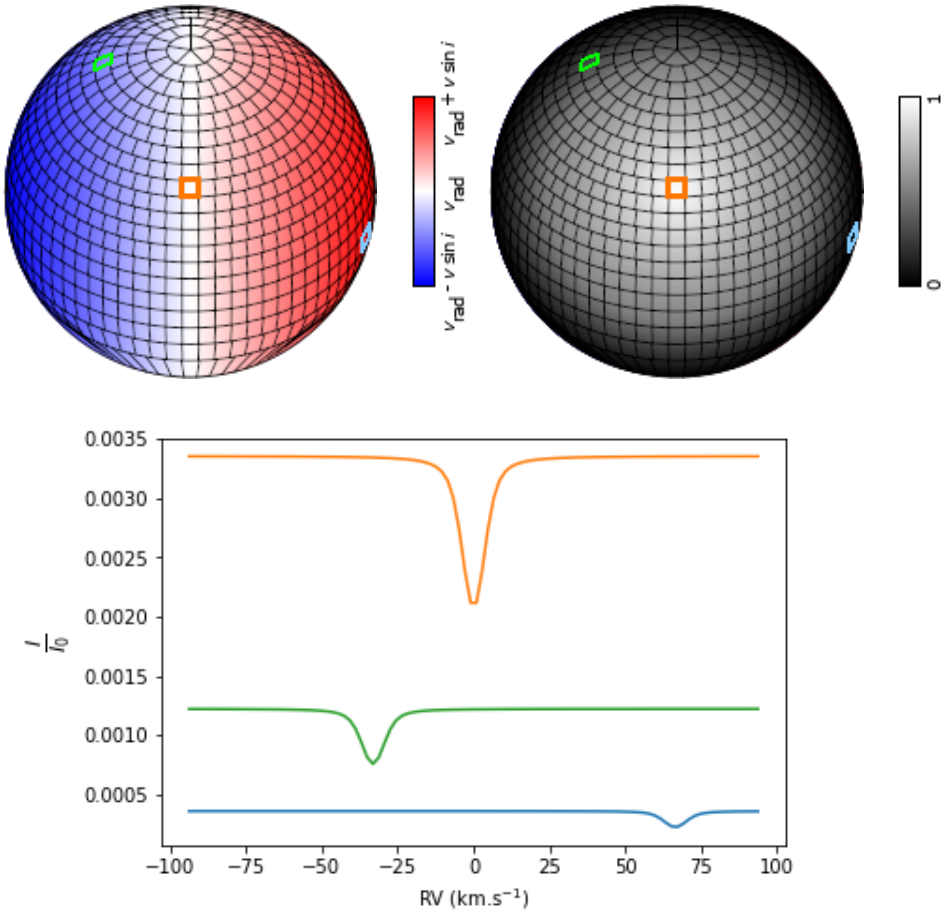

Figure 2.5 – **Top**: ZDI mesh with $i = 50°$ and 1000 cells, at phase 0. There are 20 rings of 5 to 70 cells. Three cells are colored in green, orange and blue respectively, to show their relation with the curves in the bottom plot. *Left*: Local radial velocity at the surface of the star. *Right*: Limb darkening factor. **Bottom**: Individual contributions of the highlighted cells to the synthetic Stokes I line profile, with $v \sin i = 70\,\mathrm{km\,s^{-1}}$ and $v_{\mathrm{rad}} = 0\,\mathrm{km\,s^{-1}}$, and assuming uniform brightness and no magnetic field.

increase as high as possible. The inclination of the rotation axis i, the $v \sin i$ and the bulk RV of the star v_{rad} are all quantities that intervene in the direct problem of ZDI; it is therefore possible to measure them by applying ZDI with different values of these parameters and looking for the maximal entropy reached at convergence.

Since Donati et al. (2000), differential rotation was added to the model of ZDI, by allowing the mesh cells to rotate at different rates depending on their latitude, following a two-parameter sine-square law (see equation A.1). Thus, the equatorial rotation rate, Ω_{eq}, and the difference between the equatorial and polar rotation rates, $d\Omega$, are also parameters that we can optimize using ZDI.

Chapter 3 shows the study of the stellar activity of three wTTSs using ZDI.

2.3.3 Activity proxies

Some particular spectral lines are interesting to study individually (Donati et al., 2010a).

For example, the emission detected in the Hα Stokes I line (located at 656 nm) comes from the magnetically heated high atmosphere and its equivalent width (EW, the integral of the continuum-subtracted line) can undergo periodic modulations due to the stellar rotation. It can also trace the presence of prominences in the chromosphere, which are tied to the stellar surface by magnetic

field lines and rotate together with the star, absorbing some of the Hα emission when passing in front of the visible disc (Collier Cameron & Robinson, 1989).

We use averaged profiles of the Ca II infrared triplet (IRT) in Stokes I, located at 850 nm, 854 nm and 866 nm, whose emission component reflect the heated material in the corona. The emission core EW also presents quasi-periodical modulations of period $P_{\rm rot}$.

The last particular line we use is the He I D_3 line at 588 nm. This line, thought to be produced during accretion shocks when the accreted matter hits the chromosphere, is a good marker of accretion and, for wTTSs, its EW and modulations are expected to be low. This line is also a good indicator for flares, during which its EW greatly increases.

2.4 Velocimetry of wTTSs

2.4.1 Searching for planetary signatures

The general idea of the velocimetry detection method for exoplanets is that, if there is an exoplanet around the star, then its gravitational pull will cause the star to follow a small orbit around the star-planet barycenter. This reflex motion of the star should be detectable in its RVs as a periodic signal (unless the orbit is in the plane perpendicular to the line of sight, in which case the planet is undetectable with this method), the period corresponding to the revolution period of the planet. Using Newton's laws of motion and Kepler's laws of planetary motion, one can derive the RV variation in the general case of an elliptic orbit (see appendix A.4). For example, in the case of a unique planet on a circular orbit, the RV modulation is expected to be:

$$V_r(t) = K\cos\left(2\pi\left(\frac{t}{P_{\rm orb}} - \phi\right)\right) + V_{r,\rm B}, \tag{2.1}$$

$$K \simeq M_{\rm J}\sin i_{\rm J}\sqrt{\frac{\mathcal{G}}{dM_\star}} \quad \text{for } M_{\rm J} \ll M_\star,$$

$$P_{\rm orb} \simeq \frac{2\pi d^{3/2}}{\sqrt{\mathcal{G}M_\star}} \quad \text{for } M_{\rm J} \ll M_\star.$$

where $P_{\rm orb}$ is the orbital period, ϕ depends on the chosen origin of time, $V_{r,\rm B}$ is the constant RV of the star-planet barycenter, $i_{\rm J}$ is the inclination of the orbital axis to the line of sight, $\mathcal{G}$ is the gravitational constant, d is the star-planet separation and $M_\star$ and $M_{\rm J}$ are the masses of the star and of the planet respectively. The amplitude K is higher the more massive and the closer to the star the planet is, which is why hJs are the easiest planets to detect with this method.

For a Jupiter-size planet around a solar-size star, $M_J/M_\star \simeq 10^{-3}$ so we consider that $M_J \ll M_\star$ and derive information on M_J and d as follows:

$$M_J \sin i_{\rm J} \simeq K\left(\frac{P_{\rm orb}M_\star^2}{2\pi\mathcal{G}}\right)^{1/3}$$

$$d \simeq \left(\frac{P_{\rm orb}\sqrt{\mathcal{G}M_\star}}{2\pi}\right)^{2/3}.$$

We note that, with V_r alone, it is not possible to derive M_J and $i_{\rm J}$ individually. To pinpoint the value of M_J, it is therefore necessary to constrain $i_{\rm J}$, for example by using ZDI to find the inclination of the stellar rotation axis i, and assuming that the planet has a null obliquity with respect to the stellar equatorial plane. We can also find $i_{\rm J}$ if the planet transits, or by studying atmospheric signatures (Brogi et al., 2012). We also underline the importance of knowing stellar parameters, in particular the mass of the star, to be able to characterize the planet precisely.

2.4.2 RV activity jitter for wTTSs

Measuring the Doppler shift in Stokes I LSD profiles of wTTSs is far from trivial, because the profiles are highly broadened and distorted. In the context of this thesis, we derive the RVs as the first-order moment of the continuum-subtracted Stokes I LSD profiles. This method is close to computing a weighted average of the local surfacic RV over the visible disc.

$$\mathrm{RV} = \alpha \int_{-\infty}^{+\infty} (I_c - I(v)) v \, \mathrm{d}v,$$

where $\alpha = \left(\int_{-\infty}^{+\infty} (I_c - I(v)) \, \mathrm{d}v \right)^{-1}$ is the normalization constant and the inverse of the line equivalent width (in units of velocity).

To link it to the actual bulk RV of the star V_r, we represent the Doppler effect as: $I(v) = I_0(v - Vr)$, where I_0 is the Stokes I LSD profile of a star identical to ours except with no bulk RV. Thus:

$$\begin{aligned}
\mathrm{RV} &= \alpha \int_{-\infty}^{+\infty} (I_c - I_0(v - Vr)) v \, \mathrm{d}v \\
&= \alpha \int_{-\infty}^{+\infty} (I_c - I_0(v')) (v' + V_r) \, \mathrm{d}v' \\
&= \alpha \int_{-\infty}^{+\infty} (I_c - I_0(v')) v' \, \mathrm{d}v' + V_r \alpha \int_{-\infty}^{+\infty} (I_c - I_0(v')) \, \mathrm{d}v' \\
&= \mathrm{RV}_{\mathrm{jitter}} + V_r
\end{aligned}$$

because $\int_{-\infty}^{+\infty} (I_c - I_0(v')) \, \mathrm{d}v' = \int_{-\infty}^{+\infty} (I_c - I(v)) \, \mathrm{d}v = \alpha^{-1}$.

The measured RV is therefore the sum of a quantity called the activity jitter and of the bulk RV of the star. For a star with no activity, the activity jitter is zero and $\mathrm{RV} = V_r$. Figure 2.6 sums up the contributions of activity and of a planet to observed RVs.

2.4.3 Time-frequency analysis tools

To study the periodicity in our activity proxies, RVs and photometric data, we use Lomb-Scargle periodograms (see appendix A.5.1). In particular, the activity jitter can be modelled from ZDI brightness maps, as the first-order moment of the continuum-subtracted Stokes I synthetic profiles. Once the activity jitter is subtracted from the RVs, we compute Lomb-Scargle periodograms of the filtered RVs to look for any periodicity standing out, which could betray the presence of a hJ. Basically, this method looks for a periodic signature in the Stokes I LSD profiles which ZDI does not manage to model with spots and plages, because its period is not commensurable with the stellar rotation period. However this method does not account for intrinsic variability, whether in the ZDI-modelling of activity jitter or when investigating activity proxies.

This is why we also used another numerical tool, called Gaussian Process Regression (GPR, see appendix A.5.2), to model our activity proxies, RVs and photometric data. GPR does not use a physical model, but a priori knowledge on the statistical behaviour of the data, given under the form of a covariance function. The covariance function informs how correlated any two measurements should be, depending on the time at which they are taken. For example, for the RV activity jitter of a wTTS, we use a pseudo-periodic covariance function:

$$k(t, t') = \theta_1^2 \ \exp\left(-\frac{(t - t')^2}{\theta_3^2} - \frac{\sin^2\left(\frac{\pi(t - t')}{\theta_2}\right)}{\theta_4^2} \right), \tag{2.2}$$

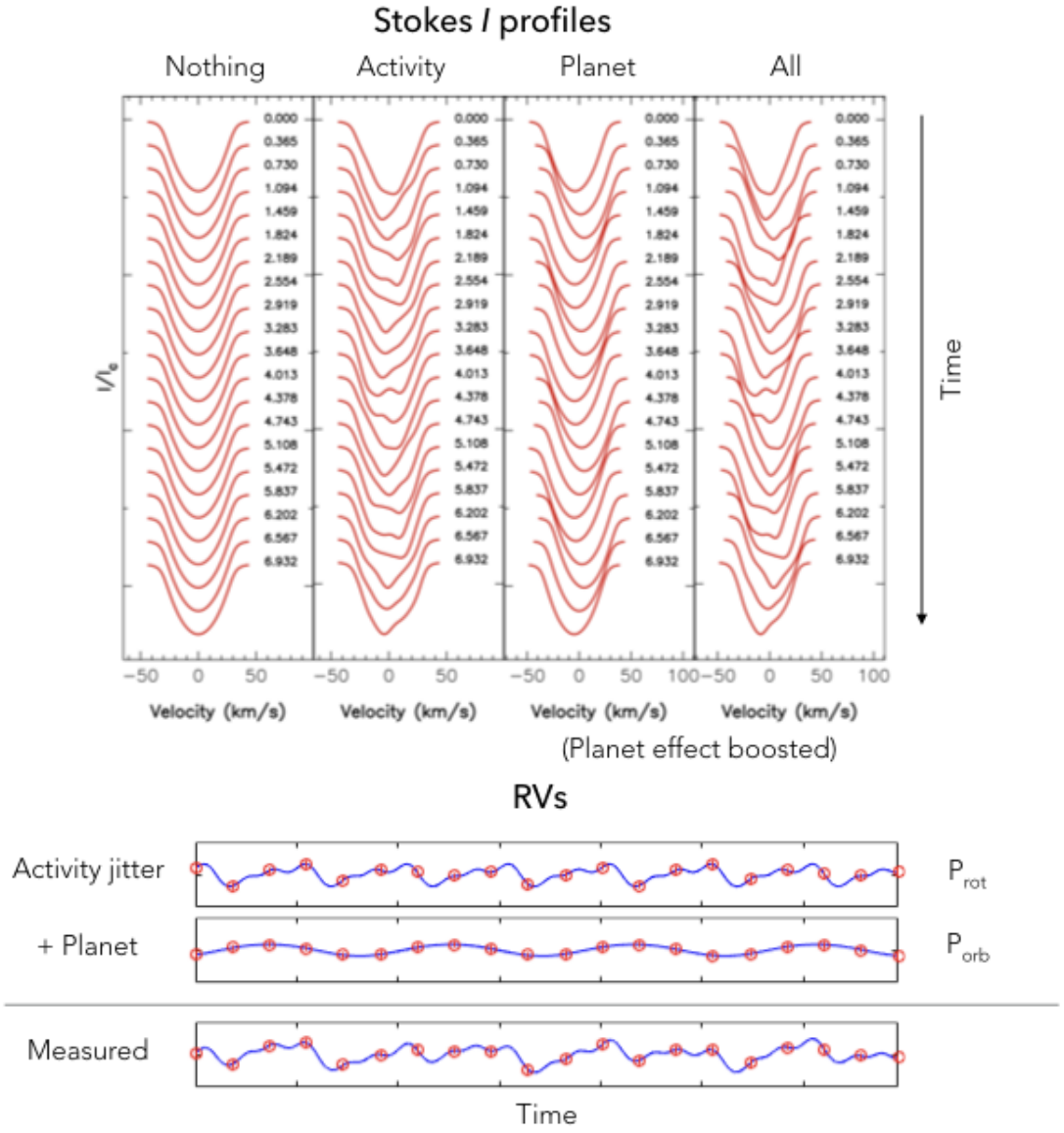

Figure 2.6 – *Top*: Time series of Stokes I LSD profiles for various cases. Activity distorts the profiles while the presence of a planet shifts them without distorting them. The effect of the planet is artificially boosted here for visualization purposes. *Bottom*: corresponding RVs. The activity jitter presents modulations of period P_{rot}, the rotation period of the star, while the reflex motion caused by the presence of a planet is a sine curve of period P_{orb}.

where the amplitude $\theta_1 > 0$, the cycle $\theta_2 > 0$, the decay time $\theta_3 > \theta_2$ and the smoothing parameter $\theta_4 \in [0; 1[$ are called the hyperparameters of the model (Aigrain et al., 2012; Haywood et al., 2014). GPR then uses the data to predict RV jitter values at all times, according to the covariance function. The output is actually a probability distribution over the space of time functions, as illustrated in figure 2.7.

We note that it is possible to add a mean function $m(t)$ to the prior knowledge that GPR uses, which in our case would be the expected planetary signature (a sine wave for a circular orbit, or a keplerian curve for an elliptic orbit). The likelihood $\mathcal{L}$ of the resulting model is given by (Rasmussen

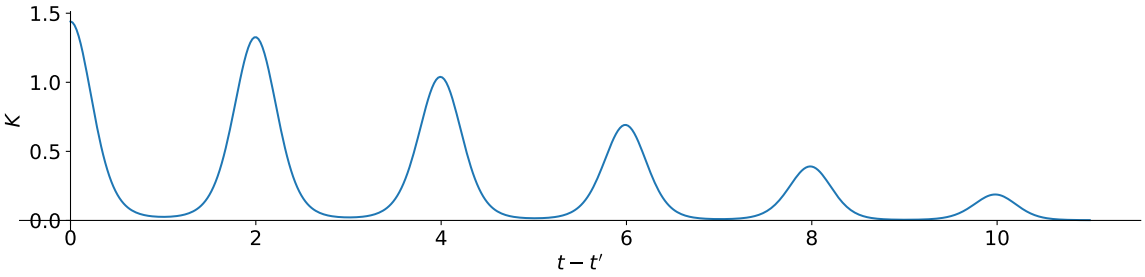

(a) Covariance function

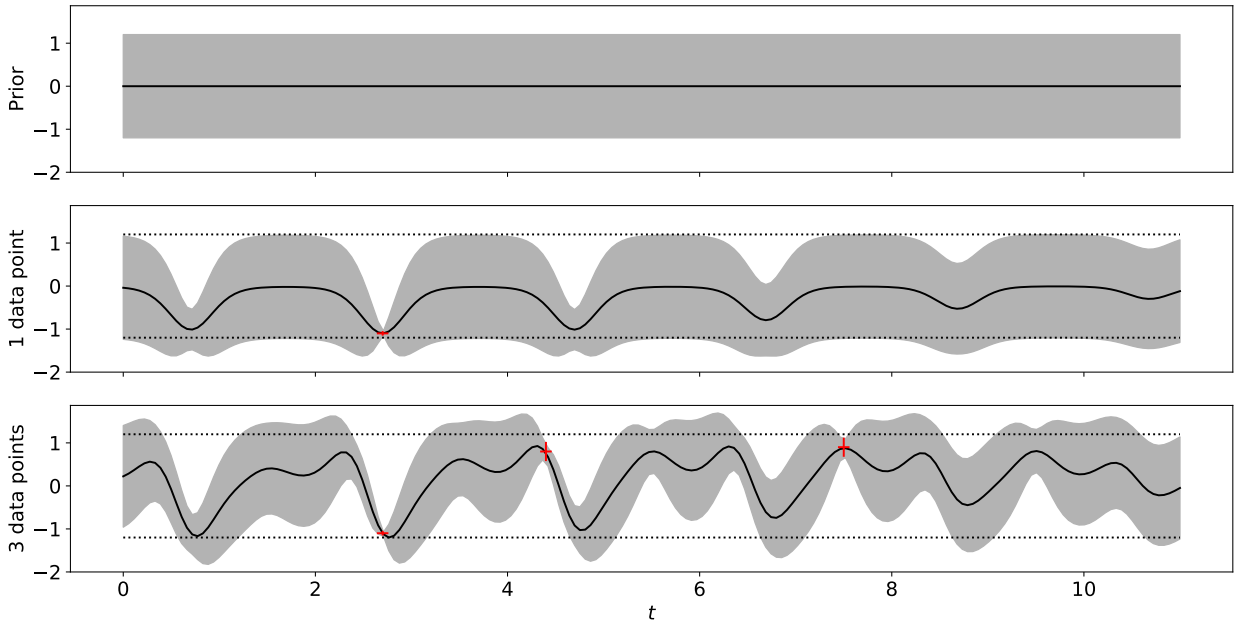

(b) Gaussian process regression with 0, 1 or 3 data points

Figure 2.7 – Example of GPR with a pseudo-periodic covariance function. *Top:* covariance function for a pseudo-periodic GPR model, as defined in equation 2.2 with $\theta_1 = 1.2$, $\theta_2 = 2$, $\theta_3 = 7$, $\theta_4 = 0.5$ (arbitrary units). *Bottom:* result of the GPR depending on the number of data points. When no data point exist, the probability distribution at t is the prior $\mathcal{N}(0, \theta_1^2)$. The black line represents the mean of the point-wise probability distribution while the grey area represents the standard deviation of the point-wise probability distribution. The prior is also reproduced on the second and third graph as dotted black lines. The data points (2.7, -1.1, 0.03), (4.4, 0.8, 0.2), (7.5, 0.9, 0.2) are represented as red crosses whose vertical extension indicates the error bar. Note how measurements constrain the point-wise probability distribution, especially how the sizes of the standard deviations are decreased.

& Williams, 2006):

$$\log \mathcal{L}(m, k) = -\frac{1}{2}\Big(N \log(2\pi) + \log(\det C) + (\mathbf{y} - \mathbf{m})^T C^{-1} (\mathbf{y} - \mathbf{m})\Big), \tag{2.3}$$

where C is the covariance matrix between all the times of observations, $\mathbf{y}$ is the vector of observed RV values and $\mathbf{m}$ is the vector of planetary signature values at all observed times. In general, m and k are not well-constrained a priori, so modelling the RV curve actually consists of looking for the likelihood distribution over the space of hyperparameters of m and k, namely: K, P_{orb}, ϕ for the planetary signature (see equation A.3), potentially with two additional parameters for eccentric orbits (see appendix A.4), and $\theta_1, \theta_2, \theta_3$ and θ_4 for the activity jitter.

GPR comes in handy when data sets span more than a month, as ZDI cannot model intrinsic variability of the brightness distribution (spots/plages fading or intensifying over time), and therefore loses accuracy in the jitter modelling over time, or requires the data set to be split into short subsets. With the pseudo-periodic covariance function, in particular hyperparameter θ_3, GPR allows the signal to lose coherence after a certain amount of time, which can account for, and even inform on, the photospheric intrinsic variability.

Chapter 4 details the analysis of the RVs of three wTTSs carried through within this thesis.

3 | Modelling stellar activity - imaging brightness inhomogeneities and magnetic topologies

Contents

3.1 Chosen targets within the MaTYSSE programme

During this thesis, I analyzed MaTYSSE data on two wTTSs, TAP 26 and V410 Tau, and I closely followed the analysis of the V830 Tau observations, which I partially describe here as well for comparison purposes. These three stars, whose location and physical parameters are displayed in figure 3.1 and table 3.1, are all of particular interest in their own respect. Prior to my thesis, V830 Tau was discovered to host a hJ, and became the youngest star around which a hJ detection was confirmed (other hJs around TTSs are candidates CVSO 30 b, van Eyken et al. 2012 and CI Tau b, Johns-Krull et al. 2016; ∼5 Myr K2-33 has a confirmed hot Neptune Mann et al. 2016; David et al. 2016 and ∼23 Myr V1298 Tau has four confirmed hot giants, David et al. 2019b).

V410 Tau and V830 Tau are evidence that disc dissipation for PMS stars in Taurus may occur on time-scales as short as 1 – 2 Myr (Williams & Cieza, 2011; Ingleby et al., 2012), even though 80 – 90 % of single stars in this star formation region still host discs at similar ages (Kraus et al., 2012). This makes them atypical in this respect, and thus of obvious interest for MaTYSSE. Looking back to figure 1.4, we focus on the rotation rates during the disc-locking phase (see section 1.2.2). Observations of cTTSs (e.g. Affer et al., 2013) seem to suggest that, somehow, cTTSs tend to rotate with a period of 5 – 10 d rather than with arbitrary rotation rates. Supposing that the angular momentum has not changed significantly since the liberation from disc-locking, we could roughly estimate, from the current angular momentum of our stars, the age at which they freed themselves from their discs. Using the moments of inertia from the evolutionary models by Siess et al. (2000), we over-plotted rough iso-angular-momentum tendencies (orange dashed lines) passing through our target stars, as well as the rotation rate of AA Tau (black dashed line at $\Omega/\Omega_\odot \simeq 3.1$) in figure 3.2. Assuming that all disc-locked stars rotate with periods of ∼8 d, the intersection between those dashed lines should indicate the age at which our stars got freed from disc-locking. Of course this is a very rough estimation, but the main conclusion is that our target stars most likely got liberated from disc-locking at very young ages (< 1 Myr). Since their magnetic dipoles are expected to be strong at such young ages, it is then plausible that TAP 26, V410 Tau and V830 Tau dissipated their inner discs, stopped accreting and became wTTSs at those young ages.

In particular, TAP 26 closely resembles an evolved version of V830 Tau, with the same mass and angular momentum, that would have contracted and spun up by four times towards the zero-age main sequence. The increase in rotation rate matches quite well the predicted decrease in the moment of inertia between both epochs according to evolutionary models of Siess et al. (2000). Given the prominent role of the disc in braking the rotation of the star and thus decreasing its angular momentum (Gallet & Bouvier, 2015; Davies et al., 2014), this suggests that TAP 26 dissipated its accretion disc very early, typically as early as, or earlier than V830 Tau.

Finally, V410 Tau, as one of the brightest wTTSs, has been the subject of numerous studies, is one of the youngest observed wTTSs, and is part of a binary star of sky-projected separation ∼17 au (see section 3.1.2).

3.1.1 TAP 26

TAP 26 is a well-studied single wTTSs (Feigelson et al., 1987; Grankin et al., 2008; Grankin, 2013) located in the Taurus star-forming region. TAP 26 was observed in late 2015 and early 2016 with both the ESPaDOnS spectropolarimeter and the 1.25 m telescope at the Crimean Astrophysical Observatory (CrAO). The full journal of observations is available at Yu et al. (2017).

TAP 26 was observed in November 2015 and January 2016 using the high-resolution spectropolarimeter ESPaDOnS at the 3.6-m CFHT at Mauna Kea (Hawaii). A total of 29 Stokes I and Stokes V spectra were collected over a timespan of 72 d, 16 spectra over 16 nights in 2015 Nov, and 13 spectra over 13 nights in 2016 Jan. The frequency of visits was one per night, except at the beginning of the 2015 Nov session where a three-day gap following the first observation was

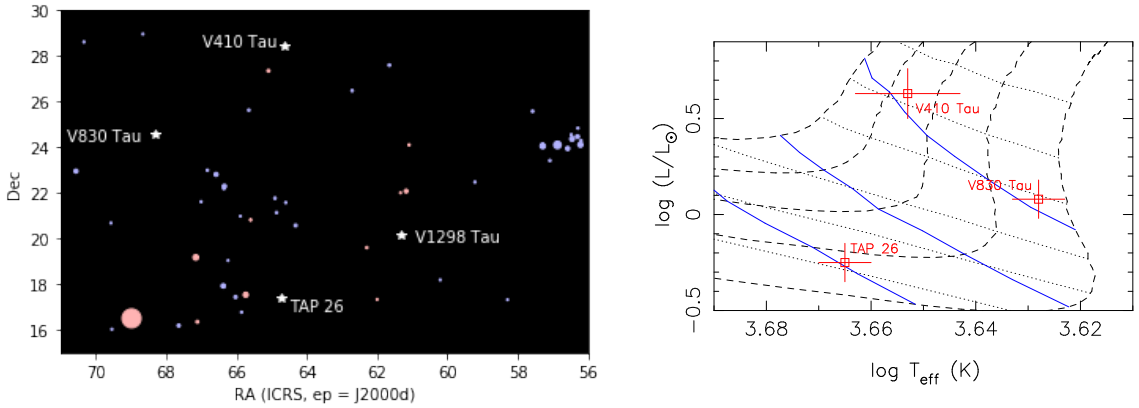

Figure 3.1 – *Left*: positions of TAP 26, V410 Tau and V830 Tau in the sky. Astronomical coordinates are given in the J2000 reference system and surrounding stars are represented with size proportional to their luminosity in the V band according to the Simbad database (Wenger et al., 2000), colored red if their B-V is positive and blue otherwise. The luminous red star in the bottom left corner is α Tau a.k.a. Aldebaran, and the blue cluster in the middle right is the Pleiades cluster. *Right*: observed location of TAP 26, V410 Tau and V830 Tau in the HR diagram. The PMS evolutionary tracks are displayed in dashed lines, for 1.7 $M_\odot$, 1.5 $M_\odot$, 1.3 $M_\odot$, 1.1 $M_\odot$ and 0.9 $M_\odot$ from top to bottom. Isochrones are displayed in dotted lines, for 0.5 Myr, 1 Myr, 2 Myr, 5 Myr, 10 Myr and 20 Myr from top to bottom. The thresholds where the radiative core starts developping and where it reaches 50% and 60% of the stellar radius are marked in blue (from top to bottom). These models (Siess et al., 2000) assume solar metallicity and include convective overshooting.

compensated by pairs of observations on Nov 25, Nov 29 and Dec 01. However, given the 0.71 d rotation period of TAP 26, phase coverage is not optimal and the 2015 Nov data set presents gaps of 0.15 – 0.25 rotation cycle.

Rotational cycles (noted E in the following equation) are computed from Barycentric Julian Dates (BJDs) according to the ephemeris:

$$\text{BJD (d)} = 2,457,344.8 + P_{\text{rot}} E \tag{3.1}$$

in which the photometrically-determined rotation period P_{rot} (equal to 0.7135 d, Grankin, 2013) is taken from the literature and the initial Julian date (2,457,344.8 d) is chosen arbitrarily. The stellar rotational phase is defined as the decimal part of the cycle E.

Applying the automatic spectral classification tool especially developed in the context of MaPP (Magnetic Protostars and Planets) and MaTYSSE, following that of Valenti & Fischer (2005) and discussed in Donati et al. (2012), we find that the photospheric temperature and logarithmic surface gravity of TAP 26 are respectively equal to $T_{\text{eff}} = 4620 \pm 50$ K and $\log g = 4.5 \pm 0.2$ (base-10 logarithm with g in cgs units).

To derive the mass and age of TAP 26, we use the evolutionary models for PMS stars by Siess et al. (2000), assuming solar metallicity and including convective overshooting, for compatibility purposes with MaPP and previous MaTYSSE studies. These models provide $\log g$ as a function of mass and age, so one way to proceed would be to derive the mass and age of TAP 26 from the measured T_{eff} and $\log g$ above. However we prefer to infer them from an HR diagram, with the absolute bolometric luminosity of TAP 26 being derived from photometric measurements and from T_{eff}, as well as results of our imaging code ZDI (see section 3.2), deemed more reliable. Using ZDI, we derived from the spectra that the inclination of the star rotation axis is $i = 55 \pm 10\,^\circ$ and its $v \sin i$ is $68.2 \pm 0.5\,\text{km}\,\text{s}^{-1}$. Since the star rotation period is $P_{\text{rot}} = 0.7135\,\text{d}$, we derive $R_\star \sin i = 0.962 \pm 0.007\,R_\odot$ and $R_\star = 1.17 \pm 0.15\,R_\odot$, which corresponds to a logarithmic luminos-

Table 3.1 – Physical parameters of TAP 26, V410 Tau and V830 Tau. From top to bottom: distance from Earth, mass, radius, minimum stellar radius, effective temperature, base-10 logarithm of surface gravity, logarithmic luminosity, age, rotation period, inclination of the rotation axis to the line of sight, line-of-sight-projected equatorial rotation velocity, equatorial rotation rate, difference between equatorial and polar rotation rates, mean RV in the Solar System barycentric rest frame. References: most values for V830 Tau are taken from Donati et al. (2015), for the rest, *a* is Gaia Collaboration et al. (2018), *b* Grankin (2013), *c* Galli et al. (2018), *d* Stelzer et al. (2003), *e* Donati et al. (2016). The rest are derived in sections 3.1.1, 3.1.2 or 3.2.1.

Parameter	TAP 26	V410 Tau	V830 Tau
d (pc)	121.8 ± 0.6^a	129.0 ± 0.5^c	130.6 ± 0.7^a
$M_\star$ ($\mathrm{M}_\odot$)	1.04 ± 0.10	1.42 ± 0.15	1.00 ± 0.05
$R_\star$ ($\mathrm{R}_\odot$)	1.17 ± 0.15	3.4 ± 0.5	2.0 ± 0.2
$R_\star \sin i$ ($\mathrm{R}_\odot$)	0.962 ± 0.007	2.708 ± 0.007	1.65 ± 0.03
T_{eff} (K)	$4{,}620 \pm 50$	4500 ± 100	4250 ± 50
$\log g$	4.5 ± 0.2	3.8 ± 0.2	3.9 ± 0.2
$\log_{10}(L_\star/\mathrm{L}_\odot)$	-0.25 ± 0.11	0.63 ± 0.13	0.08 ± 0.10
Age (Myr)	$\sim$17	0.84 ± 0.20	$\sim$2.2
P_{rot} (d)	0.7135^b	$1.871\,97 \pm 0.000\,10^d$	2.741^b
i (°)	55 ± 10	50 ± 10	55 ± 10
$v \sin i$ ($\mathrm{km\,s^{-1}}$)	68.2 ± 0.5	73.2 ± 0.2	30.5 ± 0.5
Ω_{eq} ($\mathrm{mrad\,d^{-1}}$)	8819.9 ± 0.3	3359.57 ± 0.06	2295.25 ± 0.20^e
$d\Omega$ ($\mathrm{mrad\,d^{-1}}$)	49.2 ± 1.0	9.7 ± 0.3	17.2 ± 1.4^e
v_{rad} ($\mathrm{km\,s^{-1}}$)	16.25 ± 0.20	$\sim$16.45 (see Chap. 3)	17.5 ± 0.1

ity $\log_{10}(L_\star/\mathrm{L}_\odot) = -0.25 \pm 0.11$ and a bolometric absolute magnitude of 5.36 ± 0.28. To compare this value to the minimum apparent V magnitude of TAP 26 (12.16, see Grankin et al., 2008), we have to account for the following effects:

- A spot coverage of r % adds $-2.5 \log_{10}(1 - r/100)$ to the magnitude (r % of the light is suppressed because of spots). The spot coverage of a wTTS at its brightest varies from star to star (Grankin, 1998; Gully-Santiago et al., 2017, note that, in those papers, the derived quantity is not the fraction of suppressed luminosity, but the fractional area of cool spots of a given temperature).
- The visual extinction caused by the interstellar medium is equal to $A_{\mathrm{V}} = 3.1\ E_{\mathrm{B-V}}(T_{\mathrm{eff}})$. The $\mathrm{B} - \mathrm{V}$ index expected at T_{eff} =4620 K being 0.99 ± 0.02 (Pecaut & Mamajek, 2013, Table 6), and the averaged value measured for TAP 26 being 1.13 ± 0.05 (Kenyon & Hartmann, 1995; Grankin et al., 2008), and given the very weak impact of starspot on $\mathrm{B} - \mathrm{V}$ (Grankin et al., 2008), we derive that the amount of visual extinction that TAP 26 suffers is A_{V} =0.43 ± 0.17 (within 1.5σ of the value of Herczeg & Hillenbrand, 2014, despite the very different methods used to estimate this parameter).
- The bolometric correction to subtract from the bolometric magnitude in order to obtain the apparent magnitude is -0.55 ± 0.05 for $T_{\mathrm{eff}} = 4620$ K (Pecaut & Mamajek, 2013, Table 6).
- The distance d between the star and Earth adds a distance modulus of $-5\ \log_{10}(d/(10\,\mathrm{pc}))$. TAP 26 is at a distance $d = 121.8 \pm 0.6$ pc (Gaia Collaboration et al., 2018), so the distance modulus is 5.84 ± 0.04.

We obtain that $\mathrm{Mag}_{\mathrm{abs},\star} + 2.5 \log_{10}(1 - r/100) = 11.77 \pm 0.33$, and that the minimum V magnitude measured by Grankin et al. (2008) is compatible with a spot coverage of 30 ± 20 %.

Using the Siess et al. (2000) evolutionary models, we obtained that TAP 26 is a $\sim$17 Myr star (in good agreement with the estimate of Grankin, 2013, 18.6 ± 4.0 Myr) and that its mass is $M_\star = 1.04 \pm 0.10\,\mathrm{M}_\odot$ (see figure 3.1). This leads to a $\log g$ of 4.32 ± 0.17, which is consistent

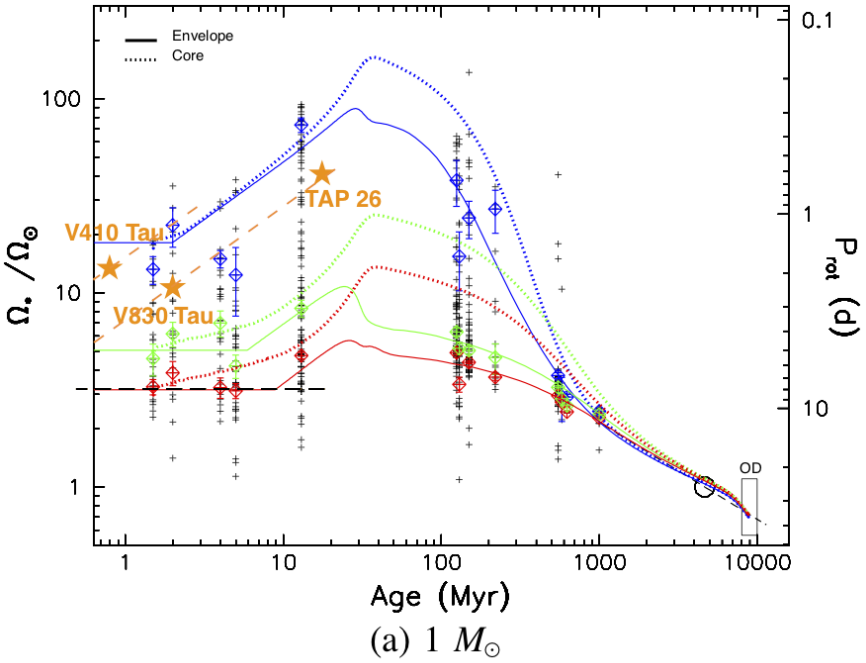

Figure 3.2 – Position of V830 Tau, TAP 26 and V410 Tau on the plot of figure 1.4. The rotation rate of AA Tau (∼8 d, Bouvier et al., 2007) is shown as a horizontal black dashed line. Following the evolution models for the rotation of cores (solid lines) and envelopes (dotted lines), a rough trend for an evolution track passing through V830 Tau and TAP 26 was plotted as an orange dashed line. One can speculate that cTTSs in disc-locked configuration like AA Tau rotate approximately at the same rate, and extrapolate from these black and orange dashed lines that V830 Tau and TAP 26 might have lost their discs before the age of 1 Myr. The same treatment was applied to V410 Tau even though its stellar mass is larger, so its position should not be compared to the percentiles, but similar speculations about its age at disc dissipation can be drawn.

with the value derived from our spectra. The average EW of the 670.7 nm Li line is equal to 0.045 nm, in good agreement with that measured for solar-mass PMS stars in the 10 – 15 Myr Sco-Cen association at the corresponding temperature (Pecaut & Mamajek, 2016), which further confirms our age estimate and thus the evolutionary status of TAP 26. We also note that our target is located past the theoretical threshold at which stars start to be more than half radiative in radius, suggesting that the magnetic field of TAP 26 already started to evolve into a complex topology, if the magnetic topologies of wTTSs follow the same trends as those of cTTSs (Gregory et al., 2012).

The emission core of the Ca II IRT lines exhibits an average EW of $\sim$10 km s^{-1}, corresponding to the amount expected from chromospheric emission for such a wTTS. The He I D_3 line is relatively faint (average EW of $\sim$5 km s^{-1}), demonstrating that accretion is no longer taking place at its surface, in agreement with previous studies (Donati et al., 2014, 2015). The Hα line is also relatively weak by wTTS standards (Kenyon & Hartmann, 1995), with an average EW of 40 km s^{-1}, thereby confirming that TAP 26 is a bona fide wTTS.

Least-Squares Deconvolution (LSD, Donati et al., 1997) was applied to all spectra. The Stokes I and Stokes V LSD profiles can be seen in figure 3.3. Significant distortions are visible in all Stokes I LSD profiles, indicating the presence of brightness inhomogeneities covering a large fraction of the surface of TAP 26 at the time of our observations. Among the 29 profiles we used, 11 were contaminated by solar light reflected off the Moon (5 in 2015 Nov, the Moon being at 9.5° from TAP 26 and at 99% illumination on 2015 Nov 26, and 6 in 2016 Jan, the Moon being at 12° from

TAP 26 and at 85% illumination on 2016 Jan 19); we filtered out this contamination from our Stokes I LSD profiles.

The contemporaneous VR_J photometric observations indicate a brightness modulation with a period of 0.7138 ± 0.0001 d of full amplitude 0.116 mag in V. By analogy with other wTTSs, these photometric variations can be safely attributed to the presence of brightness features at the surface of TAP 26 modulated by rotation. The small difference with the value found in Grankin (2013) suggests the presence of differential rotation in TAP 26 (see section 3.2.2).

3.1.2 V410 Tau

V410 Tau is a three-star system located in the Taurus constellation, composed of an inner binary (V410 Tau A-B Ghez et al., 1995) around which orbits the third component (C, Ghez et al., 1997). V410 Tau B was estimated to have a mass 0.2 ± 0.1 times that of V410 Tau A, and V410 Tau C to have a mass $0.08^{+0.10}_{-0.08}$ times that of V410 Tau AB (Kraus et al., 2011). The sky-projected separation between V410 Tau A and V410 Tau B was measured at $0.13 \pm 0.01''$ for a distance of 16.8 ± 1.4 au, and that between V410 Tau AB and V410 Tau C was measured at $0.28 \pm 0.01''$ for a distance of 36 ± 3 au. Given that V410 Tau A is much brighter than V410 Tau B and V410 Tau C in the optical bandwidth (Ghez et al., 1997), we consider that the spectra analysed in this study characterize the light of V410 Tau A predominantly.

V410 Tau is a very well-observed ∼1 Myr disc-less wTTS (Skelly et al., 2010; Luhman et al., 2010) with a well-constrained rotation period of $1.871\,97 \pm 0.000\,10$ d (Stelzer et al., 2003). One of the most observed wTTSs, it has been the target of both photometric and spectropolarimetric observation campaigns. High variability detected in its light curve (Bouvier & Bertout, 1989; Sokoloff et al., 2008; Grankin et al., 2008) indicates a high level of activity, confirmed with Doppler maps (Skelly et al., 2010; Rice et al., 2011; Carroll et al., 2012) showing that the photosphere features large polar and equatorial cool spots, responsible for the observed temporal modulation as the star rotates. Magnetic maps made by Skelly et al. (2010) and Carroll et al. (2012) have shown a largely toroidal and non-axisymmetric large-scale field despite the mostly convective structure of the star.

Our spectropolarimetric data set spanned 2008 Oct to 2016 Jan, totalling 144 high-resolution optical spectra, both in Stokes I and Stokes V, collected by ESPaDOnS and NARVAL. It is composed of 8 runs, most of which cover around 15 days, taken during 4 different seasons: 2008b-2009a and 2011a prior to MaTYSSE, and 2013b and 2015b-2016a within the frame of MaTYSSE. The full journal of observations is available in the online appendix of Yu et al. (2019). Phase coverage is of different quality depending on the observation epoch. The 2008b data set, with only 6 points, covers only half the surface of the star (phases -0.20 – 0.30). The 2009a data set, although the densest with 48 points in 16 days and including data from both instruments, lacks observations between phases 0.05 and 0.20. The 2011a data set presents a large gap between phases -0.05 and 0.15, and a smaller one between phases 0.65 and 0.80. The 2013b and 2015b data sets are well sampled at the expense of no continuous observations throughout the night like in early 2009, and the 2016a data set, with only 9 points, lacks observations between phases 0.25 – 0.45 and -0.15 – 0.05.

Contemporaneous BVR_JI_J photometric measurements were taken from the Crimean Astrophysical Observatory 1.25 m and 0.60 m telescopes between August 2008 and March 2017, counting 420 observations distributed over 9 runs at a rate of one run per year, each run covering 3 – 7 months. We also used 2703 data points of visible magnitude from the Wide Angle Search for Planets (WASP, Pollacco et al., 2006) photometric campaign covering semesters 2010b-2011a.

Rotational cycles (noted E in the following equation) are computed from Barycentric Julian Dates (BJDs) according to the ephemeris:

$$\mathrm{BJD\ (d)} = 2,454,832.58033 + P_{\mathrm{rot}}E, \tag{3.2}$$

where the reference date and rotation period are chosen to be the same as in Skelly et al. (2010), in particular $P_{\rm rot} = 1.871\,970 \pm 0.000\,010$ d (Stelzer et al., 2003).

Applying the automatic spectral classification tool, we constrain the temperature and logarithmic gravity of V410 Tau to, respectively, $T_{\rm eff} = 4500 \pm 100$ K and $\log g = 3.8 \pm 0.2$. V410 Tau is at $d = 129.0 \pm 0.5$ pc from Earth (Galli et al., 2018, we chose this value over the Gaia result, 130.4 ± 0.9 pc, because it is both in agreement with it and more precise). We find a minimum measured magnitude of 10.52 ± 0.02 and a mean B − V index of 1.17 ± 0.02, from which we derive an absolute bolometric magnitude of 3.93 ± 0.11.

Assuming a spot coverage at maximum brightness of 50 ± 15 %, we derive an absolute unspotted magnitude of 3.17 ± 0.33, a logarithmic luminosity $\log_{10}(L_\star/{\rm L}_\odot) = 0.63 \pm 0.13$, and a stellar radius $R_\star = 3.4 \pm 0.5\,{\rm R}_\odot$. Since our ZDI optimization yields $v \sin i = 73.2 \pm 0.2\,{\rm km\,s^{-1}}$, this implies an inclination of $53 \pm 11\,^\circ$, which is in agreement with the value derived from the imaging code: $i = 50 \pm 10\,^\circ$.

The position of V410 Tau on the Hertzsprung-Russell diagram is displayed in figure 3.1. According to Siess et al. (2000) PMS stellar evolution models, V410 Tau is a $1.42 \pm 0.15\,{\rm M}_\odot$ star, aged 0.84 ± 0.20 Myr and fully convective. Our values are in good agreement with Welty & Ramsey (1995) and Skelly et al. (2010), who had previously derived masses of $\sim$1.5 $\rm M_\odot$ and $1.4 \pm 0.2\,{\rm M}_\odot$, radii of $\sim$2.64 $\rm R_\odot$ and $\sim$3.0 $\rm R_\odot$, and ages of $1 - 2$ Myr 1.2 ± 0.3 Myr respectively. Moreover, Skelly et al. (2010) had deduced that V410 Tau could have a radiative core of radius between $0.0\,R_\star$ and $0.28\,R_\star$. Table 3.1 sums up the stellar parameters of V410 Tau found in this study.

The emission core of the Ca II IRT presents an average EW of $\sim$13 $\rm km\,s^{-1}$ (0.37 Å). The He I D_3 line is relatively weak with an average EW of 13 $\rm km\,s^{-1}$ as well (0.25 Å), in agreement with the non-accreting status of V410 Tau. The Hα line has an average EW of 14 $\rm km\,s^{-1}$ (0.33 Å) and a rms EW of 27 $\rm km\,s^{-1}$.

We detected three small flares from the He I D_3 line, which affected 5 spectra, and one big flare that was visible in He I D_3, Ca II and Hα (EW in Hα: $\sim$ 230 $\rm km\,s^{-1}$). We removed the 6 flare-subjected observations from our data sets for the rest of the analysis.

Least-squares deconvolution (LSD, see Donati et al., 1997) was applied to all our spectra, moonlight pollution affected 15 of our Stokes I LSD profiles and was filtered out. Some of the Stokes I and Stokes V LSD profiles are visible in figure 3.3.

In each run, the visible magnitude presents modulations of a period $\sim$1.87 d and amplitude varying from 0.04 – 0.24 mag.

3.1.3 V830 Tau

V830 Tau is another wTTS within the MaTYSSE sample, it is $\sim$2.2 Myr, has a mass of $1.00 \pm 0.05\,{\rm M}_\odot$, a radius of $2.0 \pm 0.2\,{\rm R}_\odot$ and a rotation period of 2.741 d. As such, it has the same mass and same angular momentum as TAP 26 so it could be a 2 Myr version of TAP 26. I did not personally analyze the data on that star but comparing the results on V830 Tau to the results on TAP 26 and V410 Tau is of very high interest. The text below is partially extracted from Donati et al. (2015) and Donati et al. (2017).

V830 Tau is a well-studied single wTTS (from direct imaging and spectroscopic monitoring; e.g. Kraus et al., 2011; Nguyen et al., 2012) and bona fide member of the Taurus L1495 dark cloud (Xiao et al., 2012), showing clear photometric variations of large amplitudes (Grankin et al., 2008; Xiao et al., 2012).

It was observed in 2014 December and 2015 January using ESPaDOnS at the CFHT. A total of 15 Stokes V and Stokes I spectra were collected over a time-span of 28 nights, corresponding to 10 rotation cycles (Donati et al., 2015). In late 2015, 48 high-resolution spectra were collected (Donati et al., 2016). V830 Tau was re-observed from 2016 Jan 14 to Feb 10 (Donati et al., 2017),

using again ESPaDOnS at the CFHT, its clone Narval at the TBL, and ESPaDOnS coupled to Gemini-North through the GRACES fibre link (Chene et al., 2014). A total of 15, 6, and 6 spectra were, respectively, collected with ESPaDOnS, Narval, and ESPaDOnS/GRACES, at a daily rate from Jan 14 – 30 and more sparsely afterwards. For the 2016a run, contemporaneous BVR_JI_J photometric observations were also collected from the CrAO 1.25 metre telescope.

We note that our target is located close to the theoretical threshold at which $1\,M_\odot$ stars cease to be fully convective (see Fig. 3.1). This may suggest that V830 Tau is still fully convective; our error bars on the location of the star in the HR diagram is, however, still too large to reach a firm conclusion. V830 Tau shows no traces of leftover dust from the original disc (e.g. Cieza et al., 2013).

The next two sections give a detailed account of the application of ZDI to TAP 26 and V410 Tau, as well as an overview of the results of ZDI on V830 Tau. The ZDI model we used constitutes a good approximation for wTTSs unless they are undergoing flares, which is why observations taken during flares were removed.

3.2 Zeeman-Doppler imaging of TAP 26 and V410 Tau

With ZDI, we reconstructed brightness and magnetic surface maps at all observation epochs for both TAP 26 and V410 Tau. Thanks to our data sets spanning more than two months, we were also able to measure the surfacic latitudinal differential rotation of our targets. Finally, with the 8 years worth of data we have on V410 Tau, we investigated the mid-term variability of that wTTS.

3.2.1 Brightness and magnetic reconstruction

Applying ZDI to our data sets, we derived the surface brightness and magnetic maps of TAP 26 and V410 Tau. For numerical computation, the default brightness value given to the quiet photosphere here was 1, meaning that cells with brightness $0 < Q < 1$ had dark spots and cells with brightness $Q > 1$ had bright plages (Donati et al., 2014).

Parameter optimization was done with $n_{\rm cell} = 1000$ cells for the stellar surface mesh, and spherical harmonics for the magnetic reconstruction up to order $\ell_{\rm max} = 15$ (see appendix A.3), for both stars. We produced our final figures with $n_{\rm cell} = 10000$ for aesthetic purposes, the differences in model optimization induced by the change in $n_{\rm cell}$ are negligible.

The local profile used for TAP 26 is described by a central wavelength, a Doppler width and a Landé factor of typical values 670 nm, $1.8\,{\rm km\,s^{-1}}$ and 1.2 respectively, and an EW of $4.6\,{\rm km\,s^{-1}}$. To fit the LSD profiles of V410 Tau, we chose a spectral line of mean wavelength, Doppler width, Landé factor and EW of respective values 640 nm, $1.8\,{\rm km\,s^{-1}}$, 1.2 and $3.8\,{\rm km\,s^{-1}}$.

In a first pass, we set a null differential rotation ($\beta = \gamma = 0$, see appendix A.1) and we tried a grid of values for i, $v \sin i$ and $v_{\rm rad}$. Because ZDI does not reconstruct intrinsic temporal variability except for differential rotation, there is a limit to the duration a fittable data set can span. For that reason, ZDI was applied separately to observation runs that spanned at most one month.

The stellar parameters that yield the maps with highest entropy are, for TAP 26, $i = 55 \pm 10\,^\circ$, $v \sin i = 68.2 \pm 0.5\,{\rm km\,s^{-1}}$ and $v_{\rm rad} = 17.0 \pm 0.2\,{\rm km\,s^{-1}}$, and, for V410 Tau, $i = 50 \pm 10\,^\circ$ and $v \sin i = 73.2 \pm 0.5\,{\rm km\,s^{-1}}$ for all observation epochs, while $v_{\rm rad}$ was found to vary over the years for V410 Tau (see table 3.2).

In a second pass, we optimized differential rotation parameters at fixed values of i, $v \sin i$ and $v_{\rm rad}$ for extended data sets that each spanned at most six months. The models shown next are the final models after this second optimization and the results concerning the differential rotation are discussed in section 3.2.2.

Stokes I and V LSD profiles are displayed in figures 3.3 and 3.4, together with the corresponding synthetic spectra from ZDI. For both stars, the synthetic profiles presented in the figure match the observed ones at $\chi^2_{\rm r} = 1$, whereas unspotted magnetic maps corresponded to much higher $\chi^2_{\rm r}$ values, for example $\chi^2_{\rm r} = 13$ and 9 for the 2015 Nov and 2016 Jan data sets on TAP 26. This shows that the iterative algorithm of ZDI successfully manages to reproduce the data at noise level.

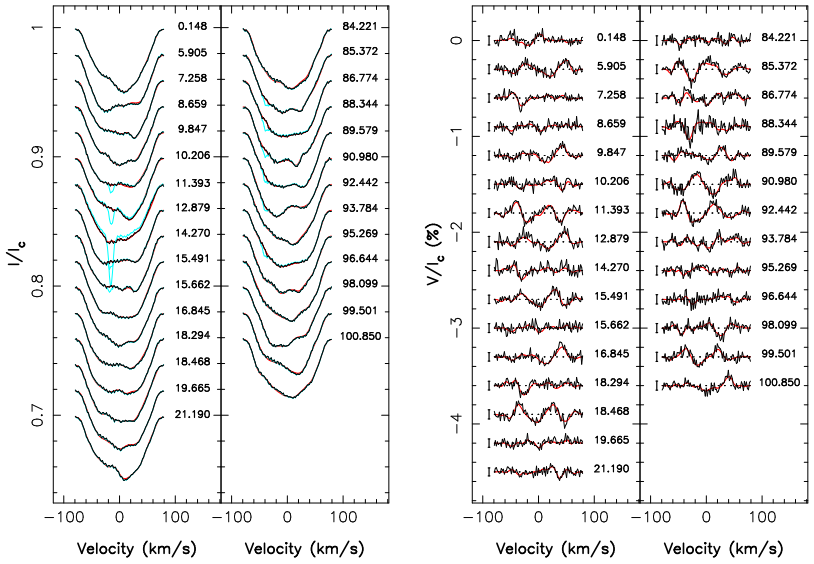

Figure 3.3 – Maximum entropy fit (thin red lines) to the observed (thick black lines) Stokes I (*left*) and V (*right*) LSD profiles of TAP 26. The 2015 Nov data set is represented in the 1st and 3rd panels and the 2016 Jan data set in the 2nd and 4th panels. The Stokes I LSD profiles before the removal of lunar pollution are coloured in cyan, and 3σ-error bars are displayed for the Stokes V profiles. The rotational cycles are written beside their corresponding profiles.

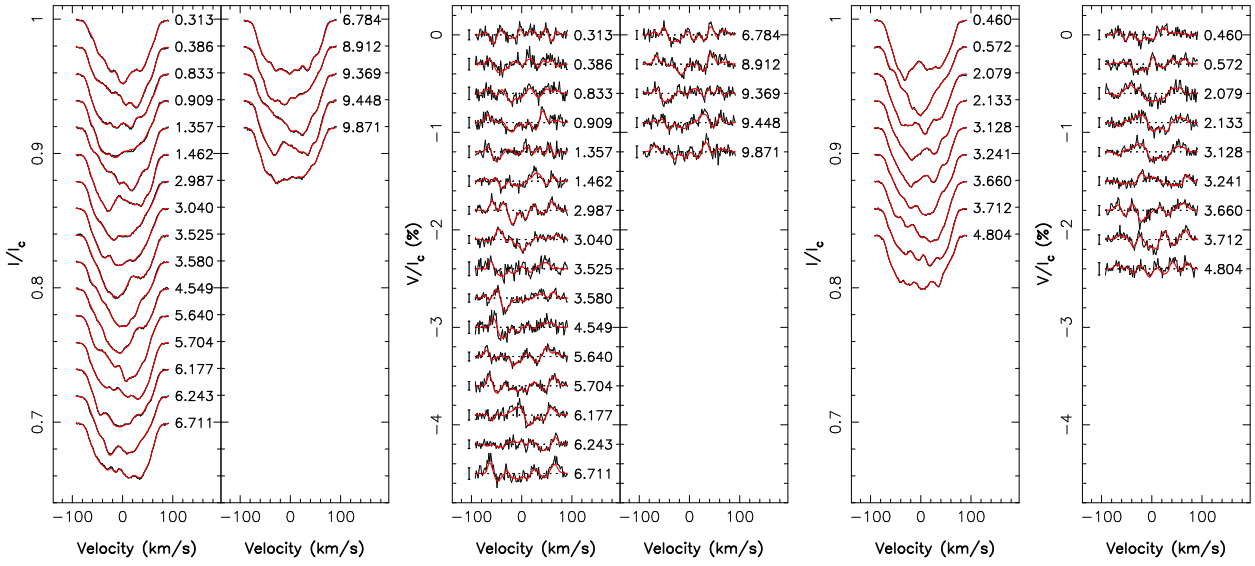

Figure 3.4 – Stokes I (1st and 3rd panels) and Stokes V (2nd and 4th panels) LSD profiles of V410 Tau for observation epochs 2015 Dec (*left*) and 2016 Jan (*right*). The black and red lines represent respectively the oberved profiles and the maximum-entropy fit obtained with Zeeman Doppler Imaging.

The reconstructed brightness and magnetic maps are shown in figures 3.5 and 3.6. Properties of these reconstructed maps are listed in table 3.2.

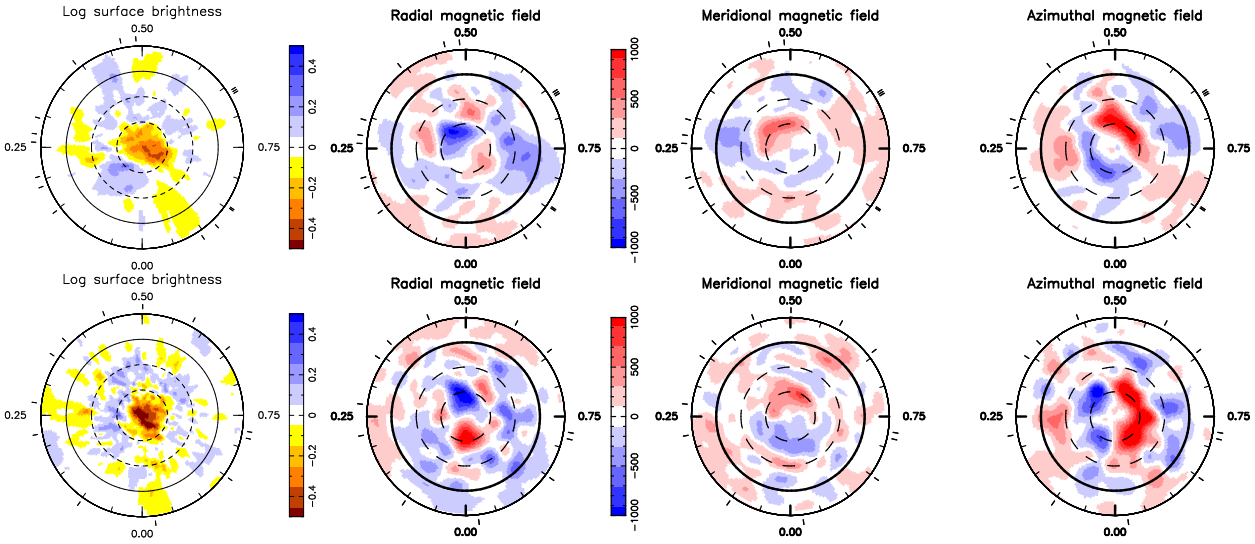

Figure 3.5 – Flattened polar view of the surface brightness (1st column) and magnetic (2nd to 4th columns) maps for the TAP 26 2015 Nov (top) and 2016 Jan (bottom) data sets. The equator and the 60°, 30° and -30° latitude parallels are depicted as solid and dashed black lines respectively. In brightness maps, the colour scale indicates the logarithm of the relative brightness, with brown/blue areas representing cool spots/bright plages. In the magnetic maps, the radial, meridional and azimuthal components are displayed from left to right, using a colour scale in G, with red representing outwards and anti-clockwise field on the radial and azimuthal field maps respectively, and the direction pointing towards the visible pole on the meridional field maps. Finally, the outer ticks mark the phases of observation.

Table 3.2 – Characteristics of the ZDI models for TAP 26 (first subset or rows) and V410 Tau (second subset or rows) at each observation epoch. *Column 1*: observation epoch. *Column 2*: number of spectropolarimetric observations used for ZDI. *Column 3*: contribution of cool ("spots") and hot ("plages") areas on the brightness map. *Column 4*: average magnetic strength, defined as the square root of the average squared magnetic field over the surface of the star. *Columns 5 to 7*: normalized contribution of the poloidal field, part of the poloidal field that is dipolar and part of the poloidal field that is symmetric. *Columns 8-9*: part of the toroidal field that is dipolar and part of the toroidal field that is symmetric. *Column 10*: dipole characteristics: field strength, tilt with respect to the rotation axis and phase of the pole. *Column 11*: systemic RV of the star as measured with ZDI, the error bar on those values is $0.20\,\mathrm{km\,s^{-1}}$. Error bars on the magnetic field ratios are typically of 0.1.

Run	N_{sp}	Sp.+pl. cov. (%)	$\langle B \rangle$ (G)	r_{pol}	Poloidal		Toroidal		Dip. str. (G), tilt, phase	v_{rad} ($\mathrm{km\,s^{-1}}$)
					r_{dip}	r_{sym}	r_{dip}	r_{sym}		
2015 Nov	16	5+5	328	0.69	0.15	0.51	0.14	0.73	171, 25°, 0.73	17.0
2016 Jan	13	7+5	428	0.65	0.07	0.42	0.02	0.90	141, 36°, 0.85	17.0
2008 Dec	6	5.8+4.4	486	0.32	0.13	0.37	0.89	0.96	129, 23°, 0.71	16.30
2009 Jan	48	9.6+7.1	556	0.55	0.26	0.09	0.54	0.79	165, 54°, 0.54	16.30
2011 Jan	20	8.1+6.6	560	0.40	0.24	0.23	0.72	0.85	239, 44°, 0.62	16.40
2013 Dec	25	11.0+7.5	568	0.49	0.23	0.34	0.66	0.81	254, 18°, 0.56	16.50
2015 Dec	21	8.9+6.7	600	0.68	0.37	0.45	0.62	0.78	458, 30°, 0.54	16.65
2016 Jan	9	7.9+6.5	480	0.77	0.38	0.30	0.68	0.87	400, 44°, 0.51	16.65

The 2008 Dec data set on V410 Tau has a phase coverage of only half the star, so the derived parameters at this epoch are no more than weakly meaningful and are not further discussed.

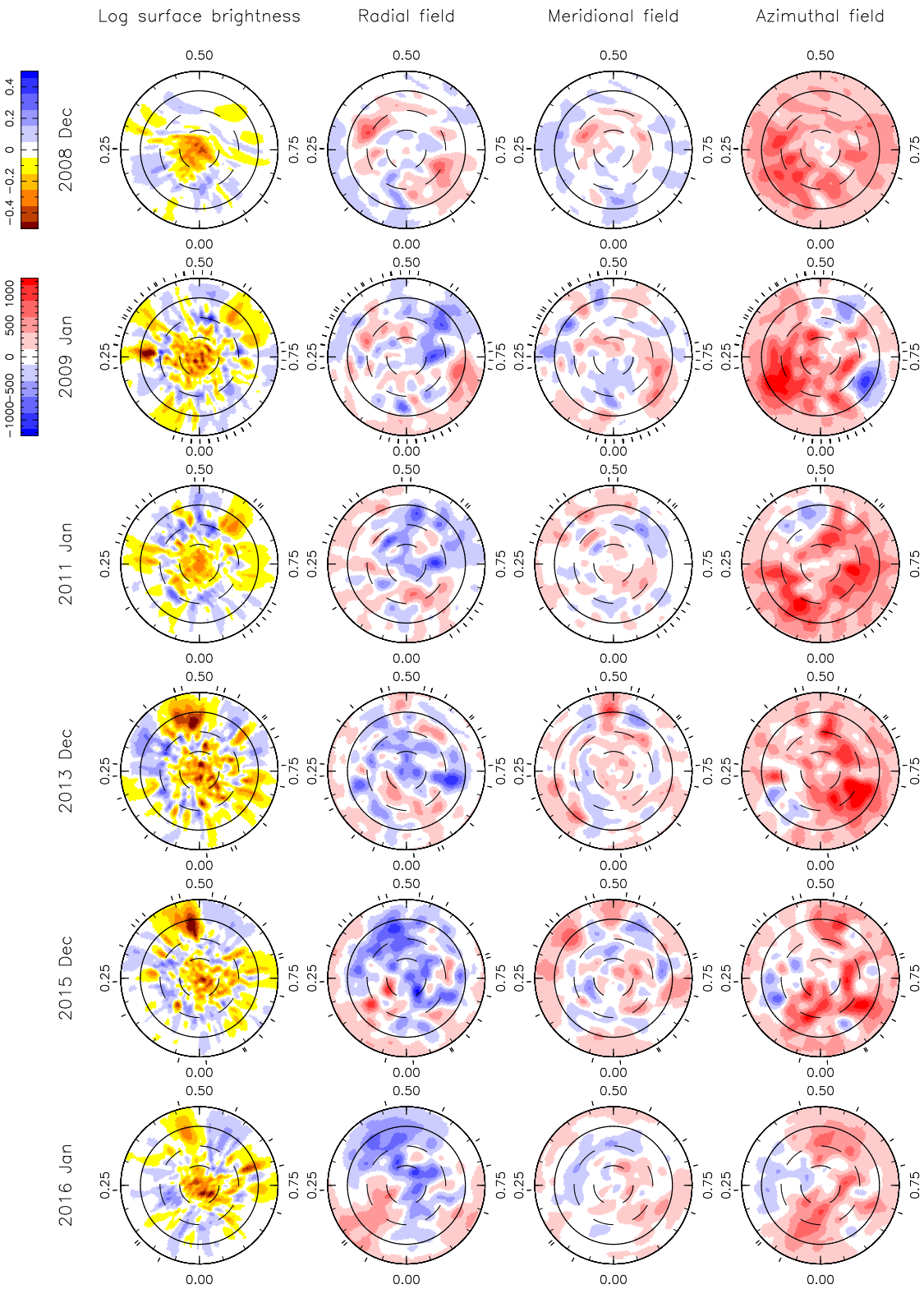

Figure 3.6 – ZDI maps of the logarithmic relative surface brightness (first column), and the radial, meridional and azimuthal magnetic field (second to fourth columns) of V410 Tau, reconstructed from data collected in 2008 Dec, 2009 Jan, 2011 Jan, 2013 Dec, 2015 Dec and 2016 Jan (top to bottom rows). Refer to the caption of figure 3.5 for more details.

Brightness maps

The ZDI models suggest that V410 Tau is significantly more spotted than TAP 26, with 15 – 18 % versus 10 – 12 % spot coverage respectively. This is consistent with the spottedness assumptions in sections 3.1.1 and 3.1.2, considering that ZDI is only sensitive to mid- to large-scale surface features, and thus underestimates the total spot coverage.

For both stars, the brightness maps exhibit a number of small-scale features, with a large cool polar cap at all epochs, like in the previous V410 Tau maps published in Skelly et al. (2010); Rice et al. (2011); Carroll et al. (2012), and those reconstructed on other rapidly rotating wTTSs (e.g. LkCa 4, Donati et al., 2014).

For TAP 26, both reconstructed maps share two equatorial spots, located at phases 0.22 and 0.92 in 2015 Nov, and 0.27 and 0.97 in 2016 Jan, interleaved with bright plages. We observe a number of differences between both images potentially attributable to differential rotation and / or intrinsic variability (see sections 3.2.2 and 3.2.4); however, the limited phase coverage at both epochs makes the direct comparison of individual surface features between maps ambiguous and hazardous.

For V410 Tau, brightness maps display a high contrast. In 2009 Jan, 2013 Dec and 2015 Dec, the brightness map exhibits a strong equatorial spot, respectively at phases 0.27, 0.48 and 0.48. The equatorial spot at phase 0.27, and another equatorial spot at phase 0.60 from the 2009 Jan map are also visible in both Skelly et al. (2010) and Rice et al. (2011) (figure 8), albeit less contrasted compared to other features than they are on our map. A remnant of the 2015 Dec equatorial spot is observed on the 2016 Jan map, where its intensity seems to have decreased, but this has to be taken with caution since ZDI maps are somewhat dependent on phase coverage.

To get a rough estimate of the temperature in the spotted regions of V410 Tau, we computed B − V (V) models from the Kurucz models for colors of main sequence stars with $\log g = 3.5$, $T_{\rm eff} = 4500\,{\rm K}$ and $\mathrm{E(B-V)} = 0.10\,{\rm mag}$ (Kurucz, 1993): we fit a two-temperature model with a photospheric temperature of 4500 K and different values for the spot temperature. Then, for each tested spot temperature, for all values of spot coverage from 0 – 100 %, we computed the resulting B and the resulting V using the following formulas, from which we derived the B − V.

$$\mathrm{V}(r) = -2.5\log_{10}(r\ 10^{-\frac{\mathrm{V_{spot}}}{2.5}} + (1-r)10^{-\frac{\mathrm{V_{star}}}{2.5}})$$
$$\mathrm{B}(r) = -2.5\log_{10}(r\ 10^{-\frac{\mathrm{B_{spot}}}{2.5}} + (1-r)10^{-\frac{\mathrm{B_{star}}}{2.5}})$$

The resulting models are plotted in figure 3.7. We find that a spot temperature of 3750 K fits our B − V measurements well, from which we deduce that the spot coverage on V410 Tau varies between 50 – 75 %, in agreement with the assumption in section 3.1.2. This implies a contrast of ∼750 K between dark spots and the photosphere. This contrast is slightly lower than the one retrieved for the 2 Myr wTTS LkCa 4 in Gully-Santiago et al. (2017).

Photometry curves from the ZDI brightness maps were synthesized and a comparison to contemporary CrAO data, and WASP data in the case of the V410 Tau 2011 Jan set, is shown in figures 3.8 and 3.9. Despite a slightly underestimated amplitude at some phases, ZDI manages to retrieve the measured photometric variations rather satisfyingly. The most obvious evidence of mid-term variability is the small temporal evolution in the 2010b-2011a WASP data of V410 Tau, where the regions around phases 0.20 and 0.70 globally darken by 0.02 – 0.03 mag ($\sim 4\sigma$) over the 4 months that the data set spans.

Magnetic maps

The large-scale field reconstructed for TAP 26 features a rms magnetic flux of 330 and 430 G in 2015 Nov and 2016 Jan respectively. The field is found to be mainly poloidal (70 % of the reconstructed

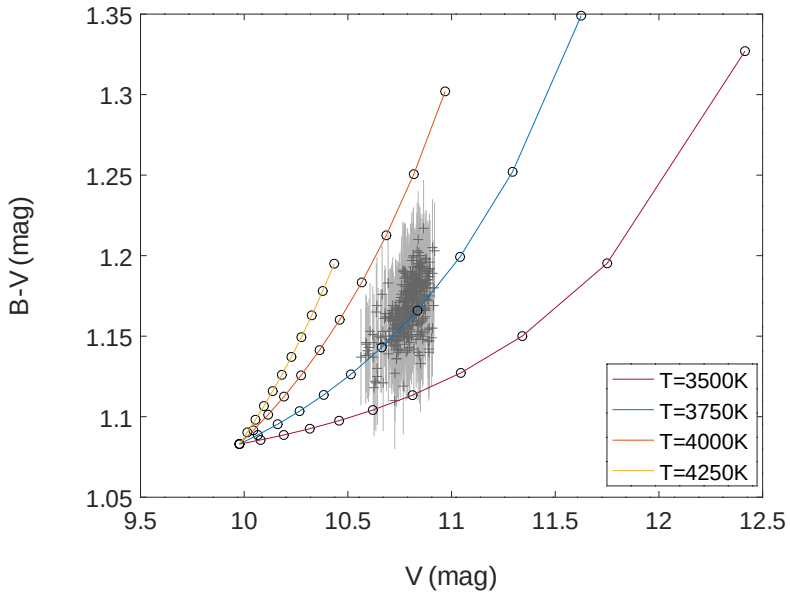

Figure 3.7 – Fit of the B − V (V) curve with Kurucz models, with a photosphere temperature of 4500 K, $\log g$ of 3.5, E(B − V) of 0.10. Each full line corresponds to a particular value of the spot temperature, and dots mark the spot coverage with steps of 10 % (the dot at V = 10.0 and B − V = 1.08 corresponding to a 0 % spot coverage). The extension of our data correspond to a spot coverage constantly between 50 – 75 %.

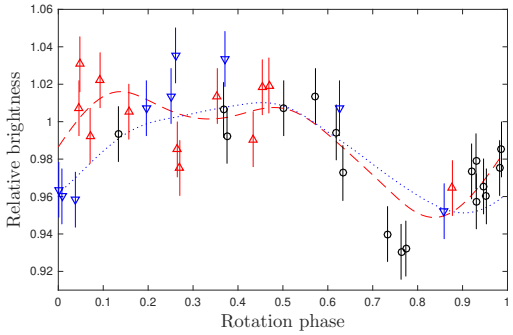

Figure 3.8 – Photometry curves of the relative brightness as function of the rotation phase for TAP 26. The light curves synthesised from the reconstructed brightness maps for 2015 Nov and 2016 Jan are represented by a dashed red line and a dotted blue line respectively. The CrAO measurements are represented as dots with 1σ error bars, with the observations from 2015 Aug to 2015 Oct in black circles, the observations from 2015 Oct to 2015 Dec in red upward-pointing triangles and the observations from 2015 Dec to 2016 Mar in blue downward-pointing triangles.

magnetic energy), though with a significant toroidal component (30 % of the reconstructed magnetic energy). It is also largely axisymmetric (50 % and 80 % of the poloidal and toroidal field energy respectively). The dipolar component of the large-scale field has a strength of 140 ± 10 G at both epochs, corresponding to about 10 % of the reconstructed poloidal field energy, and is tilted at $40 \pm 5°$ to the line of sight, i.e., midway to the equator, towards phase 0.73 ± 0.03 and 0.85 ± 0.03 in 2015 Nov and 2016 Jan respectively. The increase in the phase towards which the dipole is tilted suggests that intermediate to high latitudes (at which the dipole poles are anchored) are rotating more slowly than average by 0.19 %, i.e., with a period of ∼0.7148 d; this is confirmed by the fact

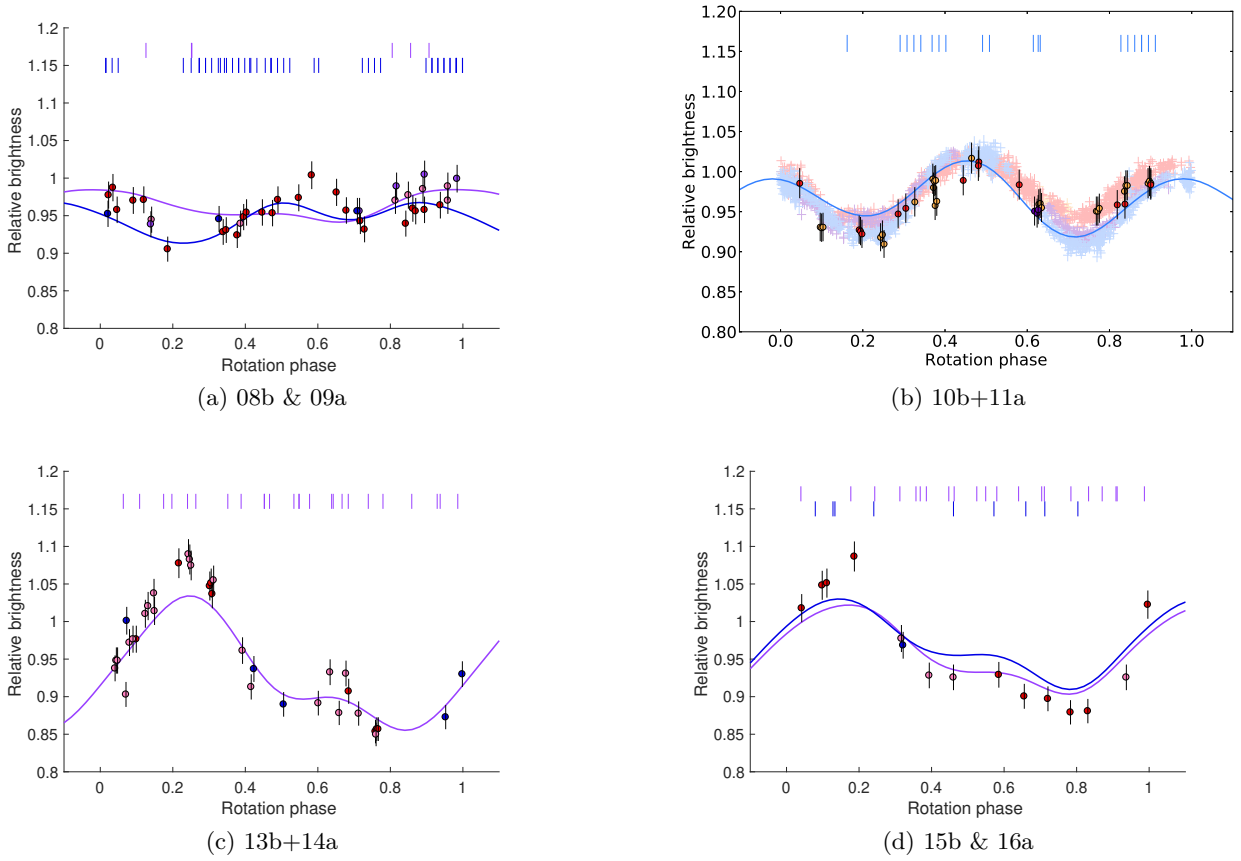

(a) 08b & 09a

(b) 10b+11a

(c) 13b+14a

(d) 15b & 16a

Figure 3.9 – Phase-folded photometry data (dots with 1σ error bars) and ZDI models (lines) for V410 Tau in our four observation epochs. In the case of 08b & 09a and 15b & 16a, two ZDI curves are plotted for the two ZDI maps reconstructed within each epoch. Red, pink, purple and blue colors each indicate a quarter of the total time span of the observations (photometric and spectropolarimetric together), in chronological order. Spectropolarimetric observations are marked by ticks above the light curves. In figure b, WASP data were added as desaturated crosses, with the size of the cross branches indicating their 1σ error bars.

that the longitudinal magnetic field B_ℓ (proportional to the first moment of the Stokes V profiles, e.g., Donati et al., 1997, and most sensitive to the low-order components of the large-scale field) exhibits a recurrence timescale of $1.0014 \pm 0.0003\,P_{\rm rot}$ (see section 3.1.1), i.e., slightly longer than $P_{\rm rot}$ by a similar amount. Higher order terms in the spherical harmonics expansion describing the field (in particular the quadrupolar and octupolar modes) get stronger between 2015 Nov and 2016 Dec, with total magnetic energies increasing from 85 % to 93 % of the poloidal field. Similarly to the brightness maps, the magnetic maps seem to point to a variation of the surface topology between late 2015 and early 2016, which is not explained by differential rotation alone, though the limited phase coverage calls for caution when comparing features between those maps.

V410 Tau has a relatively strong large-scale magnetic field, with an average surface intensity that is roughly constant over the years at 550 ± 50 G. Its radial field reaches local values beyond -1 kG and 1 kG in several epochs. The brightness and magnetic surface maps both present some variability from epoch to epoch (figure 3.6, table 3.2), which points to a dynamo-generated magnetic field rather than a fossil one. The magnetic energy is, at all epochs, equally distributed between the poloidal and toroidal components of the field, with the poloidal component being rather non-dipolar and non-axisymmetric, whereas the toroidal component is mostly dipolar and axisymmetric. The poloidal dipole, tilted towards a phase that stays within 0.6 ± 0.1 during the whole survey,

but at an angle varying between 20° and 55° depending on the epoch, sees its intensity increase almost monotonously from 165 G to 458 G over 8 years, and the dipolar contribution to the poloidal field also increases from ∼25 % to ∼40 % (see table 3.2). We note that the maximum emission of Hα corresponds to the phase at which the dipole is tilted (figure 3.19). The toroidal component of V410 Tau, which displays a constant orientation throughout our data set, is unusually strong compared to other fully convective rapidly-rotating stars (e.g. V830 Tau is 90 percent poloidal, see Donati et al., 2017). This is further discussed in section 3.4.

At ∼0.8 Myr, V410 Tau is one of the youngest observed wTTSs (Kraus et al., 2012, figure 3). Assuming that, when the disc was present, V410 Tau was magnetically locked to it at a rotation period of ∼8 d with a cavity of ∼0.085 au (similarly to cTTSs BP Tau, AA Tau and GQ Lup, see Donati et al., 2008a, 2010a, 2012, resp.), then V410 Tau should have had a radius of ∼7 $R_\odot$ when the disc dissipated, to match the angular momentum that we measure today (Bouvier, 2007). According to the Siess models (Siess et al., 2000), this corresponds to an age of ∼0.2 Myr. With a radius of ∼7 $R_\odot$, V410 Tau would have needed a magnetic dipole barely above 100 G to maintain the assumed magnetospheric cavity, even with an accretion rate of $\sim 1 \times 10^{-8}$ $M_\odot$/yr just before disc dissipation. That value is compatible with the ∼400 G dipole we measure on the ∼3.5 $R_\odot$ star today and assuming magnetic flux conservation between both epochs. Kraus et al. 2012 shows a correlation between the presence of a close companion and the early depletion of the accretion disc, which indicates that V410 Tau B, observed at a projected separation of 16.8 ± 1.4 au (Ghez et al., 1995), could have been responsible for the early depletion of the disc.

We do not observe a particular correlation between our brightness and our magnetic maps, which shows that there is also medium to strong magnetic fields outside spots, according to the ZDI reconstruction. The spots probably host strong magnetic fields, but we are most likely missing them due to the low level of emitted light in those areas.

For visualisation purposes, 3-dimensional potential fields were extrapolated from the radial components of the magnetic maps, and displayed in Figure 3.10.

3.2.2 Differential rotation

Whether for the TAP 26 or the V410 Tau data sets, when applying ZDI without differential rotation to subsets spanning more than a month, it is impossible to reach χ^2_r =1. In fact, even when taking into account differential rotation, the χ^2_r reaches lower values but still not 1. This indicates that intrinsic variability occurs over ∼40 – 50 d.

Despite this variability, we attempted to retrieve differential rotation from longer data sets. The search for differential rotation parameters is done by minimising the value of χ^2_r at a fixed amount of information, in this present case using the Stokes I profiles and brightness map reconstruction only. From the curvature of the χ^2_r paraboloid around the minimum, one can infer error bars on differential rotation parameters (Donati et al., 2003).

For TAP 26, the whole 2015 Dec-2016 Jan data set was modeled together, and the spot coverage was fixed at 13 % (chosen to be slightly higher than the values found in each reconstruction). The values we found are Ω_{eq} =8.8199 ± 0.0003 rad/d and $d\Omega$ =0.0492 ± 0.0010 rad/d, with a minimum χ^2_r of 1.4116. A map of $\Delta\chi^2$ is shown in figure 3.11, which presents a very clear paraboloid around the minimum we found, even if, due to our phase coverage, these precise values ask for further confirmation with the help of future data. This value of $d\Omega$ is close to the solar differential rotation (0.055 rad/d). To assess the false-alarm probability (i.e. the probability that differential rotation was detected in the noise, whereas it has no physical existence), we found that the case with no differential rotation yields χ^2_r = 2.6907. Normalising $\Delta\chi^2$ by the minimum χ^2 achieved over the map (to scale up error bars as a way to account for the contribution from the reported intrinsic variability) still yields a value in excess of 3300 and a negligible false alarm probability (FAP),

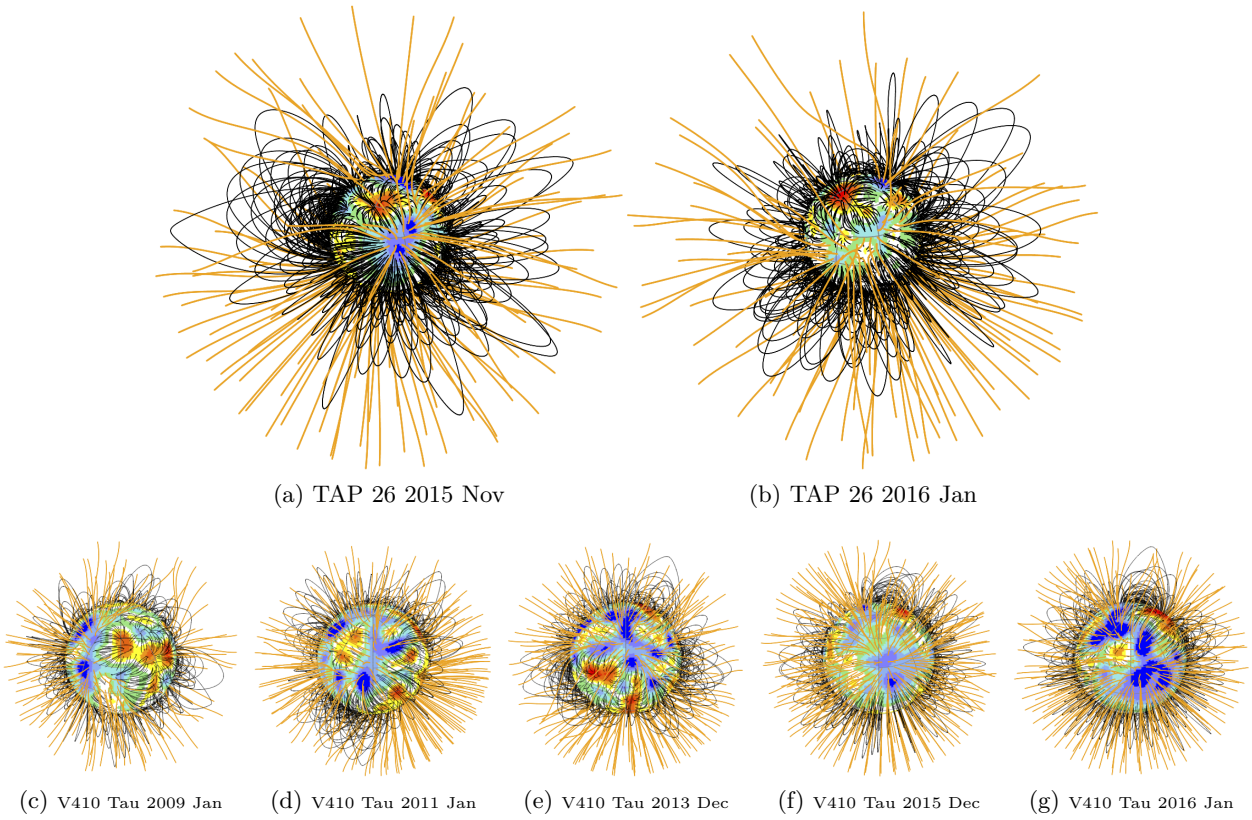

(a) TAP 26 2015 Nov (b) TAP 26 2016 Jan

(c) V410 Tau 2009 Jan (d) V410 Tau 2011 Jan (e) V410 Tau 2013 Dec (f) V410 Tau 2015 Dec (g) V410 Tau 2016 Jan

Figure 3.10 – Potential field extrapolations of the ZDI-reconstructed surface radial fields, as seen by an Earth-based observer, at phase 0.8 for TAP 26 and 0.5 for V410 Tau. Open/closed field lines are shown in orange/black respectively, and colours on the stellar surface depict the local value of the radial field (in G, as shown in the left-hand panels of figures 3.5 and 3.6). The source surface at which the field becomes radial is set to 4 $R_\star$ for TAP 26 and 2.1 $R_\star$ for V410 Tau, corresponding to the corotation radius (at which the Keplerian period equals the stellar rotation period) and beyond which field lines are expected to quickly open under centrifugal forces.

unambiguously demonstrating that the star is not rotating as a solid body.

The differential rotation parameters we obtain imply a lap time of 128 ± 3 d, with rotation periods of $0.712\,39 \pm 0.000\,03$ d and $0.716\,38 \pm 0.000\,08$ d for the equator and pole respectively, in good agreement with the range of rotation periods derived from photometry (ranging from 0.7135 – 0.7138 , Grankin, 2013). The 0.7132 d period found for the EW of the Hα line and the 0.7145 d period found for the longitudinal magnetic field B_ℓ (see figures 3.12 and 3.13) are also consistent. We note that the rotation periods found with photometry, the longitudinal magnetic field and Hα line correspond to latitudes between 30 – 50 °, indicating that an important amount of activity is concentrated at these mid-latitudes, with the dipole pole located in the upper part of this range, in good agreement with the ZDI reconstruction (see section 3.2.1).

For V410 Tau, we obtained six values for $\Omega_{\rm eq}$ and for $d\Omega$, by using separately our Stokes I and Stokes V LSD profiles from each of the three data sets 2008b+2009a, 2013b and 2015b+2016a hereafter shortened to 08b+09a, 13b and 15b+16a resp.). From the resulting $\chi^2_{\rm r}$ maps over the $\{\Omega_{\rm eq}$,$d\Omega$ $\}$ space, one can plot the contours of the 1σ- (68.3 %) and 3σ- (99.7 %) areas of confidence for each observation epoch. Figure 3.11, which shows such contours, highlights clear minima surrounded by almost elliptic areas of confidence at each epoch, and shows that each 3σ-confidence area overlaps at least two other 3σ-confidence areas. Numerical results for each epoch are given

in table 3.3. We chose to use a unique set of parameters to reconstruct all images shown in Chapter 3: the weighted means of the six seasonal minima, $\Omega_{\rm eq} = 3.359\,57 \pm 0.000\,06$ rad/d and $d\Omega = 0.0097 \pm 0.0003$ rad/d. The differential rotation of V410 Tau is thus relatively weak, with a pole-to-equator rotation rate difference 5.6 times smaller than that of the Sun, and a lap time of 648 ± 73 d.

The differential rotation of V410 Tau is similar to that of V830 Tau (see section 3.3) but much smaller than that of TAP 26, which is almost of solar level, consistent with the fact that TAP 26 is no longer fully convective and has developped a radiative core.

Table 3.3 – Summary of differential rotation parameters obtained for V410 Tau on each season. All rotation rates are given in mrad d^{-1}. Column 2 gives the total number of data points used in the imaging process, then columns 3 to 7 correspond to Stokes I data while column 8 to 12 correspond to Stokes V data. Columns 3 and 8 list the derived equatorial rotation rate $\Omega_{\rm eq}$, with its 68% (i.e. 1σ) confidence interval, columns 4 and 9 the difference in rotation rate $d\Omega$ between the equator and pole, with its 68% confidence interval, columns 5 and 10 give the reduced chi square of the ZDI model compared to the data, columns 6 and 11 give the inverse slope of the ellipsoid in the $\Omega_{\rm eq}$-$d\Omega$ plane (also equal to $\cos^2\,\theta_s$, where θ_s denotes the colatitude of the gravity centre of the spot distribution, see Donati et al. 2000), and columns 7 and 12 give the rotation rate Ω_s at colatitude θ_s.

	Stokes I data / brightness reconstruction					
Epoch	n	$\Omega_{\rm eq}$	$d\Omega$	$\chi^2_{\rm r}$	$\cos^2\,\theta_s$	Ω_s
08b+09a	5562	3360.0 ± 0.1	11.1 ± 0.6	1.276	0.12 ± 0.03	3358.7 ± 0.4
13b	2781	3360.0 ± 0.1	8.1 ± 0.7	1.341	0.11 ± 0.03	3359.1 ± 0.3
15b+16a	3090	3358.6 ± 0.1	8.8 ± 0.5	2.583	0.18 ± 0.03	3357.0 ± 0.4
	Stokes V data / magnetic field reconstruction					
Epoch	n	$\Omega_{\rm eq}$	$d\Omega$	$\chi^2_{\rm r}$	$\cos^2\,\theta_s$	Ω_s
08b+09a	5562	3358.7 ± 0.3	8.1 ± 1.8	1.127	0.11 ± 0.03	3357.9 ± 0.5
13b	2781	3361.8 ± 1.3	19.0 ± 4.3	1.038	0.23 ± 0.03	3354.6 ± 2.1
15b+16a	3090	3361.3 ± 0.4	13.7 ± 1.0	1.046	0.32 ± 0.03	3352.7 ± 0.8

Following the method described in Donati et al. (2003), we computed, for each epoch, the colatitude at which the rotation rate is constant along the confidence ellipse major axis. This value corresponds to the colatitude where the barycenter of the brightness/magnetic features imposing a correlation between $\Omega_{\rm eq}$ and $d\Omega$ are located. For both Stokes I and Stokes V, we note a slight increase with time of the cosine of this colatitude (table 3.3), i.e. an increase in the barycentric latitude of the dominant features of $5 \pm 2\,^\circ$ and $15 \pm 5\,^\circ$ respectively.

Our ZDI reconstructions exclude solid-body rotation at a level of 3.6 to 22σ depending on the epoch. Again, we note that, even with differential rotation, ZDI cannot fit the data of 08b+09a and of 15b+16a down to $\chi^2_{\rm r} = 1$, no matter the amount of information allowed. This indicates that surface features are also altered by a significant level of intrinsic variability within the 2-month span of our data sets. This issue is further discussed in the next section.

3.2.3 Activity proxies

In this section we investigate the spectral line Hα and the integrated longitudinal (i.e. line-of-sight projected) magnetic field B_ℓ. The latter can be derived from the Stokes V LSD profiles (Donati et al., 1997) as:

$$B_\ell = \frac{-2.14 \times 10^{11}}{\lambda_0 g_{\rm eff} c} \frac{\int v V(v) {\rm d}v}{\int (I_c - I(v)) {\rm d}v}.$$

The Hα emission EW and the longitudinal magnetic field B_ℓ of TAP 26 feature modulations of periodicities 0.7145 ± 0.0002 d and 0.7132 ± 0.0002 d respectively. Periodograms for Hα and B_ℓ are

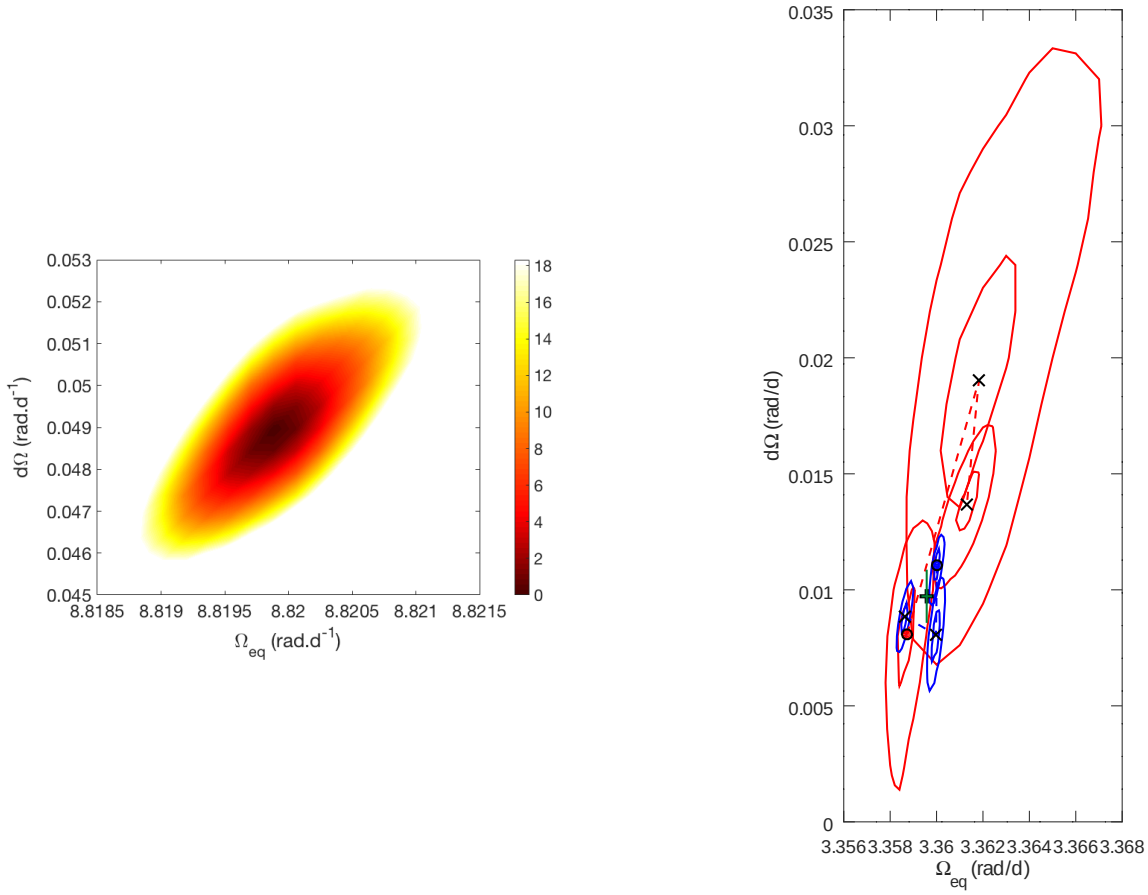

Figure 3.11 – *Left*: map of $\Delta\chi^2$ as a function of $\Omega_{\rm eq}$ and $d\Omega$, derived from the modelling of our Stokes I LSD profiles of TAP 26 at constant information content. A well-defined paraboloid is observed with the outer colour contour corresponding to the 99.99 % confidence level area (i.e., a χ^2 increase of 18.4 for the 2581 Stokes I data points). The minimum value of $\chi^2_{\rm r}$ is 1.4116. The minimum $\chi^2_{\rm r}$ achieved is above unity due to intrinsic variability affecting the LSD profiles but not being taken into account within ZDI. The derived differential rotation parameters are $\Omega_{\rm eq} = 8.8199 \pm 0.0003$ rad/d and $d\Omega = 0.0492 \pm 0.0010$ rad/d. *Right*: evolution of the differential rotation of V410 Tau as measured from Stokes I (blue) and Stokes V (red) profiles. The points corresponding to observation epoch 2008b-2009a are marked with o symbols, then the dashed lines link the epochs in chronological order (2013b-2014a and 2015b-2016a are marked with x symbols). 68.3 % and 99.7 % contours of confidence are displayed for each observation epoch. The weighted average of the six measurements, chosen to produce the maps shown in chapter 3, is represented as a black +, with overlayed error bars in green.

shown in figures 3.12 and 3.13 respectively: peak frequencies and their aliases are clearly outlined. Corresponding phase-folded plots are shown in figure 3.14.

Plotting phase-folded curves of B_ℓ and the Hα emission EW for TAP 26 (where the x-axis indicates the rotation phase as defined in Eq. 3.1), in figure 3.14, we observe a decrease in B_ℓ around phase 0.77 in 2015 Nov and phase 0.97 in 2016 Jan, which correspond approximately to the phases where the dipole pole points towards the Earth (0.73 ± 0.03 and 0.85 ± 0.03 respectively), causing B_ℓ to have strong negative values and showing the correlation between the dipole and B_ℓ. Similarly, the increase in emission EW of the Hα line between phases 0.6 and 0.9 illustrates the correlation between the lower harmonics of the magnetic field of TAP 26 and this activity proxy.

For V410 Tau, applying GPR with MCMC parameter exploration to the Hα EWs and to B_ℓ, we found rotation periods of 1.8720 ± 0.0009 d and 1.8700 ± 0.0007 d respectively. It is worth mentioning that we also find long decay times for these two activity proxies: 589^{+774}_{-335} d and 604^{+553}_{-289} d

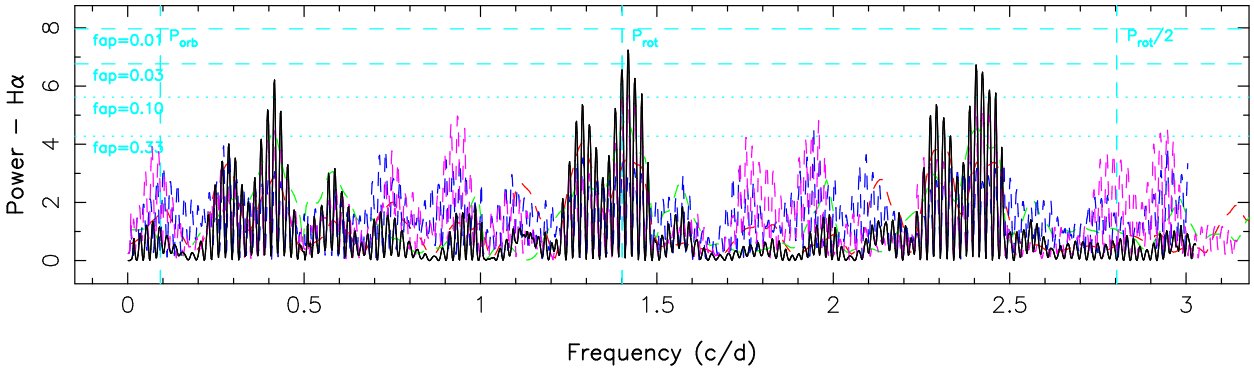

Figure 3.12 – Periodogram of the Hα line EW. The rotation period at 0.7135 d is represented by a dashed vertical cyan line.

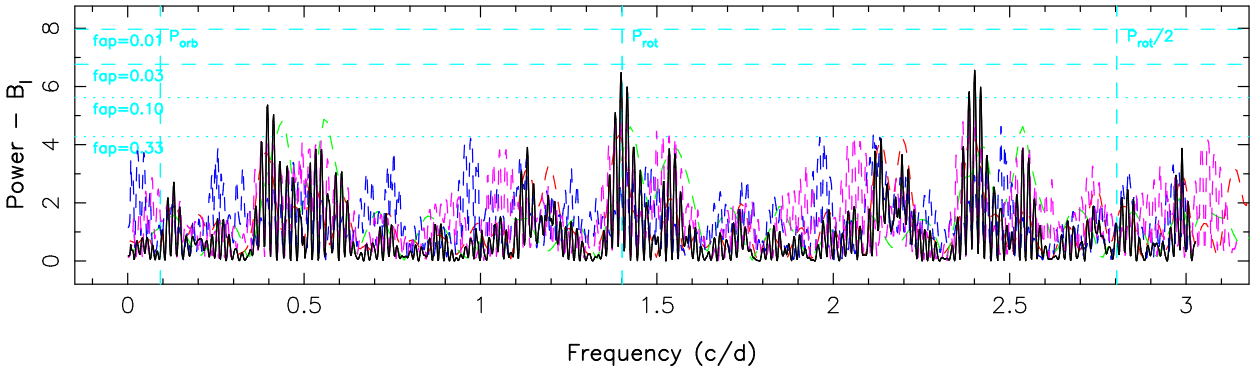

Figure 3.13 – Periodogram of the longitudinal magnetic field. The rotation period at 0.7135 d is represented by a dashed vertical cyan line.

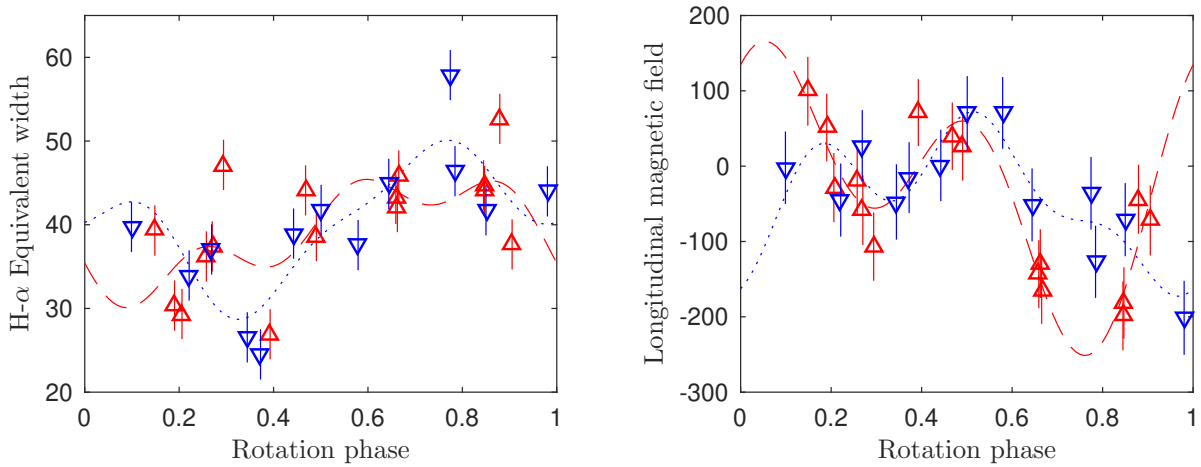

Figure 3.14 – *Left*: folded curve of the EW of Hα against the rotation phase. 2015 Nov (red upward-pointing triangles) and 2016 Jan (in blue) data are fitted with the sum of a sine curve and 2 harmonics (red dashed line and blue dotted line respectively). *Right*: folded curve of the longitudinal magnetic field against the rotation phase. 2015 Nov (red upward-pointing triangles) data are fitted with the sum of a sine curve and 1 harmonic (red dashed line) and 2016 Jan (blue downward-pointing triangles) data are fitted with the sum of a sine curve and 2 harmonics (blue dotted line).

respectively, which suggests, with the caution needed with such high error bars, that the Hα and B_ℓ modulations are particularly sensitive to large, long-lasting features. The MCMC phase plots are displayed in figure 3.15.

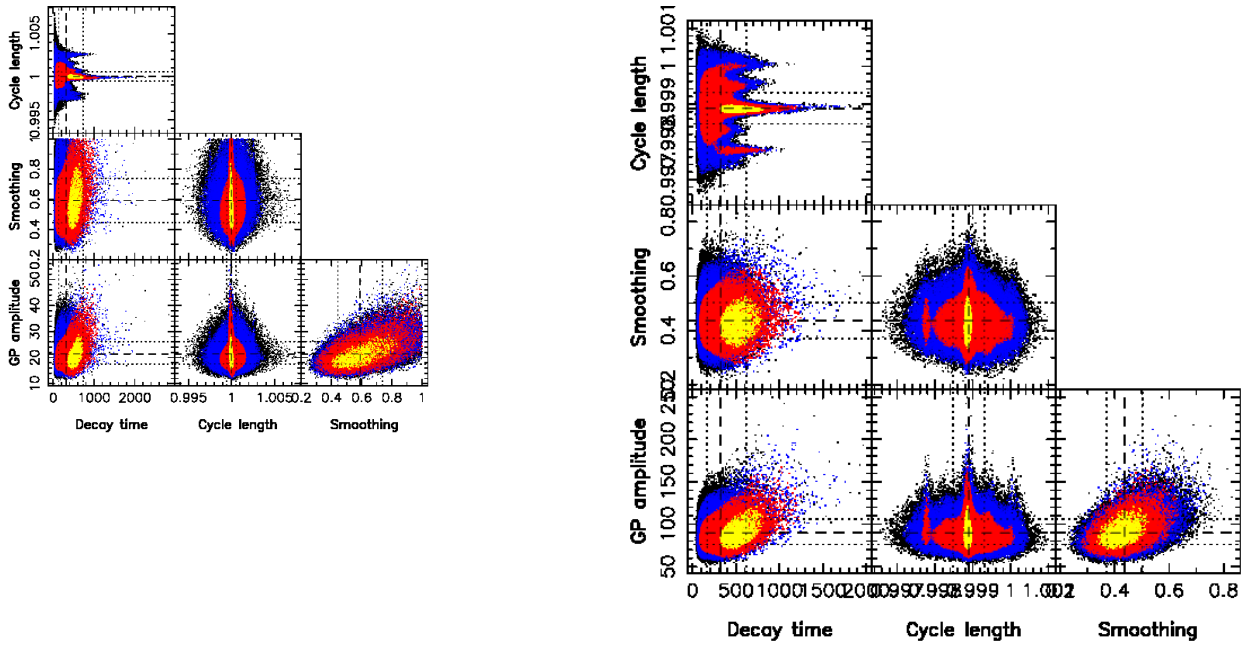

Figure 3.15 – *Left:* GPR-MCMC phase plot for V410 Tau Hα EW data. Amplitude $\theta_1 = 21.4^{+4.7}_{-3.9}$ km s^{-1}, decay time $\theta_3 = 315^{+414}_{-179}$ $P_{\rm rot}$, Cycle length $\theta_2 = 1.0000 \pm 0.0005$ $P_{\rm rot}$, Smoothing $\theta_4 = 0.59 \pm 0.15$ $P_{\rm rot}$. *Right:* GPR-MCMC phase plot for V410 Tau B_ℓ. GP amplitude $\theta_1 = 90^{+16}_{-14}$ G, cycle length $\theta_2 = 0.9989 \pm 0.0004$ $P_{\rm rot}$, decay time $\theta_3 = 322^{+295}_{-154}$ $P_{\rm rot}$, smoothing $\theta_4 = 0.436 \pm 0.066$ $P_{\rm rot}$.

We derived mean latitudes of features constraining the modulations of Hα EWs and B_ℓ from our measurement of their rotation periods (figure 3.16). The period found from Hα, equal within error bars to the one derived in Stelzer et al. 2003 from photometry, corresponds to latitudes around 35°, whereas the period found from B_ℓ seems tied to equatorial features.

3.2.4 Mid-term variability

Even with differential rotation, it is impossible for our current version of ZDI to model data sets spanning a few months down to noise level, which shows that the surfaces of TAP 26 and V410 Tau undergo significant instrinsic variability.

For the rest of this section, we focus on V410 Tau for which we have data over several years. The dipole doubles in strength throughout our observation run (see table 3.3). However measures of $d\Omega$ on individual yearly data sets do not show an increase, which, if we are to assume a cyclic dynamo, would imply a phase shift between the magnetic field and the differential rotation.

We looked for long-term variability in our photometric data. We retrieved the stellar rotation period at each epoch to see how this period evolves along the years. To retrieve the stellar rotation period, we applied two types of models to our V magnitude curves: a periodic fit involving the fundamental frequency and the first two harmonics to each of the 9 data sets individually (as well as a periodic fit involving the fundamental frequency and the first four harmonics to the whole data set), and GPR (see section 2.4.3). Since the data sets 15b+16a and the 16b+17a are particularly small (15 and 13 points respectively) and consecutive, we grouped them together for the GPR.

Placing the periods found from the photometric data on a period-latitude diagram representing the modeled differential rotation (figure 3.17), we observe that the latitudes corresponding to the

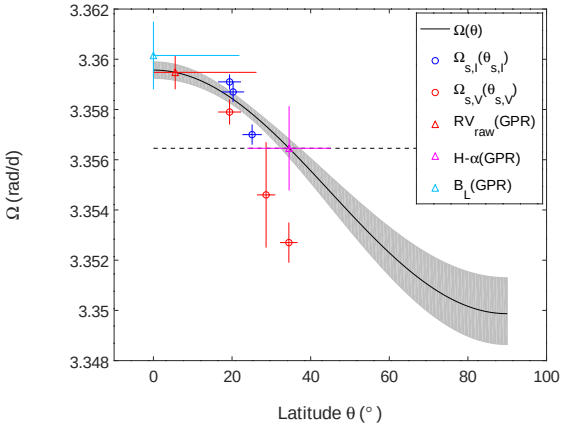

Figure 3.16 – Differential rotation curve of V410 Tau (black full line) with 1σ uncertainty in gray, with $\Omega_{\rm eq} = 3.359\,57 \pm 0.000\,06$ rad/d and $d\Omega = 0.0097 \pm 0.0003$ rad/d. The stellar rotation rate chosen to phase our data is represented as a dashed horizontal line. The rotation rates derived from the RVs (red), from the Hα equivalent widths (magenta) and from the longitudinal field measurements (cyan) are positioned on the differential rotation curve as triangles with 1σ error bars, thus yielding the barycentric latitude of the features determining the period. The dots represent couples $\{90 - \theta_s, \Omega_s\}$ derived in our epoch-wise differential rotation measurements, those coming from Stokes I/ Stokes V data being plotted in blue / red respectively.

successive periods tend to increase from 0 in 2008 to $\sim$50° in 2016. We note that this trend is observed with both the periods derived from sine fits to the photometric data and those derived from GPR. This implies that the largest features, i.e. those with the biggest impact on the photometric curve, underwent a poleward migration, reminiscent of the Solar butterfly diagram, albeit reversed. This would suggest that the dynamo wave, if cyclic, has a period of at least 8 yr and likely much longer (16 yr if our data covers only one half of a full cycle). Previous studies using different data have suggested the existence of an activity cycle on V410 Tau, with periods of 5.4 yr and 15 yr respectively (Stelzer et al., 2003; Hambálek et al., 2019). Photometric data over the past 60 yr show a complex evolution of the light curve of V410 Tau with time scales of 4 – 5 yr and $\sim$11 yr appearing (Sokoloff et al., 2008). We also observe a decrease in the amplitude of the V magnitude modulations in the 1970s (Sokoloff et al., 2008) and around 2008 (figure 3.18), which could be attributed to either a lower level of activity or a more axisymmetric distribution of surface brightness features. We further note that our differential rotation measurements confirm that the barycenter of surface features migrates to higher latitudes over time (see Fig 3.11).

All derived rotation periods, from sine fits and GPR, are plotted against their corresponding latitude using the ZDI-retrieved differential rotation, and the thus-derived latitudes are plotted against time in figure 3.17, showing a global increasing trend of that latitude, regardless of the period retrieval method.

We summarize the long-term variation time scales of V410 Tau, found from applying GPR-MCMC to various activity proxies, as well as the differential rotation lap time, in table 3.4.

On another hand, the bulk RV of V410 Tau exhibits a drift throughout our 8-year campaign, from 16.30 ± 0.05 km s^{-1} in 2008b-2009a to 16.65 ± 0.05 km s^{-1} in 2015b-2016a. This drift could reflect the binary motion with V410 Tau B (see section 4.2.2). An alternative interpretation could be a variation in the suppression of convective blueshift in regions of strong magnetic field (Haywood et al., 2016; Meunier et al., 2010), which could further support a secular evolution of the magnetic topology.

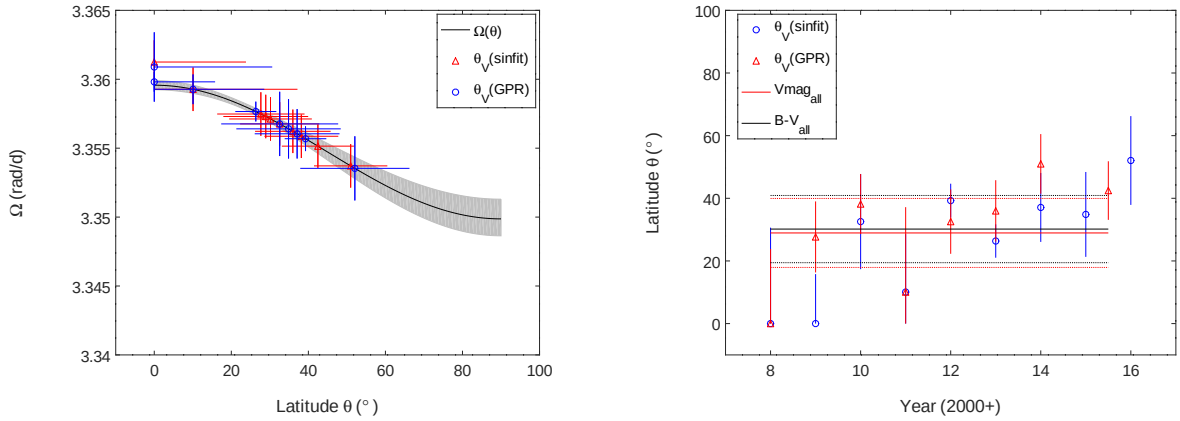

Figure 3.17 – *Left*: Differential rotation curve of V410 Tau in blue. Red: Hα rotation rates, green: B_ℓ rotation rates, circles: derived from 2013 Dec data set, triangles: derived from 2015 Dec data set, x symbols: derived from the whole data set (143 points for Hα and 135 for B_ℓ). Photometry rotation rates are displayed, derived with sine fits in green and with GPR in magenta. *Right*: Colatitude found for the V magnitude, for each epoch and for the whole data set.

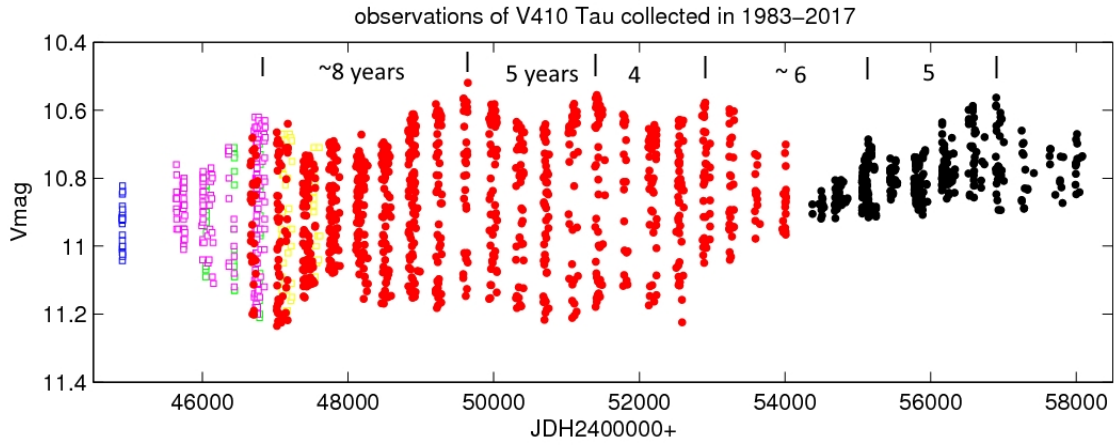

Figure 3.18 – V410 Tau light curve between 1983 and 2017. BJD 2400000+46000, 50000, 54000 and 58000 correspond to years 1984, 1995, 2006 and 2017 respectively. Yellow dots are data from Herbst (1989), pink dots from Vrba et al. (1988), green dots from Bouvier et al. (1988), blue dots from Rydgren & Vrba (1983), red dots are Maidanak observations collected by K. Grankin and the black dots are CrAO observations collected by K. Grankin. We thank Pr. Konstantin Grankin for communicating this figure to us.

3.2.5 Prominences

In our Hα dynamic spectra (figure 3.19), we observe a conspicuous absorption feature in the second part of the 2009 Jan run, crossing the spectral line from blue to red between phases 0.9 and 1, that could be the signature of a prominence (see e.g. Collier Cameron & Robinson, 1989). We also

Table 3.4 – Various evolution time scales of V410 Tau.

Quantity	Time scale (d)
RV decay time (see section 4.2.1)	160^{+45}_{-35}
V magnitude decay time	314^{+31}_{-29}
Hα decay time	589^{+774}_{-335}
B_ℓ decay time	604^{+553}_{-289}
Differential rotation lap time	648 ± 73

observe similar absorption features in 2009 Jan around phase 0.8 and in 2011 Jan around phase 0.35, but they are less well-covered by our observations. Fitting a sine curve in the absorption features yields amplitudes of $\sim 2\, v \sin i$ for all three, corresponding to prominences $\sim 2\, R_\star$ away from the center of V410 Tau, i.e. close to the corotation radius.

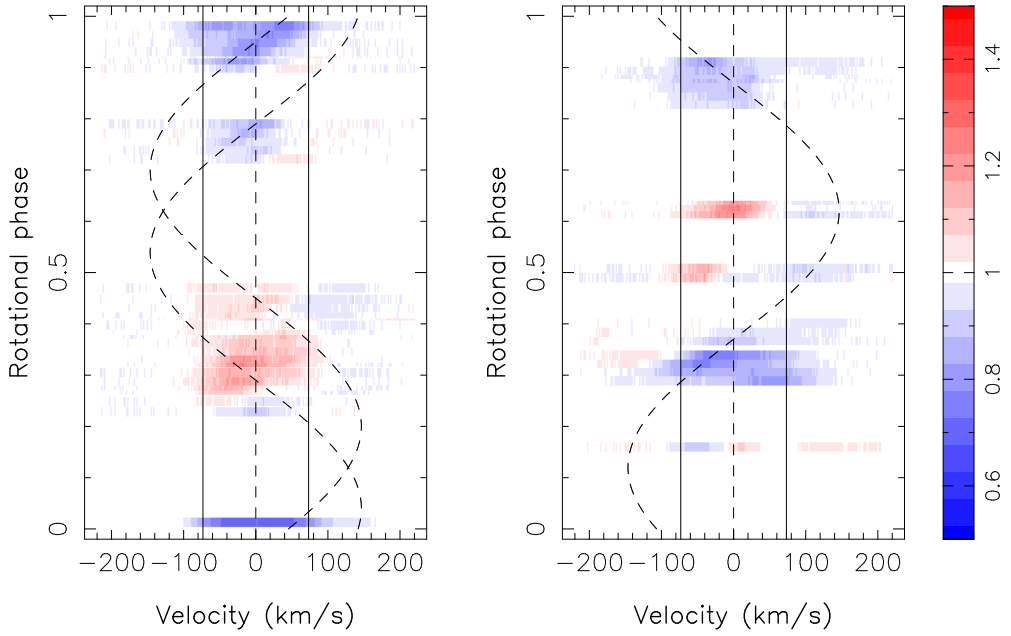

Figure 3.19 – Hα dynamical spectra for epochs 2009 Jan cycles 5 to 8 (left) and 2011 Jan (right).

Plotting the 3D potential field extrapolation of the reconstructed surface radial field for 2009 Jan and 2011 Jan, we observe the presence of closed field lines reaching $\sim 2\, R_\star$ at phases 0.95 and 0.8 in 2009 Jan, and at phase 0.35 in 2011 Jan, which may be able to support the observed prominences (figure 3.20).

3.3 Application to V830 Tau

In Donati et al. (2015), V830 Tau is found to have an inclination $i = 55 \pm 10\,^\circ$, a $v \sin i$ of $30.5 \pm 0.5\,\mathrm{km\,s^{-1}}$ and a $v_{\rm rad}$ of $17.5 \pm 0.1\,\mathrm{km\,s^{-1}}$. ZDI maps yield a 12 % spot and plage coverage and a 300 G field that is 90 % poloidal, and where the poloidal component is mainly dipolar. The dipole is tilted at an angle of $\sim 30°$ towards phase 0.65. The differential rotation parameters are found to be $\Omega_{\rm eq}$ $= 2.2950 \pm 0.0005\,\mathrm{rad/d}$ and $d\Omega$ $= 0.0124 \pm 0.0029\,\mathrm{rad/d}$. The results from the 15b-16a data do not differ much (Donati et al., 2017), though the dipole pole moves slightly

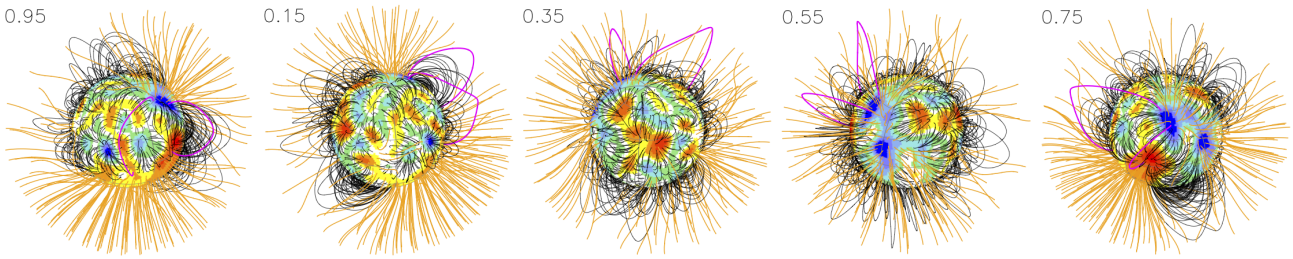

(a) V410 Tau 2009 Jan

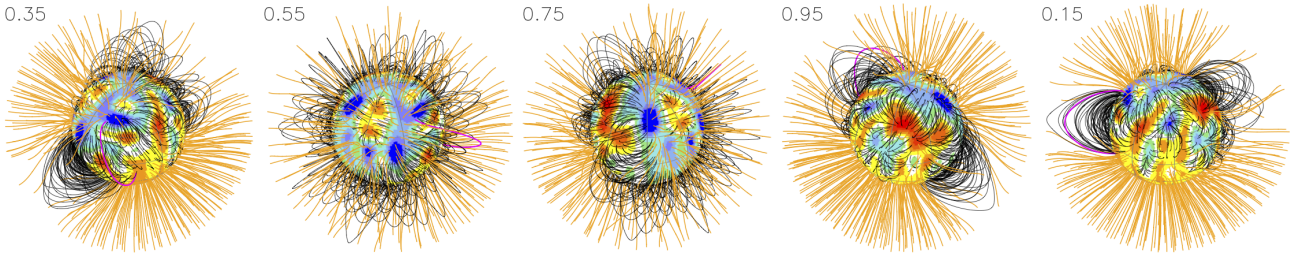

(b) V410 Tau 2011 Jan

Figure 3.20 – Potential field extrapolations of the ZDI-reconstructed surface radial field, as seen by an Earth-based observer, for observation epochs 2009 Jan (top) and 2011 Jan (bottom) at different phases. Open/closed field lines are shown in orange/black respectively, and colours at the stellar surface depict the local value of the radial field (in G, as shown in the left-hand panels of Fig. 3.6). The source surface at which field lines open is set to $2.18\,R_\star$. The field lines that would carry the potential observed prominences (phase 0.95 and 0.8 in 2009, phase 0.35 in 2011) are colored in magenta. Animated versions with the star rotating are available at `http://userpages.irap.omp.eu/~lyu/jan09a.gif` and `http://userpages.irap.omp.eu/~lyu/jan11n.gif`.

(tilted at an angle $22 \pm 5\,^\circ$ towards phases 0.79 ± 0.03 and 0.88 ± 0.03 in 2015 Dec and 2016 Jan respectively).

3.4 Contribution of our ZDI reconstructions to the MaTYSSE programme

Some main characteristics of magnetic topologies of wTTSs found within MaTYSSE so far can be summarized in a plot, commonly known as "confusogram", which is an HR diagram where the size, shape and color of each pictogram give information on the magnetic topology of the star it represents (figure 3.21). Given the variety of stars in the sample (in terms of mass, age, and evolutionary status), it is still too early to draw general conclusions on the magnetic topologies of wTTSs. We stress that the pattern seen on cTTSs, i.e. with fields that are strong and poloidal when the star is largely convective and getting weaker and more complex when the star gets radiative (see e.g. Hill et al., 2019), does not really show up clearly here.

V830 Tau, at $\sim$2 Myr, has a mainly axisymmetric magnetic topology where the dipole contributes a major part of the energy. Such topologies, with strong dipoles, are expected for fully convective stars. TAP 26, on the other hand, is one of the most evolved stars within the MaTYSSE sample, and we found that it has a rather complex magnetic topology, where the poloidal dipole only constitutes 10 % of the magnetic energy. Its toroidal component, contributing to 30 % of the total magnetic energy, is relatively high compared to other wTTSs (see figure 3.21). This level of complexity in the field topology is somewhat expected from a star that has a substantial radiative core, such as TAP 26.

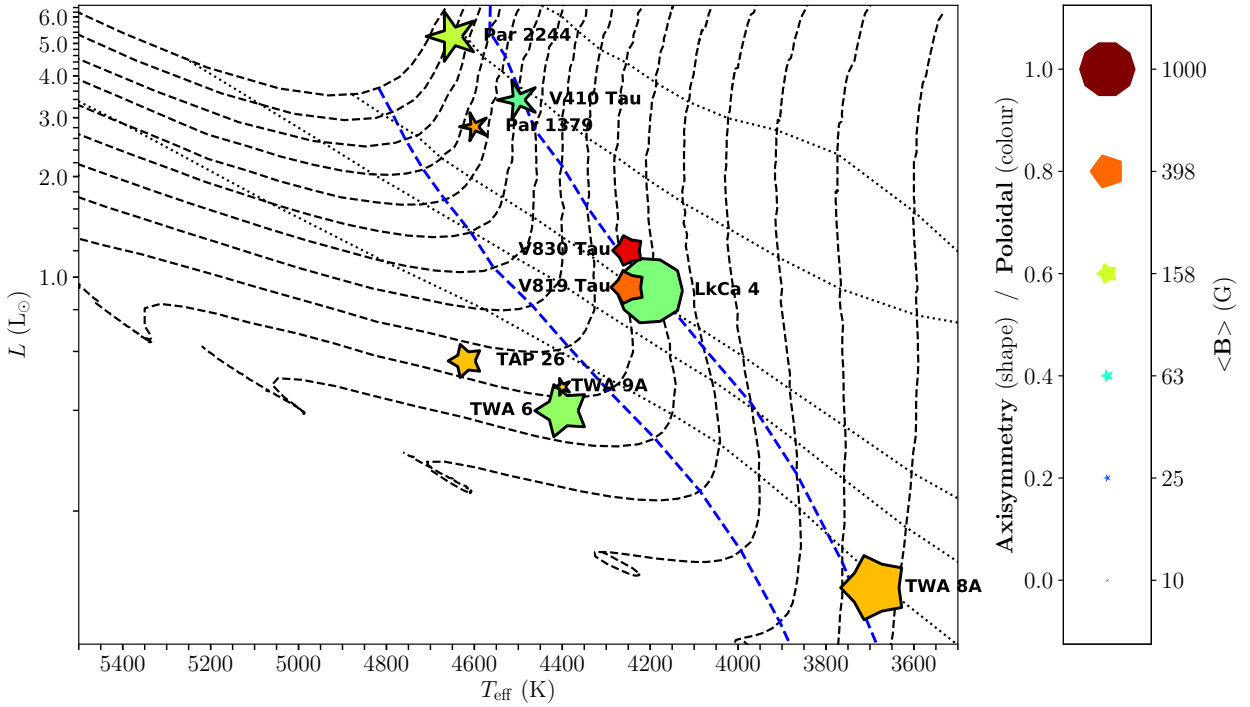

Figure 3.21 – MaTYSSE stars on the HR diagram, with the size, shape and colour of the pictograms representing respectively the strength, degree of axisymmetry and contribution of the poloidal component of their magnetic topologies, as derived with ZDI. Siess et al. (2000) evolution tracks from 0.1 – 0.9 $M_\odot$ are plotted in dashed lines and isochrones for 0.5, 1, 3, 5 and 10 Myr in dotted lines, while locations of radiative core formation start and half-radius-reaching-point are also represented as dotted lines.

The magnetic topology of V410 Tau displays a stronger toroidal component (half of the magnetic energy), that keeps a constant orientation throughout the span of our data, and a non-axisymmetric poloidal field, both not typical to fully convective stars. Only three other stars within the MaTYSSE sample (out of eleven) have exhibited similarly important toroidal components, among which only one is still fully convective like V410 Tau, the ∼2 Myr, $0.79 \pm 0.05\,M_\odot$ LkCa 4 (Donati et al., 2014). The only two other fully convective wTTSs for which magnetic topologies were reconstructed within MaTYSSE so far have mainly poloidal magnetic topologies (V830 Tau and TWA 8A, resp. Donati et al., 2015; Hill et al., 2019), and none is as massive as V410 Tau (1.00 ± 0.05 and $0.45 \pm 0.10\,M_\odot$ resp.). The origin of this strong toroidal component is unclear: in terms of rotation rate, both V410 Tau and LkCa 4 find themselves around the middle of the spectrum within the MaTYSSE sample, so standard dynamo processes due to their fast rotation would not be sufficient to explain the phenomenon, not to mention that dynamos are expected to be saturated in these stars. Maybe it is generated through an α^2 dynamo (like in the simulations of low-Rossby fully convective stars by Yadav et al., 2015), or maybe it is he remnants of a subsurfacic radial shear between internal layers accelerating due to contraction, and disc-braked outer layers. If it is the remnant of the original toroidal field from when the star formed (as found in the simulations of Vaytet et al., 2018), we lack an explanation on how this field escaped dissipation until now, and why it does not show up in cTTSs. Would the early dissipation of the disc, a common factor between LkCa 4 and V410 Tau, have something to do with this?

Completing the analysis of the MaTYSSE sample is therefore necessary to hope for a better overview on this phenomenon and its possible roots. More data, e.g. collected with SPIRou, are also needed to clarify the magnetic panorama of wTTSs.

3.5 Towards a new version of ZDI

Because ZDI does not reconstruct intrinsic temporal variability, its use is limited to short data sets. We explored two ways to implement some degree of variability in the ZDI model, beyond differential rotation, but this work is far from finished.

3.5.1 First approach

We try to improve our ZDI filtering process by implementing a new feature: instead of only having one brightness value in each cell, we give it a brightness value and an evolution parameter, so that ZDI brightness maps are allowed to evolve with time to better fit time-series of LSD profiles with variability. Thus we reconstruct two maps for the brightness: the brightness at time 0 and the map of the evolution parameter. We choose, for now, a simple model where the logarithmic relative brightness of each cell k is allowed to evolve linearily with time:

$$\log Q_k(t) = \log Q_k(0) + m_k t, \tag{3.3}$$

where $Q_k(t)$ is the local surface brightness and m_k is the evolution parameter.

Applying this new method to the V410 Tau 2015-2016 extended data set, we manage to fit the whole data set down to a χ^2_r of 1 where classical ZDI, even with differential rotation, could not reach lower than $\chi^2_r = 2.5$ (see Section 3.2.2). Maps associated to this reconstruction are shown in figure 3.22. We observe for instance that, in the reconstruction, the dark equatorial spot at phase 0.45 gets weaker with time since it coincides with a blue patch in the brightness evolution map, while the polar spot itself does not evolve much.

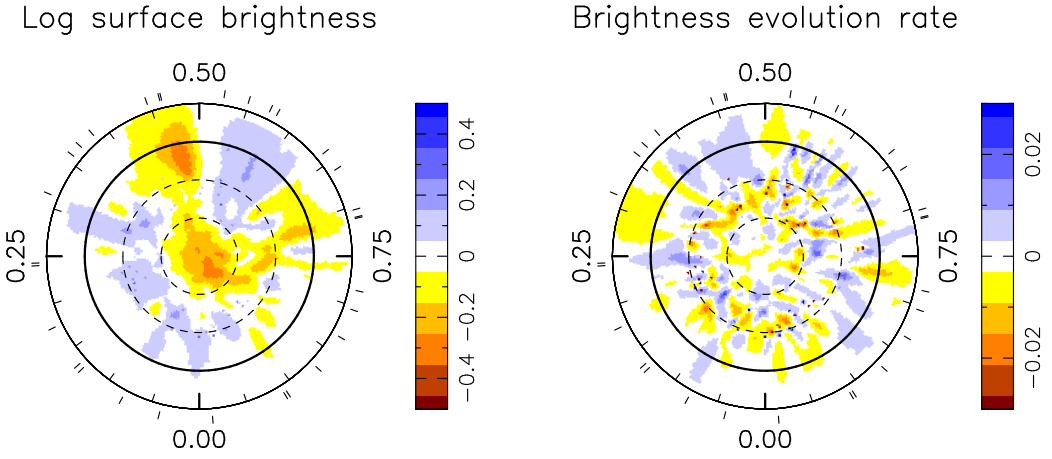

Figure 3.22 – Brightness map and evolution rate reconstructed by ZDI on data set Dec 2015-Jan 2016. Pole-on view with the equator being represented as a full line, and 60°, 30°, and −30° latitude parallels as dashed lines. Cool spots are colored in brown and bright plages in blue, and ticks around the star mark the spectropolarimetric observations.

3.5.2 Next objective

The approach above increases the amount of intrinsic variability that ZDI can model, but it is still restrictive, as the brightness of a cell can only evolve monotonously. We are thus incapable of modeling the successive appearance and disappearance of a spot at the same location. To remedy this, we wish to model the brightness variability with GPs, however, with thousands of cells in the ZDI mesh, this would amount to a huge number of parameters in the ensuing GPR-MCMC exploration, which would end up in very time-consuming computations.

The next idea is thus to express the brightness map no longer as independent cells, but as a weighted sum of a limited number of base maps, such as spherical harmonics (akin to the magnetic topology), and to model the evolving brightness map by using GPR on the spherical harmonics coefficients. We use spherical harmonics in a preliminary attempt, but other bases can be investigated in future developments. Figure 3.23 shows example of spherical harmonics modes and their corresponding spectra.

So far, only a code to decompose a classical ZDI map into a sum of spherical harmonics was written, to show that there is little difference in the corresponding spectra when only the lowest orders of spherical harmonics are kept (see figure 3.24, with $\ell_{\max} = 15$).

A main challenge of the remaining work is to reconcile the fact that the data are in the spectral space, yet the quantities to be modelled with GPR are in the image space.

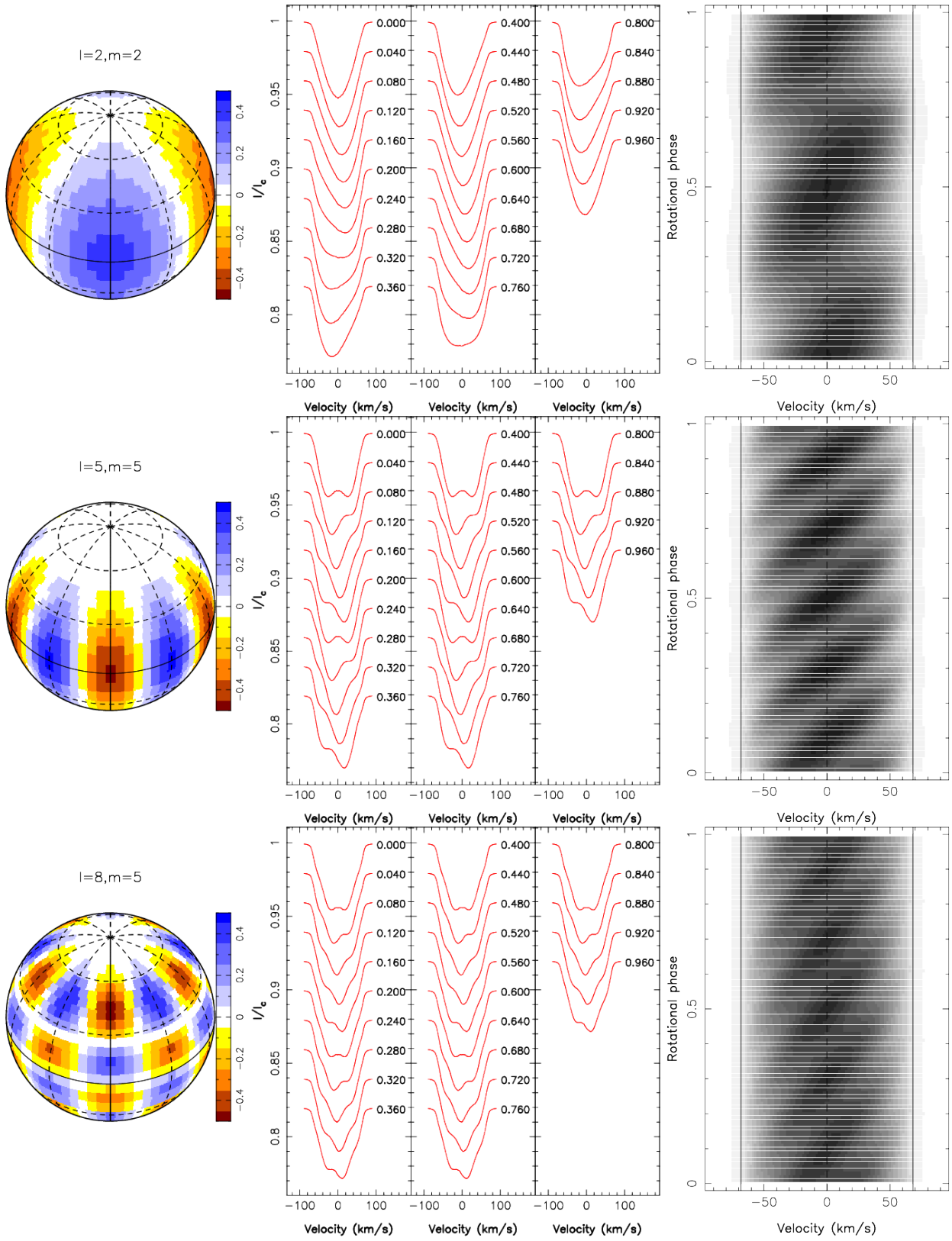

Figure 3.23 – Examples of spherical harmonics modes for the brightness map and corresponding spectra. *Top:* $\ell = 2, m = 2$, *Middle:* $\ell = 5, m = 5$, *Bottom:* $\ell = 8, m = 5$.

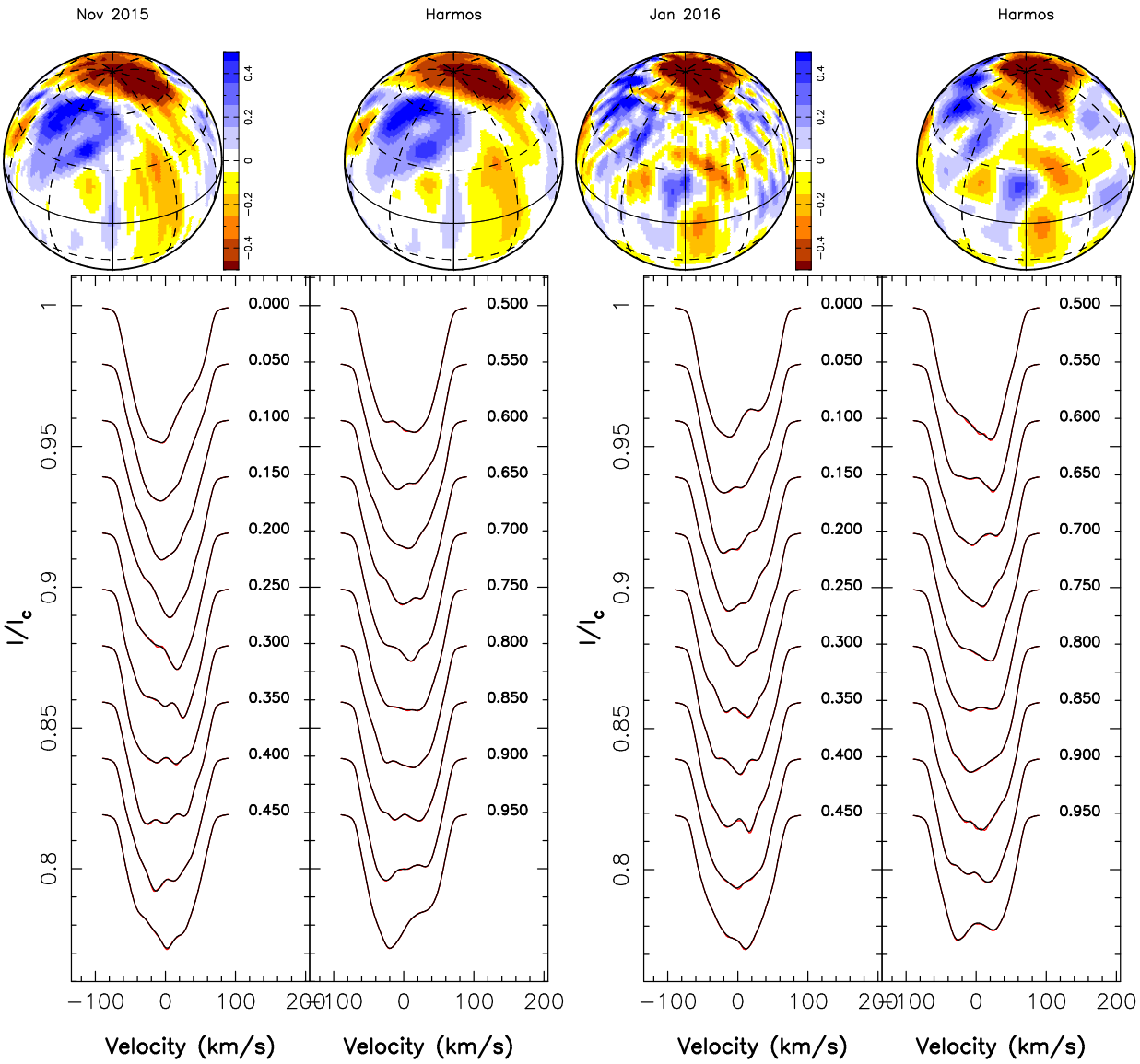

Figure 3.24 – *Top:* Classical ZDI maps, shown at phase 0, which are the ZDI-reconstructed maps for TAP 26 at observation epochs 2015 Nov (1st map) and 2016 Jan (3rd map). Their spherical harmonics approximations, up to order $\ell = 15$, are displayed beside them (2nd and 4th maps). *Bottom:* Stokes I LSD profiles synthesized over one rotation cycle from the classical ZDI maps (red) and the spherical harmonics approximations (black), with 2015 Nov spectra in the left panels and 2016 Jan spectra in the right panels.

4 | RV analyses

Contents

After having modelled the activity of our stars, we aim at filtering out the activity jitter from the RV curves to investigate the potential presence of hot Jupiters around our targets.

4.1 The hot Jupiter of TAP 26

We describe below three different techniques aimed at characterising the RV curve of TAP 26. The first two are those used in Donati et al. (2016): filtering out the activity modelled with the help of ZDI, and the simultaneous fit of the planet parameters and the stellar activity in the Stokes I LSD profiles. The third method uses GPR-MCMC (section 2.4.3) to model the activity directly from the raw RVs. The results obtained from these three methods are outlined and discussed in the following sections.

4.1.1 Filtering out the ZDI-modelled jitter

The first technique consists of using the previously reconstructed maps to predict the pollution to the RV curve caused by activity (the activity jitter) and subtract it from the raw RVs. From the observed Stokes I LSD profiles, we compute, at both epochs, the raw RVs $\mathrm{RV_{raw}}$, as the first-order moment of the continuum-subtracted corresponding profiles (Donati et al., 2017). Likewise, the synthesised Stokes I LSD profiles yield the synthesised activity jitter of the star (RV signal caused by the brightness distribution and stellar rotation). By subtracting the activity jitter from the raw RVs, we obtain filtered RVs $\mathrm{RV_{filt}}$. We observe that the jitter has a mean semi-amplitude of $1.81\,\mathrm{km\,s^{-1}}$ in 2015 Nov and $1.21\,\mathrm{km\,s^{-1}}$ in 2016 Jan, whereas the filtered RV curve features a signal with a semi-amplitude of $\simeq 0.15\,\mathrm{km\,s^{-1}}$ (figure 4.1), i.e., 8 to 12 times smaller than the activity signal we filtered out. We note the very significant evolution in the activity curve between 2015 Nov and 2016 Jan, demonstrating that the brightness distribution has evolved at the surface of TAP 26, through differential rotation and intrinsic variability (see chapter 3).

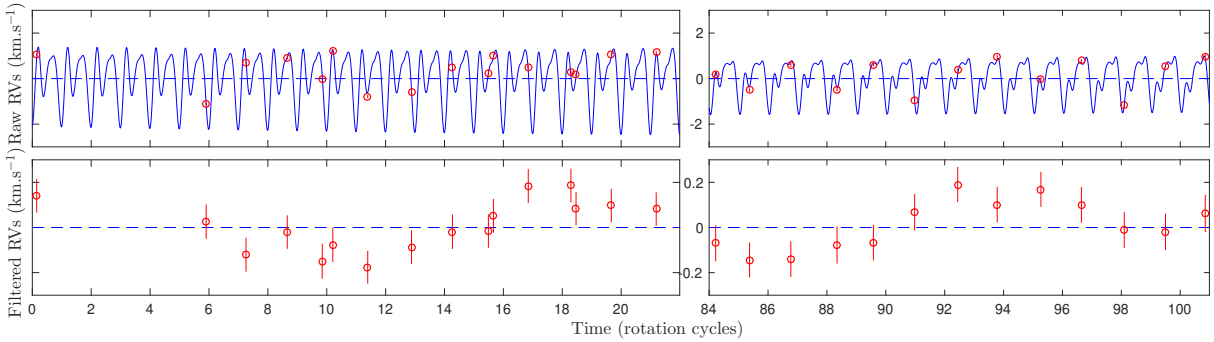

Figure 4.1 – *Top:* RV (in the stellar rest frame) of TAP 26 as a function of rotation phase, as measured from our observations (open circles) and predicted by the tomographic maps (blue line). The synthesised raw RV curves exhibit only low-level temporal evolution resulting from differential rotation. *Bottom:* filtered RVs derived by subtracting the modelled activity jitter from the raw RVs, with a 10x zoom-in on the vertical axis.

With a rms dispersion of 109 $\mathrm{m\,s^{-1}}$, the filtered RVs clearly show the presence of a signal. Looking for a planet signature, we want to fit a sine curve (of semi-amplitude K, period P_{orb}, phase of inferior conjunction ϕ, and offset $\mathrm{RV_0}$) to these filtered RVs, which corresponds to a circular orbit (see figure 4.2). The phase of inferior conjunction ϕ, i.e., corresponding to the epoch at which the planet is closest to us, is defined relatively to the reference date $\mathrm{BJD_{c\,0}}$=2,457,352.6485 (rotation cycle 11.0, approximately at the centre of the 2015 Nov observation run), such that the inferior conjunction occurs at $\mathrm{BJD_c} = \mathrm{BJD_{c\,0}} + (\phi\text{-}1)P_{\mathrm{orb}}$. Due to the gap between both observing

runs, several sine fits with different frequencies match the RV_{filt} as local minima of χ^2_r. This demonstrates the need for observations that are as continuous as possible to avoid such aliases in the determination of the orbital period. The four best fits are shown in figure 4.2 and their characteristics are given in table 4.1, with the value of the log likelihood as computed from the $\Delta\chi^2$ over these 29 RV data points. The residual RVs, derived from subtracting the best sine fit to the filtered RVs (shown in figure 4.2), feature a rms value of 51 $m\,s^{-1}$.

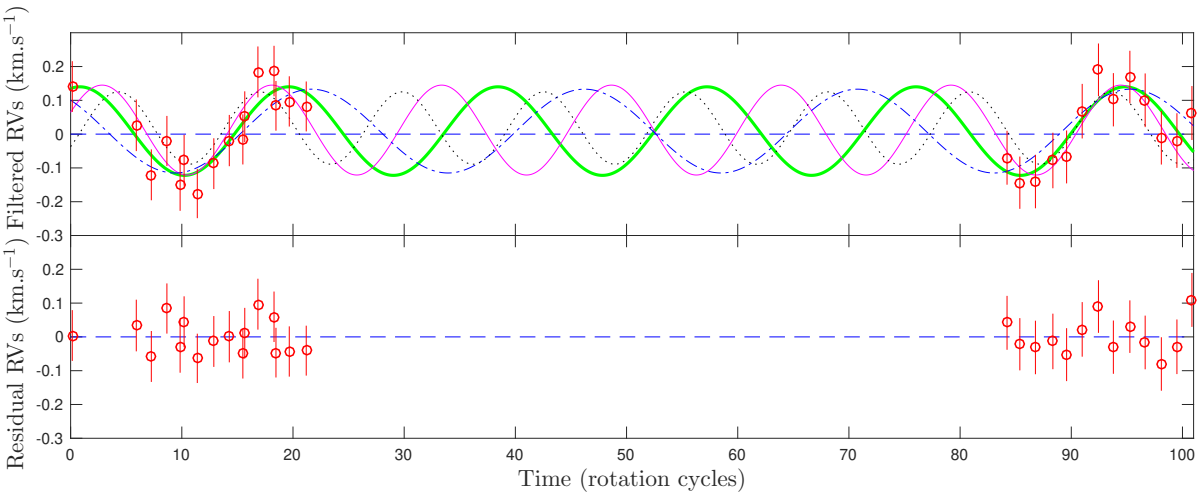

Figure 4.2 – *Top:* filtered RVs of TAP 26 and four sine curves representing the best fits. The thick green curve represents the case P_{orb}/P_{rot} =18.80, the thin magenta one P_{orb}/P_{rot} =15.27, the dash-and-dotted blue one P_{orb}/P_{rot} =24.56 and the dotted black one P_{orb}/P_{rot} =12.76. *Bottom:* residual RVs resulting from the subtraction of the best fit (green curve) from the filtered RVs. The residual RVs feature a rms value of 51 $m\,s^{-1}$.

Table 4.1 – Characteristics of the four best sine curve fits to the filtered RVs, and the case without planet. Respectively: semi-amplitude K, orbital period P_{orb} in units of P_{rot}, orbital period P_{orb} in days, phase of inferior conjunction ϕ relative to cycle 11.0 (see ephemeris in Eq. 3.1), BJD of inferior conjunction (reference BJD: 2,457,340), mean RV, corresponding χ^2_r, difference in χ^2 with the best fit ($\Delta\chi^2$, summed on the 29 data points), and natural logarithm ($\log_e$) of the likelihood $\mathcal{L}_{r1}$ relative to the best fit. ϕ relates to the epoch of inferior conjuntion BJD_c through BJD_c =2,457,352.6485+ϕP_{orb}, the reference date being chosen so as to minimise the variation of ϕ between the four cases.

K ($km\,s^{-1}$)	P_{orb} (P_{rot})	P_{orb} (d)	ϕ	BJD_c	RV_0 ($km\,s^{-1}$)	χ^2_r	$\Delta\chi^2$	$\log\mathcal{L}_{r1}$	style in fig. 4.2
0.131 ±0.020	18.80 ±0.23	13.41 ±0.16	0.709 ±0.026	8.75 ±0.35	0.009 ±0.014	0.445	0	0.00	thick green
0.133 ±0.021	15.27 ±0.14	10.90 ±0.10	0.715 ±0.024	9.54 ±0.26	0.012 ±0.014	0.542	2.80	-0.53	thin magenta
0.124 ±0.020	24.56 ±0.41	17.52 ±0.30	0.684 ±0.028	7.11 ±0.50	0.009 ±0.016	0.673	6.61	-1.85	dashed blue
0.107 ±0.021	12.76 ±0.14	9.11 ±0.10	0.724 ±0.031	10.14 ±0.28	0.018 ±0.015	1.079	18.38	-6.87	dotted black
0					0.013 ±0.014	2.025	45.82	-19.73	

Plotting Lomb-Scargle periodograms for the raw RVs, filtered RVs and residual RVs further demonstrates the presence of a periodic signal in the filtered RVs (figure 4.3). The above-mentioned

dominant periods are seen as peaks in the periodogram; periodograms of partial data (only the 2015 Nov dataset, only the 2016 Jan dataset, odd points and even points) are also shown, yielding peaks at the same frequencies albeit with a lower power. We highlight the fact that the highest peaks in the raw RVs correspond to the activity jitter and are located at $P_{\rm rot}/2$ and its aliases, whereas little power concentrates at $P_{\rm rot}$ itself. A zoom-in of the filtered RV periodogram is also shown in figure 4.3 (bottom panel). The FAP is 0.06% for the highest peak ($P_{\rm orb}$ = 13.41 d = 18.80 $P_{\rm rot}$), and no significant period stands out in the residual RVs after filtering out both the activity jitter and the planet signal corresponding to the highest peak. We carried out simulations to ensure that the detected peaks are not generated by the filtering process, see details in Yu et al. (2017). Study of other activity proxies shows that the detected orbital periods are not present in the activity signal either (Yu et al., 2017).

By fitting the filtered RVs with a Keplerian orbit rather than a circular orbit, we obtain an eccentricity of 0.16 ± 0.15, indicating that there is no evidence for an eccentric orbit (following the precepts of Lucy & Sweeney, 1971). We can thus conclude that the orbit of TAP 26 b is likely close to circular, or no more than moderately eccentric.

4.1.2 Deriving the planetary parameters from the LSD profiles

A second technique, following the method of Petit et al. (2015), consists of taking into account the presence of a planet into the ZDI model. Rather than fitting the measured Stokes I LSD profiles with a synthetic activity jitter directly, we first apply a translation in velocity to each of them, to remove the reflex motion caused by a planet of given parameters, and then apply ZDI to the corrected data set. Practically speaking, we repeat the experiment for a range of values for the orbital parameters (K, $P_{\rm orb}$, ϕ) at the vicinity of the minima previously identified, and look for the set of values that yields the best result. The same way as for differential rotation, we derive the error bars on all parameters from the curvature of the 3D $\chi^2_{\rm r}$ paraboloid around the minimum.

In the present case, since we have two datasets separated by a 45 d gap and we know that intrinsic variability occurred (see chapter 3 and section 4.1.1), a modification to the method described above was implemented: after correcting the global dataset from the reflex motion, ZDI is applied separately on each dataset, reconstructing two different brightness maps (one for late 2015 and one for early 2016) in order to obtain a more precise reconstruction. The quantity used to measure the likelihood of each set of parameters is therefore a global $\chi^2_{\rm r}$, computed as a weighted average of both individual $\chi^2_{\rm r}$, with respective weights proportional to the number of data points in each set (1424 for 2015 Nov and 1157 for 2016 Jan).

As in the previous section, several minima are found, which are listed in table 4.2. We also computed the relative likelihood of each case compared to the best one from the corresponding difference in $\chi^2_{\rm r}$. We note that the case with no planet yields $\Delta\chi^2_{\rm r} = 0.0181$, which leads to a relative probability lower than 10^{-9} compared to the case with a 10.91 d period planet.

Figure 4.4 displays a $\Delta\chi^2$ map around the local minimum $P_{\rm orb}/P_{\rm rot}$ =15.29, at ϕ=0.67, showing the 99.99% confidence area.

4.1.3 Applying GPR-MCMC

The third method consists in applying GPR-MCMC, as described in sections 2.4.3 and A.5.2, on the raw RVs, with the following GP prior:

$$m(t) = K\sin(2\pi t/P_{\rm orb} + \phi) \quad \text{or} \quad m(t) = K\big(e\cos(\omega) + \cos(\omega + \nu(t, e, \phi, P_{\rm orb}))$$

$$k(t,t') = \theta_1^2 \ \exp\left(-\frac{(t-t')^2}{\theta_3^2} - \frac{\sin^2\left(\frac{\pi(t-t')}{\theta_2}\right)}{\theta_4^2}\right),$$

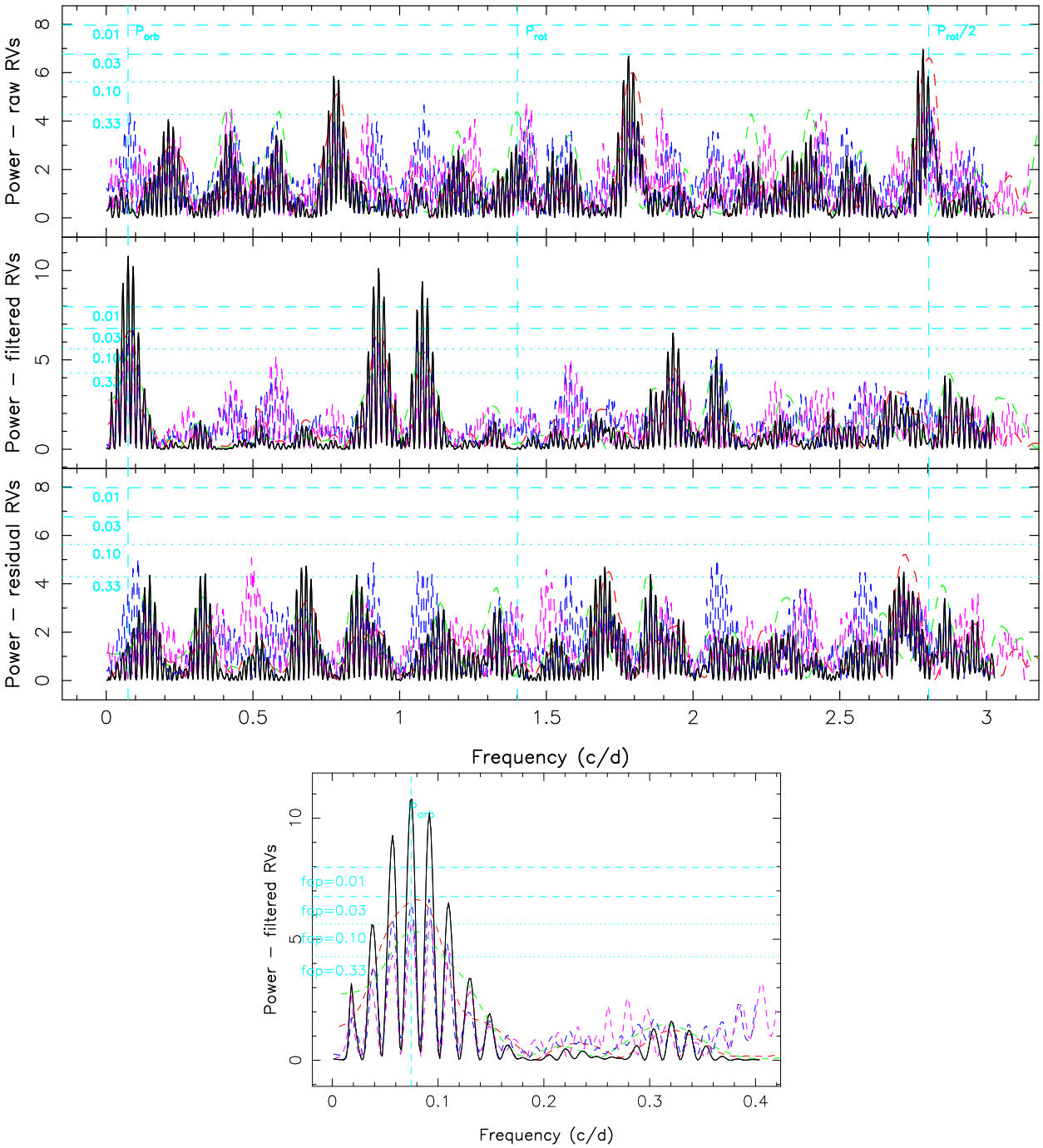

Figure 4.3 – *Top:* Periodograms of the raw (top), filtered (middle) and residual (bottom) RV curves over the TAP 26 15b-16a dataset (black line). The red line represents the 2015 Nov dataset, the green line the 2016 Jan dataset, the blue line the odd data points and the magenta line the even data points. FAP levels of 0.33, 0.10, 0.03 and 0.01 are displayed as horizontal dashed cyan lines. The rotation frequency (1.402 cycles per day) is marked by a cyan dashed line, as well as its first harmonic (2.803 cycles per day) and the frequency that has the smallest FAP (0.06% at 0.075 cycles per day, corresponding to $P_{\rm orb}$ =13.41 d). Aliases of the highest peaks, related to the observation window, appear as lower peaks separated by one cycle per day. *Bottom:* Zoom in the periodogram of filtered RVs.

where θ_1 is the amplitude (in $\mathrm{km\,s^{-1}}$) of the GP, θ_2 the recurrence timescale (in units of $P_{\rm rot}$), θ_3 the decay timescale (i.e., the typical spot lifetime in the present case, in units of $P_{\rm rot}$) and

Table 4.2 – Optimal orbital parameters derived with the method described in section4.1.2, respectively: semi-amplitude K, orbital period $P_{\rm orb}$ in units of $P_{\rm rot}$, orbital period $P_{\rm orb}$ in days, phase of inferior conjunction ϕ relative to cycle 11.0, BJD of inferior conjunction, $\chi^2_{\rm r}$, $\Delta\chi^2$ summed on 2581 data points, and natural logarithm of the likelihood $\mathcal{L}_{r2}$ relative to the best fit. The case where no planet is taken into account in the model is given for comparison.

K ($\mathrm{km\,s^{-1}}$)	$P_{\rm orb}$ ($P_{\rm rot}$)	$P_{\rm orb}$ (d)	ϕ	BJD$_{\rm c}$ (2,457,340+)	$\chi^2_{\rm r}$	$\Delta\chi^2$	$\log\mathcal{L}_{r2}$
0.154 ±0.022	15.29 ±0.15	10.91 ±0.11	0.671 ±0.035	9.06 ±0.38	0.9682	0.00	0.00
0.144 ±0.023	18.78 ±0.25	13.40 ±0.18	0.685 ±0.041	8.43 ±0.55	0.9698	4.00	-1.34
0.148 ±0.025	12.83 ±0.12	9.16 ±0.09	0.677 ±0.038	9.69 ±0.35	0.9718	9.17	-3.61
0					0.9863	46.62	-21.60

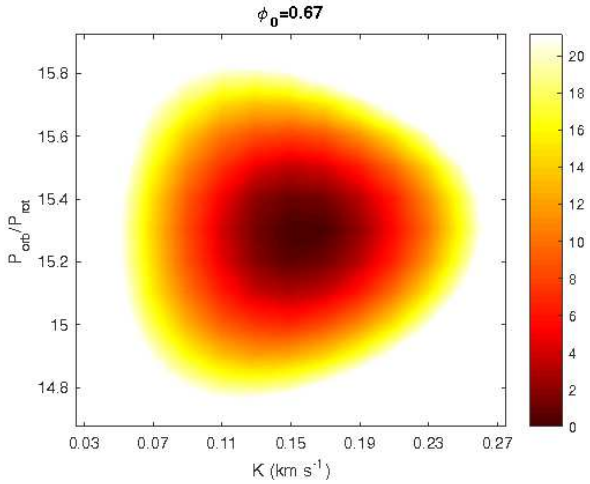

Figure 4.4 – $\Delta\chi^2$ map as a function of K and $P_{\rm orb}/P_{\rm rot}$, derived with ZDI from corrected Stokes I LSD profiles at constant information content. Here the phase is fixed at 0.67, i.e., the value of ϕ at which the 3D paraboloid is minimum. The outer colour delimits the 99.99% confidence level area (corresponding to a χ^2 increase of 21.10 for 2581 data points in our Stokes I LSD profiles). The minimum value of $\chi^2_{\rm r}$ is 0.96824.

θ_4 a smoothing parameter (within [0,1]) setting the amount of high frequency structures that we allow the fit to include. The two possibilities for m correspond to circular and keplerian orbits respectively (see section 2.4.1), where $\nu = \theta - \omega$ in equation A.9. In practice in the Keplerian case, e and ω themselves are not directly hyperparameters, but instead $C = \sqrt{e}\cos\omega$ and $S = \sqrt{e}\sin\omega$ for computational reasons, following the prescription in Haywood et al. (2014).

After an initial run where all the parameters are free to vary, we fix θ_4 and θ_3 to their respective best values (0.50 ± 0.09 and $180 \pm 60\,P_{\rm rot}$=128 ± 43 d) before carrying out the main MCMC run to find the best estimates of the 5 remaining parameters. We note that the best value found for the decay time is exactly equal to the differential rotation lap time within error bars, and to twice the total span of our data. This decay time corresponds to both the differential rotation lap time and the starspot coherence time, since these are the most influent phenomena on the periodicity of the activity jitter. Such a starspot coherence time is consistent with previous studies (Grankin et al., 2008; Bradshaw & Hartigan, 2014; Lanza, 2006).

As shown in figure 4.5, this method succesfully recovers the different minima previously found with the first two techniques, with little correlation between the various parameters thus minimum

bias in the derived values. Applying the method of Chib & Jeliazkov (2001) to the MCMC posterior samples, we obtain that the marginal likelihood of the case $P_{\rm orb}$ =12.61 $P_{\rm rot}$ is larger than that of the case $P_{\rm orb}$ =15.12 $P_{\rm rot}$ by a Bayes factor of only 1.28, which implies that there is as yet no clear evidence in favor of either of them. The third most likely case, $P_{\rm orb}$ =18.74 $P_{\rm rot}$, has a marginal likelihood which is inferior to the first one by a Bayes' factor of > 8, and the case with no planet has a marginal likelihood which is smaller than that of the first case by a Bayes factor of 2 10^5. The three most likely sets of parameters are summarised in table 4.3.

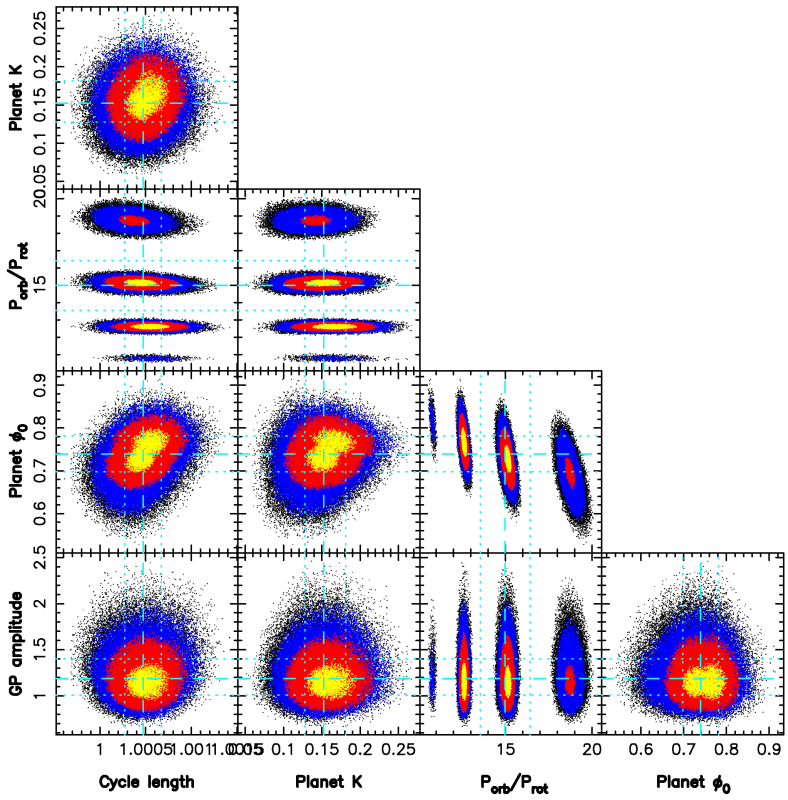

Figure 4.5 – Phase plots of our 5-parameter MCMC run with yellow, red and blue points marking respectively the 1σ, 2σ and 3σ confidence regions. The optimal values found for each parameters are: θ_1=1.19 $\pm$ 0.21 km s^{-1}, θ_2=1.0005 $\pm$ 0.0002 $P_{\rm rot}$, K=0.152 $\pm$ 0.029 km s^{-1}. Several optima are detected for $P_{\rm orb}$: 12.61 $\pm$ 0.13 $P_{\rm rot}$, 15.12 $\pm$ 0.20 $P_{\rm rot}$ and 18.74 $\pm$ 0.34 $P_{\rm rot}$, ordered by decreasing likelihood. The corresponding phases ϕ are: 0.766 $\pm$ 0.030, 0.728 $\pm$ 0.033 and 0.694 $\pm$ 0.042 respectively.

Trying to fit a non-circular Keplerian orbit to our data, i.e. adding the periapsis argument and the eccentricity e to the parameters in our MCMC run, we obtain e=0.05 $\pm$ 0.18, with a marginal likelihood slightly smaller than that of the case of a circular orbit. This further supports that the planet eccentricity is low if non-zero.

The best fit with our third method is shown in figure 4.6, where we see the raw RVs and the modelled RV curve predicted with this method, i.e., the sum of the GPR-fitted activity jitter and of the planet signal. Zooming in shows that this curve presents similarities with the RV jitter curve derived by ZDI (figure 4.1), indicating that, although working only with the RV data points, GPR successfully retrieves a convincing model for the activity. We also note the ability of the GP to model the activity jitter not only during our observing runs, but also during the 45 d gap between them, emphasising the variability of the RV signal with time. The residual RVs in the case presented here have a rms value of 29 m s^{-1} (close to the instrument RV precision 20-30 m s^{-1}) whereas the residual RVs derived with the 1st method yield a rms value of 51 m s^{-1}. Though the rms value is 2.5 times smaller than the error bar, GPR only fits 2 parameters, which illustrates its

Table 4.3 – Sets of orbital parameters that allow to fit the corrected RV curve best, using a GP with a covariance function given in Eq. 2.2, derived from the MCMC run. Respectively: reflex motion RV semi-amplitude K, orbital period $P_{\rm orb}$ in units of $P_{\rm rot}$, orbital period $P_{\rm orb}$ in days, phase of inferior conjunction ϕ relative to rotation cycle 11.00 (ephemeris defined in Eq. 3.1), BJD of inferior conjunction, natural logarithm of the marginal likelihood $\mathcal{L}$ and natural logarithm of the relative marginal likelihood $\mathcal{L}_{r3}$ as compared to the best case. The case where no planet is taken into account in the model is given for comparison.

K ($\mathrm{km\,s^{-1}}$)	$P_{\rm orb}$ ($P_{\rm rot}$)	$P_{\rm orb}$ (d)	ϕ	$\mathrm{BJD_c}$ (2,457,340+)	$\log\mathcal{L}$	$\log\mathcal{L}_{r3}$
0.163	12.61	8.99	0.766	10.54	-3.48	0.00
±0.028	±0.13	±0.09	±0.030	±0.27		
0.149	15.12	10.79	0.728	9.71	-3.73	-0.25
±0.026	±0.20	±0.14	±0.033	±0.36		
0.139	18.74	13.37	0.694	8.56	-5.60	-2.12
±0.026	±0.34	±0.24	±0.042	±0.57		
0					-15.80	-12.52

flexibility without decreasing its reliability, since the results are consistent with those found using independent methods (sections 4.1.1, 4.1.2). This demonstrates that GPR does a better job at modelling the activity jitter and its temporal evolution than the 2 previous methods, in agreement with the conclusions of Donati et al. (2017) in the case of the wTTS V830 Tau. As a result, we consider the optimal planet parameters derived with GPR as the most reliable ones, and therefore conclude that the orbital periods of 10.8 and 9.0 d are more or less equally likely.

4.1.4 Conclusions about TAP 26 b

Table 4.4 summarises the likelihood of the different periods found with each method.

We find that GPR succeeds best at modelling the intrinsic variability occurring at the surface of TAP 26, and is able to fit raw RVs at a rms precision of 29 $\mathrm{m\,s^{-1}}$, i.e., close to the instrumental precision of ESPaDOnS (20-30 $\mathrm{m\,s^{-1}}$, Moutou et al., 2007; Donati et al., 2008b) and 30% better than with our first method (yielding a rms precision of 51 $\mathrm{m\,s^{-1}}$).

For Hα and B_ℓ, no signal is detected at the planet periods found with any of those three methods.

All three methods demonstrate the clear presence of a planet signature in the data, although the gap between both data sets generates aliasing problems, causing multiple nearby peaks to stand out in the periodogram. Of the dominant periods, the 10.8 d one emerges strongly for all three methods. It is the most likely with the second method, and equally likely as other periods when using the first and third methods (13.4 d and 9.0 d respectively). Although the 9.0 d orbital period ranks low (and in particular lower than the 13.4 d period) with our first and second methods, we nonetheless consider it as the second most likely given its first rank with GPR; the most probable explanation for this apparent discrepancy lies in the higher ability of GPR at modelling intrinsic variability of the activity jitter plaguing the RV curve. Allowing ZDI to model temporal evolution of spot distributions and magnetic topologies should bring all methods on an equal footing; this upgrade is planned for a forthcoming study.

Assuming the 10.79 ± 0.14 d period is the true orbital period, and using the values yielded by GPR for K and ϕ, we find a circular orbit of semi-major axis $a = 0.0968 \pm 0.0032$ au $= 17.8 \pm 2.7\,R_\star$, epoch of inferior conjunction $\mathrm{BJD_c}$ =2,457,349.71 ± 0.36 and $M \sin i$ =1.66 ± 0.31 $\mathrm{M_{Jup}}$. If the orbital plane is aligned with the equatorial plane of TAP 26, with an assumed inclination of 55°, we obtain a mass M=2.03 ± 0.46 $\mathrm{M_{Jup}}$ for TAP 26 b. The 8.99 ± 0.09 d period leads to a=0.086 ± 0.003 au, $\mathrm{BJD_c}$ =2,457,350.54 ± 0.27 and $M \sin i$ =1.71 ± 0.31 $\mathrm{M_{Jup}}$.

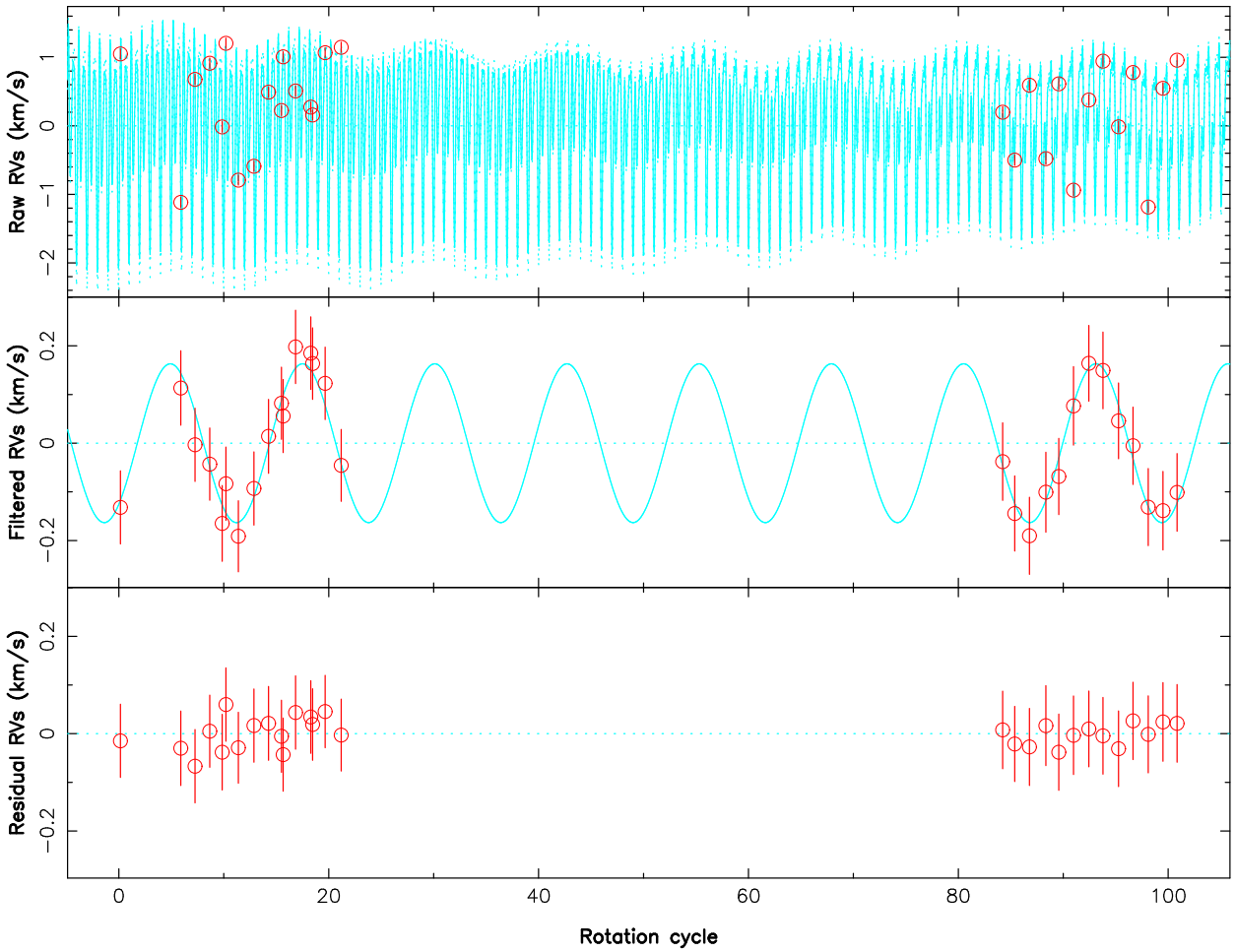

Figure 4.6 – RV curves for a GPR fit of the activity jitter, with parameters K=0.163 km s^{-1}, $P_{\rm orb}$ =12.61 $P_{\rm rot}$, ϕ=0.766, θ_1=1.19 km s^{-1}, θ_2=1.0005 $P_{\rm rot}$, θ_3=180 $P_{\rm rot}$, θ_4=0.50 $P_{\rm rot}$. *Top:* raw RVs and their error bars are shown in red, the solid cyan curve is the sum of the activity jitter predicted by GPR and the planet signal, and the dashed cyan lines show the 68.3% confidence intervals about the prediction around this model. Middle panel: filtered RVs and their error bars, resulting from the subtraction of the GP-fitted activity jitter from the raw RVs (in red), and the sine curve corresponding to the assumed planet signal (in cyan). *Bottom:* residual RVs resulting from the subtraction of the planet signal from the filtered RVs, and their error bars. The residual RVs feature a rms value of 29 m s^{-1}, i.e. the GP fits the RVs down to $\chi^2_{\rm r}$ =0.151.

With an age of $\simeq$17 Myr, TAP 26 is already an aging T Tauri star and on the verge of becoming a post T Tauri star, as demonstrated by its complex geometry and weaker dipole field component (consistent with TAP 26 having a mostly radiative interior). The hJ in a nearly circular orbit that we have discovered in the young system TAP 26 is better explained by type II disc migration than by planet-planet scattering coupled to tidal circularisation.

More observations of TAP 26, featuring in particular a more regular temporal sampling, are currently under analysis to better determine the characteristics of the newborn hJ we detected.

Table 4.4 – Results yielded by the methods ZDI #1, ZDI #2 and GPR, for the two periods ≃15 $P_{\rm rot}$ and ≃13 $P_{\rm rot}$. From top to bottom: reflex motion semi-amplitude K, phase of inferior conjunction ϕ relative to cycle 11.0, orbital period $P_{\rm orb}$ in units of $P_{\rm rot}$, orbital period $P_{\rm orb}$ in days, semi-major axis a, $M \sin i$, BJD of inferior conjunction $\mathrm{BJD_c}$, natural logarithm of relative likelihood as compared to the best case $\mathcal{L}_r$, GP amplitude θ_1 and GP recurrence timescale θ_2. Results are displayed in bold font when the period is found with the highest likelihood using the corresponding method.

	ZDI #1	ZDI #2	GPR
K ($\mathrm{km\,s^{-1}}$)	0.133 ± 0.021	$\mathbf{0.154 \pm 0.022}$	0.149 ± 0.026
ϕ	0.715 ± 0.024	$\mathbf{0.671 \pm 0.035}$	0.728 ± 0.033
$P_{\rm orb}$ ($P_{\rm rot}$)	15.27 ± 0.14	$\mathbf{15.29 \pm 0.15}$	15.12 ± 0.20
$P_{\rm orb}$ (d)	10.90 ± 0.10	$\mathbf{10.91 \pm 0.11}$	10.79 ± 0.14
a (au)	0.0974 ± 0.0032	$\mathbf{0.0975 \pm 0.0032}$	0.0968 ± 0.0032
$M \sin i$ ($\mathrm{M_{Jup}}$)	1.49 ± 0.25	$\mathbf{1.73 \pm 0.27}$	1.66 ± 0.31
$\mathrm{BJD_c}$ (2,457,340+)	9.54 ± 0.26	$\mathbf{9.06 \pm 0.38}$	9.71 ± 0.36
$\log \mathcal{L}_r$	-0.53	**0.00**	-0.25
θ_1 ($\mathrm{km\,s^{-1}}$)			1.19 ± 0.21
θ_2 ($P_{\rm rot}$)			1.0004 ± 0.0002
K ($\mathrm{km\,s^{-1}}$)	0.107 ± 0.021	0.148 ± 0.025	$\mathbf{0.163 \pm 0.028}$
ϕ	0.724 ± 0.031	0.677 ± 0.038	$\mathbf{0.766 \pm 0.030}$
$P_{\rm orb}$ ($P_{\rm rot}$)	12.76 ± 0.14	12.83 ± 0.12	$\mathbf{12.61 \pm 0.13}$
$P_{\rm orb}$ (d)	9.11 ± 0.10	9.16 ± 0.09	$\mathbf{8.99 \pm 0.09}$
a (au)	0.0864 ± 0.0028	0.0868 ± 0.0028	$\mathbf{0.0858 \pm 0.0028}$
$M \sin i$ ($\mathrm{M_{Jup}}$)	1.13 ± 0.23	1.56 ± 0.28	$\mathbf{1.71 \pm 0.31}$
$\mathrm{BJD_c}$ (2,457,340+)	10.14 ± 0.28	9.69 ± 0.35	$\mathbf{10.54 \pm 0.27}$
$\log \mathcal{L}_r$	-6.87	-3.61	**0.00**
θ_1 ($\mathrm{km\,s^{-1}}$)			$\mathbf{1.19 \pm 0.21}$
θ_2 ($P_{\rm rot}$)			$\mathbf{1.0005 \pm 0.0002}$

4.2 Results on V410 Tau

4.2.1 Jitter filtering

Radial velocity values were derived for all spectra except the 3 with low S/N and the 6 in which we identified flares (see section 3.1.2). The raw RVs present modulations whose amplitude vary between 4 – 8.5 $\mathrm{km\,s^{-1}}$, with a global rms of 1.8 $\mathrm{km\,s^{-1}}$. Like with the photometric data, the RV variations are the lowest in 2009 Jan and the strongest in 2013 Dec.

The activity jitter is modelled with two different techniques, ZDI and GPR. Raw RVs and jitter models are plotted in figure 4.7 and listed in Yu et al. (2017). The phase plot of the MCMC is displayed in figure 4.8 and the best fit is shown in figure 4.7, together with the ZDI fits. We note that, contrary to ZDI, GPR, being capable of describing intrinsic variability in a consistent way, is able to fit our whole 8-year-long data set with one model. We obtain $\theta_1 = 1.8^{+0.2}_{-0.2}$ $\mathrm{km\,s^{-1}}$, $\theta_2 = 0.9991 \pm 0.0002$ $P_{\rm rot}$, $\theta_3 = 86^{+24}_{-19}$ $P_{\rm rot}$ and $\theta_4 = 0.35 \pm 0.03$ $P_{\rm rot}$.

The rms of the filtered RVs for each epoch and each method are summarized in table 4.5. The RV curve filtered from the ZDI model presents a global rms of 0.167 $\mathrm{km\,s^{-1}}$, i.e. $\sim 2\langle\sigma_{\rm RV}\rangle$. The epoch where the filtering is most efficient is 2009 Jan, although the rms of the filtered RVs is only at $1.5\langle\sigma_{\rm RV}\rangle$, and it goes up to $3\langle\sigma_{\rm RV}\rangle$ in 2011 Jan and 2013 Dec. On the other hand, the GPR model filters the RV out down to 0.076 $\mathrm{km\,s^{-1}} = 0.94\langle\sigma_{\rm RV}\rangle$.

Lomb-Scargle periodograms for both raw and filtered RVs, for both methods (figure 4.9 for each individual epoch, 4.10 for the whole data set), show that the stellar rotation period or its

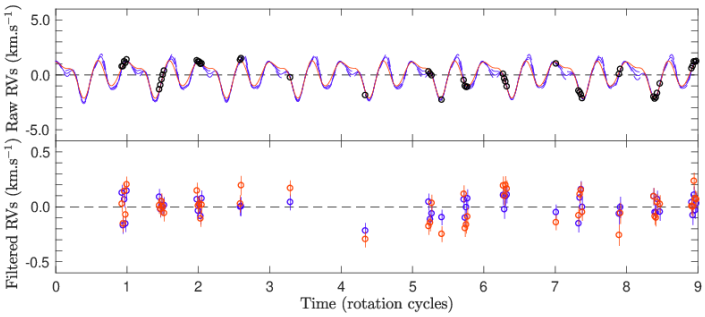

(a) 2009 Jan. Respective rms: 1.20, 0.13, 0.08 km s^{-1}

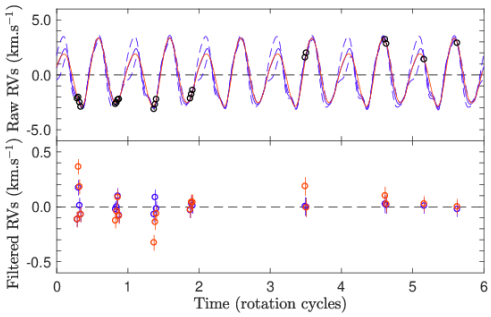

(b) 2011 Jan. Respective rms: 2.40, 0.14, 0.06 km s^{-1}

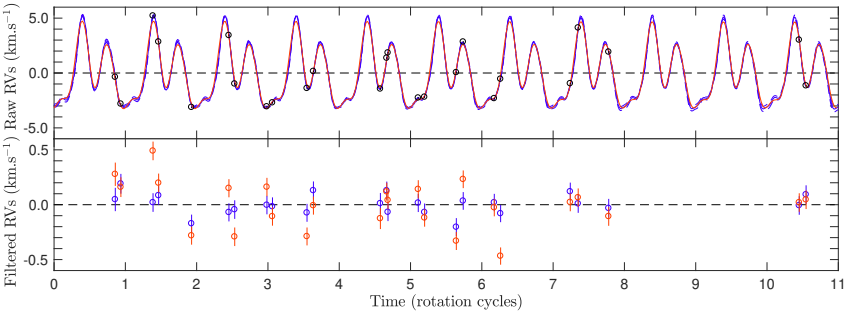

(c) 2013 Dec. Respective rms: 2.43, 0.22, 0.09 km s^{-1}

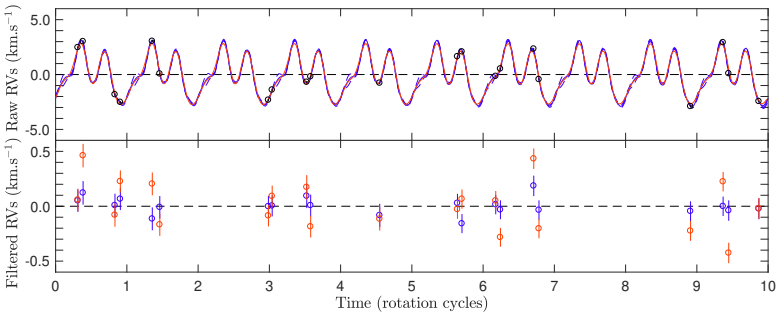

(d) 2015 Dec. Respective rms: 1.93, 0.22, 0.08 km s^{-1}

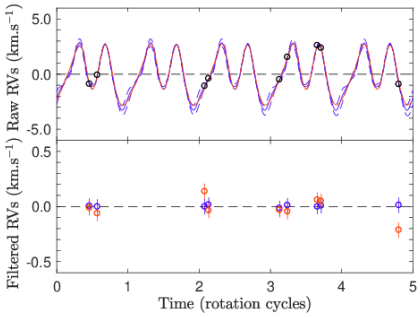

(e) 2016 Jan. Respective rms: 1.41, 0.09, 0.01 km s^{-1}

Figure 4.7 – Raw and filtered RVs of V410 Tau for each observation epoch. On each figure, the top plot depicts the raw RVs (red dots), the ZDI reconstruction (red full line) and the GP fit (blue full line with 1-σ area of confidence marked as blue dashed lines). The bottom plot depicts the RVs filtered from the ZDI-modelled activity (red dots) and the RVs filtered from the GP-modelled activity (blue dots). Note the different scales on the y-axis between the filtered and raw RVs. The subcaptions indicate the rms of the raw RVs, the ZDI-filtered RVs and the GPR-filtered RVs respectively. All rotational cycles are displayed as in table A1 of Yu et al. (2019).

first harmonic are clearly present in 2009 Jan and 2011 Jan, but not well retrieved in 2013 Dec, 2015 Dec and 2016 Jan. However the periodogram for the whole $\mathrm{RV_{raw}}$ data set presents neat peaks at P_{rot} and its first two harmonics. P_{rot} and its first harmonic are well filtered out by both modelling methods, and the second harmonic is well filtered out in the GP residuals. A weak signal remains at $P_{\mathrm{rot}}/3$ in the ZDI residuals but looking at a phase-folded plot does not reveal any particularly obvious tendency, leading us to suspect that it mostly reflects the contribution of a few stray points. No other period stands out with a false-alarm-probability lower than 5%, which

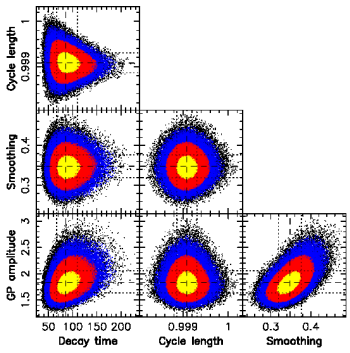

Figure 4.8 – Phase plot of the MCMC-GPR run on the raw RVs of V410 Tau, model without planet. The yellow, red and blue colors indicate respectively the 1σ-, 2σ- and 3σ-areas of confidence, and the optimal values for the hyperparameters are marked with black dashed lines, with 1σ-intervals marked with black dotted lines. GP amplitude (θ_1): $1.8^{+0.2}_{-0.2}$ km s^{-1}, Cycle length (θ_2): $0.9991 \pm 0.0002\, P_{\rm rot}$, Decay time ($\theta_3$): $86^{+24}_{-19}\, P_{\rm rot}$, Smoothing ($\theta_4$): 0.35 ± 0.03.

Table 4.5 – Rms of V410 Tau raw and filtered RVs, using either ZDI or GPR-MCMC. All rms RVs are given in km s^{-1}.

Epoch	2009	2011	2013	2015	2016	All
Raw	1.200	2.392	2.429	1.932	1.411	1.8
ZDI filt.	0.131	0.141	0.215	0.222	0.094	0.167
GP filt.	0.084	0.064	0.087	0.075	0.009	0.076

allows us to conclude that no planet signature is found in this data set with our filtering methods.

For the 2015-2016 points, the ability of the new version of ZDI (presented in section 3.5.1) to filter the jitter out was tested. RVs derived from the maps shown in figure 3.22 are plotted in figure 4.11 and 4.12, to be compared with RVs derived from classical ZDI maps. The rms of the filtered RVs here, 0.194 km s^{-1}, does not decrease compared to when using classical ZDI, despite the significant better fit to the profile (see section 3.5), which means our model is still too simple and cannot fully account for the observed variability. However, figure 4.12 shows that global trends in the temporal evolution of the RV curve are well-reproduced by this new ZDI model, such as the jitter maximum moving from phase 0.37 to 0.32, or the local minimum at phase 0.54 in 2015 Dec moving to 0.50 in 2016 Jan.

The period derived from the GPR on our raw RVs is shorter than the period we used to phase our data, and corresponds to a latitude of 5.5°. This period is much closer to the period derived with GPR from B_ℓ than to the period derived from Hα, showing that in this case, B_ℓ is a better activity proxy than Hα (for a more systematic study of the correlation of B_ℓ with stellar activity, see Hébrard et al., 2016). The decay time associated to RVs is much shorter than the differential rotation lap time and the decay times of the V magnitude, Hα and B_ℓ (see Table 3.4), which suggests that RVs are more sensitive to small-scale short-lived features while the photometry, Hα and B_ℓ are more sensitive to large-scale long-lasting features.

Through both processes, the residual RVs present no significant periodicity which would betray the presence of a potential planet. To estimate the planet mass detection threshold, GPR-MCMC was run on simulated data sets, composed of a base activity jitter (our GP model), and a circular planet signature, plus a white noise of level 0.081 km s^{-1}. Various planet separations and masses were tested, and for each case, GPR-MCMC was run several times with different randomization seeds, to mitigate statistical bias. For every randomization seed, GPR-MCMC was run with a model

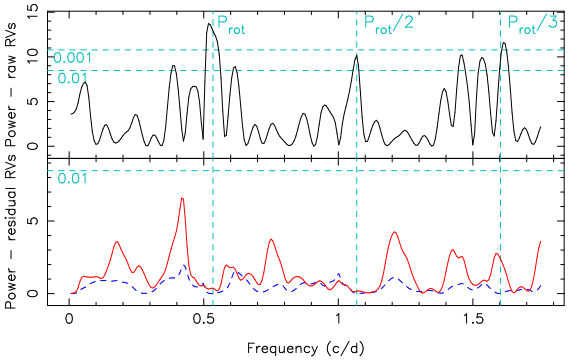

(a) 2009 Jan

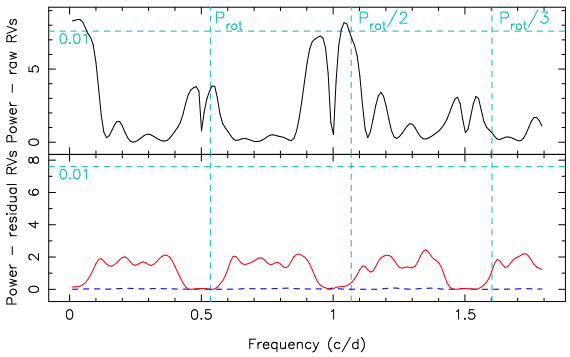

(b) 2011 Jan

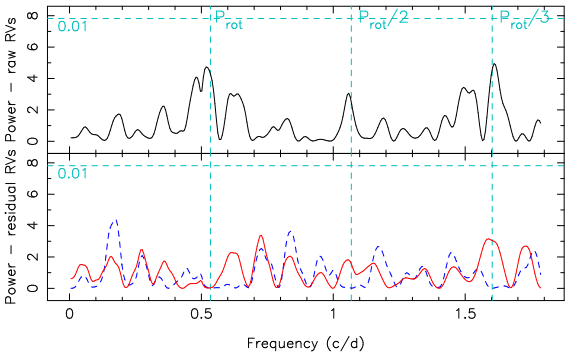

(c) 2013 Dec

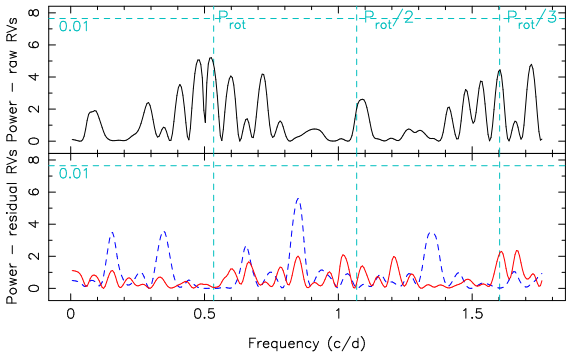

(d) 2015 Dec

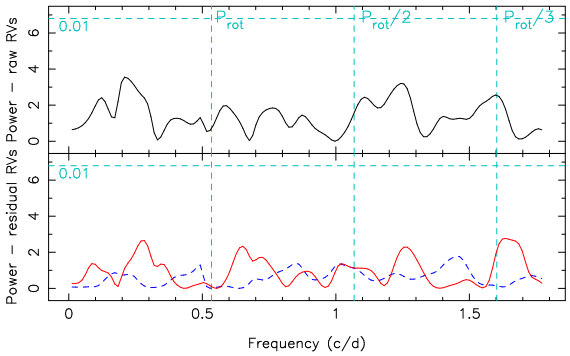

(e) 2016 Jan

Figure 4.9 – Periodograms of the raw RVs (top), of the ZDI-filtered RVs (bottom, red full line) and of the GP-filtered RVs (bottom, blue dashed line), for observation epochs 2009 Jan (a), 2011 Jan (b), 2013 Dec (c), 2015 Dec (d) and 2016 Jan (e). False-alarm probability levels of 1% and 0.1% are represented as horizontal cyan dashed lines, and $P_{\rm rot}$ and its first two harmonics as vertical cyan dashed lines.

including a planet and a model including no planet, and the difference of logarithmic marginal likelihood between them (hereafter $\Delta\mathcal{L}$) was computed. Finally, the detection threshold was set at $\Delta\mathcal{L} = 10$ (4.5σ) and the minimum detectable mass at each separation was interpolated from the mass/$\Delta\mathcal{L}$ curve. Figure 4.13 shows the planet mass detection threshold as a function of planet-star separation: we thus obtained a detectability threshold of $\sim$1 $M_{\rm Jup}$ for $a < 0.09$ au and $\sim$4.6 $M_{\rm Jup}$ for $a = 0.15$ au. The figure also shows the parameters of V830 Tau b and TAP 26 b, showing that we would likely have detected a planet like TAP 26 b but not one like V830 Tau b. Planets beyond $a = 0.15$ au are difficult to detect due to the temporal coverage of our data, that never exceeds 19 d at any given epoch. The early depletion of the disc may have prevented the formation and/or the

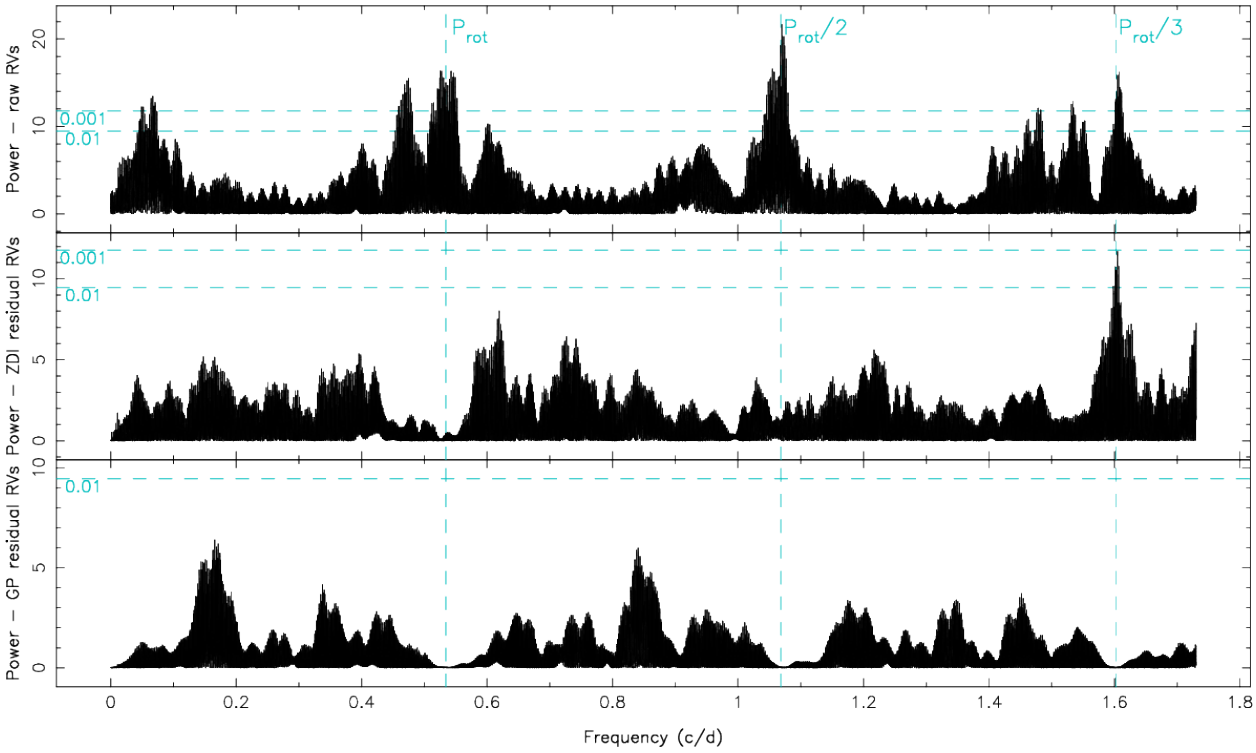

Figure 4.10 – Periodograms of the raw RVs (top), of the RVs filtered from ZDI-modelled activity (middle) and of the RVs filtered from GP-modelled activity (bottom, blue dashed line), for observation epochs 2009 Jan (a), 2011 Jan (b), 2013 Dec (c), 2015 Dec (d) and 2016 Jan (e). Periodograms of the whole data set raw RVs (top), RVs filtered from ZDI-modelled activity (middle) and RVs filtered from GP-modelled activity (bottom). False-alarm probability levels of 1% and 0.1% are represented as horizontal cyan dashed lines, and $P_{\rm rot}$ and its first two harmonics as vertical cyan dashed lines.

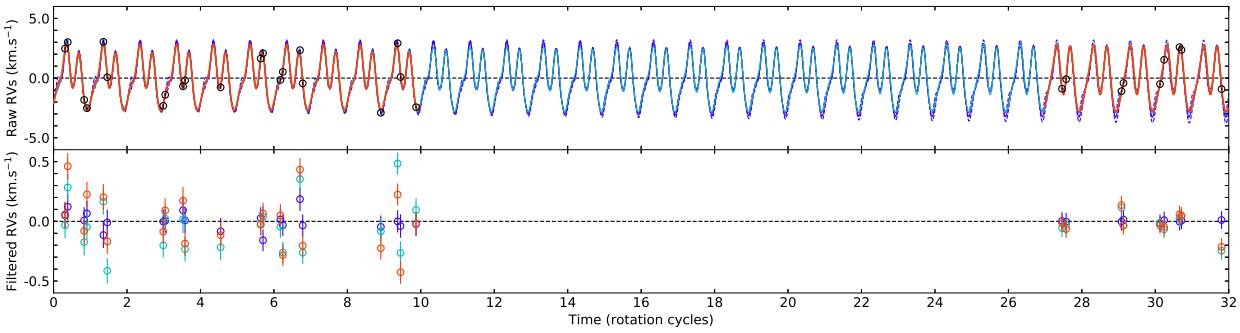

Figure 4.11 – Comparison between the GP model, the new ZDI model and the classical ZDI models for V410 Tau RVs in season 2015b-2016a. Rotation cycles are offset to concur with table A1 of Yu et al. (2019). *Top:* raw RVs (black dots) with 1σ-error bars, GP model (purple full line), new ZDI model (cyan full line) and classical ZDI models for both observation epochs 2015 Dec and 2016 Jan (red full lines). *Bottom:* RVs filtered from the GP model (purple dots), from the new ZDI model (cyan dots) or from the classical ZDI models (red dots). The rms of the filtered RVs with GP, new ZDI and classical ZDI are respectively 0.065, 0.194 and 0.193 km s^{-1}.

migration of giant exoplanets.

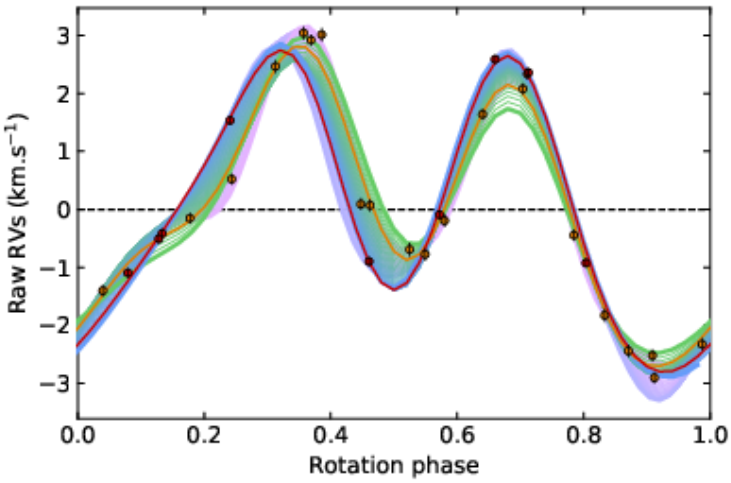

Figure 4.12 – Raw RVs of V410 Tau in the 2015b-2016a season, between cycles 1349 and 1381 as referenced in table A1 of Yu et al. (2019), plotted against stellar rotation phase. The GPR and new ZDI models are represented by full lines colored in gradients, from earliest to latest cycle, respectively pink to purple and green to blue, while the classical ZDI models for 2015 Dec and 2016 Jan are plotted in orange and red respectively. Observations are plotted as dots with 1σ-error bars, orange for 2015 Dec and 2016 Jan.

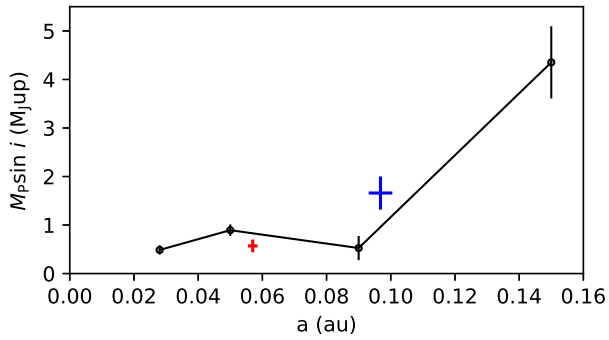

Figure 4.13 – Detectability threshold (associated to $\Delta(L) = 10$, or equivalently 4.5σ) in terms of $M \sin i$ for planets at various a, with the RV filtering technique involving GPR. V830 Tau b is plotted in red (parameters from Donati et al., 2017) and TAP 26 b in blue (parameters from Yu et al., 2017).

4.2.2 Long-term RV drift

As mentioned in section 3.2.4, the bulk RV of V410 Tau exhibits a drift throughout our 8-year campaign, from $16.30 \pm 0.05\,\mathrm{km\,s^{-1}}$ in 2008b-2009a to $16.65 \pm 0.05\,\mathrm{km\,s^{-1}}$ in 2015b-2016a. It could be a manifestation of the binary motion of V410 Tau A-B. The central binary of V410 Tau was observed twice, with a sky-projected separation of $16.8 \pm 1.4\,\mathrm{au}$ in 1991 Oct and $9.5 \pm 0.3\,\mathrm{au}$ in 1994 Oct (0.13 ± 0.01 arcsec and 0.074 ± 0.002 arcsec resp. in Ghez et al., 1995), and a mass ratio of 0.20 ± 0.10 (Kraus et al., 2011). Assuming a mass ratio of 0.2 and an edge-on circular orbit, we find that an orbit of the primary star of radius 6.0 au, i.e. binary separation 36.0 au and period 166 yr, fits our bulk RVs and the sky-projected separations at a level of 2σ (see figure 4.14). No binary motion was detected in the 2013 to 2017 astrometry measurements of Galli et al. (2018), which is consistent with our model where the sky-projected velocity varies by only $0.13\,\mathrm{m''\,yr^{-1}}$ over these 3.5 years (roughly a 50th of the orbital period). More measurements would enable to estimate the eccentricity and potentially fit the sky-projected separations to a better level, as well as to decide whether the binary motion can explain the RV drift observed in this study.

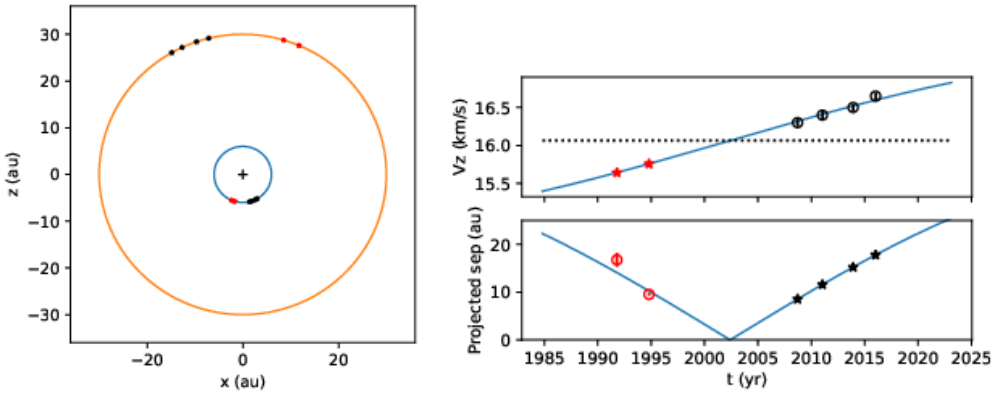

Figure 4.14 – Circular model for the binary motion of V410 Tau A and V410 Tau B: edge-on orbit, separation 36.0 au, period 166 yr and systemic radial velocity 16.06 km s^{-1}. **Left:** top-view of the model orbit, with the z-axis parallel to the line-of-sight, where the positions of V410 Tau A and B according to the model are marked by red and black stars at the times of the separation measurements and of our spectropolarimetric seasons (2008b-2009a, 2011a, 2013b and 2015b-2016a) respectively. **Right:** *Top:* RV_{bulk} of V410 Tau A with time, as measured by us in black dots with 1σ error bars and as derived from the model orbit in blue. The predicted RV_{bulk} at the times of the separation measurements are represented by red stars. *Bottom:* Sky-projected binary separation as a function of time, as measured by Ghez et al. 1995 in red dots with 1σ error bars, and as derived from the model orbit in blue. The predicted sky-projected separations at the dates of our observing seasons are marked in black stars.

Kraus et al. 2016 outlines a correlation between the presence of a companion under 50 au and a lack of planets, in a sample of binary stars with mass ratios $q > 0.4$, which could support the hypothesis that V410 Tau B, although having a slightly lower mass ratio ($q = 0.2 \pm 0.1$, Kraus et al., 2011), played a role in the early disc dissipation, which in turn prevented the formation of a hJ.

4.3 Results on V830 Tau

Raw RVs were computed for V830 Tau at all observation epochs: 2014b-2015a, 2015b, 2016a (Donati et al., 2015, 2016, 2017). After applying GPR-MCMC on them, we find that those RVs present modulations of semi-amplitude 0.878 ± 0.135 km s^{-1}, period 2.737 ± 0.002 d, decay time 120 ± 30 d and smoothing parameter 0.6 ± 0.1. All three methods described in 4.1 enable to detect a planetary signature of orbital period $\sim$4.93 d (4.927 ± 0.008 d with GPR-MCMC on the whole data set, compatible within error bars with the values yielded by other methods, see Donati et al., 2017) and amplitude $\sim$70 m s^{-1} (68 ± 11 m s^{-1} with GPR-MCMC on the whole data set). With GPR-MCMC, the likelihood of the model including a planet is found to be higher than that of the model without planet by a Bayes factor of 10^9. Absence of a peak at the derived orbital frequency in the periodograms of activity proxies (Hα and B_ℓ) further cements the confirmed status of this detection. V830 Tau b is a planet orbiting at 0.057 ± 0.001 au from its host star, with a mass that verifies $M_p \sin i = 0.57 \pm 0.10\,M_{Jup}$. If modelled with an eccentric orbit, the filtered RVs yield an eccentricity of 0.21 ± 0.15, not significantly high enough to say that the hJ is on an eccentric orbit. Like TAP 26 b, this detection thus suggests that V830 Tau b underwent type II migration across the protoplanetary disc.

4.4 Synthesis on MaTYSSE hot Jupiters

Regarding the hJs we detected around the ∼17 Myr TAP 26 and the ∼2 Myr V830 Tau and despite their differences (in mass in particular), it is intesting to investigate whether the evolutionary link noted between the host stars (see section 3.1) also applies to their hJs. This would actually imply that TAP 26 b migrated outwards under tidal forces from a distance of ∼0.057 au (where V830 Tau b is located) to its current orbital distance of 0.094 au, as a result of the spin period of TAP 26 being ∼15x shorter than the orbital period of TAP 26 b. This option seems however unlikely given the latest predictions of tidal interactions between a young TTS and its close-in hJ (Bolmont & Mathis, 2016), indicating that tidal forces can only have a significant impact on a hJ within 0.06 au of a solar-mass host star (for a typical TTS with a radius of $\sim 2\,R_\odot$). The most likely explanation we see is thus that TAP 26 b:

- ended up its type-II migration in the accretion disc at the current orbital distance, when TAP 26 was still young, fully convective and hosting a large-scale dipole field of a few kG similar to that of AA Tau (Donati et al., 2010a), i.e., strong enough to disrupt the disc up to a distance of 0.09 au,
- was left over once the disc has dissipated at an age significantly smaller than 2 Myr, i.e., before the large-scale field had time to evolve into a weaker and more complex topology, and the inner accretion disc to creep in as a result of the decreasing large-scale field and the subsequent chaotic accretion (e.g., Blinova et al., 2016).

Admittedly, this scenario requires favorable conditions to operate; in particular, it needs the accretion disc to vanish in less than 2 Myr, which happens to occur in no more than 10 % of single TTSs in Taurus (Kraus et al., 2012). In fact, since both TAP 26 and V830 Tau have the same angular momentum content, it is quite likely that TAP 26 indeed dissipated its disc very early as otherwise the disc would have dissipated a larger amount of angular momentum of the host star through disc coupling (see Sec. 3.5). Quantitatively speaking, assuming (i) that the hJ we detected tracks the location of the inner disc when the disc dissipated, (ii) that the spin period at this time was locked on the Keplerian period of the inner disc (equal to the orbital period of the detected hJ) and (iii) that stellar angular momentum was conserved since then, we derive that the disc would have dissipated when TAP 26 was about three times larger in radius, at an age of less than 1 Myr (according to Siess et al., 2000). Generating a magnetospheric cavity of the adequate size (0.085 – 0.097 au depending on the orbital period) would have required TAP 26 to host at this time a large scale dipole field of 0.3 – 1.0 kG for mass accretion rates in the range $\sim 10^{-9}$ – $10^{-8}\,M_\odot$/yr, compatible with the large-scale fields found in cTTSs of similar masses (e.g., GQ Lup, Donati et al., 2012).

Along with other recent reports of close-in giant planets (or planet candidates) detected (or claimed) around young stars (van Eyken et al., 2012; Donati et al., 2016; David et al., 2016; Mann et al., 2016; Johns-Krull et al., 2016; David et al., 2019b), our result may suggest a higher frequency of hJs around young solar-type stars than around more evolved stars ($\simeq$1%, Wright et al., 2012). However, this may actually reflect no more than a selection bias in the observation samples (as for their mature equivalents in the early times of velocimetric planet detections). Planets are obviously much easier to detect around non-accreting TTSs as a result of their lower level of intrinsic variability; observation samples (like that of MaTYSSE) are thus naturally driven towards young TTSs whose accretion discs vanished early, i.e., at a time when their large-scale fields were still strong and their magnetospheric gaps large, and thus for which hJs had more chances to survive type-II migration. A more definite conclusion must wait for a complete analysis of the full MaTYSSE sample. Ultimately, only a full-scale planet survey of young TTSs such as that currently carried out with SPIRou, the new generation spectropolarimeter installed at CFHT since 2018, will be able to bring a consistent picture of how young close-in planets form and migrate, how their

population relates to that of mature hJs, and more generally how young hJs impact the formation and early architecture of planetary systems like our Solar System.

5 | Conclusion and future prospects

This thesis was focused on bringing observational constraints to the theoretical scenarii of formation and migration of hot Jupiters, by searching for hJs around weak-line T Tauri stars and by characterizing their orbital properties. In order to be able to detect potential signatures of hJs in the radial velocities of such active stars, an accurate understanding of their activity is mandatory so as to filter out the RV jitter introduced by the stellar activity that contributes to RV variations at a typical level of $1\,\mathrm{km\,s^{-1}}$. Our observations also help constraining theories of stellar dynamos, as well as theories of star / planet formation. Constraining both hJ formation and stellar formation theories in parallel is crucial as the planet-star interactionsplay a major role in the evolution of both bodies and of the whole system.

5.1 Activity and magnetic fields of wTTSs

5.1.1 Surface brightness and magnetic fields of WTTSs

Our results enable to see and compare the surface brightness and magnetic topologies of three wTTSs of different masses and ages. The brightness maps of TAP 26,V410 Tau and V830 Tau all exhibit a cool polar cap, like other MaTYSSE stars LkCa 4 (Donati et al., 2014), Par 1379 (Hill et al., 2017) and V1095 Sco (Nicholson et al., 2018). However, unlike the low-complexity maps of LkCa 4, Par 1379 and V1095 Sco, our stars display a relatively spread-out distribution of spots and plages over the surface, similarly to MaTYSSE stars Par 2244 (Hill et al., 2017) and TWA 6 (Hill et al., 2019). While both TAP 26 and V830 Tau have brightness maps with 10 – 12 % spot+plage coverage, the V410 Tau brightness maps display a higher 14 – 18 % feature coverage, comparable to that of Par 2244 and TWA 6. Drawing trends from these results is not trivial, as V830 Tau, V410 Tau and Par 2244 are young ($\lesssim 2\,\mathrm{Myr}$) while TAP 26 and TWA 6 are more evolved ($> 15\,\mathrm{Myr}$), and TWA 6 is of similar mass to TAP 26 and V830 Tau ($\sim 1\,\mathrm{M_\odot}$) whereas V410 Tau and Par 2244 are more massive (1.3 – $1.8\,\mathrm{M_\odot}$).

Concerning magnetic topologies (see figure 3.21), V830 Tau has a mainly poloidal, dipolar and axisymmetric topology, as expected from this fully convective star. TAP 26, on the other hand, was found to have a rather complex magnetic topology, where the poloidal dipole only constitutes 10 % of the magnetic energy whereas the toroidal component, contributing to 30 % of the total magnetic energy, is relatively high. The level of complexity in the field topology of TAP 26 is somewhat expected from a star that has a substantial radiative core.

The magnetic topology of V410 Tau however displays an atypical topology for a fully convective star, with a strong toroidal component (half of the magnetic energy) that keeps a constant orientation throughout the 8-year span of our data, and a non-axisymmetric poloidal field. The origin of this strong toroidal component, also observed on fully convective, $0.79 \pm 0.05\,\mathrm{M_\odot}$ LkCa 4, is unclear. Perhaps the high toroidal energy stems from a non-standard dynamo, or from remnants of subsurfacic radial shears dating back to the cTTS years, or even from a miraculous survival of the primordial toroidal energy generated after the second core collapse. For the latter hypothesis,

the early dissipation of the disc could be a lead to explore as to why such toroidal energy is not observed on cTTSs.

Completing the analysis of the MaTYSSE sample and analyzing more data, e.g. collected with SPIRou, is therefore necessary to clarify the magnetic panorama of wTTSs.

5.1.2 Intrinsic variability of surface brightness and magnetic topologies

Thanks to the span of our data sets, we were able to outline the presence of intrinsic variability of brightness distribution and magnetic topology at the surface of our three targets.

Made obvious by comparing the ability of ZDI to fit longer data sets versus shorter data sets, even with differential rotation modelling, this intrinsic variability was studied thanks to Gaussian processes. By fitting the RVs, the light curves, the Hα EW and the longitudinal field B_ℓ, we obtained variation time scales of $\sim$130 d for TAP 26 and $\sim$160 d for the RVs of V410 Tau, and $\geq$ 250 d for the V magnitude, Hα EW and B_ℓ for V410 Tau. These quantities are paramount to gauge the activity level of a star (e.g. the correlation of B_ℓ with stellar activity, Hébrard et al., 2016), and our study of V410 Tau offers a comparison between them on a 144-spectra 8-year-spanning high-resolution spectropolarimetric data set. The period derived from GPR on our V410 Tau raw RVs is shorter than the photometric period found by Stelzer et al. (2003) by 0.03 %, and is much closer to the period derived with GPR from B_ℓ than to the period derived from the Hα EW. It demonstrates that, for studying RV curves, B_ℓ is in this case a better activity proxy than Hα and that all activity indexes are not equal as far as what they can tell us about surface features affecting RV curves (see also Haywood et al., 2016). The decay time associated to RVs is much shorter than the differential rotation lap time and the decay times of the V magnitude, which suggests that RVs are more sensitive to small-scale short-lived features while the photometry is more sensitive to large-scale long-lasting features. The Hα EW and B_ℓ also exhibit long decay times, albeit with uncertainties too large to draw a definite conclusion.

A tentative new implementation of ZDI, where a map of the brightness variation rate is fitted alongside the brightness itself, was applied to a combined V410 Tau data set with mixed results: it significantly improves χ^2_r (from $\chi^2_\mathrm{r} = 2.5$ with classical ZDI to $\chi^2_\mathrm{r} = 1$ with new ZDI) and major trends in the evolution of the RV curve are well reproduced compared to classical ZDI models for each subset and to the GPR model, but residuals still display a significant rms of $\gtrsim 2\sigma$. In the future, self-consistent methods that combine the physical realism of ZDI and the flexibility of GPR will be developped and applied to more MaTYSSE data, as well as data from SPIRou (SpectroPolarimetre InfraRouge), the new infrared spectropolarimeter installed at CFHT.

5.1.3 Differential rotation and dynamos of wTTSs

Our results also brought new observational constraints on the differential rotation of young stars, with our three targets displaying an equator rotating faster than the poles, and TAP 26 having an almost solar level of differential rotation (0.0492 ± 0.0010 rad/d). The differential rotation of V410 Tau is on average much lower, at 0.0097 ± 0.0003 rad/d, i.e. 5 – 6 times weaker than that of the Sun, with values in individual epochs varying between 8.1 ± 1.8 mrad/d and 19.0 ± 4.3 mrad/d. Not many observational results have been obtained on the differential rotation of wTTSs yet; within MaTYSSE, the young V830 Tau displays a differential rotation of 17.2 ± 1.4 mrad/d, suggesting a trend that differential rotation increases with age, as the radiative core develops. This is consistent with what is observed for M dwarfs (Morin et al., 2010).

The combination of our differential rotation estimate and the 8-year-long span of our photometric V410 Tau data set allowed us to follow the latitudinal evolution of the main brightness features year after year, and to notice that they underwent a poleward migration from latitude 0 in 2008 to $\sim$50° in 2016. This is reminiscent of the Solar butterfly diagram, albeit reversed, and would suggest

that the dynamo wave, if cyclic, has a period of at least 8 yr and likely much longer (16 yr if our data covers only one half of a full cycle). This is accompanied by an almost-monotonous increase in the strength of the poloidal dipole from ∼200 to ∼500 G. This shows at least the existence of long-term variations on the surface of V410 Tau. Besides, for V410 Tau, the poloidal field almost doubles in strength throughout our observation run, but measures of $d\Omega$ on individual yearly data sets do not show an increase, which, if we are to assume a cyclic dynamo, would imply a phase shift between the magnetic field and the differential rotation. Photometric data over the past 60 yr show a complex evolution of the light curve of V410 Tau, and previous studies have showed cyclical variations of the light curve amplitude and extrema (Stelzer et al., 2003; Sokoloff et al., 2008; Oláh et al., 2009; Grankin & Artemenko, 2009; Savanov, 2012; Hambálek et al., 2019), but whether or not V410 Tau has a full-fledged cycle with polarity reversals like the Sun remains to be determined.

5.2 Angular momentum evolution of young stars & disc lifetimes

We observe that mildly accreting cTTSs with a strong dipolar/poloidal component in their magnetic fields tend to have rotation periods around 6 – 9 d (Donati et al., 2008a, 2010a, 2012). Taking this as a starting assumption, we computed the ages at which our wTTSs lost their coupling with their discs (see figure 3.2). In both cases, this loss would have been caused by the depletion of the inner disc. To do so, we used the stellar evolution models of Siess et al. (2000) to extract the moments of inertia, and, assuming that the wTTSs contracted at constant angular momentum after being decoupled from their disc, derived their radii at the time when they started spinning up. The stellar evolution models gave us the ages corresponding to those radii.

V410 Tau is already one of the youngest observed wTTSs, but its age at disc dissipation was estimated to ∼0.2 Myr, albeit with a relatively low precision, from our measurement of the stellar radius, and corroborated with the magnetic topologies we reconstructed from our spectra. It is a three-star system composed of an inner close binary A-B (mass ratio 0.2 ± 0.1, sky-projected eparation 16.8 ± 1.4 au) and a third component C further away (mass ratio $0.08^{+0.10}_{-0.08}$, sky-projected eparation 36 ± 3 au). V410 Tau was accounted for in the survey of Kraus et al. (2012) showing a correlation between the presence of a companion within 50 au and the early depletion of the accretion disc; our measurements of the age of V410 Tau, our guess of its age at disc dissipation and our guess at the separation between V410 Tau A-B (36 au) corroborate the trend found by that study, as well as give more precise parameters for that star.

Moreover, from the orbital separation of the hot Jupiter discovered within this work, TAP 26 was estimated to have lost its disc also at an age of less than 1 Myr.

The age estimates vary depending on which evolution model is chosen, but newer models (BHAC15, Baraffe et al. 2015, STAREVOL3.4, Amard et al. 2019) give our stars even younger ages (∼0.5, ∼13 and ∼1.5 Myr for V410 Tau, TAP 26 and V830 Tau resp.) than the models of Siess et al. (2000), which reinforces the evidence that these stars dissipated their discs in less than 1 Myr. This makes our three stars some of the wTTSs that lost their discs the earliest (Richert et al., 2018), and, as a result, they are among the fastest rotating wTTSs as they started spinning up early (Gallet & Bouvier, 2015).

5.3 Formation, migration, subsequent evolution of hot Jupiters

As of today, seven giant planets have been detected around wTTSs: V830 Tau b (Donati et al., 2016), K2-33 b(David et al., 2016), TAP 26 b and V1298 Tau b, c, d and e (David et al., 2019b), with a few other candidate close-by giant planets around young stars (e.g. CI Tau, Johns-Krull et al., 2016). V830 Tau b ($0.77 \pm 0.15\,M_{Jup}$, 4.93 ± 0.05 d) and TAP 26 b ($1.66 \pm 0.31\,M_{Jup}$, 10.79 ± 0.14 d)

were discovered through MaTYSSE, while K2-33 b and V1298 Tau b, c, d and e were detected via transits in the stellar light curve, and their masses are not yet well constrained. While not yet a statistically representative sample, we can outline important conclusions from these first results:

- it is possible to form hJs in time scales of as low as 2 Myr,
- both V830 Tau b and TAP 26 b have a quasi-circular orbit, which favors the planet-disc type II migration scenario over planet-planet scattering followed by tidal circularization,
- with two detections in a ∼30-star sample (not all of which having been studied as of today), one may wonder whether (i) the frequency of hJs is higher around young stars than around mature ones (≃1%, Wright et al., 2012), or (ii) our sample is biased towards planet-hosting stars. Concerning (i), hypotheses explaining the depletion of hJs as the star ages towards the MS include tidal and magnetic star-planet interactions that can end up ejecting the planet out of the system, or on the contrary precipitating it into the star (Strugarek et al., 2017). Concerning (ii), because planets are easier to detect around non-accreting TTSs as a result of their lower level of variability, observation samples like that of MaTYSSE are naturally driven towards young TTSs whose accretion discs vanished early, i.e. at a time when their large-scale fields were still strong and their magnetospheric gaps large, and thus for which hJs had more chances to survive type-II migration. A more definite conclusion must wait for a complete analysis of the full MaTYSSE sample.

No hJ was found around V410 Tau, and our results exclude the presence of a $> 1\,M_{Jup}$ planet within a 0.1 au radius of the star at a 3σ-level. The formation and/or the migration of giant exoplanets was perhaps prevented by the very early depletion of the disc, which, in turn, could potentially be related to the M dwarf companion. To tie in to the previous paragraph, there might exist an optimal age to dissipate the disc for forming hJs, i.e. not before planets have had the time to grow, but not after the field has weakened, causing the magnetospheric gap to shrink. Our age estimates would place this optimum somewhere in 0.3 – 1 Myr, but statistically significant conclusions must wait for the results of many more large surveys, including the SPIRou (Spectropolarimetre InfraRouge) Legacy Survey (SLS), where ∼60 wTTSs are to be monitored in the near-infrared wavelength domain.

5.4 Future perspectives

Concerning the stars studied in this thesis, it will be interesting to analyze further RV curves of TAP 26, in order to better constrain the orbital period of the planet and make it stand out from the aliases caused by the sampling of the observations analyzed so far. V410 Tau is a very interesting target for the study of dynamo because of the wealth of data and studies published about it; in particular, on top of the 60-year-long photometric monitoring mentioned above, several Doppler maps have been reconstructed. A study compiling all the Doppler maps, put in parallel with the light curve of V410 Tau, would perhaps enable to learn more on the secular magnetic activity of this young and massive wTTS.

In the near future, completing the analysis of the MaTYSSE sample will help getting a better general picture of the magnetic topologies of wTTSs, and better understand their dynamos. The ongoing aforementioned SLS will include the observation of ∼60 wTTSs by high-resolution spectropolarimeter SPIRou, in the near-infrared wavelength domain, where the Zeeman effect is larger and thus the magnetic field can be reconstructed with more precision. This will also be an important addition to the statistical study of wTTS dynamos. Moreover, new imaging techniques that can reconstruct the intrinsic variability of the stellar surfaces are under development, which will enable to finely model the evolution of wTTS activity on month-long / year-long time scales.

The study of young planetary systems will also benefit from the completion of the MaTYSSE analysis and the SLS. With the ∼60-strong sample of the SLS, we will be able to draw more reliable

statistics from our young-hJ-seeking campaigns. Moreover, magnetic activity manifests differently in the spectra, and a fortiori in the RV curves, depending on wavelength, whereas hJ signatures do not. Therefore, adding infrared spectropolarimetric observations of planet-hosting stars that have been observed by ESPaDOnS and/or NARVAL would enable to confirm the planetary signatures in the RVs and better constrain them.

Transiting young giant planets have been detected in the past few years from K2 light curves (K2-33 b, Mann et al. 2016; David et al. 2016 and V1298 Tau b, c, d and e, David et al. 2019b), and observing them with SPIRou would potentially enable to measure their obliquity, and observe their atmoshere. With the arrival of more space-based photometry data for the detection of exoplanets (from the currently operating telescope TESS, or from the upcoming CHEOPS, PLATO and ARIEL), we can expect more transiting young giant planets to be detected. Characterizing their orbits and atmospheres thanks to both photometry data and spectroscopic monitoring, with for example SPIRou or the upcoming nIRPS to be placed in Chile, will be a huge step forward in the study of the early evolution of giant planets.

Conclusion et perspectives futures

Cette thèse a visé à apporter des contraintes observationnelles aux scénarios théoriques de formation et de migration des Jupiters chauds (hJs), en recherchant les hJs autour des étoiles T Tauri à raies faibles (wTTSs) et en caractérisant leurs propriétés orbitales. Afin de pouvoir détecter les signatures potentielles des hJs dans les vitesses radiales (RVs) de ces étoiles actives, une compréhension précise de leur activité est nécessaire afin de filtrer la perturbation en RV introduite par l'activité stellaire qui contribue aux variations de RV à un niveau typique de $1\,\mathrm{km\,s^{-1}}$. Nos observations contribuent également à contraindre les théories des dynamos stellaires, ainsi que les théories de la formation des étoiles / des planètes. Il est crucial de contraindre en parallèle les théories de la formation de hJ et de la formation stellaire, car les interactions étoile-planète jouent un rôle majeur dans l'évolution des deux corps et de l'ensemble du système.

Activité et champs magnétiques des wTTSs

Brillance et champs magnétiques à la surface des WTTSs

Nos résultats permettent de voir et de comparer les cartes de brillance et les topologies magnétiques de trois wTTSs de masses et d'âges différents. Les cartes de brillance de TAP 26, V410 Tau et V830 Tau montrent toutes une calotte polaire froide, comme les autres étoiles MaTYSSE LkCa 4 (Donati et al., 2014), Par 1379 (Hill et al., 2017) et V1095 Sco (Nicholson et al., 2018). Cependant, contrairement aux cartes peu complexes de LkCa 4, Par 1379 et V1095 Sco, nos étoiles présentent une distribution relativement étalée des taches et des plages à leur surface, comme les étoiles MaTYSSE Par 2244 (Hill et al., 2017) et TWA 6 (Hill et al., 2019). Tandis que TAP 26 et V830 Tau ont des cartes de luminosité avec une couverture en taches et plages de 10 – 12 %, les cartes de brillance de V410 Tau montrent une couverture plus large, 14 – 18 %, comparable à celles de Par 2244 et TWA 6. Trouver des tendances dans ces résultats n'est pas trivial, car V830 Tau, V410 Tau et Par 2244 sont jeunes ($\lesssim 2\,\mathrm{Myr}$) tandis que TAP 26 et TWA 6 sont plus évoluées ($> 15\,\mathrm{Myr}$), et TWA 6 est de masse similaire à TAP 26 et V830 Tau ($\sim 1\,\mathrm{M_\odot}$) alors que V410 Tau et Par 2244 sont plus massives (1.3 – $1.8\,\mathrm{M_\odot}$).

En ce qui concerne les topologies magnétiques (voir figure 3.21), V830 Tau a une topologie principalement poloïdale, dipolaire et axisymétrique, comme attendu pour cette étoile entièrement convective. TAP 26, d'autre part, révèle une topologie magnétique plutôt complexe, où le dipôle poloïdal ne constitue que 10 % de l'énergie magnétique alors que la composante toroïdale, contribuant à 30 % de l'énergie magnétique totale, est relativement élevée. Le niveau de complexité de la topologie du champ de TAP 26 n'est pas inattendu pour une étoile avec un noyau radiatif bien développé.

La topologie magnétique de V410 Tau présente cependant une topologie atypique pour une étoile entièrement convective, avec une forte composante toroïdale (50 % de l'énergie magnétique) qui maintient une orientation constante pendant les 8 années que couvrent nos données, ainsi qu'un champ poloïdal non axisymétrique. L'origine de cette forte composante toroïdale, également

observée pour la wTTS entièrement convective LkCa 4, de masse $0.79 \pm 0.05\,\mathrm{M}_\odot$, n'est pas claire. Peut-être cette forte énergie toroïdale provient-elle d'une dynamo non standard, ou des restes d'un cisaillement radial subsurfacique remontant à la phase cTTS, ou même d'une survie miraculeuse de l'énergie toroïdale primordiale produite après le deuxième effondrement du cœur pré-stellaire. Pour cette dernière hypothèse, la dissipation précoce du disque pourrait être une piste à explorer pour expliquer pourquoi une telle énergie toroïdale n'est pas observée sur les cTTSs.

Il est donc nécessaire de compléter l'analyse de l'échantillon MaTYSSE et d'analyser d'autres données, par exemple celles recueillies avec SPIRou, pour clarifier le panorama magnétique des wTTSs.

Variabilité intrinsèque de la brillance surfacique et des topologies magnétiques

Grâce à l'étendue de nos jeux de données, nous avons pu mettre en évidence la présence d'une variabilité intrinsèque de la distribution de brillance et de la topologie magnétique à la surface de nos trois cibles.

Mise en évidence en comparant la capacité de ZDI à ajuster des jeux de données plus longs par rapport à des jeux de données plus courts, même avec la modélisation de la rotation différentielle, cette variabilité intrinsèque a été étudiée grâce aux processus gaussiens. En ajustant les RVs, les courbes de lumière, la largeur équivalente (EW) de Hα et le champ longitudinal B_ℓ, nous avons obtenu des échelles de temps de variation de $\sim$130 d pour TAP 26, de $\sim$160 d pour les RVs de V410 Tau, et ≥ 250 d pour la magnitude V, la EW de Hα et le B_ℓ de V410 Tau. Ces quantités sont primordiales pour mesurer le niveau d'activité d'une étoile (pour la corrélation de B_ℓ avec l'activité stellaire, voir par exemple Hébrard et al., 2016), et notre étude de V410 Tau offre une comparaison entre elles sur un jeu de données spectropolarimétriques haute résolution de 144 spectres sur 8 ans. La période dérivée de la régression par processus gaussiens (GPR) sur nos RVs brutes est plus courte que la période photométrique trouvée par Stelzer et al. (2003) de 0.03 %, et est beaucoup plus proche de la période dérivée avec GPR de B_ℓ que de la période dérivée de la EW de Hα. Ceci montre que, pour l'étude des courbes RV, B_ℓ est dans ce cas un meilleur indicateur d'activité que Hα et que tous les indices d'activité ne sont pas égaux dans la mesure où ils peuvent nous renseigner sur les caractéristiques de surface affectant les courbes RV (voir aussi Haywood et al., 2016). Le temps caractéristique de variation intrinsèque associé aux RVs est beaucoup plus court que le temps caractéristique de rotation différentielle et que le temps caractéristique de variation intrinsèque de la magnitude V, ce qui suggère que les RVs sont plus sensibles aux taches de courte vie et de petite taille alors que la photométrie est plus sensible aux taches de longue vie et de grande taille. La EW de Hα et B_ℓ présentent également des temps caractéristiques longs, bien qu'avec des incertitudes trop grandes pour en tirer une conclusion définitive. Nous avons noté que le temps caractéristique de rotation différentielle de TAP 26 est proche de son échelle de temps de variabilité intrinsèque, alors qu'il est beaucoup plus long ($\sim$600 d) pour V410 Tau, au moins comparé à l'échelle de temps de variation des RVs.

Une nouvelle implémentation provisoire de ZDI, où une carte du taux de variation de la brillance est ajustée parallèlement à la brillance elle-même, a été appliquée à un jeu de données étendu de V410 Tau, avec des résultats mitigés : elle améliore considérablement χ^2_r (de $\chi^2_\mathrm{r} = 2.5$ avec ZDI classique à $\chi^2_\mathrm{r} = 1$ avec le nouveau ZDI) et les grandes tendances dans l'évolution de la courbe RV sont bien reproduites par rapport aux modèles ZDI classique pour chaque sous-ensemble et au modèle GPR, mais les résidus affichent toujours une valeur efficace significative de $\gtrsim 2\sigma$. Dans le futur, des méthodes cohérentes combinant le réalisme physique de ZDI et la flexibilité du GPR seront développées et appliquées à d'autres données MaTYSSE, ainsi qu'aux données de SPIRou (SpectroPolarimetre InfraRouge), le nouveau spectropolarimètre infrarouge installé au CFHT.

Rotation différentielle et dynamos des wTTSs

Nos résultats ont également apporté de nouvelles contraintes observationnelles sur la rotation différentielle des étoiles jeunes, nos trois cibles présentant un équateur tournant plus vite que les pôles, et TAP 26 ayant un niveau de rotation différentielle presque solaire (0.0492 ± 0.0010 rad/d). La rotation différentielle de V410 Tau est en moyenne beaucoup plus faible, de 0.0097 ± 0.0003 rad/d, c'est-à-dire 5 – 6 fois plus faible que celle du Soleil, les valeurs aux époques individuelles variant entre 8.1 ± 1.8 mrad/d et 19.0 ± 4.3 mrad/d. Peu de résultats observationnels ont été obtenus sur la rotation différentielle des wTTSs ; au sein de MaTYSSE, la jeune V830 Tau affiche une rotation différentielle de 17.2 ± 1.4 mrad/d, suggérant une tendance selon laquelle la rotation différentielle augmente avec l'âge, à mesure que le noyau radiatif se développe. Ceci est cohérent avec ce qui est observé pour les naines M (Morin et al., 2010).

La combinaison de notre estimation de la rotation différentielle et de la durée de 8 ans de notre jeu de données photométriques sur V410 Tau nous a permis de suivre l'évolution latitudinale des principales taches et plages année après année, et de constater qu'elles ont subi une migration vers les pôles depuis la latitude 0 en 2008 vers $\sim 50°$ en 2016. Cela rappelle le diagramme papillon solaire, quoique inversé, et suggère que la dynamo, si elle est cyclique, a une période d'au moins 8 yr et probablement beaucoup plus (16 yr si nos données couvrent seulement une moitié de cycle complet). Ceci s'accompagne d'une augmentation presque monotone de la force du dipôle poloïdal de ~ 200 à ~ 500 G. Cela montre au moins l'existence de variations à long terme sur la surface de V410 Tau. En outre, pour V410 Tau, le champ poloïdal double presque en intensité tout au long de notre observation, mais les mesures de $d\Omega$ sur des jeux de données annuels individuels ne montrent pas d'augmentation, ce qui, si nous supposons une dynamo cyclique, implique un déphasage entre le champ magnétique et la rotation différentielle. Les données photométriques des 60 dernières années montrent une évolution complexe de la courbe de lumière de V410 Tau, et des études antérieures ont montré des variations cycliques de l'amplitude et des extrema de la courbe de lumière (Stelzer et al., 2003; Sokoloff et al., 2008; Oláh et al., 2009; Grankin & Artemenko, 2009; Savanov, 2012; Hambálek et al., 2019), mais il reste à déterminer si V410 Tau a ou non un cycle complet avec inversion de polarité comme pour le Soleil.

Évolution du moment angulaire et durée de vie des disques pour les étoiles jeunes

Nous observons que les cTTSs à accrétion modérée ayant une forte composante dipolaire/poloïdale dans leurs champs magnétiques ont tendance à avoir des périodes de rotation autour de 6 – 9 d (Donati et al., 2008a, 2010a, 2012). En partant de cette hypothèse, nous avons calculé l'âge auquel nos wTTSs ont perdu leur couplage avec leurs disques (voir figure 3.2). Dans les deux cas, cette perte aurait été causée par l'épuisement du disque interne. Pour ce faire, nous avons utilisé les modèles d'évolution stellaire de Siess et al. (2000) pour extraire les moments d'inertie, et, en supposant que les wTTSs se sont contractées à moment angulaire constant après avoir été découplées de leur disque, nous avons dérivé leurs rayons au moment où leur rotation a commencé à accélérer. Les modèles d'évolution stellaire nous ont donné les âges correspondant à ces rayons.

V410 Tau est déjà l'une des plus jeunes wTTSs observées, mais son âge de dissipation du disque a été estimé à ~ 0.2 Myr, avec une précision relativement faible, d'après notre mesure du rayon stellaire, et corroboré par les topologies magnétiques que nous avons reconstruites à partir de nos spectres. Il s'agit d'un système à trois étoiles composé d'une binaire A-B centrale (rapport massique 0.2 ± 0.1, séparation projetée sur le ciel 16.8 ± 1.4 au) et d'une troisième composante C plus lointaine (rapport massique $0.08^{+0.10}_{-0.08}$, séparation projetée sur le ciel 36 ± 3 au). V410 Tau a été prise en compte dans l'étude de Kraus et al. (2012) montrant une corrélation entre la présence

d'un compagnon à moins de 50 au et l'épuisement précoce du disque d'accrétion ; nos mesures de l'âge de V410 Tau, notre estimation de son âge à la dissipation du disque et notre estimation de la séparation entre V410 Tau A-B (36 au) confirment la tendance trouvée par cette étude, et donnent des paramètres plus précis pour cet astre.

De plus, d'après la séparation orbitale du Jupiter chaud découvert dans le cadre de ce travail, on estime que TAP 26 a également perdu son disque à un âge inférieur à 1 Myr.

Les estimations de l'âge varient selon le modèle d'évolution choisi, mais les modèles plus récents (BHAC15, Baraffe et al. 2015, STAREVOL3.4, Amard et al. 2019) donnent des âges encore plus jeunes ($\sim$0.5, $\sim$13 et $\sim$1.5 Myr pour V410 Tau, TAP 26 et V830 Tau resp.) que les modèles de Siess et al. (2000), ce qui renforce la conviction que ces étoiles ont dissipé leurs disques en moins de 1 Myr. Cela place nos trois étoiles parmi les wTTSs qui ont perdu leurs disques à l'âge le plus précoce (Richert et al., 2018), et, par conséquent, elles sont parmi les wTTSs qui tournent le plus vite car leur rotation a commencé à accélérer tôt (Gallet & Bouvier, 2015).

Formation, migration, évolution ultérieure des Jupiter chauds

À ce jour, sept planètes géantes ont été détectées autour de wTTSs : V830 Tau b (Donati et al., 2016), K2-33 b(David et al., 2016), TAP 26 b et V1298 Tau b, c, d et e (David et al., 2019a), avec quelques autres planètes géantes chaudes candidates autour d'étoiles jeunes (par exemple CI Tau, Johns-Krull et al., 2016). V830 Tau b ($0.77 \pm 0.15\,M_{Jup}$, 4.93 ± 0.05 d) et TAP 26 b ($1.66 \pm 0.31\,M_{Jup}$, 10.79 ± 0.14 d) ont été découverts dans le cadre de MaTYSSE, tandis que K2-33 b et V1298 Tau b, c, d et e ont été détectés via leurs transits dans les courbes de lumière de leurs étoiles, et leurs masses ne sont pas encore bien contraintes. Bien qu'il ne s'agisse pas encore d'un échantillon statistiquement représentatif, nous pouvons tirer des conclusions importantes de ces premiers résultats :

- il est possible de former des hJs dans des échelles de temps aussi faibles que 2 Myr,
- V830 Tau b et TAP 26 b ont tous deux une orbite quasi-circulaire, ce qui favorise le scénario de migration planète-disque de type II plutôt que les interactions planète-planète suivies de la circularisation par effet de marées,
- avec deux détections dans un échantillon de $\sim$30 étoiles (dont les données n'ont pas toutes été analysées à ce jour), nous pouvons nous demander si (i) la fréquence des hJs est plus élevée autour des étoiles jeunes que des étoiles matures ($\simeq$1%, Wright et al., 2012), ou (ii) notre échantillon est biaisé vers des étoiles hôtes de hJs. Concernant (i), les hypothèses expliquant l'appauvrissement en hJs au fur et à mesure que l'étoile vieillit vers la séquence principale incluent les interactions de marée et magnétiques entre étoile et planètes, qui peuvent finir par éjecter la planète du système, ou au contraire la précipiter dans l'étoile (Strugarek et al., 2017). En ce qui concerne (ii), puisque les planètes sont plus faciles à détecter autour des TTS non accrétantes en raison de leur variabilité plus faible, les échantillons d'observation comme celui de MaTYSSE sont naturellement biaisés vers de jeunes TTS dont les disques d'accrétion ont disparu tôt, c'est-à-dire à un moment où leurs champs à grande échelle étaient encore forts et leurs cavités magnétosphériques importantes, et où les hJs avaient donc plus de chances de survivre à une migration de type-II. Une conclusion plus précise doit attendre une analyse complète de l'échantillon MaTYSSE.

Aucun hJ n'a été trouvé autour de V410 Tau, et nos résultats excluent la présence d'une planète $> 1\,M_{Jup}$ dans un rayon de 0.1 au autour de l'étoile, à un niveau de 3σ. La formation et/ou la migration d'exoplanètes géantes a peut-être été empêchée par l'épuisement très précoce du disque, qui, à son tour, pourrait être lié à la présence du compagnon de type naine M. Pour faire le lien avec le paragraphe précédent, il pourrait exister un âge optimal pour dissiper le disque afin de former des hJs, c'est-à-dire pas avant que les planètes aient eu le temps de grandir, mais pas après que le

champ se soit affaibli, ce qui causerait la réduction de la cavité magnétosphérique. Nos estimations de l'âge placeraient cet optimum quelque part dans la plage 0.3 – 1 Myr, mais des conclusions statistiquement significatives devront attendre les résultats de nombreuses autres études, y compris la SPIRou (Spectropolarimetre InfraRouge) Legacy Survey (SLS), qui prévoit l'observation de ∼60 wTTS dans le domaine de longueurs d'onde du proche infrarouge.

Perspectives d'avenir

Concernant les étoiles étudiées dans cette thèse, il sera intéressant d'analyser d'autres courbes de RV de TAP 26, afin de mieux contraindre la période orbitale de la planète et de la différencier des alias causés par l'échantillonnage des observations analysées jusqu'ici. V410 Tau est une cible très intéressante pour l'étude de la dynamo en raison de la richesse des données et des études publiées au sujet de cette étoile ; en particulier, en plus des observations photométriques sur 60 ans mentionnées ci-dessus, plusieurs cartes Doppler ont été reconstruites. Une étude compilant toutes les cartes Doppler, mises en parallèle avec la courbe de lumière de V410 Tau, permettrait peut-être d'en savoir plus sur l'activité magnétique séculaire de cette wTTS jeune et massive.

Dans un avenir proche, la complétion de l'analyse de l'échantillon MaTYSSE permettra d'obtenir une meilleure vision d'ensemble des topologies magnétiques des wTTSs et de mieux comprendre leurs dynamos. Le SLS mentionné ci-dessus inclura l'observation de ∼60 wTTSs par le spectropolarimètre à haute résolution SPIRou, dans le domaine de longueurs d'onde du proche infrarouge, où l'effet Zeeman est plus grand et donc le champ magnétique peut être reconstruit avec plus de précision. Ce sera également un ajout important à l'étude statistique des dynamos des wTTSs. De plus, de nouvelles techniques d'imagerie permettant de reconstituer la variabilité intrinsèque des surfaces stellaires sont en cours de développement, ce qui permettra de modéliser finement l'évolution de l'activité des wTTSs sur des échelles de temps de l'ordre du mois / de l'année.

L'étude des jeunes systèmes planétaires bénéficiera également de la complétion de l'analyse MaTYSSE et du SLS. Grâce à l'échantillon de ∼60 étoiles du SLS, nous serons en mesure de tirer des statistiques plus fiables de nos campagnes de recherche de jeunes hJs. De plus, l'activité magnétique se manifeste différemment dans les spectres, et a fortiori dans les courbes de RV, selon la longueur d'onde, alors que les signatures hJs ne varient pas. Par conséquent, l'ajout d'observations spectropolarimétriques infrarouges d'étoiles hôtes de planètes qui ont été observées par ESPaDOnS et/ou NARVAL permettrait de confirmer les signatures planétaires dans les RVs et de mieux les contraindre.

Des jeunes planètes géantes en transit ont été détectées ces dernières années à partir des courbes de lumière K2 (K2-33 b, Mann et al. 2016; David et al. 2016 et V1298 Tau b, c, d et e, David et al. 2019b), et leur observation avec SPIRou permettrait potentiellement de mesurer leur obliquité, et d'observer leur atmosphère. Avec l'arrivée d'un plus grand nombre de données photométriques spatiales pour la détection d'exoplanètes (provenant du télescope TESS actuellement en service ou des prochains CHEOPS, PLATO et ARIEL), on peut s'attendre à ce que davantage de jeunes planètes géantes en transit soient découvertes. La caractérisation de leurs orbites et de leurs atmosphères grâce aux données photométriques et aux observations spectroscopiques, avec par exemple SPIRou ou nIRPS qui sera placé au Chili, sera un grand pas en avant dans l'étude de l'évolution précoce des planètes géantes.

Bibliography

Adams, F. C., Lada, C. J., & Shu, F. H. 1987, ApJ, 312, 788

Affer, L., Micela, G., Favata, F., Flaccomio, E., & Bouvier, J. 2013, MNRAS, 430, 1433

Agnew, M. T., Maddison, S. T., & Horner, J. 2018, MNRAS, 477, 3646

Aigrain, S., Pont, F., & Zucker, S. 2012, MNRAS, 419, 3147

ALMA Partnership, Brogan, C. L., Pérez, L. M., et al. 2015, ApJ, 808, L3

Amard, L., Palacios, A., Charbonnel, C., et al. 2019, arXiv e-prints, arXiv:1905.08516

André, P. 2002, in EAS Publications Series, ed. J. Bouvier & J.-P. Zahn, Vol. 3, 1–38

André, P. 2015, Spectral Classification of Embedded Stars, Gargaud M. et al. (eds) Encyclopedia of Astrobiology (Springer, Berlin, Heidelberg), 2308

André, P., Di Francesco, J., Ward-Thompson, D., et al. 2014, in Protostars and Planets VI, ed. H. Beuther, R. S. Klessen, C. P. Dullemond, & T. Henning, 27

Andre, P., Ward-Thompson, D., & Barsony, M. 2000, in Protostars and Planets IV, ed. V. Mannings, A. P. Boss, & S. S. Russell, 59

Andrews, S. M., Rosenfeld, K. A., Kraus, A. L., & Wilner, D. J. 2013, ApJ, 771, 129

Armitage, P. J. 2018, A Brief Overview of Planet Formation, Handbook of Exoplanets, ISBN 978-3-319-55332-0. (Springer International Publishing AG, part of Springer Nature), 135

Bachiller, R. 1996, ARA&A, 34, 111

Baraffe, I., Homeier, D., Allard, F., & Chabrier, G. 2015, A&A, 577, A42

Barbato, D., Sozzetti, A., Desidera, S., et al. 2018, A&A, 615, A175

Baruteau, C., Bai, X., Mordasini, C., & Mollière, P. 2016, Space Sci. Rev., 205, 77

Baruteau, C., Barraza, M., Pérez, S., et al. 2019, MNRAS, 486, 304

Baruteau, C., Crida, A., Paardekooper, S.-J., et al. 2014, Protostars and Planets VI, 667

Batygin, K., Bodenheimer, P. H., & Laughlin, G. P. 2016, ApJ, 829, 114

Benz, A. O. 2017, Living Reviews in Solar Physics, 14, 2

Bessolaz, N., Zanni, C., Ferreira, J., Keppens, R., & Bouvier, J. 2008, A&A, 478, 155

Blinova, A. A., Romanova, M. M., & Lovelace, R. V. E. 2016, MNRAS, 459, 2354

Bobylev, V. V. 2014, Astrophysics, 57, 583

Bodenheimer, P. H. 2011, Principles of Star Formation (Springer-Verlag Berlin Heidelberg)

Bolmont, E. & Mathis, S. 2016, Celestial Mechanics and Dynamical Astronomy, 126, 275

Bontemps, S., Andre, P., Terebey, S., & Cabrit, S. 1996, A&A, 311, 858

Boss, A. P. 2009, ApJ, 697, 1940

Boss, A. P., Butler, R. P., Hubbard, W. B., et al. 2007, Transactions of the International Astronomical Union, Series A, 26A, 183

Bouvier, J. 2007, in IAU Symposium, Vol. 243, IAU Symposium, ed. J. Bouvier & I. Appenzeller, 231–240

Bouvier, J., Alencar, S. H. P., Boutelier, T., et al. 2007, A&A, 463, 1017

Bouvier, J. & Bertout, C. 1989, A&A, 211, 99

Bouvier, J., Bertout, C., & Bouchet, P. 1988, A&AS, 75, 1

Bouvier, J., Matt, S. P., Mohanty, S., et al. 2014, in Protostars and Planets VI, ed. H. Beuther, R. S. Klessen, C. P. Dullemond, & T. Henning, 433
Bouvier, J., Wichmann, R., Grankin, K., et al. 1997, A&A, 318, 495
Bouy, H. & Alves, J. 2015, A&A, 584, A26
Bradshaw, S. J. & Hartigan, P. 2014, ApJ, 795, 79
Brogi, M., Snellen, I. A. G., de Kok, R. J., et al. 2012, Nature, 486, 502
Brown, S. F., Donati, J.-F., Rees, D. E., & Semel, M. 1991, A&A, 250, 463
Brun, A. S. & Browning, M. K. 2017, Living Reviews in Solar Physics, 14, 4
Carroll, T. A., Strassmeier, K. G., Rice, J. B., & Künstler, A. 2012, A&A, 548, A95
Chandrasekhar, S. 1961, Hydrodynamic and hydromagnetic stability (Oxford: Clarendon)
Charbonneau, P. 2013, Solar and Stellar Dynamos, Saas-Fee Advanced Course
Chene, A.-N., Padzer, J., Barrick, G., et al. 2014, in Society of Photo-Optical Instrumentation Engineers (SPIE) Conference Series, Vol. 9151, Proc. SPIE, 915147
Chib, S. & Jeliazkov, I. 2001, Journal of the American Statistical Association, 96, 270
Cieza, L. A., Olofsson, J., Harvey, P. M., et al. 2013, ApJ, 762, 100
Claret, A. 2000, A&A, 363, 1081
Coleman, G. A. L., Papaloizou, J. C. B., & Nelson, R. P. 2017, MNRAS, 470, 3206
Collier Cameron, A. & Li, J. 1994, MNRAS, 269, 1099
Collier Cameron, A. & Robinson, R. D. 1989, MNRAS, 236, 57
Crockett, C. J., Mahmud, N. I., Prato, L., et al. 2012, ApJ, 761, 164
Crutcher, R. M. 2012, ARA&A, 50, 29
David, T. J., Cody, A. M., Hedges, C. L., et al. 2019a, AJ, 158, 79
David, T. J., Hillenbrand, L. A., Petigura, E. A., et al. 2016, Nature, 534, 658
David, T. J., Petigura, E. A., Luger, R., et al. 2019b, ApJ, 885, L12
Davies, C. L., Gregory, S. G., & Greaves, J. S. 2014, MNRAS, 444, 1157
Dawson, R. I. & Johnson, J. A. 2018, ARA&A, 56, 175
de Zeeuw, P. T., Hoogerwerf, R., de Bruijne, J. H. J., Brown, A. G. A., & Blaauw, A. 1999, AJ, 117, 354
Donati, J., Skelly, M. B., Bouvier, J., et al. 2010a, MNRAS, 409, 1347
Donati, J., Skelly, M. B., Bouvier, J., et al. 2010b, MNRAS, 402, 1426
Donati, J.-F. 2001, in Lecture Notes in Physics, Berlin Springer Verlag, Vol. 573, Astrotomography, Indirect Imaging Methods in Observational Astronomy, ed. H. M. J. Boffin, D. Steeghs, & J. Cuypers, 207–+
Donati, J.-F. 2003, in Astronomical Society of the Pacific Conference Series, Vol. 307, Astronomical Society of the Pacific Conference Series, ed. J. Trujillo-Bueno & J. Sanchez Almeida, 41–+
Donati, J.-F. & Brown, S. F. 1997, A&A, 326, 1135
Donati, J.-F., Collier Cameron, A., & Petit, P. 2003, MNRAS, 345, 1187
Donati, J.-F., Gregory, S. G., Alencar, S. H. P., et al. 2012, MNRAS, 425, 2948
Donati, J.-F., Gregory, S. G., Alencar, S. H. P., et al. 2013, MNRAS, 436, 881
Donati, J.-F., Hébrard, E., Hussain, G., et al. 2014, MNRAS, 444, 3220
Donati, J.-F., Hébrard, E., Hussain, G. A. J., et al. 2015, MNRAS, 453, 3706
Donati, J.-F., Howarth, I. D., Jardine, M. M., et al. 2006, MNRAS, 370, 629
Donati, J.-F., Jardine, M. M., Gregory, S. G., et al. 2008a, MNRAS, 386, 1234
Donati, J.-F., Mengel, M., Carter, B. D., et al. 2000, MNRAS, 316, 699
Donati, J.-F., Moutou, C., Farès, R., et al. 2008b, MNRAS, 385, 1179
Donati, J. F., Moutou, C., Malo, L., et al. 2016, Nature, 534, 662
Donati, J.-F., Semel, M., Carter, B. D., Rees, D. E., & Collier Cameron, A. 1997, MNRAS, 291, 658
Donati, J. F., Semel, M., & Praderie, F. 1989, A&A, 225, 467

Donati, J.-F., Yu, L., Moutou, C., et al. 2017, MNRAS, 465, 3343
Dong, R., Liu, S.-y., Eisner, J., et al. 2018, ApJ, 860, 124
Duchêne, G. & Kraus, A. 2013, ARA&A, 51, 269
Evans, Neal J., I., Dunham, M. M., Jørgensen, J. K., et al. 2009, ApJS, 181, 321
Fabrycky, D. C. & Winn, J. N. 2009, ApJ, 696, 1230
Feigelson, E. D., Jackson, J. M., Mathieu, R. D., Myers, P. C., & Walter, F. M. 1987, AJ, 94, 1251
Gaia Collaboration, Brown, A. G. A., Vallenari, A., et al. 2018, A&A, 616, A1
Gallet, F. & Bouvier, J. 2015, A&A, 577, A98
Galli, P. A. B., Loinard, L., Ortiz-Léon, G. N., et al. 2018, ApJ, 859, 33
Ghez, A. M., Weinberger, A. J., Neugebauer, G., Matthews, K., & McCarthy, Jr., D. W. 1995, AJ, 110, 753
Ghez, A. M., White, R. J., & Simon, M. 1997, ApJ, 490, 353
Ghosh, P. & Lamb, F. K. 1979, ApJ, 234, 296
Gilliland, R. L., Brown, T. M., Christensen-Dalsgaard, J., et al. 2010, PASP, 122, 131
Goodwin, S. P., Kroupa, P., Goodman, A., & Burkert, A. 2007, in Protostars and Planets V, ed. B. Reipurth, D. Jewitt, & K. Keil, 133
Grankin, K. N. 1998, Astronomy Letters, 24, 497
Grankin, K. N. 2013, Astronomy Letters, 39, 251
Grankin, K. N. & Artemenko, S. A. 2009, Information Bulletin on Variable Stars, 5907, 1
Grankin, K. N., Bouvier, J., Herbst, W., & Melnikov, S. Y. 2008, A&A, 479, 827
Gregory, S. G., Donati, J.-F., Morin, J., et al. 2012, ApJ, 755, 97
Gully-Santiago, M. A., Herczeg, G. J., Czekala, I., et al. 2017, ApJ, 836, 200
Hambálek, Ä., VaÅko, M., Paunzen, E., & Smalley, B. 2019, MNRAS, 483, 1642
Han, E., Wang, S. X., Wright, J. T., et al. 2014, PASP, 126, 827
Haywood, R. D. 2015, PhD thesis, University of St Andrews
Haywood, R. D., Collier Cameron, A., Queloz, D., et al. 2014, MNRAS, 443, 2517
Haywood, R. D., Collier Cameron, A., Unruh, Y. C., et al. 2016, MNRAS, 457, 3637
Hébrard, É. M., Donati, J.-F., Delfosse, X., et al. 2016, MNRAS, 461, 1465
Hennebelle, P. & Ciardi, A. 2009, A&A, 506, L29
Herbst, W. 1989, AJ, 98, 2268
Herczeg, G. J. & Hillenbrand, L. A. 2014, ApJ, 786, 97
Hill, C. A., Carmona, A., Donati, J.-F., et al. 2017, MNRAS, 472, 1716
Hill, C. A., Folsom, C. P., Donati, J. F., et al. 2019, MNRAS, 484, 5810
Holman, M. J., Fabrycky, D. C., Ragozzine, D., et al. 2010, Science, 330, 51
Huerta, M., Johns-Krull, C. M., Prato, L., Hartigan, P., & Jaffe, D. T. 2008, ApJ, 678, 472
Hussain, G. A. J., Jardine, M., & Collier Cameron, A. 2001, MNRAS, 322, 681
Ingleby, L., Calvet, N., Herczeg, G., & Briceño, C. 2012, ApJ, 752, L20
Johns-Krull, C. M. 2007, ApJ, 664, 975
Johns-Krull, C. M., McLane, J. N., Prato, L., et al. 2016, ApJ, 826, 206
Johns-Krull, C. M., Valenti, J. A., & Koresko, C. 1999, ApJ, 516, 900
Kennedy, G. M. & Kenyon, S. J. 2008, ApJ, 673, 502
Kenyon, S. J. & Hartmann, L. 1987, ApJ, 323, 714
Kenyon, S. J. & Hartmann, L. 1995, ApJS, 101, 117
Kounkel, M., Hartmann, L., Loinard, L., et al. 2017, ApJ, 834, 142
Kraus, A. L., Ireland, M. J., Hillenbrand, L. A., & Martinache, F. 2012, ApJ, 745, 19
Kraus, A. L., Ireland, M. J., Huber, D., Mann, A. W., & Dupuy, T. J. 2016, AJ, 152, 8
Kraus, A. L., Ireland, M. J., Martinache, F., & Hillenbrand, L. A. 2011, ApJ, 731, 8
Kurucz, R. 1993, CDROM # 13 (ATLAS9 atmospheric models) and # 18 (ATLAS9 and SYNTHE routines, spectral line database) (Smithsonian Astrophysical Observatory, Washington D.C.)

Lada, E. A. 1992, ApJ, 393, L25
Landi degl'Innocenti, E. & Landolfi, M. 2004, Polarisation in spectral lines (Dordrecht/Boston/London: Kluwer Academic Publishers)
Lanza, A. F. 2006, MNRAS, 369, 1773
Lin, D. N. C., Bodenheimer, P., & Richardson, D. C. 1996, Nature, 380, 606
Lucy, L. B. & Sweeney, M. A. 1971, AJ, 76, 544
Luhman, K. L., Allen, P. R., Espaillat, C., Hartmann, L., & Calvet, N. 2010, ApJS, 186, 111
Machida, M. N. & Basu, S. 2019, ApJ, 876, 149
Machida, M. N. & Matsumoto, T. 2011, MNRAS, 413, 2767
Madhusudhan, N. 2019, ARA&A, 57, 617
Maeder, A. 2009, Physics, Formation and Evolution of Rotating Stars (Springer)
Mahmud, N. I., Crockett, C. J., Johns-Krull, C. M., et al. 2011, ApJ, 736, 123
Mann, A. W., Newton, E. R., Rizzuto, A. C., et al. 2016, AJ, 152, 61
Masunaga, H. & Inutsuka, S.-i. 2000, ApJ, 531, 350
Maury, A. J., André, P., Hennebelle, P., et al. 2010, A&A, 512, A40
Maury, A. J., André, P., Testi, L., et al. 2019, A&A, 621, A76
Mayor, M. & Queloz, D. 1995, Nature, 378, 355
Meunier, N., Desort, M., & Lagrange, A.-M. 2010, A&A, 512, A39
Meunier, N., Mignon, L., & Lagrange, A. M. 2017, A&A, 607, A124
Mordasini, C. 2018, Planetary Population Synthesis, Handbook of Exoplanets, ISBN 978-3-319-55332-0. (Springer International Publishing AG, part of Springer Nature), 143
Morin, J., Donati, J., Petit, P., et al. 2010, MNRAS, 407, 2269
Moutou, C., Donati, J.-F., Savalle, R., et al. 2007, A&A, 473, 651
Narain, U. & Ulmschneider, P. 1996, Space Sci. Rev., 75, 453
Nguyen, D. C., Brandeker, A., van Kerkwijk, M. H., & Jayawardhana, R. 2012, ApJ, 745, 119
Nicholson, B. A., Hussain, G. A. J., Donati, J. F., et al. 2018, MNRAS, 480, 1754
Nomura, H., Tsukagoshi, T., Kawabe, R., et al. 2016, ApJ, 819, L7
Offner, S. S. R., Clark, P. C., Hennebelle, P., et al. 2014, in Protostars and Planets VI, ed. H. Beuther, R. S. Klessen, C. P. Dullemond, & T. Henning, 53
Oláh, K., Kolláth, Z., Granzer, T., et al. 2009, A&A, 501, 703
Ortiz-León, G. N., Loinard, L., Kounkel, M. A., et al. 2017, ApJ, 834, 141
Parker, E. N. 1955, ApJ, 122, 293
Pecaut, M. J. & Mamajek, E. E. 2013, ApJS, 208, 9
Pecaut, M. J. & Mamajek, E. E. 2016, MNRAS, 461, 794
Perrot, C. A. & Grenier, I. A. 2003, A&A, 404, 519
Perryman, M. 2011, The Exoplanet Handbook (Cambridge University Press)
Perryman, M. 2018, The Exoplanet Handbook (Cambridge University Press)
Petit, P., Donati, J.-F., Hébrard, E., et al. 2015, A&A, 584, A84
Pollacco, D. L., Skillen, I., Collier Cameron, A., et al. 2006, PASP, 118, 1407
Pollack, J. B., Hubickyj, O., Bodenheimer, P., et al. 1996, Icarus, 124, 62
Preibisch, T., Kim, Y.-C., Favata, F., et al. 2005, ApJS, 160, 401
Press, W. H., Teukolsky, S. A., Vetterling, W. T., & Flannery, B. P. 1992, Numerical recipes in FORTRAN. The art of scientific computing (Press Syndicate of the University of Cambridge)
Press, W. H., Teukolsky, S. A., Vetterling, W. T., & Flannery, B. P. 2007, Numerical recipes. The art of scientific computing. Third Edition (Cambridge University Press)
Rasmussen, C. E. & Williams, C. K. I. 2006, Gaussian Processes for Machine Learning (The MIT Press)
Raymond, S. N., Izidoro, A., & Morbidelli, A. 2018, arXiv e-prints, arXiv:1812.01033
Rebull, L. M., Wolff, S. C., & Strom, S. E. 2004, AJ, 127, 1029

Rice, J. B., Strassmeier, K. G., & Kopf, M. 2011, ApJ, 728, 69
Richert, A. J. W., Getman, K. V., Feigelson, E. D., et al. 2018, MNRAS, 477, 5191
Romanova, M. M., Ustyugova, G. V., Koldoba, A. V., & Lovelace, R. V. E. 2004, ApJ, 616, L151
Rydgren, A. E. & Vrba, F. J. 1983, ApJ, 267, 191
Savanov, I. S. 2012, Astronomy Reports, 56, 722
Schneider, J. 2018, Definition of Exoplanets and Brown Dwarfs, Handbook of Exoplanets, ISBN 978-3-319-55332-0. (Springer International Publishing AG, part of Springer Nature), 119
Schneider, J., Dedieu, C., Le Sidaner, P., Savalle, R., & Zolotukhin, I. 2011, A&A, 532, A79
Semel, M. 1989, A&A, 225, 456
Semel, M., Donati, J.-F., & Rees, D. E. 1993, A&A, 278, 231
Siess, L., Dufour, E., & Forestini, M. 2000, A&A, 358, 593
Skelly, M. B., Donati, J.-F., Bouvier, J., et al. 2010, MNRAS, 403, 159
Skilling, J. & Bryan, R. K. 1984, MNRAS, 211, 111
Skumanich, A. 1972, ApJ, 171, 565
Sokoloff, D. D., Nefedov, S. N., Ermash, A. A., & Lamzin, S. A. 2008, Astronomy Letters, 34, 761
Southworth, J. 2011, MNRAS, 417, 2166
Stelzer, B., Fernández, M., Costa, V. M., et al. 2003, A&A, 411, 517
Stelzer, B., Flaccomio, E., Briggs, K., et al. 2007, A&A, 468, 463
Strassmeier, K. G. 2009, A&ARv, 17, 251
Strugarek, A., Bolmont, E., Mathis, S., et al. 2017, ApJ, 847, L16
Valenti, J. A. & Fischer, D. A. 2005, ApJS, 159, 141
van Eyken, J. C., Ciardi, D. R., von Braun, K., et al. 2012, ApJ, 755, 42
Vaytet, N., Commerçon, B., Masson, J., González, M., & Chabrier, G. 2018, A&A, 615, A5
Vogt, S. S. & Penrod, G. D. 1983a, PASP, 95, 565
Vogt, S. S. & Penrod, G. D. 1983b, in Astrophysics and Space Science Library, Vol. 102, IAU Colloq. 71: Activity in Red-Dwarf Stars, ed. P. B. Byrne & M. Rodono, 379–385
Vogt, S. S., Penrod, G. D., & Hatzes, A. P. 1987, ApJ, 321, 496
Vrba, F. J., Herbst, W., & Booth, J. F. 1988, AJ, 96, 1032
Welty, A. D. & Ramsey, L. W. 1995, AJ, 110, 336
Wenger, M., Ochsenbein, F., Egret, D., et al. 2000, A&AS, 143, 9
White, R. J., Greene, T. P., Doppmann, G. W., Covey, K. R., & Hillenbrand, L. A. 2007, in Protostars and Planets V, ed. B. Reipurth, D. Jewitt, & K. Keil, 117
Williams, J. P. & Best, W. M. J. 2014, ApJ, 788, 59
Williams, J. P. & Cieza, L. A. 2011, ARA&A, 49, 67
Wilson, R. W., Jefferts, K. B., & Penzias, A. A. 1970, ApJ, 161, L43
Winn, J. N. & Fabrycky, D. C. 2015, ARA&A, 53, 409
Wright, J. T., Marcy, G. W., Howard, A. W., et al. 2012, ApJ, 753, 160
Wurster, J., Bate, M. R., & Price, D. J. 2018, MNRAS, 480, 4434
Xiao, H. Y., Covey, K. R., Rebull, L., et al. 2012, ApJS, 202, 7
Yadav, R. K., Christensen, U. R., Morin, J., et al. 2015, ApJ, 813, L31
Youdin, A. N. & Goodman, J. 2005, ApJ, 620, 459
Yu, L., Donati, J. F., Grankin, K., et al. 2019, MNRAS, 489, 5556
Yu, L., Donati, J.-F., Hébrard, E. M., et al. 2017, MNRAS, 467, 1342
Zanni, C. & Ferreira, J. 2013, A&A, 550, A99

List of Figures

List of Tables

A | Complements

A.1 Zeeman effect and polarimetry

We write the electric component of a monochromatic wave propagating in vacuum along direction z at angular frequency ω as:

$$\vec{\boldsymbol{E}} = \mathrm{Re}\left[\begin{pmatrix} E_{0,x}\mathrm{e}^{i(kz-\omega t+\phi_x)} \\ E_{0,y}\mathrm{e}^{i(kz-\omega t+\phi_y)} \\ 0 \end{pmatrix}\right] = \mathrm{Re}\left[\begin{pmatrix} E_{0,x}\mathrm{e}^{i\phi_x} \\ E_{0,y}\mathrm{e}^{i\phi_y} \\ 0 \end{pmatrix}\mathrm{e}^{i(kz-\omega t)}\right].$$

The vector defined in the (x, y) plane as $(E_{0,x}\mathrm{e}^{i\phi_x}, E_{0,y}\mathrm{e}^{i\phi_y})$ is called the Jones vector. We define:

$$\begin{aligned} E_{\leftrightarrow} &= E_{0,x}\exp^{i\phi_x} \\ E_{\updownarrow} &= E_{0,y}\exp^{i\phi_y} \\ E_{45^\circ} &= (E_{\leftrightarrow} + E_{\updownarrow})/\sqrt{2} \\ E_{-45^\circ} &= (E_{\leftrightarrow} - E_{\updownarrow})/\sqrt{2} \\ E_{\circlearrowleft} &= (E_{\leftrightarrow} - iE_{\updownarrow})/\sqrt{2} \\ E_{\circlearrowright} &= (E_{\leftrightarrow} + iE_{\updownarrow})/\sqrt{2} \end{aligned}$$

Noting $I_{\leftrightarrow} = |E_{\leftrightarrow}|^2, I_{\updownarrow} = |E_{\updownarrow}|^2, I_{45^\circ} = |E_{45^\circ}|^2, I_{-45^\circ} = |E_{-45^\circ}|^2, I_{\circlearrowleft} = |E_{\circlearrowleft}|^2, I_{\circlearrowright} = |E_{\circlearrowright}|^2$, the Stokes parameters I, Q, U and V are defined and represented schematically in figure A.1.

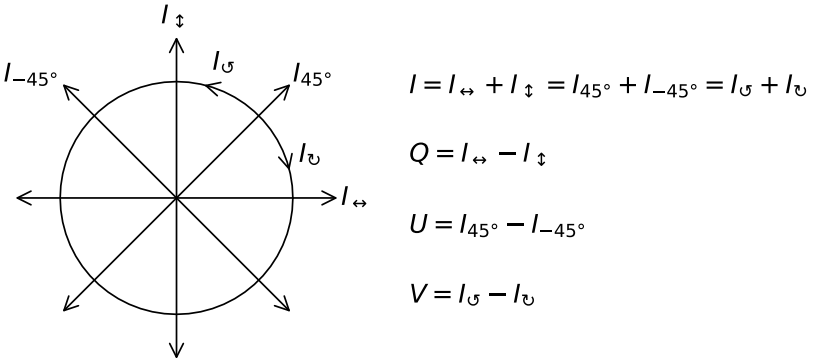

Figure A.1 – Stokes parameters and polarization. This convention considers that the observer is facing the source and $V > 0$ when the light wave propagates in a clockwise fashion as perceived by the observer.

The Zeeman effect The light associated to π and $\sigma_{b,r}$ transitions is polarized: for π, it vibrates along the same direction as $\vec{B}$ and for $\sigma_{b,r}$ the it vibrates circularly in the plane perpendicular to $\vec{B}$. If $\vec{B}$ points towards the observer, the polarization of the light associated with σ_b/σ_r transitions is positive/negative respectively. Thus, if $\vec{B}$ is aligned with the line of sight, π transitions are perceived as unpolarized and σ transtitions as circularly polarized, while, if $\vec{B}$ is perpendicular to the line of sight, π and σ transitions are perceived as linearly polarized.

Thus, if $\vec{B}$ is points towards the observer, then for a particular absorption line, the σ_b transitions will add a blueshifted absorption profile to $I_{\circlearrowleft}$ and the σ_r transitions a redshifted absorption profile to $I_{\circlearrowright}$, resulting in a net Stokes V profile as illustrated on figure A.2.

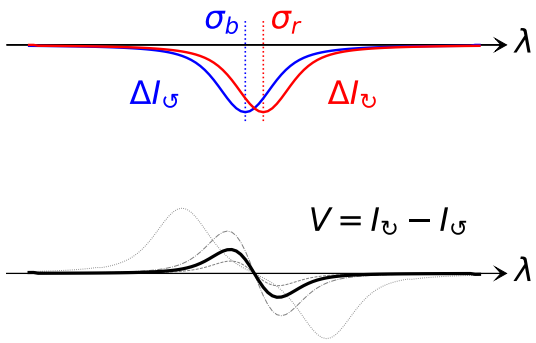

Figure A.2 – Stokes V line profile (black) in the presence of a magnetic field. Gray curves show how the Stokes V profiles would look under different intensities of magnetic field.

To produce unpolarized (Stokes I) and circularly polarized (Stokes V) spectra, ESPaDOnS and NARVAL use the double-beam method described in Donati et al. (1997) where the incident light beam is split into two beams that go through different optic paths, one from which $I_{\circlearrowleft}$ is measured and the other from which $I_{\circlearrowright}$ is measured. This is why there are two channels within each order in figure 2.1: they are the two beams after being reunited on the detector. To remove all spurious polarisation signatures at first order, each polarisation exposure sequence is a combination of 4 individual subexposures taken in different polarimeter configurations:

$$I = \sum_{1}^{4} I_{\circlearrowleft 1} + I_{\circlearrowright 1} + I_{\circlearrowleft 2} + I_{\circlearrowright 2} + I_{\circlearrowleft 3} + I_{\circlearrowright 3} + I_{\circlearrowleft 4} + I_{\circlearrowright 4},$$

$$V = I\frac{R-1}{R+1} \text{ where } R^4 = \frac{I_{\circlearrowleft 1}/I_{\circlearrowright 1}}{I_{\circlearrowleft 2}/I_{\circlearrowright 2}} \frac{I_{\circlearrowleft 4}/I_{\circlearrowright 4}}{I_{\circlearrowleft 3}/I_{\circlearrowright 3}}.$$

ESPaDOnS and NARVAL can also produce Q and U spectra following the same principle.

A.2 Least-Squares Deconvolution

Each spectral line of the observed spectra is affected by the characteristics of the corresponding chemical element and atomic transition, as well as by the distribution of RV, brightness and magnetic field at the surface of the star. Some particular lines trace particular phenomena, but for a large number of lines (Fe I lines for example, which are very numerous in wTTSs optical spectra), only the depth and Landé factor differ and the lines are otherwise affected the same way by the distribution of RV, brightness and magnetic field. A way to gather the information on those distributions within a compact form of data is thus to build an average line profile, which is representative of the way all those spectral lines were distorted in order to add up information from all spectral lines and boost the resulting S/N of both Stokes I and V LSD profiles.

The technique used in this study is called Least-Squares Deconvolution (LSD, see Donati et al., 1997). As its name spells it, it deconvolves the spectrum by a spectral mask and selects the kernel that yields the lowest χ^2_r fit. The weight of each line in the mask is proportional to the product of its wavelength, depth and Landé factor, so that the convolution between the final LSD profile and the mask should fit the shape of the observed spectrum at the locations of the used spectral lines. This process takes into account the way the Doppler effect varies with source wavelength, and removes the linear dependency of the Doppler broadening with the wavelength, which results in a LSD profile whose x-axis is directly the RV (see figure A.3).

The spectral masks, or line lists, employed in his thesis for LSD are computed from an ATLAS9 LTE model atmosphere (Kurucz, 1993) featuring adapted values of $T_{\rm eff}$ and $\log g$. Only moderate to strong atomic spectral lines are included in these lists (see e.g. Donati et al., 2010a, for more details). Altogether, about 7,800 spectral features (with about 40% from Fe I) are used.

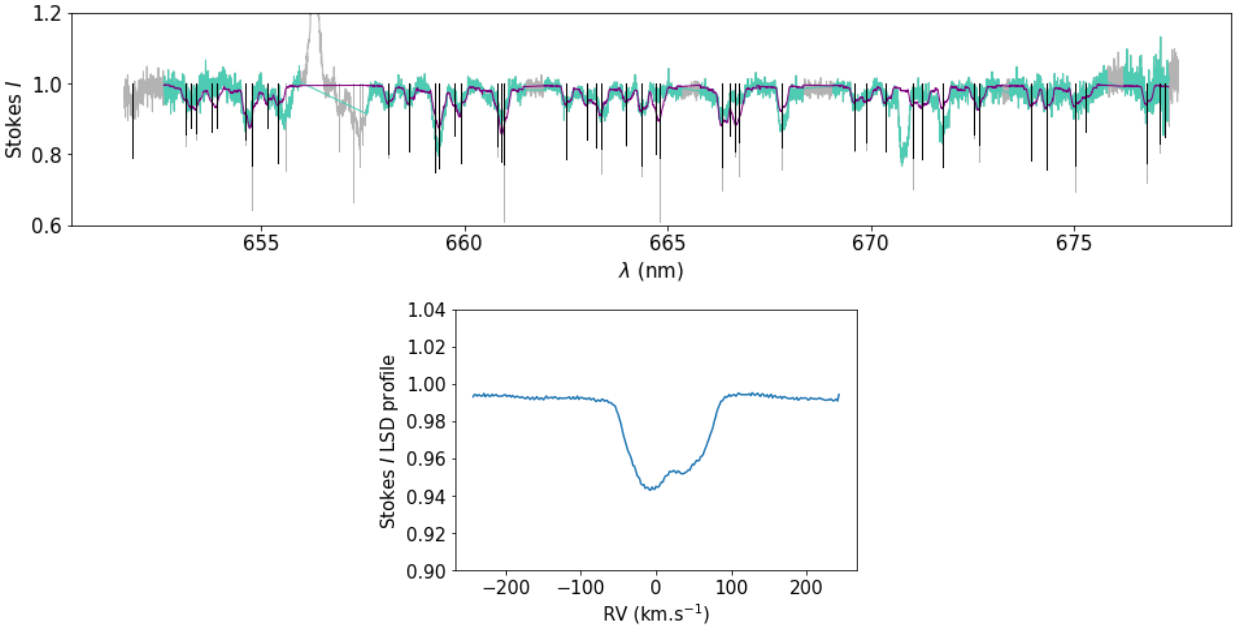

Figure A.3 – *Top*: order 27 of Stokes I observation of TAP 26 on 2017 Jan 20, with the spectrum in gray, the extracted part to be used for deconvolution in cyan, the complete list of atomic lines in gray, the lines selected for the deconvolution (the spectral mask) in black, and the model spectrum (i.e. the convolution of the LSD profile by the spectral mask) in purple. The length of the gray lines are proportional to their depth times their Landé factor times their wavelength, whereas the length of the black lines are proportional to their weight in the deconvolution. We note that the Hα line at $\lambda = 656.3$ nm was ignored for the deconvolution, and that the Lithium line at $\lambda = 670.7$ nm was not included in the spectral mask. We show only one spectral order, but LSD is applied to the whole spectrum at once. *Bottom*: LSD profile for this observation.

A.3 Zeeman-Doppler Imaging: stellar tomography

We apply a technique called Zeeman-Doppler Imaging (ZDI) to time series of LSD Stokes I and Stokes V profiles in order to reconstruct brightness and magnetic surface maps of the observed wTTSs. The details of ZDI were first described in papers Semel (1989), Donati et al. (1989), Semel et al. (1993), Brown et al. (1991) and Donati & Brown (1997), and successive improvements are described in Donati (2001), Donati et al. (2014). We provide here a simplified explanation adapted to the use we made of it.

ZDI takes inspiration from medical tomography, which consists of constraining a 3D distribution using series of 2D projections as seen from various angles. In our context, ZDI inverts simultaneous time series of 1D Stokes I and V LSD profiles into 2D brightness and magnetic field maps of the stellar surface. That is to say, ZDI looks for a solution $\mathcal{I}$ to the problem

$$\mathcal{D} = f(\mathcal{I}) + \epsilon,$$

where $\mathcal{D}$ represents the time series of Stokes I and Stokes V observations, f represents the ZDI direct process, $\mathcal{I}$ represents the brightness and magnetic maps and ϵ is noise.

The following section describes the model $\mathcal{I}$ and the direct process f, and the one after it explains the inversion process.

A.3.1 Model

The ZDI model $\mathcal{I}$ consists of a cell-covered truncated sphere, representing the part of a stellar surface which can be visible from Earth (see figure 2.5): with $\boldsymbol{i}$ the user-provided **inclination**, i.e. the angle between the rotation axis and the line of sight, the sphere is truncated at latitude $-i$. That surface is covered with a user-provided number of cells $\boldsymbol{n_{\mathrm{cell}}}$, organized in latitude rings. The number of latitude rings, the width of each ring and the number of cells per ring are computed so as to make the projected area of the cells facing the observer as homogeneous as possible. Each cell has a local brightness value as well as a local magnetic field expressed as the sum of its radial, meridional and azimuthal components.

We note that, while the brightness value can vary freely from cell to cell, the global magnetic field of the star is expressed as the sum of its poloidal and toroidal components, which in turn are expressed as spherical harmonics expansions, up to a user-provided maximum order $\boldsymbol{\ell_{\mathrm{max}}}$, and the projections of the field onto spherical coordinates are computed from there, as detailed in Donati et al. 2006 (section 5.1). This means that $\mathcal{I}$ is a vector of $n_{\mathrm{cell}} + 3\ \ell_{\mathrm{max}}(\ell_{\mathrm{max}} + 2)$ coefficients.

From these brightness and magnetic maps, ZDI computes synthetic Stokes I and Stokes V profiles of a model spectral line, of given wavelength λ_0, Landé factor g, width and depth, by adding the contributions of all visible cells. To compute the contribution of each cell to an observation, ZDI takes as input the **timestamp** of the observation, expressed in units of rotation cycles, the **differential rotation parameters**, the rotation-induced Doppler broadening, written $\boldsymbol{v \sin i}$ (where v is the equatorial rotation velocity), and the line-of-sight-projected proper motion of the star (or bulk radial velocity), $\boldsymbol{v_{\mathrm{rad}}}$. Here, we used a two-parameter sine-squared model for the differential rotation (Donati et al., 2000):

$$\Omega(\theta) = \Omega_{\mathrm{eq}} - (\sin\theta)^2 d\Omega, \tag{A.1}$$

where Ω is the rotation rate, θ is the latitude, Ω_{eq} is the rotation rate of the equator and $d\Omega$ is the difference between equatorial and polar rotation rates. In this work, the timestamps given to ZDI were expressed in rotational cycles (see for example ephemeris 3.1), so the differential rotation parameters were $(\boldsymbol{\beta}, \boldsymbol{\gamma})$ rather than $(\boldsymbol{\Omega_{\mathrm{eq}}}, \boldsymbol{d\Omega})$, where $\beta = 1 - \Omega_{\mathrm{eq}}/\Omega_0$ and $\gamma = d\Omega/\Omega_0$, with Ω_0 the reference rotation rate used to compute the rotational cycles.

ZDI first computes the position of each cell depending on the timestamp and the differential rotation (arranging the cells into latitude rings greatly simplifies this step), then the sky-projected area, limb darkening factor and local RV of each cell. For the limb darkening, we used the linear law (for more information on limb darkening, see for example Claret, 2000):

$$I = I_0(1 - \epsilon(1 - \mu)), \tag{A.2}$$

where μ is the cosine of the limb angle (between the line of sight and the normal to the surface, with $\mu = 1$ at the center of the visible disc), and ϵ was set at 0.75 for the stars studied in this thesis. In our ZDI version, the RV of each cell is computed from $v \sin i$ and v_{rad} as:

$$\mathrm{RV}(\theta, \phi) = v \sin i \sin\phi \cos\theta + v_{\mathrm{rad}}, \tag{A.3}$$

where ϕ is the azimuth of the cell ($\phi = 0$ corresponds to the meridian facing the observer). Thus ZDI takes into account only the stellar proper motion and solid-body rotation into the computation of the local RV, and not the differential rotation, stellar pulsations, convection or any other effects.

This means that when projected onto the sky plane, the iso-RVs appear parallel to the rotation axis (see figure 2.5).

The contribution of each cell is its local line profile, weighted by its brightness value, sky-projected area and limb darkening factor, and Doppler-shifted according to its RV. The local Stokes I and Stokes V profiles are computed following Unno-Rachkovsky's analytical solution to the polarised radiative transfer equations in a Milne-Eddington model atmosphere (Landi degl'Innocenti & Landolfi, 2004), from pre-defined global line properties (wavelength, Landé factor, depth, width) and from the local magnetic field. All the individual contributions are thus summed into integrated Stokes I and Stokes V profiles, which are then normalized so as to bring the continuum in the Stokes I profiles to 1.

Unno-Rachkovsky's analytical solution to the polarised radiative transfer equations in a Milne-Eddington model atmosphere is (normalized solution):

$$
\begin{aligned}
I &= \frac{\beta\mu(\eta_I+1)}{\Delta(\beta\mu+1)}\Big((\eta_I+1)^2+\rho_Q^2+\rho_U^2+\rho_V^2\Big)+\frac{1}{\beta\mu+1}\\
Q &= -\frac{\beta\mu}{\Delta(\beta\mu+1)}\Big((\eta_I+1)^2\eta_Q+(\eta_Q\rho_Q+\eta_U\rho_U+\eta_V\rho_V)\rho_Q-(\eta_I+1)(\eta_U\rho_V-\eta_V\rho_U)\Big)\\
U &= -\frac{\beta\mu}{\Delta(\beta\mu+1)}((\eta_I+1)^2\eta_U+(\eta_Q\rho_Q+\eta_U\rho_U+\eta_V\rho_V)\rho_U-(\eta_I+1)(\eta_V\rho_Q-\eta_Q\rho_V))\\
V &= -\frac{\beta\mu}{\Delta(\beta\mu+1)}((\eta_I+1)^2\eta_V+(\eta_Q\rho_Q+\eta_U\rho_U+\eta_V\rho_V)\rho_V)
\end{aligned}
$$

where

$$
\begin{aligned}
\eta_I &= \frac{\eta}{2}\left(h_\pi(\sin\gamma)^2+\frac{h_{\sigma,\mathrm{red}}+h_{\sigma,\mathrm{blue}}}{2}\Big((\cos\gamma)^2+1\Big)\right)\\
\eta_Q &= \frac{\eta}{2}\left(h_\pi-\frac{h_{\sigma,\mathrm{red}}+h_{\sigma,\mathrm{blue}}}{2}\right)(\sin\gamma)^2\cos 2\chi\\
\eta_U &= \frac{\eta}{2}\left(h_\pi-\frac{h_{\sigma,\mathrm{red}}+h_{\sigma,\mathrm{blue}}}{2}\right)(\sin\gamma)^2\sin 2\chi\\
\eta_V &= \frac{\eta}{2}(h_{\sigma,\mathrm{red}}-h_{\sigma,\mathrm{blue}})\cos\gamma\\
\rho_Q &= \eta\left(f_\pi-\frac{f_{\sigma,\mathrm{red}}+f_{\sigma,\mathrm{blue}}}{2}\right)(\sin\gamma)^2\cos 2\chi\\
\rho_U &= \eta\left(f_\pi-\frac{f_{\sigma,\mathrm{red}}+f_{\sigma,\mathrm{blue}}}{2}\right)(\sin\gamma)^2\sin 2\chi\\
\rho_V &= \eta(f_{\sigma,\mathrm{red}}-f_{\sigma,\mathrm{blue}})\cos\gamma\\
\Delta &= (\eta_I+1)^2\Big((\eta_I+1)^2-\eta_Q^2-\eta_U^2-\eta_V^2+(\rho_Q^2+\rho_U^2+\rho_V^2)\Big)-(\eta_Q\rho_Q+\eta_U\rho_U+\eta_V\rho_V)^2
\end{aligned}
$$

where β is the Milne-Eddington parameter (slope of the Planck function with respect to t_c, the continuum optical depth measured along the vertical), μ is the cosine of the limb angle, η is the ratio between line and continuum absorption coefficients, and γ and χ are respectively the inclination and azimuth angles of the magnetic field. h_π, $h_{\sigma,\mathrm{red}}$ and $h_{\sigma,\mathrm{blue}}$ are Voigt functions and f_π, $f_{\sigma,\mathrm{red}}$ and $f_{\sigma,\mathrm{blue}}$ are Faraday-Voigt functions, of damping constant 0.95 for the stars studied in this thesis; the shift in reduced wavelength is $4.67\times10^{-12}\times\frac{\lambda_0^2 gB}{\Delta\lambda}$ (with $\Delta\lambda$ equal to 40×10^{-4} nm for the stars studied in this thesis).

In short, ZDI:

- assumes a chemically homogeneous photosphere,
- considers small-scale RV dispersion to be the same everywhere on the photosphere (same local profile before application of the Zeeman effect),

◦ considers macro-RV dispersion being driven uniquely by stellar solid-body rotation (iso-RVs are parallel to the sky-projected rotation axis).

This choice is justified for the study of wTTSs because their $v \sin i$ is usually of the order of several tens of $\mathrm{km\,s^{-1}}$, making the stellar rotation a largely dominant factor in the dispersion of RV within the visible disc.

To sum things up,

f depends on:	$\mathcal{I}$ has:
- the number n_{cell} of cells covering the visible surface, - the timestamps of the spectropolarimetric observations, - the maximum spherical harmonics order $\ell_{\max}$, - the characteristics of the intrinsic line profile, - the inclination i of the rotation axis with respect to the line of sight, - $\beta = 1 - \Omega_{\mathrm{eq}}/\Omega_0$, - $\gamma = d\Omega/\Omega_0$, - the line-of-sight-projected equatorial rotation velocity $v \sin i$, - the line-of-sight-projected stellar proper motion v_{rad}.	- n_{cell} free parameters for the brightness - 3 $\ell_{\max}(\ell_{\max}+2)$ free parameters for the magnetic field.

A.3.2 Inversion algorithm

To invert Stokes I and Stokes V profiles into brightness and magnetic maps, ZDI follows a maximum entropy image reconstruction algorithm heavily inspired from Skilling & Bryan (1984). This algorithm relies on two quantities respectively called the reduced chi-square and the entropy.

$$\chi^2_{\mathrm{r}} = \frac{1}{N_{\mathrm{obs}}} \sum_{k=1}^{N_{\mathrm{obs}}} \frac{(F_k - D_k)^2}{\sigma_k^2} \tag{A.4}$$

is the reduced chi-square and is used to compare a series of observations $(D_k)_k$, with error bars $(\sigma_k)_k$, to a model $(F_k)_k$. If $\chi^2_{\mathrm{r}} = 1$, it is said the model fits the observations down to the noise level. In our case, F represents the ZDI synthetic profiles $f(\mathcal{I})$, D represents the observed profiles $\mathcal{D}$ and N_{obs} is the total number of points in $\mathcal{D}$.

$$S = \sum_{j=1}^{n_{\mathrm{tot}}} w_j S_j \tag{A.5}$$

is the information entropy of a model where w_j and S_j are respectively the weight and the entropy of the j-th model parameter. Here n_{tot} is the number of model parameters ($n_{\mathrm{cell}} + 3\ \ell_{\max}(\ell_{\max}+2)$). For the brightness cells, $S_j = -Q_j(\log(Q_j/A) - 1)$ is the Shannon entropy and the weights w_j are proportional to the cell area and to a user-provided ratio wcb between brightness entropy and magnetic entropy. For the magnetic field coefficients, $S_j = \sqrt{\alpha_j^2 + B^2} - B - \alpha_j \log\left(\frac{\sqrt{\alpha_j^2+B^2}+\alpha_j}{B}\right)$ and the weights are $w_j = 3\ell$ for the $2\ell_{\max}(\ell_{\max}+2)$ poloidal field coefficients, and $w_j = \ell$ for the $\ell_{\max}(\ell_{\max}+2)$ toroidal field coefficients (see also Brown et al., 1991; Hussain et al., 2001, section 2.1). According to Shannon's information theory, the level of information within a model decreases as its entropy increases.

Reduced chi-square and entropy can be defined slightly differently in other data analysis works, so we warn the reader not to immediately assume these exact expressions when encountering these quantities elsewhere.

For a high enough given $\chi^2_{\mathrm{r,aim}}$, there are often many solutions that can fit a time-series of Stokes I and Stokes V observations down to $\chi^2_{\mathrm{r}} = \chi^2_{\mathrm{r,aim}}$. Among all of them, ZDI looks for the one that maximizes S (for proof of unicity, see Skilling & Bryan, 1984). That model thus bears an amount of information as low as possible while still fitting the data, which makes it the most reliable. To find that model, ZDI uses a conjugate gradient algorithm to iteratively decrease χ^2_{r} towards $\chi^2_{\mathrm{r,aim}}$ while increasing S. At each step, ZDI:

- synthesizes Stokes I and Stokes V profiles for all observation dates from the current model,
- computes χ^2_{r}, S and their gradients,
- modifies the brightness and magnetic maps accordingly.

The algorithm is initialized with a user-provided default brightness and an initial magnetic field strength (shared among all the spherical harmonics modes), and converges when $\chi^2_{\mathrm{r,aim}}$ is reached and the gradients of χ^2_{r} and S are parallel.

A.4 Velocimetry method for the detection of hJs around wTTSs

This section gives the equation of RVs for a star around which a planet orbits on an elliptical orbit (see figure A.4), as a function of the planet mass and orbital parameters.

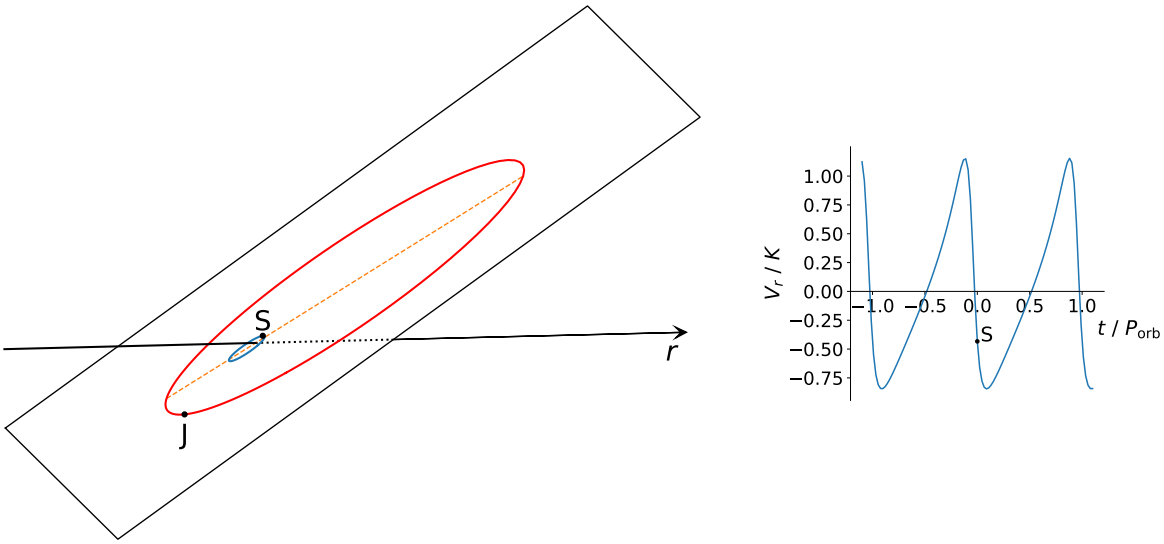

Figure A.4 – *Left:* orbits of a star S and of its hJ J around an assumedly immobile barycenter, in blue and red respectively. The r-axis represents the line of sight. The apsides line is plotted as an orange dashed line. *Right:* RV curve of the star S as a function of time t. K is the semi-amplitude of the RV modulations while P_{orb} is the orbital period.

To obtain the exact equation of V_r, the RV of the star, as a function of time t, we define notations as illustrated in figure A.5: the line of sight is called the r-axis, the acute angle between the r-axis and the normal to the orbit plane is called i, and (x, y) is an orthonormal coordinate

system of the orbit plane where the x-axis is perpendicular to the r-axis and is used as the reference for the polar coordinates system in the orbit plane.

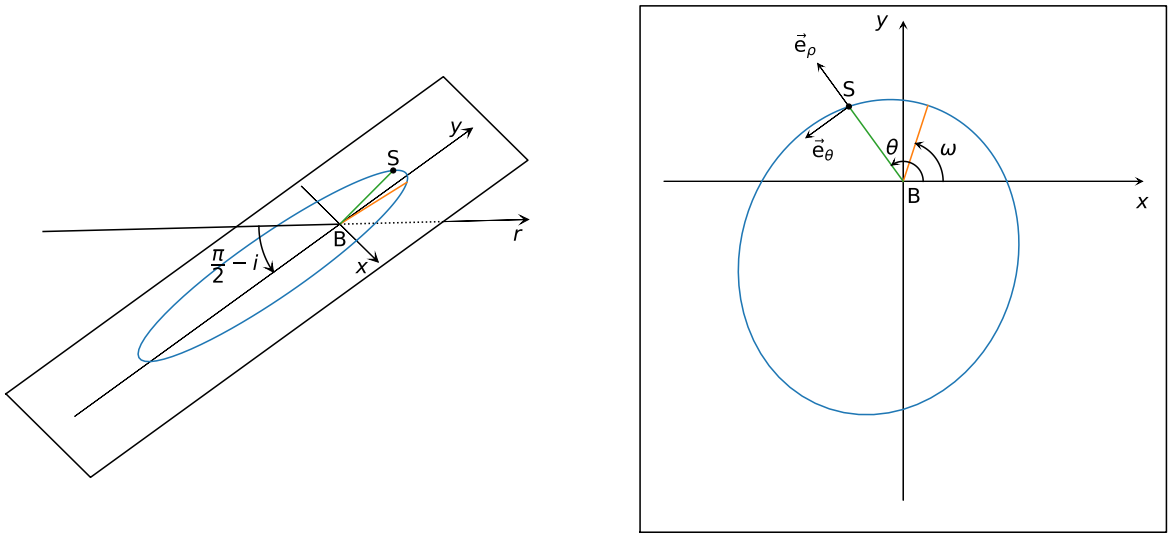

Figure A.5 – Orbit of a star S around an assumedly immobile barycenter B. *Left:* the r-axis represents the line of sight. The x-axis is the intersection between the sky plane and the orbit plane; it is perpendicular to the r-axis. (x, y) is an orthonormal coordinate system of the orbit plane. *Right:* polar coordinates in the orbit plane: ω is the argument of the periapsis, $(\vec{e}_\rho, \vec{e}_\theta)$ is the polar orthonormal base associated with the position of S.

We can derive from the laws of motion (see for example Perryman, 2011) that the orbit of the star verifies, in polar coordinates in the orbital plane:

$$\rho = \frac{p}{1 + e\cos(\theta - \omega)} \quad \text{where} \quad p = a(1 - e^2), \tag{A.6}$$

$$\rho^2\dot{\theta} = C \quad \text{where} \quad \dot{\theta} \equiv \frac{\partial\theta}{\partial t} \quad \text{and} \quad C \equiv \frac{2\pi a^2\sqrt{1-e^2}}{P_{\rm orb}}, \tag{A.7}$$

$$P_{\rm orb} = \frac{2\pi(M_\star + M_{\rm J})}{\sqrt{\mathcal{G}}}\left(\frac{a}{M_{\rm J}}\right)^{3/2} \simeq \frac{2\pi M_\star}{\sqrt{\mathcal{G}}}\left(\frac{a}{M_{\rm J}}\right)^{3/2} \quad \text{for } M_J \ll M_\star \tag{A.8}$$

with a the semi-major axis of the elliptic orbit of the star, $e \in [0; 1[$ its eccentricity, ω the argument of its periapsis, $P_{\rm orb}$ the orbital period, $\mathcal{G}$ the gravitational constant, and $M_\star$ and $M_{\rm J}$ the masses of the star and of the hJ respectively.

At time t, the position of the star S with respect to barycenter B is:

$$\overrightarrow{BS}(t) = \rho(t)\ \vec{e}_\rho(t),$$

therefore, with $\overrightarrow{V}_{\rm B}$ the constant velocity of B, the velocity of the star is:

$$\begin{aligned}
\overrightarrow{V}_\star &= \dot\rho\ \vec e_\rho + \rho\ \dot{\vec e}_\rho + \overrightarrow{V}_{\rm B} \\
\overrightarrow{V}_\star &= \frac{pe\dot\theta\sin(\theta-\omega)}{\big(1+e\cos(\theta-\omega)\big)^2}\ \vec e_\rho + \rho\dot\theta\ \vec e_\theta + \overrightarrow{V}_{\rm B} \qquad \text{(using A.6)} \\
\overrightarrow{V}_\star &= \frac{peC\sin(\theta-\omega)}{\rho^2\big(1+e\cos(\theta-\omega)\big)^2}\ \vec e_\rho + \frac{C}{\rho}\ \vec e_\theta + \overrightarrow{V}_{\rm B} \qquad \text{(using A.7)} \\
\overrightarrow{V}_\star &= \frac{eC\sin(\theta-\omega)}{p}\ \vec e_\rho + \frac{C\big(1+e\cos(\theta-\omega)\big)}{p}\ \vec e_\theta + \overrightarrow{V}_{\rm B} \qquad \text{(using A.6).}
\end{aligned}$$

To project on the line of sight and obtain $V_r = \overrightarrow{V}_\star \cdot \vec e_r$, we use:

$$\begin{aligned}
\vec e_\rho \cdot \vec e_r &= (\cos\theta\ \vec e_x + \sin\theta\ \vec e_y)\cdot\vec e_r = \sin\theta(\vec e_y\cdot\vec e_r) = \sin\theta\sin i \\
\vec e_\theta \cdot \vec e_r &= (-\sin\theta\ \vec e_x + \cos\theta\ \vec e_y)\cdot\vec e_r = \cos\theta(\vec e_y\cdot\vec e_r) = \cos\theta\sin i.
\end{aligned}$$

Finally:

$$\begin{aligned}
V_r &= \frac{eC\sin(\theta-\omega)}{p}\sin\theta\sin i + \frac{C\big(1+e\cos(\theta-\omega)\big)}{p}\cos\theta\sin i + V_{r,\rm B} \\
&= \frac{C\sin i}{p}\Big(e\big(\sin(\theta-\omega)\sin\theta + \cos(\theta-\omega)\cos\theta\big) + \cos\theta\Big) + V_{r,\rm B} \\
&= \frac{C\sin i}{p}\big(e\cos(\omega) + \cos\theta\big) + V_{r,\rm B} \\
&= \frac{2\pi a^2\sqrt{1-e^2}}{P_{\rm orb}}\frac{\sin i}{a(1-e^2)}\big(e\cos(\omega)+\cos\theta\big) + V_{r,\rm B} \\
V_r &= K\big(e\cos(\omega)+\cos\theta\big) + V_{r,\rm B} \quad \text{with } K \equiv \frac{2\pi a\sin i}{P_{\rm orb}\sqrt{1-e^2}}.
\end{aligned} \tag{A.9}$$

The dependency of θ with time is given by:

$$\theta(t) = \begin{cases} \omega + 2\tan^{-1}\left(\sqrt{\dfrac{1+e}{1-e}}\tan\left(\dfrac{E(t)}{2}\right)\right) & \text{for } E \neq \pi[2\pi], \\ \omega+\pi & \text{otherwise} \end{cases}$$

where $E(t)$ is the solution of

$$E - e\sin E = 2\pi(t/P_{\rm orb} - \phi),$$

with ϕ depending on the choice for the origin of time. E is called the eccentric anomaly.

Fitting such a curve into RV data points therefore requires to optimize the 6 parameters K, $P_{\rm orb}$, e, ω, ϕ and $V_{r,\rm B}$. For a circular orbit, $e = 0$ and we can set ω arbitrarily, so, choosing $\omega = 0$:

$$V_r = K\cos\left(2\pi\left(\frac{t}{P_{\rm orb}} - \phi\right)\right) + V_{r,\rm B},$$

which leaves 4 parameters to optimize: K, $P_{\rm orb}$, ϕ and $V_{r,\rm B}$.

For a Jupiter-size planet around a solar-size star, $M_J/M_\star \simeq 10^{-3}$ so we consider that $M_J \ll M_\star$

and derive information on a, on M_J and on the semi-major axis of the planet a_J as follows:

$$\begin{aligned} a\sin i &= \frac{KP_{\rm orb}\sqrt{1-e^2}}{2\pi} \\ M_J \sin i &\simeq a\sin i\left(\frac{2\pi M_\star}{P_{\rm orb}\sqrt{\mathcal{G}}}\right)^{2/3} \qquad \text{(using A.8)} \\ M_J \sin i &\simeq K\sqrt{1-e^2}\left(\frac{P_{\rm orb}M_\star^2}{2\pi\mathcal{G}}\right)^{1/3} \\ a_J = \frac{aM_\star}{M_J} &\simeq \left(\frac{P_{\rm orb}\sqrt{\mathcal{G}M_\star}}{2\pi}\right)^{2/3}. \end{aligned}$$

We note that, with V_r alone, it is not possible to derive M_J and i individually.

A.5 Numerical tools for analyzing pseudo-periodic signals

A.5.1 Lomb-Scargle periodogram

In order to look for dominant frequencies in signals that are unevenly sampled, such as astronomical observations, we use a tool called Lomb-Scargle periodograms. The content of this section is heavily inspired from chapter 13 of Press et al. (1992). For a set of times $(t_i)_{i=1,\dots,N}$ and corresponding observations $(h_i)_i$, the Lomb normalized periodogram gives the spectral power of angular frequency $\omega \equiv 2\pi f$:

$$P_N(\omega) \equiv \frac{1}{2\sigma^2}\left\{\frac{\left[\sum_j\left(h_j-\bar{h}\right)\cos\omega(t_j-\tau)\right]^2}{\sum_j\cos^2\omega(t_j-\tau)} + \frac{\left[\sum_j\left(h_j-\bar{h}\right)\sin\omega(t_j-\tau)\right]^2}{\sum_j\sin^2\omega(t_j-\tau)}\right\} \tag{A.10}$$

where:

$$\begin{aligned} \bar{h} &\equiv \frac{1}{N}\sum_1^N h_i \\ \sigma^2 &\equiv \frac{1}{N-1}\sum_1^N (h_i-\bar{h})^2 \\ \tan(2\omega\tau) &= \frac{\sum_j \sin 2\omega t_j}{\sum_j \cos 2\omega t_j}. \end{aligned}$$

τ is defined so that shifting all t_i by any constant leaves P_N unchanged: P_N is independent from the choice of the origin of time. Furthermore, for any angular frequency ω, equation A.10 is equivalent to the spectral power one would obtain when fitting $A\cos\omega t + B\sin\omega t$ into $(h_i)_i$ with a least-squares approach.

The advantage of Lomb-Scargle periodograms is the ability to easily estimate the significance of a peak in the periodogram: if $(h_i)_i$ is a white noise realization, then, for a given angular frequency ω, the probability that its spectral power is larger than a given $z > 0$ is e^{-z}. Therefore, if the spectral power of M independent frequencies is computed, the probability that none of them is larger than z is $(1-e^{-z})^M$. As a consequence, if a peak of value z is observed in a periodogram, the probability for it to be a false alarm is:

$$\mathcal{P}(>z) = 1-(1-e^{-z})^M.$$

With a given range of sampled frequencies, the number of independent frequencies M remains to be determined. For small false-alarm probabilities $\mathcal{P}(> z) \ll 1$, we have $\mathcal{P}(> z) \simeq Me^{-z}$, so an error of $x\%$ on M induces an error of $\sim x\%$ on the levels of false-alarm. We usually look for levels spaced by factors of ~ 3, so the accuracy on the estimation of M does not need to be very high. In general, noting $T \equiv t_{\max} - t_{\min}$, for a dense sampling of the range $[0, f_{\max}]$ with $f_{\max} > f_c \equiv N/(2T)$, the following is a good enough estimate of M:

$$M \simeq N \frac{f_{\max}}{f_c}.$$

An example is displayed in figure A.6.

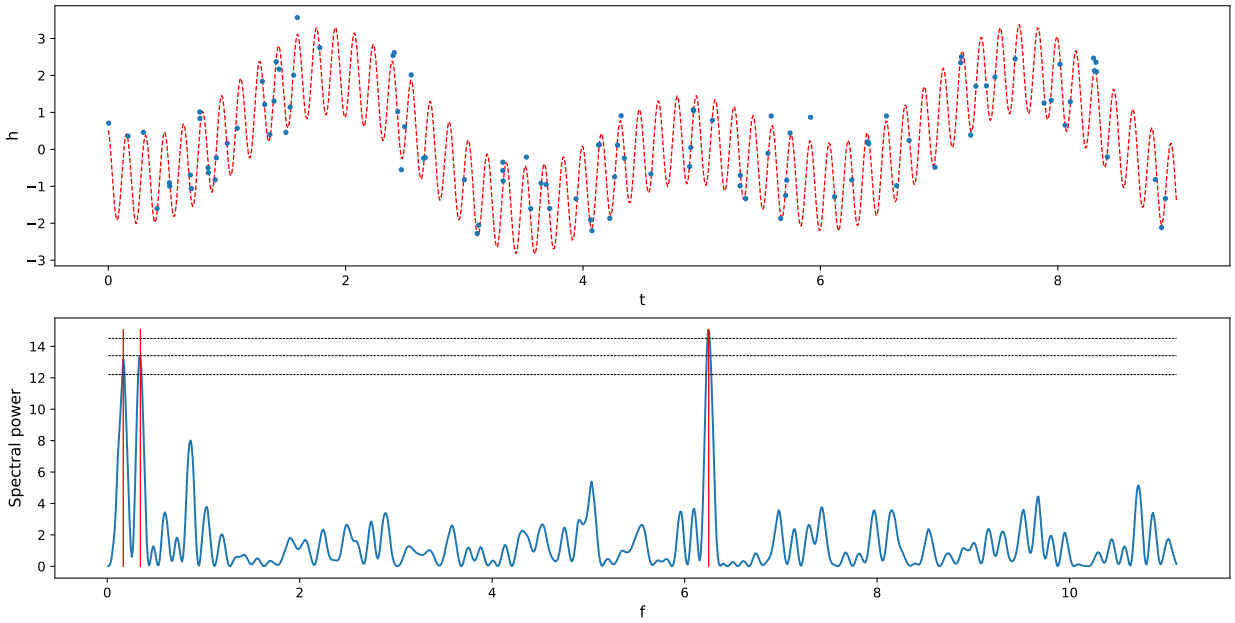

Figure A.6 – Example of a noised signal (top) and its Lomb-Scargle periodogram (bottom). *Top:* the theoretical signal, represented as a red dashed curve, is the sum of three sine curves whose frequencies are indicated by the red vertical lines in the bottom plot. The observed signal is a sample of $N = 100$ points in a time span $T = 9$ (arbitrary units), where a white noise of standard deviation 0.3 (arbitrary units) was added. *Bottom:* Lomb-Scargle periodogram for 1000 different frequencies evenly sampled between 0.01 and $f_{\max} = 2f_c \simeq 11.11$. The false-alarm probability levels of 0.1%, 0.03% and 0.01% are represented as horizontal black dashed lines (from bottom to top respectively).

A.5.2 Gaussian process regression

In the case of wTTSs, measurements such as the light curve are quasi-periodic on time spans of a few days, with the effect of stellar rotation dominating over other effects of shorter or longer time scales. However, when an observation run lengthens, the signal progressively loses its periodicity as the surface of the star evolves due to differential rotation, appearances and disappearances of spots, etc... Lomb-Scargle periodograms thus become less reliable and a new method is needed which can model these changes on longer time scales. Gaussian process regression (GPR, Rasmussen & Williams, 2006; Aigrain et al., 2012; Haywood et al., 2014; Donati et al., 2017) offers a welcome flexibility here. Let us explain it step by step.

Gaussian process By definition, a Gaussian process (GP) is a collection (finite or infinite) of random variables, any finite subset of which have a joint Gaussian distribution. A GP is characterized by its **mean** m and **covariance function** k and noted $\mathcal{GP}(m,k)$. Here the random variables will be predictions of a certain quantity evolving with time, for example the light curve $L(t)$. Modelling $L(t)$ by a GP of mean and covariance function $(\tilde{L}(t), k_L(t,t'))$ means that, for any times $t_1, t_2, ..., t_N$, the corresponding $L(t_1), L(t_2), ..., L(t_N)$ are correlated Gaussian random variables of joint probability distribution $\mathcal{N}(\tilde{\mathbf{L}}, K)$, where $\tilde{\mathbf{L}} = (\tilde{L}(t_1), \tilde{L}(t_2), ..., \tilde{L}(t_N))$ and K is the matrix defined by $K_{i,j} = k_L(t_i, t_j)$.

Inputs of GPR Let $f(t)$ be a scalar quantity that we want to model with GPR, on which we have measurements at times $(t_i)_{i=1,...,N}$, that we note $(y_i)_i$, with error bars $(\sigma_i)_i$. The inputs of GPR include the data points $(t_i, y_i, \sigma_i)_i$ of course, but also a prior distribution $\mathcal{GP}(m,k)$, which can be assimilated to a blind guess on f when no data is acquired yet. Once measurements start to be acquired, the probability distribution of f becomes conditioned by them as dictated by k. The resulting GP after accounting for all the measurements is called the posterior distribution of f.

Example: pseudo-periodic covariance function For example in our case, if we want to model our data with a pseudo-periodic function, we can set $k(t, t+P_{\text{rot}})$ to be relatively high. Thus, at an arbitrarily chosen t, while the prior distribution for $f(t)$ is $f(t) \sim \mathcal{N}(m(t), k(t,t))$, a measurement $(y(t+P_{\text{rot}}), \sigma(t+P_{\text{rot}}))$ will change the distribution of $f(t)$ by making it "closer to" $\mathcal{N}(y(t+P_{\text{rot}}), \sigma(t+P_{\text{rot}}))$. Figure 2.7 illustrates how the successive measurements condition the probability distribution on each $f(t)$, for a prior of the form:

$$\begin{aligned} m(t) &= 0 \\ k(t,t') &= \theta_1^2 \ \exp\left(-\frac{(t-t')^2}{\theta_3^2} - \frac{\sin^2\left(\frac{\pi(t-t')}{\theta_2}\right)}{\theta_4^2} \right). \end{aligned}$$

This covariance function is called a **pseudo-periodic covariance function** and its parameters, called **hyperparameters**, are the amplitude $\theta_1 > 0$, the cycle $\theta_2 > 0$, the decay time $\theta_3 > \theta_2$ and the smoothing parameter $\theta_4 \in [0;1[$. On figure 2.7, as is common with GPR, the GP is represented by its mean curve $\tilde{f}(t)$ and a shaded area of semi-amplitude $s(t)$, which indicate that, for any t, the posterior probability distribution of $f(t)$ is: $f(t)|\text{data} \sim \mathcal{N}(\tilde{f}(t), s(t)^2)$. This representation alone does not indicate how $f(t), f(t')$ are correlated for any $t \neq t'$.

Mathematical expression The exact mathematics are as follows (rigorous demonstrations are given in section 2.2 of Rasmussen & Williams, 2006, we simply paste the formulae here). We note:

- $\mathbf{t} = (t_1, t_2, ..., t_N)$ the vector of times at which data was taken,
- $\mathbf{y} = (y_1, y_2, ..., y_N)$ the vector of corresponding measurements,
- $\sigma_1, \sigma_2, ..., \sigma_N$ their respective error bars,
- $\mathbf{t}^* = (t_1^*, t_2^*, ..., t_M^*)$ the vector of times at which we wish to predict f using GPR,
- $\mathbf{f}^*$ the corresponding random variable,
- $\mathcal{GP}(m(t), k(t,t'))$ the prior,
- $\mathbf{m} = (m(t_1), m(t_2), ..., m(t_N))$ and $\mathbf{m}^* = (m(t_1^*), m(t_2^*), ..., m(t_M^*))$,
- $K(\mathbf{t}, \mathbf{t}^*)$ the $N \times M$ matrix whose element at i-th row, j-th column is $k(t_i, t_j^*)$, and we can define $K(\mathbf{t}, \mathbf{t})$, $K(\mathbf{t}^*, \mathbf{t})$ and $K(\mathbf{t}^*, \mathbf{t}^*)$ in an analogous manner.

GPR gives the posterior distribution:

$$\mathbf{f}^*|\mathbf{t},\mathbf{y},\mathbf{t}^* \sim \mathcal{N}\Big(\tilde{\mathbf{f}}^*, \mathrm{cov}(\mathbf{f}^*)\Big), \tag{A.11}$$
$$\tilde{\mathbf{f}}^* = \mathbf{m}^* + K(\mathbf{t}^*,\mathbf{t})\Big(K(\mathbf{t},\mathbf{t}) + \mathrm{diag}(\sigma_1^2,\sigma_2^2,...,\sigma_N^2)\Big)^{-1}(\mathbf{y}-\mathbf{m})$$
$$\mathrm{cov}(\mathbf{f}^*) = K(\mathbf{t}^*,\mathbf{t}^*) - K(\mathbf{t}^*,\mathbf{t})\Big(K(\mathbf{t},\mathbf{t}) + \mathrm{diag}(\sigma_1^2,\sigma_2^2,...,\sigma_N^2)\Big)^{-1}K(\mathbf{t},\mathbf{t}^*).$$

Marginal likelihood of the covariance function In practice, the problem we face is that m, k are not exactly known: we can assume a parametrized form for them (for example equation 2.2), but without knowing the hyperparameters. As a matter of fact, the hyperparameters are generally the quantities we are really interested in. For a given prior $\mathcal{GP}(m,k)$, we introduce the **marginal likelihood**, defined formally as:

$$p(\mathbf{y}|\mathbf{t},(m,k)) = \int p(\mathbf{y}|\mathbf{f},\mathbf{t})p(\mathbf{f}|\mathbf{t},(m,k))\mathrm{d}\mathbf{f},$$

where $\mathbf{y}$ and $\mathbf{t}$ are the same as above. In the integrand, $\mathbf{f}$ represents a random realization of the prior distribution $\mathcal{GP}(m,k)$, so the quantity in the integrand is the probability that the actual quantity is $\mathbf{f}$ and that the measured data is $\mathbf{y}$. So the marginal likelihood is the probability of measuring $\mathbf{y}$ at times $\mathbf{t}$, integrated over all realizations of the prior $\mathcal{GP}(m,k)$. Intuitively, the more representative the prior distribution is of the data, the higher the marginal likelihood should be. In general we use the marginal likelihood in logarithmic form, which is expressed as a function of $\mathbf{t}$ and $\mathbf{y}$ as:

$$\log\mathcal{L}(m,k) = -\frac{1}{2}\Big(N\log(2\pi) + \log(\det C) + (\mathbf{y}-\mathbf{m})^T C^{-1}(\mathbf{y}-\mathbf{m})\Big),$$

where $C = K(\mathbf{t},\mathbf{t}) + \mathrm{diag}(\sigma_1^2,\sigma_2^2,...,\sigma_N^2)$. The term $\log(\det C)$ can be seen as a penalization term over the "complexity" of k, while the term $(\mathbf{y}-\mathbf{m})^T C^{-1}(\mathbf{y}-\mathbf{m})$ controls the quality of the fit. The prior of maximal marginal likelihood will thus be, roughly speaking, the simplest one among those that allow to fit the data well enough.

MCMC for the choice of the covariance function In the framework of this thesis, the covariance of the prior will always be pseudo-periodic (equation 2.2) and the mean will be, depending on the case, either zero or a keplerian curve with 3 or 5 parameters (see section 2.4.1). Our problem is thus to optimize the values of the hyperparameters $\boldsymbol{\theta} = (\theta_1,\theta_2,...,\theta_n)$. Theoretically, we should use Bayes' rule which gives us the probability for $\boldsymbol{\theta}$ given the measurements $\mathbf{y}(\mathbf{t})$:

$$p(\boldsymbol{\theta}|\mathbf{t},\mathbf{y}) = \frac{p(\mathbf{y}|\mathbf{t},\boldsymbol{\theta})p(\boldsymbol{\theta})}{p(\mathbf{y}|\mathbf{t})}.$$

$p(\mathbf{y}|\mathbf{t},\boldsymbol{\theta})$ is the marginal likelihood as defined in equation 2.3, $p(\boldsymbol{\theta})$ is the hyper-prior distribution, corresponding to a priori information we have on $\boldsymbol{\theta}$, and

$$p(\mathbf{y}|\mathbf{t}) = \int p(\mathbf{y}|\mathbf{t},\boldsymbol{\theta})p(\boldsymbol{\theta})\mathrm{d}\boldsymbol{\theta} \tag{A.12}$$

is a normalization constant. This time, there is no particular reason for the hyper-prior to follow a Gaussian probability distribution so we cannot simplify these expressions easily. Furthermore, the integral in equation A.12 is often difficult to evaluate in practice. As a result, we optimize $\boldsymbol{\theta}$ by maximizing the marginal likelihood $p(\mathbf{y}|\mathbf{t},\boldsymbol{\theta})$ instead. Despite having an analytical expression for the likelihood (equation 2.3), it is in general very time-consuming to invert it in order to obtain

the optimum. Therefore, we sample the hyperparameter space using a Markov Chain Monte-Carlo (MCMC) algorithm, which is a way to randomly sample the hyper-parameter space and compute the likelihood at each sampled point, by favoring regions of higher likelihood. A more rigorous explanation is provided for example at section 15.8 of Press et al. (2007) or in Haywood (2015). This exploration algorithm returns the posterior probability distribution in the hyper-parameter space, from prior distributions of the hyperparameters. For the pseudo-periodic covariance functions, the hyperparameters have the prior distributions as described in table A.1 within this thesis.

Table A.1 – Priors for our GPR-MCMC runs. For the modified Jeffreys prior, σ is the knee value, for the Gaussian prior m_2 is the mean and σ_2 is the standard deviation, and for the Jeffreys and the uniform priors a and b are the lower and upper boundaries.

Hyperparameter	Prior
θ_1	Modified Jeffreys (σ)
θ_2 ($P_{\rm rot}$)	Gaussian (m_2, σ_2^2)
θ_3 ($P_{\rm rot}$)	Jeffreys (a_3, b_3)
θ_4	Uniform (a_4, b_4)